Investigation of Atmospheric Transport and Chemistry of Semivolatile Organic Pollutants Using Earth System Models

Dissertation
submitted for the award of the title
"Doctor of Natural Sciences"
to the Faculty of Physics, Mathematics and Computer Science
of Johannes Gutenberg University in Mainz

Mega Octaviani

Born in Jakarta, Indonesia

Mainz, 2018

Abstract

The global atmospheric cycling of persistent organic pollutants is complex because of partitioning among phases of the aerosol and revolatilization. Many of the substances are detrimental to human health and the environment. Global dynamical multicompartmental chemistry and transport models are needed to investigate the fate and distributions of semivolatile organic compounds.

The first study investigates climate change influences on the meridional transports of dichlorodiphenyltrichloroethane (DDT) and polychlorinated biphenyls (PCBs) to and from the Arctic by application of the MPI-MCTM model. The objectives are to determine major transport gates along the Arctic Circle, the trends in import and export fluxes, and the relationships between transports and two selected patterns of climate variability, the Arctic Oscillation (AO) and the North Atlantic Oscillation (NAO), under present-day (1970−1999) and future (2070−2099) climate. The pollutants enter the Arctic by passing through the Alaska−Northwest Territories regions, Greenland, the Norwegian Sea−Northwestern Russia, and the Urals−Siberian. On the other hand, the pollutants leave the Arctic via the Canadian Arctic and Eastern Russia. There has been a decreasing trend in DDT import fluxes to the Arctic during the present climate, but the trend is expected to change to increasing import fluxes. In contrast, PCB153 export from the Arctic is expected to be increasing in the future climate. The zonal mean meridional fluxes across the Arctic Circle are positively correlated with AO and NAO in winter, corresponding to high net imports when the frequency of positive AO and NAO increases. Under the future climate, there will be an increasing significance of the correlations for DDT while the linkage between PCB153 transport and the climate indices is expected to weaken. It is concluded that the long-term accumulation trends of other persistent pollutants in the Arctic need to be studied specifically.

In the second study, the new module SVOC was developed and coupled to the ECHAM/MESSy Atmospheric Chemistry (EMAC) model to facilitate a continuous development of modeling semivolatile organic compounds through a modular framework. Several novel approaches on the parameterization of cycling processes were introduced and validated. Parameterizations of intercompartmental mass exchange between atmosphere and the underlying surfaces in the EMAC-SVOC model are similar to those in MPI-MCTM. Other physics parameterizations were improved in the following ways: The partitioning between gas and particulate phase is described using poly-parameter linear free energy relationships; and aerosol particle size is discretized into a series of log-normally distributed modes. Through a sensitivity analysis with factor separation technique, the study examined the effects of four factors. These include the aforementioned parameterizations, as well as volatilization from land and sea surfaces, and temporal resolution of emissions. The focus here is set on four polycyclic aromatic hydrocarbons (PAHs), i.e., phenanthrene (PHE), pyrene (PYR), fluoranthene (FLT), and benzo(a)pyrene (BaP). The results indicate that seasonal emissions show dominant effects on PHE concentrations, notwithstanding the non-negligible effects from revolatilization. Other species are more sensitive to the change of internal model features. For all PAHs, the degree of model response is more determined by the interactions among factors with their contributions overall being stronger than individual factor contributions. Predicted PAH concentrations near the ground using the optimum configuration of the four factors were validated against monitoring data. The model underestimates PHE concentrations in the Arctic and tropical sites but overestimates the concentrations in the mid-latitude sites. Less volatile but mostly gaseous FLT and PYR tend to be overestimated over the Arctic and mid-latitudes, and underestimated over the tropics. There is a consistent underestimation of BaP in all regions, with bias increasing from mid-latitudes to the Arctic.

The systematic underestimation of BaP concentrations far from sources is suspected to be related to a too fast particulate-phase oxidation by ozone. This issue is addressed in the third study through a better description of BaP multiphase degradation. A new kinetic scheme was developed by considering the dependence of BaP reaction rate on two environmental parameters, that is, temperature (T) and relative humidity (RH). These parameters influence not only the phase state and diffusivity of organic aerosol coating but also the chemical reactivity of BaP. The significance of the new scheme (ROI-T) for distributions and fate was quantitatively assessed by regional (WRF-Chem-BaP) and global scale (EMAC-SVOC) modeling. In comparison to laboratory-based degradation schemes, the ROI-T scheme consistently shows better predictions and improved bias against observations at near-source sites, mid-latitude sites and most substantially at Arctic sites. The new scheme reasonably simulates the effect of low T and RH conditions to increase BaP atmospheric lifetime, leading to a more efficient transport at high altitudes or in a cold season/regions. The scheme can be adopted for modeling the multiphase degradation of other semivolatile organics.

Further applications of the EMAC-SVOC model include the quantifications of the compartmental distribution, long-range transport potential, and source−receptor relationships of PHE, PYR, FLT, and BaP. These are follow-up studies upon completion of the thesis, outlined in the final chapter, Summary and Outlook.

Kurzfassung

Das globale Zyklieren von persistenten organischen Schadstoffen in der Atmosphäre ist aufgrund der Verteilung zwischen verschiedenen Phasen des Aerosols sowie der Revolatisierung ein komplexer Vorgang. Viele der Substanzen sind schädlich für die menschliche Gesundheit und die Umwelt. Globale dynamische Multikompartiment-Chemie-Transport-Modelle werden benötigt, um das Schicksal und die Verteilung von mittelflüchtigen organischen Verbindungen zu untersuchen.

Die erste Studie untersucht Einflüsse des Klimawandels auf den meridionalen Transport von Dichlordiphenyltrichlorethan (DDT) und polychlorierten Biphenylen (PCB) von und zur Arktis durch Anwendung des MPI-MCTM Modells. Ziel ist es, wichtige Transport-Tore entlang des Polarkreises, die Trends bei Import- und Exportflüssen und die Beziehungen zwischen Transporten und zwei ausgewählten Mustern der Klimavariabilität, der Arktischen Oszillation (AO) und der Nordatlantischen Oszillation (NAO) im heutigen (1970−1999) und zukünftigen (2070−2099) Klima zu bestimmen. Die Schadstoffe gelangen in die Arktis, indem sie die Regionen Alaska−Northwest Territories, Grönland, Europäisches Nordmeer−Nordwestrussland oder Uralregion−Sibirien durchqueren. Die Schadstoffe verlassen die Arktis über die Kanada oder das östliche Russland. Die DDT-Importflüsse in die Arktis haben sich während des derzeitigen Klimas rückläufig entwickelt, aber der Trend dürfte sich zu steigenden Importflüssen ändern. Im Gegensatz dazu wird erwartet, dass der PCB153-Export aus der Arktis unter dem zukünftigen Klima zunehmen wird. Die zonalen mittleren meridionalen Flüsse über den Polarkreis korrelieren im Winter mit AO und NAO, was hohen Nettoimporten entspricht, wenn die Häufigkeit von positivem AO und NAO zunimmt. Unter dem zukünftigen Klima wird die Bedeutung der Korrelationen für DDT zunehmen, während die Verbindung zwischen dem PCB153-Transport und den Klimaindizes sich voraussichtlich abschwächen wird. Es wird der Schluss gezogen, dass die Langzeit-Akkumulation persistenter Schadstoffe in der Arktis substanzspezifisch ist.

In der zweiten Studie wurde das neue Modul SVOC entwickelt und an das ECHAM / MESSy Atmospheric Chemistry (EMAC) Modell gekoppelt, um eine flexible Entwicklung der Simulation mittelflüchtiger organischer Verbindungen durch ein modulares Modellsystem zu ermöglichen. Mehrere neue Ansätze zur Parametrisierung von Prozessen wurden eingeführt und validiert. Parametrisierungen des Stoffaustausches zwischen der Atmosphäre und den darunter liegenden Oberflächen im EMAC-SVOC-Modell sind ähnlich denen in MPI-MCTM. Andere Prozessparametrisierungen wurden auf folgende Weise verbessert: Die Verteilung zwischen Gas- und Partikelphase wird unter Verwendung von Mehr-Parameter-basiertenlinearen

Freie-Energie-Beziehungen (ppLFER) beschrieben; und die Aerosolpartikelgröße wird in eine Reihe von logarithmisch normalverteilten Modi diskretisiert. Durch eine Sensitivitätsanalyse mit Faktortrennungstechnik untersuchte die Studie die Auswirkungen von vier Faktoren. Dazu gehören die oben erwähnten Parametrisierungen, die Revolatisierung von Land- und Meeresoberflächen und die zeitliche Auflösung von Emissionen. Der Schwerpunkt liegt hier auf vier polyzyklischen aromatischen Kohlenwasserstoffen (PAHs), nämlich, Phenanthren (PHE), Pyren (PYR), Fluoranthen (FLT) und Benzo(a)pyren (BaP). Die Ergebnisse zeigen, dass saisonale Emissionen trotz der nicht zu vernachlässigenden Auswirkungen der Revolatisierung dominierende Effekte auf PHE-Konzentrationen aufweisen. Die anderen Substanzen reagieren empfindlicher auf die Veränderung interner Modellmerkmale. Bei allen untersuchten PAHs wird der Grad der Modellantwort stärker durch die Wechselwirkungen zwischen den Faktoren bestimmt, wobei diese Beiträge insgesamt stärker sind als die einzelnen Faktorbeiträge. Die vorhergesagten atmosphärischen PAH-Konzentrationen in Bodennähe unter Verwendung der optimalen Konfiguration der vier Faktoren werden anhand der Beobachtungsdaten validiert. Das Modell unterschätzt die PHE-Konzentrationen an arktischen und tropischen Orten, überschätzt jedoch die Konzentrationen in den mittleren Breiten. Die weniger flüchtigen, aber dennoch vorwiegend gasförmigen FLT und PYR werden in der Arktis und den mittleren Breiten tendenziell überschätzt und in den Tropen unterschätzt. BaP wird in allen Regionen einheitlich unterschätzt, wobei der systematische Fehler von den mittleren Breiten in die Arktis zunimmt.

Es wird vermutet, dass die systematische Unterschätzung von BaP-Konzentrationen fern von Emissionsquellen mit einer zu schnellen Oxidation durch Ozon in der Partikelphasen zusammenhängt. Dieses Problem wird in der dritten Studie durch eine bessere Beschreibung des BaP-Multiphasen-Abbaus behandelt. Ein neues kinetisches Schema wurde entwickelt, indem die Abhängigkeit der BaP-Reaktionsgeschwindigkeit von zwei Umweltparametern, nämlich der Temperatur (T) und der relativen Luftfeuchtigkeit (RH), berücksichtigt wurde. Diese Parameter beeinflussen nicht nur den Phasenzustand des und die Diffusionsfähigkeit im organischen Aerosolpartikelmaterial, sondern auch die chemische Reaktivität von BaP. Die Signifikanz des neuen Schemas (ROI-T) für Verteilungen und Schicksal der Stoffe wurde quantitativ durch regionale (WRF-Chem-BaP) und globale (EMAC-SVOC) Modellierung bestimmt. Im Vergleich zu Labor-basierten Abbauschemata zeigt das ROI-T-Schema konsistent bessere Vorhersagen und eine verbesserte Einstellung des systematischen Fehlers gegenüber Beobachtungen an Standorten in der Nähe von Emissionsquellen in mittleren Breiten und am deutlichsten in der Arktis. Das neue Schema simuliert den Effekt von niedrigen T- und RH-Bedingungen angemessen, um die atmosphärische Lebensdauer von BaP zu erhöhen, was zu einem effizienteren Transport in großen Höhen oder in kalten Jahreszeiten / Regionen führt. Das Schema kann zur Modellierung des mehrphasigen Abbaus anderer mittelflüchtiger organischer Stoffe übernommen werden.

Weitere Anwendungen des EMAC-SVOC-Modells umfassen die Quantifizierung der Kompartimentverteilung, des Ferntransportpotenzials und der Quell Rezeptor-Beziehungen von PHE, PYR, FLT und BaP. Dies sind Folgestudien nach Abschluss der Doktorarbeit, die im letzten Kapitel, 'Summary and Outlook', skizziert sind.

Contents

List of Figures

List of Tables

Chapter 1
Introduction

The term 'semivolatile organic compounds' generally correspond to organic compounds that possess medium volatility with a vapor pressure between 1×10^{-11} to 1×10^{-7} atm at 25°C (Franklin et al., 2000). Many are persistent, lipophilic, bioaccumulative, and toxic; hence they are classified as persistent organic pollutants (POPs). POPs are greatly a multimedia environmental issue as they tend to be cycled through various compartments in the biosphere (Figure 1.1). They dominantly partition into organic matter in aquatic systems and soils, and into lipids in organisms. In the atmosphere, POPs can partition between gas and particles depending on ambient temperature and properties of the chemicals. They may volatilize from the surfaces into the atmosphere and, due to their resistance to degradation, travel long distances before being deposited. The repeated cycle of volatilization and deposition results in POP accumulation in areas far from where they were used or emitted (Figure 1.2). Concern also arises around their impact on human health through multiple exposure pathways. These pathways include inhalation of the polluted air, dietary uptake (risk from the bioaccumulation in food chains), and adsorption from contact with polluted water and soil or dust. The exposure to POPs can cause serious health problems including certain cancers, birth defects, reproductive and immune dysfunctions, endocrine disruption, and neurodevelopment disorders (Boffetta et al., 1997; Pauwels et al., 2000; Bolt and Degen, 2002; WHO, 2010). While available measurements of POPs have limited spatial and temporal resolution, modeling exercises have been applied to understand the global distribution of POPs and processes affecting their fate. The following describes the general characteristics and cycling processes of POPs and different types of numerical models used to study their chemical fate in the global environment.

1.1 Persistent organic pollutants

According to the 1998 Aarhus Protocol on Persistent Organic Pollutants under the 1979 Geneva Convention on Long-range Transboundary Air Pollution (CLRTAP), POPs are defined as substances that: (i) possess toxic characteristics; (ii) are persistent; (iii) bioaccumulate; (iv) are prone to long-range transboundary atmospheric transport and deposition; and (v) are likely to cause significant adverse human health or environmental effects near to and distant from

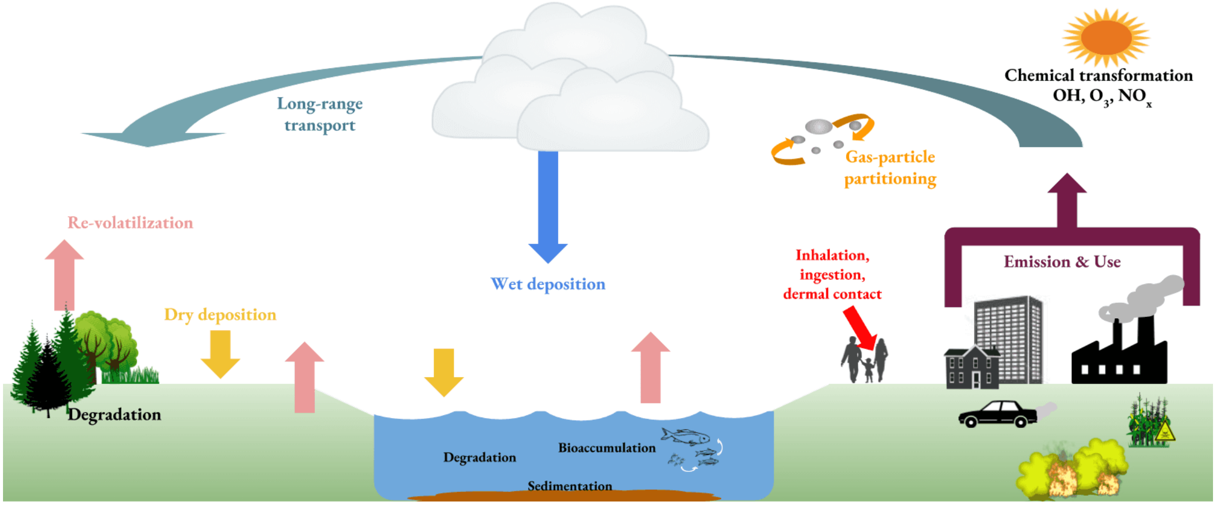

Figure 1.1: Main environmental cycling processes of POPs which determine their fate in the global environment

their sources (UNECE, 1998). The Aarhus Protocol on POPs is an agreement under the UN Economic Commission for Europe (UNECE) to control, reduce or eliminate any discharges, emissions and losses of POPs to the environment. The protocol entered into force by the end of 2003. The attention was raised to the global level in 2001 under the UNEP Stockholm convention (see http://chm.pops.int). The convention entered into force in May 2004 by 177 parties from the United Nations to cover 12 chemicals or the so-called "dirty dozen" or 'legacy' POPs (UNEP, 2008b). As of May 2017, the Stockholm Convention has been ratified by 181 parties and 16 additional chemicals ('emerging' POPs) have been added to be regulated under the treaty (UNEP, 2017).

1.1.1 Groups and properties of POPs

Table 1.1 shows the list of POPs controlled under the two aforementioned international agreements. They are generally divided between chemicals that are intentionally produced (including organochlorine pesticides and industrial chemicals) and those that are formed as accidental by-products from combustion and synthesis of other chemicals (e.g., PAHs, PCDD/Fs). The following screening criteria are set out in the Stockholm Convention for adding new substances/substance group into a POP (UNEP, 2008a), and are similarly applied in the Aarhus Protocol (UNECE, 1998):

- **Persistence**
  If there is an evidence that the half-life of the chemical in water is greater than two months, or that its half-life in soil and sediment is greater than six months, or that the chemical is sufficiently persistent to be of concern.

- **Bioaccumulation**
  If there is an evidence that the bioconcentration factor or bioaccumulation factor of the chemical in aquatic species is greater than 5000, or if the logarithm of the octanol-water partition coefficient ($\log \mathrm{K}_{\mathrm{ow}}$) is greater than 5, or if there are other monitoring data in biota that indicates the chemical bioaccumulates.

- **The potential for long-range environmental transport**
  If measured levels of the chemical in locations far from points of release are of potential concern, or if the half-life of a compound in the air is greater than two days.

- **Adverse effects**
  If there is an evidence of adverse effects to human health or to the environment, or given toxicity and ecotoxicity data that indicate the potential for damage to human health or the environment. Observed adverse effects are, e.g., effects on the reproduction, development and the immune system, and the promotion of tumors.

POPs are expected to have complex environmental distribution owing to their diverse physicochemical properties, such as vapor pressure, degradation half-lives, and phase partition coefficients. The first requirement for any assessment of a specific POP is thus the compilation of its certain properties. These properties have been compiled in various databases or software packages either from field and laboratory measurements or based on theoretical predictions (e.g,

Table 1.1: List of POPs controlled under the Stockholm Convenction (UNEP, 2008b, 2017) and the Aarhus Protocol on POPs (UNECE, 1998, 2010).

Chemicals[*]	Key source(s)	Stockholm Convention[†]	Aarhus Protocol[‡]
Pesticides			
Aldrin	Insecticide	A	I
Chlordane	Insecticide	A	I
DDT (dichlorodiphenyltrichloroethane)	Insecticide	B	I
Dieldrin	Insecticide	A	I
Endrin	Insecticide	A	I
Heptachlor	Insecticide	A	I
Mirex	Insecticide	A	I
Toxaphene	Insecticide	A	I
α-HCH (alpha-hexachlorocyclohexane)	Insecticide	A	I
β-HCH	Insecticide	A	I
Lindane (γ-HCH)	Insecticide	A	I
Chlordecone	Insecticide	A	I
PCP (pentachlorophenol) and its salts and esters	Herbicide, insecticide, fungicide, algaecide	A	-
Endosulfan and its isomers	Insecticide	A	-
Industrial chemicals			
Hexabromobiphenyl	Flame retardant	A	I
HBCD (hexabromocyclododecane)	Flame retardant	A	-
hexaBDE (hexabromodiphenyl ether) and heptaBDE	Flame retardant	A	I
tetraBDE and pentaBDE	Flame retardant	A	I
decaBDE	Flame retardant	A	-
PFOS (perfluorooctanesulfonic acid), its salts and PFOSF (perfluorooctanesulfonyl fluoride)	hydraulic fluids, fabric protector, photo imaging, fire-fighting foams	B	I, II
SCCPs (short-chain chlorinated paraffins)	Plasticizers	A	I, II
Unitentional releases			
PCDDs (pentachlorinated dibenzo-p-dioxins)	By-products during chlorination processes and combustion	C	III[a]
PCDFs (pentachlorinated dibenzofurans)	By-products during chlorination processes and combustion	C	III[a]
PAHs (polycyclic aromatic hydrocarbons)[§]	By-products from incomplete combustion of coal, wood and oil	-	III[a]
Mixed groups			
HCB (hexachlorobenzene)	Fungicide, by-products from manufacture of chlorinated industrial chemicals	A, C	I, III[a]
PCBs (polychlorinated biphenyls)	Transformers and capacitors, heat-exchange fluids, and by-products from waste incineration	A, C	I, III[b]
HCBD (hexachlorobutadiene)	Industrial solvents, by-products during chlorination processes	A, C	I
PCNs (polychlorinated naphtalenes)	Insulating coatings for electrical wires, by-products from thermal industrial processes	A, C	I
PeCB (pentachlorobenzene)	Fungicide, flame retardant, by-products from thermal industrial processes	A, C	I

[*] The 'dirty dozen' or 'legacy' POPs are given in italics.

[†] Annex A: chemicals production and use must be eliminated; annex B: chemicals restrictions for production and use; annex C: reduce the unintentional release of chemicals.

[‡] Annex I: substances scheduled for elimination; annex II: substances scheduled for restrictions on use; annex III: substances scheduled for reduction in annual emissions from the level of emission in a reference year ([a]1990 or an alternative year from 1985−1995 inclusive. [b]2005 or an alternative year from 1995−2010 inclusive.)

[§] For the purposes of emission inventories, four indicator compounds shall be used: benzo[a]pyrene, benzo[b]fluoranthene, benzo[k]fluoranthene, and indeno[1,2,3-cd]pyrene.

Shen and Wania, 2005; Mackay et al., 2006; and USEPA, 2008). They are continuously being revised and improved as many studies attempted to reduce the uncertainties related to the reported values.

Phase distribution refers to environmental partitioning in a three-phase system, that is, air, water, and octanol, with three partition coefficients: the partition coefficient between air and water, K_{aw}, between octanol and water, K_{ow}, and between octanol and air, K_{oa} (Mackay, 2010). The simplest method of estimating K_{aw} (or Henry's law constants) is as a ratio of vapor pressure to water solubility. K_{ow} is a measure of hydrophobicity or the tendency of a chemical to partition out of water. Figure 1.3 illustrates a two-dimensional physicochemical substance properties phase space, defined as a function of $\log K_{oa}$ on the x-axis and $\log K_{aw}$ on the y-axis, while the diagonal lines from the lower left to the upper right correspond to $\log K_{ow}$. The typical K_{aw} values for most known POPs are between $1{\times}10^{-1}$ and $1{\times}10^{-3}$ but for less volatile PAHs can be as low as $1{\times}10^{-6}$, K_{ow} ranges from $1{\times}10^{4}$ and $1{\times}10^{7}$, and K_{oa} between $1{\times}10^{6}$ and $1{\times}10^{12}$ (Wania and Mackay, 1999). POP partitioning into organic phases is thus higher than into water by $4-7$ orders of magnitude and higher than into air by $5-10$ orders of magnitude (that is, environmental concentrations: organic phases $\gg$ water $>$ air). Nevertheless, the air phase is typically much larger in volume than the other phases (environmental volumes: air $>$ water $\gg$ organic phases), hence the mass of POPs in these environmental phases tends to be on the same order of magnitude (Wania and Mackay, 1999). The partition coefficients are highly dependent on temperature, suggesting that a chemical will shift its location on the substance properties phase space to the lower right in response to decreasing temperatures. The temperature dependence of partition coefficients as well as degradation rate constants can be accounted for using the van't Hoff equation, given data on the internal energies of phase transition and activation energies are available.

1.1.2 Environmental distribution and transport pathways

POPs have a complex global distribution as they possess distinct physicochemical properties and their sources and transport pathways into and in the global environment vary. It is thus not possible to state a general theory of the global fate of all POPs. However, concerns have been expressed that the polar regions become 'global sinks' for POPs released/used elsewhere. A number of studies had reported significant POP concentrations in different media (air, water, snow, soil, vegetation, biota) in the Arctic (Barrie et al., 1992; Fisk et al., 2002; Fernández and Grimalt, 2003; Dalla Valle et al., 2004; Wit et al., 2004; Dalla Valle et al., 2005; Hung et al., 2005a; Li and Macdonald, 2005; Butt et al., 2007; Wit et al., 2010).

Conventional views emphasized the 'global distillation' theory as the processes responsible for the accumulation of organochlorine chemicals in polar regions (Wania and Mackay, 1993). This theory was first introduced by Goldberg (1975) and postulates that the migration pattern of chemicals to higher latitudes, so-called 'grasshopper effect', consists of successive evaporation/condensation cycles (Figure 1.2). POPs migrate at different velocities based on the degree of volatility and ambient temperature. Highly volatile POPs tend to remain airborne and migrate faster while less volatile POPs tend to deposit into water, snow, ice, soil or vegetation. As a result,

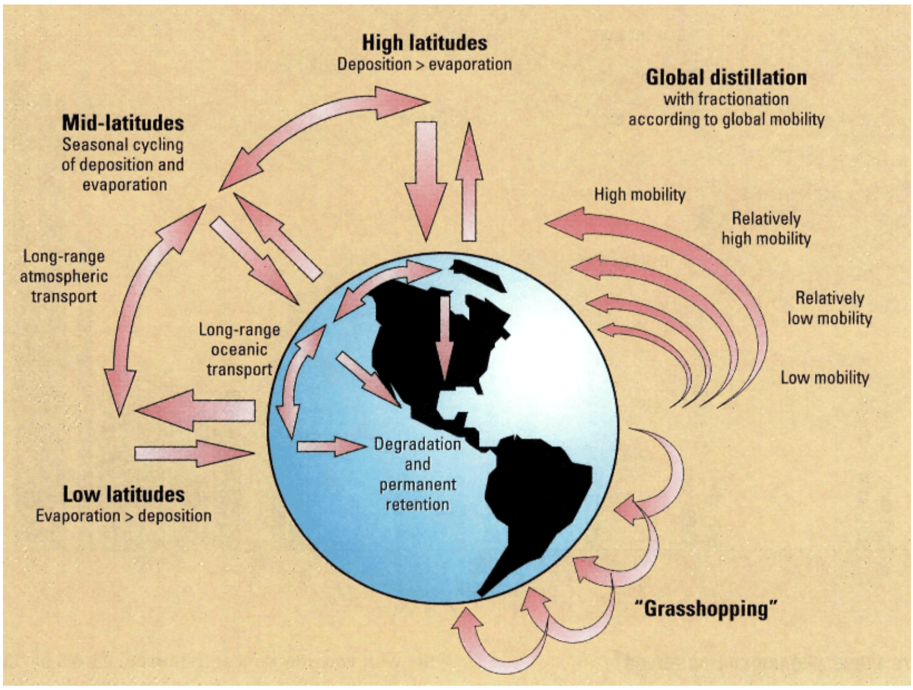

Figure 1.2: POP migration process according to the global distillation and fractionation theories. Adopted from Figure 1 of Wania and Mackay (1996)

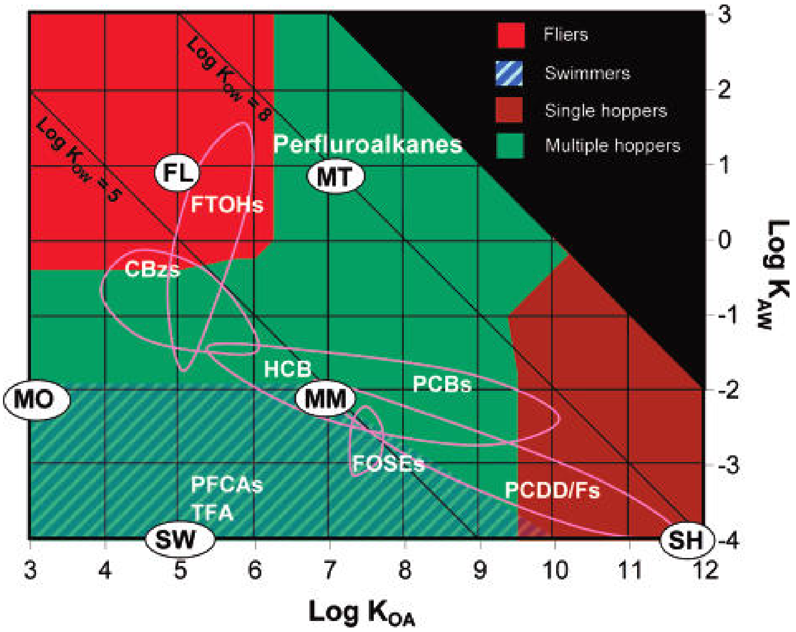

Figure 1.3: Physicochemical substance properties phase space, characterizing the major transport modes for organic chemicals, based on their octanol–air and air–water partition coefficients $\log \mathrm{K}_{\mathrm{oa}}$ and $\log \mathrm{K}_{\mathrm{aw}}$. The assessment of major transport modes was derived from model estimates of the Arctic Contamination Potential (ACP) assuming 10 years of steady emissions into air (zonal multimedia fate model; Wania, 2003). Six hypothetical combinations of partitioning properties have been selected to represent chemicals that will be transported as single hoppers (SH), swimmers (SW), multihoppers (MO, MM, and MT), and fliers (FL). MO: multihopper exchanging with the oceans, MM: multimedia multihopper, MT: multihopper exchanging with terrestrial surfaces. Adopted from Gouin and Wania (2007).

they become 'fractionated' (the composition of contaminant mixtures varies) along latitudinal or altitudinal gradients when condensing in cold environments (Wania and Mackay, 1996; Daly and Wania, 2005). Nevertheless, Wania and Mackay (1996) state that not all monitoring data support the concept of global fractionation as it appears that the role of degradation and retention in soils and sediments, spatial variability of emissions, and rate of dispersion may result in chemicals having quite different behavior.

The atmosphere has been considered as the most efficient pathway for long-range transport and the global distribution of many POPs (organochlorine pesticides, PCBs, PBDEs, PAHs, PCDD/Fs) as reported by atmospheric measurements in remote locations (Kallenborn et al., 2012 and references therein). The potential for long-range atmospheric transport largely depends on the gas−particle partitioning, the physicochemical properties of the chemicals, biogeochemical cycles and geophysical processes (Lohmann et al., 2007). For example, Wania (2003) suggests POPs accumulation in the Arctic ecosystems via atmospheric transport is more efficient for substances that are both relatively volatile and water soluble, or semivolatile and hydrophobic. Accordingly, Wania (2006) and Gouin and Wania (2007) derived a categorization of chemical transport behavior on a global scale in proportion to their specific partitioning properties. This assessment was based on the results of the Arctic Contamination Potential (ACP) calculations with a zonal multimedia fate model (Globo-POP) for hypothetical persistent chemicals conducted by Wania (2003). Figure 1.3 shows the four major transport modes, namely 'fliers', 'single hoppers', 'multihoppers', and 'swimmers'. Chemicals in 'fliers' category, with a $\log \mathrm{K_{aw}} > 0$ and $\log \mathrm{K_{oa}} < 6.5$, are so volatile that they do not deposit to the Earth's surface even in the polar environment. Those called 'single hoppers' ($\log \mathrm{K_{oa}} > 10$) tend to sorb to particles in the atmosphere and are usually deposited irreversibly to the Earth's surface, which limits the potential for Arctic contamination. Those referred to as 'multihoppers' are semivolatile substances that readily undergo atmosphere−surface exchange in response to temperature changes and they consistently led to higher calculated ACP values. Chemicals with intermediate $\log \mathrm{K_{aw}}$ values ($-4 < \log \mathrm{K_{aw}} < 0$) exchange mostly with aqueous surfaces, whereas chemicals with intermediate $\log \mathrm{K_{oa}}$ values ($6.5 < \log \mathrm{K_{oa}} < 10$) exchange primarily with land surfaces. The intersect of the two regions are chemicals that exchange with both oceanic and continental surfaces. Last, chemicals designated as 'swimmers' undergo significant meridional transport in the oceans, with the ACP values being highly sensitive to the oceanic diffusion coefficients (Wania, 2006).

Most legacy POPs (PCBs, DDT, chlorobenzene, chlordane, and toxaphene) are 'multihoppers' while HCHs and many emerging POPs (e.g., PFOS and PFOA) are in the 'swimmers' category (Wania, 2003, 2006; Lohmann et al., 2007). Because of the strong sorption of higher molecular PAHs to atmospheric particles and their atmospheric levels are presumably controlled by primary emissions, this group of substances may act as "single hoppers" (Lohmann et al., 2007).

1.2 Global change and its effects on POPs behavior

As POPs behavior depends on the complex interaction of many factors, any significant change in environmental conditions is likely to affect the biogeochemical cycle of the contaminants and consequently their distribution and fate. Numerous reviews have been published recently that discussed the potential impact of global climate change on contaminant, fate, transport, bioccumulation, and risk (e.g., Dalla Valle et al., 2007; Lamon et al., 2009a; Kallenborn et al., 2012; Teran et al., 2012; and Nadal et al., 2015). Some physical environmental parameters that have been reported to influence (directly or indirectly) the chemical behavior include temperature, large-scale wind speeds, duration and intensity of rain and snow precipitation, ocean salinity, permafrost and ice cover, radiation intensity, phytoplankton dynamics, and organic carbon content. For instance, the observed increasing trends of HCBs and PCBs in the Arctic could be attributed to the enhanced revolatilization from ocean to air induced by climate warming (Ma et al., 2011). Melting glaciers in Antarctica may act as the secondary source for DDT contamination in coastal Antarctic seas (Geisz et al., 2008), in addition to input from ongoing use in southern Africa (Brink et al., 2009). High rates of snow deposition and precipitation in high- and mid-latitude mountains may lead to a large contaminant release during snowmelt with the evaporative loss being smallest for less volatile POPs (Daly and Wania, 2005).

The synergistic effects of multiple aspects of climate change on POPs behavior and environmental fate still become the subject of ongoing research. They are often investigated through the application of either multimedia fate models or chemistry transport models (see Section 1.3). These models are a key component in understanding the environmental dynamics of POPs and how their changes may affect contamination of pristine areas such as the Arctic and mountain regions (Gouin and Wania, 2007; Teran et al., 2012; Hansen et al., 2015). Lamon et al. (2009b) have simulated the effects of changing temperature, wind speed and precipitation patterns on the fate of two PCB congeners using a multimedia box model. They found that higher temperatures drive increased primary and secondary emissions of PCBs, and the largest relative increase in air concentrations was found to occur in the Arctic and central Pacific. Furthermore, higher wind speed under a future climate scenario generally results in more efficient intercontinental transport of PCBs. Lammel and Stemmler (2012) used a global chemistry transport model to investigate the global distribution and emission pathways of four PCB congeners for the period 1950−2010. They concluded that revolatilization from surfaces are on the long term increasingly gaining importance over primary emissions and that the delivery of the contaminants to high latitudes is predicted to be more efficient than previously suggested.

Using a much finer spatial resolution of a hemispheric model, Hansen et al. (2015) investigated how climate change affects the transport of HCHs and PCBs to and their fate within the Arctic. The results indicate that the mass of HCHs was predicted to be higher, whereas the sign of change in PCB mass was predicted to depend on the congener and initial concentrations. The process that dominates the environmental behavior of POPs in the Arctic under a future climate is the mass transfer from the surface media to the atmosphere induced by the higher mean temperature. This is to some degree counteracted by higher degradation rates also following the higher mean temperature. As a result, it is not possible to state whether there is a general climate penalty or a climate benefit on POPs transport since it depends on the physicochemical properties of the compounds (Hansen et al., 2015). The study also confirms findings from previous modeling studies (Lamon et al., 2009b; Armitage and Wania, 2013; Gouin et al., 2013; Wöhrnschimmel et al., 2013) that predicted the effect of climate change on the environmental concentrations of

POPs in the Arctic is moderate (within a factor of two into the 21st century). However, the model studies do not agree in terms of the direction of the changes due to differences in process parameterizations, emission and climate change scenarios, and the substance physicochemical properties.

Climate change involves not only changes in the mean values of physical environmental parameters but also changes in their variability. Recent studies have shown correlations between observed mid-latitude air concentrations of POPs and climate teleconnections such as the Arctic Oscillation (Becker et al., 2008), the North Atlantic Oscillation (NAO), the Pacific North American (PNA) (Ma et al., 2004a,b), and the El-Niño Southern Oscillation (ENSO) (Ma et al., 2003a, 2004a). The modeling study by MacLeod et al. (2005) estimated that the maximum variability in atmospheric PCB concentrations attributable to the variability in NAO is approximately a factor of two with stronger NAO influence being apparent during winter and spring in Northern Europe and the Arctic. Despite the evidence of the short- and medium-term climate fluctuations in influencing POPs distribution, more studies are required to explore the link between variability in POPs transports and the climate variability.

1.3 Modeling the environmental fate of POPs

Two different types of models have been developed to study the environmental fate of POPs and other semivolatile contaminants, which vary in their complexity, namely, multimedia fate (box) models and chemistry transport models (CTMs).

1.3.1 Multimedia fate models

In a multimedia box model, the environment is described by a number of well-mixed compartments with homogeneous environmental characteristics (Wania and Mackay, 1999; Mackay, 2010). This type of model is particularly well suited to explain differences in environmental fate and transport among chemicals in a defined environment and explore the influence of variable environmental (and climate change-induced) factors on chemical fate and transport (Lamon et al., 2009a). Multimedia fate models apply the fugacity approach which describes the tendency of a chemical to escape from a phase and has the unit of pressure Mackay (2010). The fugacity of an organic chemical in a given phase is calculated as the ratio between the chemical concentration in the phase of interest and the 'fugacity capacity' (Z) of the phase. The Z term describes the capacity of a chemical to remain in the phase. If the Z values of a chemical for two phases are equal, there is no tendency for a mass exchange as the phases are in equilibrium. Otherwise, the chemical tends to migrate into (or stay in) the phase with the largest Z value.

The simplest multimedia model is a closed one-compartment system that only requires information on the chemical amount and physicochemical properties to calculate the fugacity using steady-state and equilibrium assumptions. The complexity can be increased by adding new connected compartments and a more detailed description of fate processes (e.g., advective inflow and outflow and chemical transformation) at the expense of additional requirements for input data describing both the environment and the chemical. A further development of this model is the spatially resolved version that covers a region or the entire globe with several climate zones each consisting of a set of environmental compartments. The input environmental parameters are inferred from geographical reference databases and climatic averages of meteorological data. In recent years, there has been a great diversity in the extent of the model domains, the number of regions and compartments, and the methods to provide input data. For instance, the Globo-POP is a multimedia fate model developed by Wania and Mackay (1995) based on ten zonally-averaged climate zones. This model takes into account nine environmental compartments: freshwater and sediment, four atmospheric layers, upper ocean layer, cultivated and uncultivated soils. Its most recent application was aimed at exploring the potential influence of climate change and particulate organic carbon scenarios on the fate of organic chemicals in the Arctic marine environment (Armitage and Wania, 2013). The ClimoChem model (Scheringer et al., 2000) divides the world into flexible number n of zones corresponding to the latitudinal range of $180°/n$. It considers four environmental compartments (coastal water, soil, vegetation, and atmosphere). The version by Stocker et al. (2007) implements the ice and snow compartments since they play a role in influencing atmospheric chemistry. Toose et al. (2004) developed the BETR-World model and applied 25 geographical regions with area ranging from 5 to 50 million km^2. The BETR-Global version represents the global environment as a connected set of 288 multimedia regions on a 15° grid, hence both latitude and longitude are resolved (MacLeod et al., 2005; Lamon et al., 2009b). Each region in both BETR model versions contains two upper and lower atmospheric compartments and five terrestrial compartments (soil, vegetation, coastal water, freshwater, and sediments).

The multimedia models are arguably less suitable to provide high spatial and temporal resolution of chemical transports and distributions. Due to simplifications of model parameters, they also have limited capability of reflecting environmental variability, e.g., the episodic character of atmospheric transports is neglected (Scheringer and Wania, 2003). In addition, most models cannot be applied to chemicals that come from transformation products of the parent compound. This is because they are built upon a set of mass-balance equations for one species circulating between different model compartments (OECD, 2004).

1.3.2 Chemistry transport models

Studying the environmental distribution of POPs by adopting chemistry transport models (CTM) implies the application of 3D dynamic Eulerian models coupled with aerosol, surface, and chemistry modules. The addition of a surface module aims to describe air−surface exchange processes and biogeochemical cycles of contaminants whereas a chemistry module describes the changes in air concentrations due to phase partitioning and chemical transformations. In comparison to the multimedia models, CTMs have considerably higher spatial and temporal resolution and require large numbers of model parameters, hence they are more resource intensive. The fate and transport of the chemicals are modeled in relation to geo-reference entities (e.g., land, sea, soil, and vegetation) and the behavior of the contaminants depends on time, location, and mode of entry into the environment (OECD, 2004). These models are applied at multiple scales from regional (e.g.: Ma et al., 2003b; Gusev et al., 2005; Galarneau et al., 2014), hemispheric (e.g.: Hansen et al., 2004; Malanichev et al., 2004), to global (e.g.: Semeena et al., 2006; Gong et al., 2007; Friedman and Selin, 2012; Shrivastava et al., 2017).

CTMs differ with respect to domain size, grid resolution, process parameterizations, and the types and numbers of environmental compartments covered. The model designs are suited to their particular needs. Some examples of global scale CTMs are as follows:

- The multicompartment chemistry-transport model MPI-MCTM is originally based on an atmosphere general circulation model with embedded aerosol and marine biogeochemistry modules and encompasses 2D surface compartments, i.e. topsoil, vegetation, and ocean mixed layer (Semeena and Lammel, 2003). The model was later improved to replace the 2D ocean by a 3D ocean model including a 2D sea-ice compartment (Guglielmo et al., 2009). Later, a land-ice compartment was included (Hofmann et al., 2012). MPI-MCTM has been implemented to serve a number of purposes — for example: to study the major features of the global fate and long-range transport of γ-HCH and DDT as well as the significance of the marine biogeochemistry for the substance cycling (Semeena and Lammel, 2005; Guglielmo et al., 2009); to follow the environmental distributions of DDT from the early years of use until far beyond the peak application (Stemmler and Lammel, 2009); to test the effect of substance properties of four PCB congeners on their global distributions, fractionation and long-term trends (Lammel and Stemmler, 2012); and to investigate ocean exposure to PCBs and DDT following long-term deposition to the oceans (Stemmler and Lammel, 2013). The model was typically run with a horizontal resolution of 2.8° × 2.8° and 19 vertical layers in the atmosphere and a mean resolution of 3° and 40 depth levels in the ocean.
- Gong et al. (2007) and Huang et al. (2007) applied the global GEM model coupled with a gas phase chemistry module and an aerosol module. They further incorporated processes into the model to describe exchanges between water/soil and atmosphere, partitioning between gaseous and particulate phases, and the removal of particle-bound POPs. The GEM/POPs model was applied at a 2° × 2° grid to simulate the transport, deposition, and partitioning of PCBs (Gong et al., 2007) and to investigate their global budgets, intercontinental transports and deposition patterns (Huang et al., 2007).
- The chemical transport model GEOS/Chem implemented extended parameterizations describing the mechanisms of gas−particle partitioning and atmospheric oxidation of semivolatiles (Friedman and Selin, 2012). Volatilization from and degradation within the surfaces were not accounted for. The first model application was dedicated for the simulations of long-range atmospheric transport of PAHs using a horizontal resolution of 4° × 5° (Friedman and Selin, 2012). The importance of oxidation, gas−particle partitioning, and deposition to global PAH concentrations and atmospheric lifetimes was also of interest. GEOS/Chem was further used to study the effects of 2000−2050 emissions and climate changes on atmospheric PAH concentrations and long-range transport (Friedman et al., 2013). Also, Friedman et al. (2014) examined the importance of secondary organic aerosols to the PAH transport by testing the ability of different partitioning configurations within the model to reproduce observed PAH concentrations.

It should be pointed out that one cannot always expect to gain better accuracy of results from CTMs than those from the multimedia models because of the uncertainties of emission estimates, chemical properties, degradation rates, and process parameterizations, as well as the complexity of the Earth system. To instill a sufficient level of confidence in the CTM predictions, the model should be evaluated against observations, and input data need to be proved reliable.

1.4 Objectives of the thesis

As mentioned above, the fate and transport of persistent and semivolatile organics in the environment is linked to climate parameters as they drive the underlying mechanisms that determine the POPs behavior. There is a growing interest among the scientific community to improve the understanding of the potential implications of global climate change on environmental cycling and long-range transport of POPs. The interest is mainly associated with historic and contemporary use of chemicals. Most legacy POPs are "multihoppers" and atmospheric transport was identified as the major pathway of their global dispersal (Lohmann et al., 2007). Some recent studies have also reported how the atmospheric transport is affected by global circulation patterns of climate variability especially when secondary emissions are the main source for the chemical release (Ma et al., 2004b; Macdonald et al., 2005; MacLeod et al., 2005). The first objective of this thesis is addressed at understanding the effects of climate change on the long-range atmospheric transports of some legacy contaminants, DDT and PCBs, into and out of the Arctic environment. The study also aims to understand the effect on the pollutant transport of two interannual climate oscillations, AO and NAO. For this purpose, simulations using the global multicompartment chemistry-model MPI-MCTM were conducted. This model was applied due to its well descriptions of environmental compartments which include the 3D atmosphere and oceans, the 2D topsoil, vegetation, and sea ice surfaces. In addition to the cycling in the atmosphere and surface media, chemicals are subject to hydrodynamics, degradation, and gravitational settling in the deep sea. For DDT and PCBs, it has been shown that the role of the ocean in global cycles is significant as it acts as a secondary source of these compounds (Stemmler and Lammel, 2013).

Much uncertainty is still present in modeling global environmental cycling of POPs due to imperfect parameterizations, lack of confidence in physicochemical properties and degradation rates, and limitations of spatial and temporal coverage of emissions. Considerable efforts have been continuously devoted to the improvement of understanding key processes in multiple compartments. There is a need to facilitate such improvement in CTMs. The second part of the thesis aims for developing a global CTM that can serve such a purpose. In this study, a new module coupled to the ECHAM/MESSy Atmospheric Chemistry-Climate model (EMAC) is developed to simulate the atmospheric cycling (for gas, aqueous, and particulate phases) and air-surface exchange processes of semivolatile organic pollutants. The new model is hereinafter referred to as EMAC-SVOC which is based on a modular framework and softcoding principle. These elements are practically essential to run simulations with flexible input and process complexity and to facilitate future improvement. The focus of the model development is on the global cycling and long-range transport of four PAHs: phenanthrene (PHE), pyrene (PYR), fluoranthene (FLT) and benzo(a)pyrene (BaP). PAHs are selected as they are a concern for human health (via inhalation exposure), their concentrations are notably higher than other legacy POPs (Laender et al., 2011), and reliable emission estimates exist for this substance group (Shen et al., 2013). Although PHE, PYR, and FLT are not of imminent concern, they are selected here to study the influence of different physicochemical properties on the global fate of semivolatile and hydrophobic organics. The ocean is interpreted as a 2D compartment in the current model version where chemicals are subject to degradation and air−ocean mass exchange. These processes are considered sufficient for PAHs as they are hypothetically known to act as "single hop" chemicals. Nevertheless, the extent by which the air concentrations are influenced by revolatilization is tested in the study. Some advances in process parameterizations are also tested, from the application of a multiparametric approach in gas−particle partitioning to the size discretization of particulate-phase tracers.

Some challenging issues remain that limit the predictive capability of the model. In particular, there are problems to accurately quantifying realistic atmospheric degradation processes of the particulate-phase PAHs. This issue is discussed in the third study. Its aim is to investigate the multiphase degradation of organic pollutants associated with their behavior sorbed to atmospheric aerosols. In the case of PAHs, especially BaP, the rate of degradation changes according to the diffusivity of aerosol coating and chemical reactivity of the compound. The cold and dry environment will slow down or even shut off the particulate-phase BaP oxidation with ozone due to shielding by the aerosol coating. In this study, a new kinetic scheme is developed and incorporated into regional and global scale CTMs to represent temperature and humidity effects on heterogeneous BaP degradation rates.

Chapter 2

Atmospheric Transport of Persistent Organic Pollutants to and from the Arctic under Present-Day and Future Climate

This chapter is comprised of the article “Atmospheric transport of persistent organic pollutants to and from the Arctic under present-day and future climate” by Mega Octaviani, Irene Stemmler, Gerhard Lammel, and Hans F. Graf published in *Environ. Sci. Technol.*, 2015, 49: 6, pp. 3593–3602 (DOI: 10.1021/es505636g). G.L., I.S., and M.O. (candidate) conceived the study. The candidate designed methods and conducted all analyses with guidance from G.L. and input from I.S. and H.G. I.S. provided the model data. All coauthors discussed the results. The article was written by the candidate and reviewed by all coauthors. The postprint version of the article and its supplementary materials were incorporated into this chapter and Appendices A−B, respectively, with minor modifications and rearrangements.

2.1 Introduction

Persistent organic pollutants (POPs), through uptake by biota (Atlas and Giam, 1981; Calamari et al., 1991) pose a hazard for the ecosystems and food chains even in remote regions (UNEP, 2003). Many of these substances are cycling between environmental compartments and are semivolatile, that is, subject to revolatilization from land and sea surfaces (Semeena et al., 2006; Stemmler and Lammel, 2009; Wania and Mackay, 1993). Cycling of POPs is expected to be influenced by meteorological parameters (wind, temperature, precipitation, and others) that affect the substance phase changes (Ma et al., 2004a; Macdonald et al., 2005, 2003). The occurrence of most POPs in the Arctic is believed to be dominated by atmospheric transports (AMAP, 2003; Wit et al., 2004; Gouin and Wania, 2007) and at the same time is undergoing fast climate change (Macdonald et al., 2005; Wit et al., 2004; Ma et al., 2011). POP cycling in remote regions under climate change has been well documented, mostly using multimedia models, including spatially resolved ones (Dalla Valle et al., 2007; Huang et al., 2007; Wöhrnschimmel et al., 2013). Based on multicompartmental modeling it was hypothesized that multihopping should enhance the atmospheric transport of POPs to the Arctic (Semeena and Lammel, 2005), and it was indicated that spring maxima of α-hexachlorocyclohexane (HCH) in the Arctic are caused by revolatilization from snow (Hansen et al., 2008). However, the spatial patterns of polarward transport and temporal trends in the import of POPs to and export from the Arctic have not been studied.

Interannual atmospheric climate fluctuations affect global pollutant distribution and transport (Ma et al., 2004a; Duncan and Bey, 2004; Eckhardt et al., 2003; Li et al., 2002). The Arctic Oscillation (AO) and the North Atlantic Oscillation (NAO) are two dominant sources of large-scale climate variability in the Arctic. The AO is a hemispheric mode of large-scale oscillation in atmospheric mass in the Northern Hemisphere (NH), with its zonally symmetric signature showing larger anomalies over the North Atlantic and North Pacific sectors (Thompson and Wallace, 1998). During a positive AO phase (AO+), when pressure is abnormally low in the polar region, the high mid-latitude westerly winds are stronger and transport of pollutants from eastern North America and Western Europe to the Arctic is most effective. Otherwise there is an increased possibility of Arctic air blowing south when the AO is in its negative phase (AO−). The influence of AO and NAO have been studied in the context of the occurrence of pollution in the Arctic (AMAP, 2003; Hirdman et al., 2010), and it was found that transport explains a major part of the interannual variability of pollution at Arctic stations (Hirdman et al., 2010). However, POP concentrations (α-HCH) were found to correlate with AO phases at only one out of two Arctic stations (Becker et al., 2008). The NAO is a more regional pattern related to the strength of the westerlies over the North Atlantic and Eurasia (Hurrell, 1995). A positive NAO phase (NAO+) causes the transpolar flow of maritime air masses, whereas under a negative NAO phase (NAO−) a stagnant, anticyclonic surface circulation prevails in the Arctic basin. NAO controls pollution outflow from the NH continents to the Arctic with polarward transport from Europe, North America, and (though less pronounced) Asia being faster under NAO+ (Eckhardt et al., 2003). This increases concentrations in the Great Lakes and Arctic regions during spring (Ma et al., 2004a). Under NAO−, transport is directed more strongly to the east and southeast (Christoudias et al., 2012). Despite all of these findings, the association between the climate fluctuations and meridional transport of POPs has not been explored yet.

In this study, we examine spatial and temporal characteristics of POPs cycling and polarward transport based on a GCM's realization of present-day (1970−1999) and future (2070−2099) climate, the latter under a medium scenario of greenhouse gas emissions. In addition, we characterize the covariation of net meridional fluxes of POPs at the Arctic Circle and two climate patterns (namely, AO and NAO).

2.2 Methods

2.2.1 Model description and setup

The present study applied the global multi-compartment chemistry transport model MPI-MCTM whose core components are the three-dimensional coupled atmosphere−ocean general circulation model ECHAM5/MPI-OM (Marsland et al., 2003; Roeckner et al., 2003) and two-dimensional mass exchange parameterizations. In the atmosphere, the model integrates the dynamic Hamburg Aerosol Model (HAM, Stier et al., 2005) whereas in the ocean, the Hamburg Ocean Carbon Cycle Model (HAMOCC5, Ilyina et al., 2013) is embedded. MPI-MCTM consists of five compartments: air (gas, particulate, and aqueous phases), ocean (dissolved, particulate, and colloidal phases), sea ice/snow, soil, and vegetation. These compartments are linked through mass exchange and deposition processes, whereas cycling within a compartment includes processes of degradation, phase partitioning, transport by advection and diffusion in atmosphere and ocean, and sedimentation in ocean. A summary of model parameterizations for the POP cycling is given in the Appendix A, Section A.1 with more detailed descriptions referring to Semeena et al. (2006), Guglielmo et al. (2009), and Hofmann et al. (2012).

We performed a simulation for the 1950−2100 period, and the meridional transport of POP to and from the Arctic was examined in two 30-year periods representing the end of the 20th (i.e., 1970−1999) and 21st centuries (i.e., 2070−2099), respectively. In our study, the SRES A1B medium greenhouse gas emission scenario of the Intergovernmental Panel on Climate Change (IPCC) was selected for future climate projections (Nakicenovic et al., 2000) and adopted in the research project ArcRisk (http://project.arcrisk.eu) this study is contributing to. The atmospheric component of MPI-MCTM was run with T31 spectral resolution, corresponding to a Gaussian grid of size 96×48 (approximately 3.75° on a lat−lon grid) and 19 hybrid-sigma pressure levels (model top at 10 hPa). Unlike spatiotemporal patterns and direction of meridional tracer fluxes, their strength is resolution dependent in ECHAM5 (Aghedo et al., 2010). It tends to be overestimated, least in coarse resolution setup (Aghedo et al., 2010; Land et al., 2002). The ocean−sea ice component was run at a resolution of GR30 (∼3°) in the horizontal with 40 unevenly spaced levels in the vertical. Selected substances in this study were p, p'-dichlorophenyltrichloroethane (DDT) and two congeners of polychlorinated biphenyl, $2, 4, 4'$-trichlorobiphenyl (PCB28) and $2, 2', 4, 4', 5, 5'$-hexachlorobiphenyl (PCB153). Substance choice was steered by environmental relevance, data availability and representativeness for a wide range of POPs. The model simulation required information on the substance physicochemical properties, such as phase partition coefficient, degradation rate, water solubility, vapor pressure, and temperature dependence of each property. This information is summarized in Table A.1. Emission data is presented in Section A.2.

2.2.2 Meridional mass flux analysis

Net meridional mass flux

Vertically integrated meridional trace substance fluxes were budgeted. The net meridional mass flux is hereafter referred to as F_{net} for conciseness. The daily simulated F_{net} at a grid cell i, j and on day d was determined by

$$F_{\text{net}}|_{ijd} = \sum_{k=1}^{K} \frac{P_{\text{air}}|_{ijd}^{k}\ \text{MW}}{R\ T_{ijd}^{k}}\ q_{ijd}^{k}\ v_{ijd}^{k}\ , \tag{2.1}$$

where k is the index of the vertical level with K denoting the total model levels. P_{air} is the atmospheric pressure (Pascal), T is the air temperature (K), q is the species mass mixing ratio (kg kg^{-1}), and v is the meridional wind speed (m s^{-1}). MW and R are the molecular mass (28.96×10^{-3} kg mol^{-1}) and the universal gas constant (8.3145 J mol^{-1} K^{-1}) for dry air. A positive F_{net} is defined as a northward (polarward) mass flux and refers in the following to a net import (hereafter, import) to the Arctic.

The study focuses on determining important features of import/export gates of POPs into/out of the Arctic in the simulated present and future climates by looking into zonal distributions of long-term mean F_{net} at the Arctic boundaries (that is, polar circle at 66.5°N). It also examined seasonal changes in the pollutant transports for the three monthly seasons: December−January−February (DJF), March−April−May (MAM), June−July−August (JJA), and September−October−November (SON). In addition, trends in F_{net} are of interest to see any indication of a response to a warming climate. To make the trends as smooth as possible excluding non-stationarity and low-frequency elements (such as seasonality), we applied the Kolmogorov−Zurbenko (KZ) filtering (Zurbenko, 1986) and used the output for the analysis. A summary of the KZ method and trend estimation is given below.

Kolmogorov−Zurbenko (KZ) filter decomposition

We assumed that F_{net} series could be partitioned as

$$O_t = E_t + S_t \tag{2.2}$$

where O_t is the original time series, E_t is the long-term component (trend), and S_t is the short-term component (cycle). The long-term component is usually related to external forcings associated with, for example, greenhouse warming, emission trends and chemical degradation by atmospheric oxidants. Therefore, the long-term component shows either smooth (very slow) oscillation or none at all. The short-term component includes periodic cycles superimposed upon the long-term tendency. We considered that only inter-annual and seasonal cycles are present in S_t, whereas the length of day variations are much less important or negligible because it has little impact on the substance fate. For this reason, a time series of monthly resolution derived from daily F_{net} was used as O_t. The decomposition of O_t into E_t and S_t was achieved by the KZ low-pass filter (Zurbenko, 1986) which is a simple method, has a clean filtering capability and is widely used (Eskridge et al., 1997; Hogrefe et al., 2004; Yang and Zurbenko, 2010). The KZ(m, p) filter is defined as p iterations of a point-centered moving average with m window size. For each iteration, the moving average series $y(t)$ is expressed as

$$y(t) = \frac{1}{m+1} \sum_{i=-m/2}^{m/2} x(t+1) \ , \tag{2.3}$$

where x is the original time series (for the first iteration) or the output from the previous iteration, and t is the time index. To filter all cycles of less than N months, the criterion $m \times \sqrt{p} \leq N$ is applied. In the study, KZ(9,3) was used on O_t to retain cycles larger than 1.3 years, thus isolating the long-term signal (E_t) from seasonality and most inter-annual variations (S_t).

Trend analysis

Annually averaged zonal mean E_t was employed in the trend analysis, derived here in two steps. First, a zonal-mean value in each month of a given year was calculated by taking the pooled average of E_t over all grid cells at the Arctic Circle (66.5°N). Next, all monthly zonal-mean values of the corresponding year were averaged. We adopted the Mann−Kendall non-parametric test with a serial correlation correction (Hamed and Ramachandra Rao, 1998) to detect the presence of a trend. When a significant trend was detected —the null hypothesis of no trend was rejected —the rate of change was calculated using the Sen's slope estimator (Sen, 1968).

2.2.3 Influence of AO and NAO on substance transport

We assessed relationships between F_{net} variability around the Arctic boundaries and interannual fluctuations of the NH large-scale atmospheric circulation for the two climate periods. The implicit working hypothesis is that, apart from emissions from ground surfaces, large-scale dynamics determines the strength and spatial distributions of atmospheric pollutant transport. Feedbacks of the climate dynamics on surface temperature may contribute to pollutant source strengths. However, no such evidence has been revealed or been indicated to be significant, and such effects and feedbacks are assumed negligible here. The two selected patterns of climate variability are the Arctic Oscillation (AO) and the North Atlantic Oscillation (NAO), quantified here as monthly indices (hereinafter, AOI and NAOI). While NAO mainly covers variability in the North Atlantic and surrounding continents, AO covers more hemispheric scale variability, including that of the North Pacific, the Pacific North America (PNA) pattern. For a discussion of the physical meaning of AO and NAO, see Ambaum et al. (2001).

AOI is defined as the principal component (PC) time series of the leading mode of the empirical orthogonal function (EOF1) of sea level pressure (SLP) anomalies in the NH extratropics (20°−90°N, 0°−360°E) (Thompson and Wallace, 1998). Positive AOI (AO+) is characterized by an air pressure below normal over the central Arctic paired with air pressure above normal over the northern Atlantic and Pacific Oceans, whereas negative AOI (AO−) features the opposite pattern. For NAOI, we chose to utilize an EOF-based index rather than station-based index since the latter is susceptible to noise from other modes of variability affecting pressure at station locations (Hurrell and Van Loon, 1997). Here, the definition of NAOI was adopted from Hurrell

(1995), described as the PC time series of EOF1 of SLP anomalies in the North Atlantic sector (20°N–80°N, 90°W–40°E). NAO reveals a north–south dipole, with the northern center of action of EOF1 near Iceland and the southern center near the Azores. Positive NAOI (NAOI+) shows an abnormally strong pressure in the southern center combined with a lower than normal pressure in the northern center.

The Pearson's correlation analysis was performed and the statistical significance of a correlation coefficient was tested against the null hypothesis of no linear correlation using a two-tailed t-test. It is essential to exclude any long-term trends present in F_{net} series to focus on the linkage between F_{net} interannual variability and large-scale climate variability. For this purpose, the detrended F_{net} was applied (refer to S_t from Equation 2.2), and its standardized values were put into the correlation. S_t was obtained by subtracting O_t from E_t.

2.3 Results

2.3.1 Characteristics of transport

Figure 2.1 shows zonal distributions of F_{net} of DDT, PCB153, and PCB28 at the Arctic boundaries, averaged seasonally (color lines) and annually (black lines) for the two periods. For reference, the distributions of annual mean F_{net} around the polar circle are shown in Appendix B, Figure B.1. Note that the raw data without KZ filtering was applied for this analysis. For model validation, we compared simulated concentrations of POPs against observations for a subset period of the present climate at four locations in the Arctic (see Section A.3).

DDT

For the present climate, annual mean F_{net} varies between -8.41 ng m^{-2} s^{-1} and 20.99 ng m^{-2} s^{-1} across longitudes, or 4.27 ng m^{-2} s^{-1} by average (which corresponds to $\approx 2.1\times10^3$ g s^{-1} across the entire Arctic Circle). Main import gates ($F_{\mathrm{net}} > 0$) of DDT are seen at regions stretching (a) from Alaska to the Northwest Territories (shortly, Alaska–Northwest Territories) (160°W–125°W), (b) Davis Strait–Greenland (60°W–40°W), (c) the Norwegian Sea–Northwestern Russia (0°–50°E), and (d) Urals–Siberian (80°E–103°E) (Figure 2.1a and Figure B.1a). In contrast, main export ($F_{\mathrm{net}} < 0$) gates are seen around (a) the Canadian Arctic (100°W–70°W), and (b) Chukotka in the Russian Far East (155°E–170°W). For other regions, the sign of F_{net} is variable by season; it is negative in JJA and positive in other seasons over the Denmark Strait–Norwegian Sea (35°W–5°W), whereas it is the other way around over Yakutia (or the Sakha Republic) in the Russian Far East (105°E–150°E). Dominant import fluxes via Scandinavia and northwestern Russia are consistent with high atmospheric concentrations at the lowest model level and coincide with high net volatilization fluxes across 45°–65°N latitudes (Figure B.2a), thus suggesting contributions from local sources. Import through Urals–Siberian is apparently related to elevated near-ground concentrations in the region. These presumably result from advection (long-range transport with both zonal and meridional components) and large-scale mixing, despite net deposition over this region (≈ -5 pg m^{-2} s^{-1}). With regard to seasonality, import fluxes over

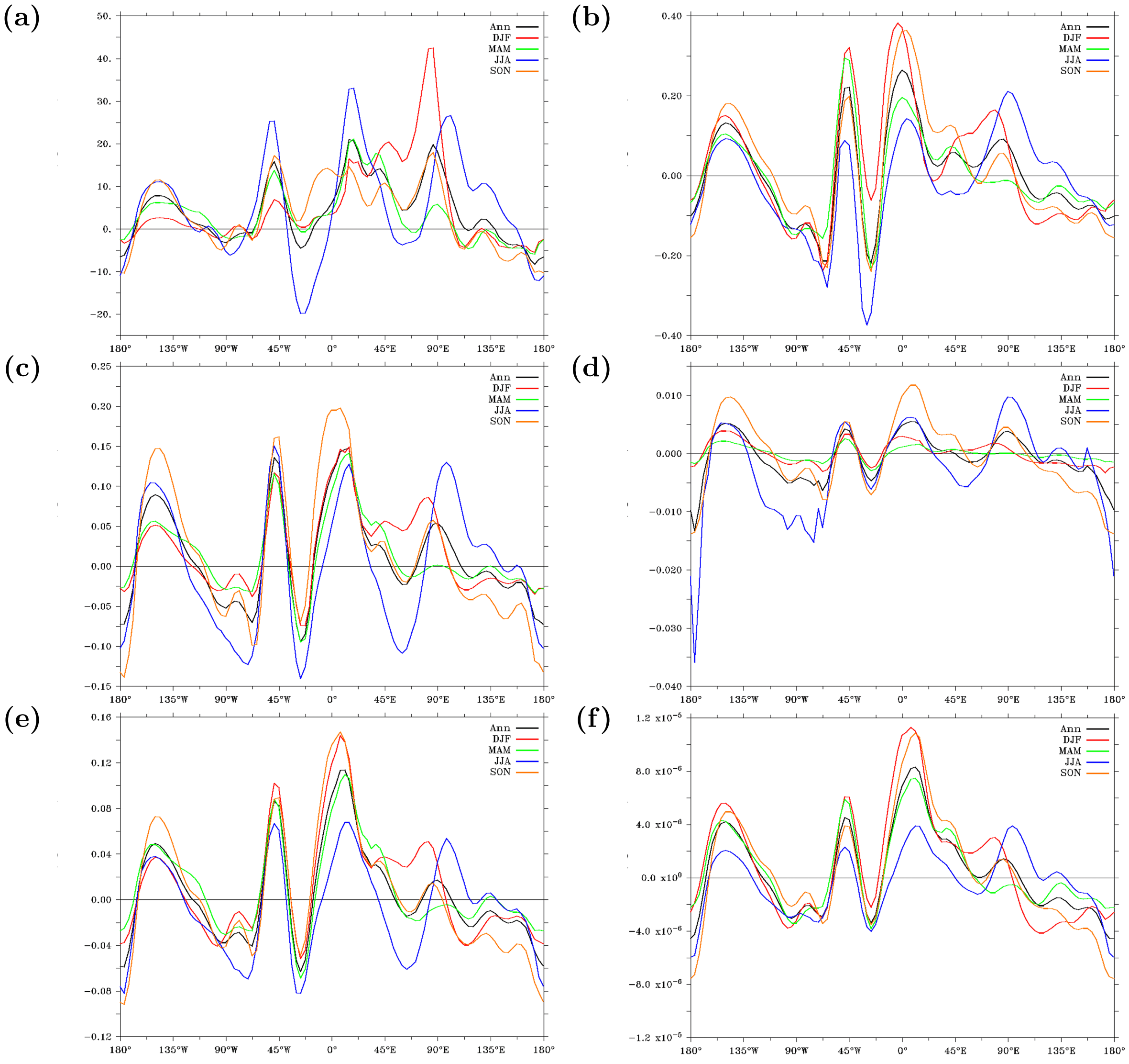

Figure 2.1: Zonal distribution of annual mean and seasonal net meridional mass flux across 65°N, F_{net} (ng m^{-2} s^{-1}) of (a,b) DDT, (c,d) PCB153, and (e,f) PCB28; mean of (a,c,e) 1970−1999 and (b,d,f) 2070−2099

Alaska, Davis Strait−Greenland, and Scandinavia are largest in JJA and smallest in DJF with $\frac{F_{\mathrm{net|JJA}}}{F_{\mathrm{net|DJF}}} > 2$. The opposite is true (largest in DJF and smallest in JJA) for import fluxes passing over Northwestern Russia and Urals. On the other hand, export fluxes over central and east parts of Chukotka stand maximum in JJA and minimum in DJF.

For the future climate, when secondary emissions control the substance fate and transport as primary emissions cease, F_{net} decreases by three orders of magnitude compared to what seen in the present (≈2.0 g s^{-1} across the entire Arctic Circle). It is evident that relatively high near-ground concentration over Greenland−Northwest Russia is in line with strong import/export fluxes. These are associated primarily with long-range atmospheric transport, despite net deposition (then ≈−0.3 pg m^{-2} s^{-1}) in these regions (Figure B.3a). Compared to the present climate, F_{net} tends to show more spatial coherence and less seasonal variability for a wide range of area spanning from the Russian Far East toward Scandinavia (140°E−20°E), except at few localities in Canada, Greenland, and Iceland (Figure 2.1b). Within this longitudinal band, for regions where F_{net} is positive (negative), the value is minimum (maximum) in JJA and maximum (minimum) in SON or DJF. Despite the above changes, the sign of future F_{net} remains approximately the same as in the present with one apparent exception, that is, F_{net} is expected to change its sign from positive to negative over the Denmark Strait−Iceland (35°W−20°W) in MAM and SON.

PCBs

In 1970−1999 F_{net} of PCB153 and PCB28 across longitudes were 0.012 (−0.095 to 0.015) ng m^{-2} s^{-1} (or ≈6 g s^{-1} across the entire Arctic circle) and 0.0054 (−0.063 to 0.113) ng m^{-2} s^{-1} (or ≈2.7 g s^{-1} across the entire Arctic Circle), respectively. Nevertheless, import gates for the two congeners are situated at relatively similar regions, including (a) Alaska−Northwest Territory (160°W−125°W), (b) Greenland (55°W−40°W), and (c) the Norwegian Sea−Northwest Russia (5°W−40°E) (Figure 2.1c,e and Figure B.1c,e). Also similar for both substances, the export gates cover areas in (a) the Canadian Arctic (105°W−60°W), (b) the Denmark Strait (35°W−20°W), and (c) the Russian Far East (145°E−170°W). F_{net} is also negative around the western part of Yakutia (100°E−115°E) in all seasons but JJA. In terms of its magnitude (absolute F_{net}), total net import is larger than net export. Like DDT, the seasonality of F_{net} varies by region. Import fluxes across Alaska are generally higher in SON when they are about 30%−80% higher than the annual means and up to three times larger than the minimum values in DJF. Import fluxes over the Norwegian Sea−Scandinavia are also maximum in SON, but the minimum values are found in JJA. Export fluxes crossing the Canadian Arctic increase in JJA by a factor of more than two (of their annual means) and decrease in DJF by less than a factor of two, whereas those crossing Chukotka increase in SON and decrease in MAM by about 1.5−3 times with regard to the annual means. A comparison of the two congeners reveals that import fluxes over Greenland are largest in SON and smallest in DJF for PCB153 whereas they are highest in DJF and lowest in JJA for PCB28. The latter finding is attributable to the fact that atmospheric degradation of PCB28 is much faster during summer.

The future climate is likely to bring a decline in absolute F_{net} by two and four orders of magnitude (on average) for PCB153 (-6.52×10^{-4} ng m^{-2} s^{-1} by average, or ≈0.35 g s^{-1} across the entire Arctic circle) and PCB28 (4.23×10^{-7} ng m^{-2} s^{-1} by average, or ≈0.2 mg s^{-1} across the entire Arctic circle), respectively, but the locations of import and export gates are overall the same as those found under present climate (Figure 2.1d,f). However, discrepancies between the two congeners become more apparent in the future. Net volatilization of PCB153 (hence contributions from local sources) is seen at import gate (c) (i.e., 5°W−40°E) and around 90°E (Figure B.3b), but more efficient polarward flows take place at higher altitudes. For PCB28 net deposition (hence no compensation by volatilization from local sources) is found at all longitude bands (Figure B.3c). The longitudinal distributions of concentration and net surface fluxes of PCB28 between the present and future climate are similar. This reflects the short atmospheric and ground compartment lifetimes of PCB28, whereas PCB153 chemodynamics (chemistry and transport) is dominated by volatilization from the major storage compartment, that is, soil. Seasonal variation of F_{net} is also different for the two congeners. In particular, net fluxes across central and east parts of Chukotka are maximum in JJA for PCB153 and in SON for PCB28, with their ratios to the minimum F_{net} in MAM ranging from 8 to 21 for PCB153 and from 2 to 3 for PCB28. Furthermore, the export fluxes of PCB153 crossing the Canadian Arctic are substantially more variable by season than those of PCB28.

2.3.2 Trends

Trends in annual F_{net} are summarized in Table 2.1, and some basic statistics pertaining to the zonal mean F_{net} are also given to support the discussion below.

DDT

Table 2.1 reveals that there has been a clear negative (downward) trend in F_{net} during the present period, statistically significant at the $p < 0.01$ level, which is superimposed on short-term fluctuations. This trend is shown in annual time series as a continuous decrease in import fluxes, as opposed to increasing export fluxes (Figure B.4a). The variability in annual F_{net} is high, as the normalized standard deviation is larger than one, and the annual values range from −0.13 to 20.32 ng m^{-2} s^{-1}. The high variance is mainly associated with a steep decline in primary emissions in the 1970s. The trend changes to positive and significant ($p < 0.01$) under the future climate, that is, polarward transport is expected to be enhanced. Specifically, negative F_{net} would turn positive in the year 2075 and then becomes progressively larger toward the end of the 21st century (Figure B.4b). This suggests that increasing import fluxes are expected to take place more than 100 years after peak emission. Comparing mean export and import fluxes through the respective main gates mentioned earlier, it is found that the mean import to the Arctic is overall higher than the mean export in all periods (Figure B.5a,b). The trends in both transport flow directions are significantly decreasing under the present climate, whereas no significant linear trends are found under the future climate.

Table 2.1: Standard descriptive statistics and linear trends of net meridional mass flux (F_{net}) across 65°N, 0−360°E[‡]

		F_{net} (ng m^{-2} s^{-1})				**Trends**
Substance	**Period**	**Mean**	**Std. deviation**	**Minimum**	**Maximum**	($\frac{\Delta F_{\mathrm{net}}}{\Delta t}$)
DDT	1970−1999	4.26	6.40	-1.26×10^{-1}	2.03×10^{1}	$-3.55\times10^{-1***}$
	2070−2099	4.11×10^{-3}	4.77×10^{-3}	-5.94×10^{-3}	1.43×10^{-2}	$4.10\times10^{-4***}$
PCB153	1970−1999	1.20×10^{-2}	4.88×10^{-3}	3.05×10^{-3}	2.29×10^{-2}	$-4.44\times10^{-4***}$
	2070−2099	-6.40×10^{-4}	6.94×10^{-4}	-2.46×10^{-3}	9.89×10^{-4}	$-3.41\times10^{-5*}$
PCB28	1970−1999	5.39×10^{-3}	2.88×10^{-3}	1.17×10^{-3}	1.33×10^{-2}	$-1.93\times10^{-4***}$
	2070−2099	4.19×10^{-7}	1.78×10^{-7}	1.25×10^{-7}	8.33×10^{-7}	$-1.38\times10^{-8***}$

[‡] The symbols *, **, *** identify statistical significance at $\alpha = 0.10$, 0.05, and 0.01, respectively. Annual mean of KZ-filtered (long-term) data. $F_{\mathrm{net}} > 0$ import, $F_{\mathrm{net}} < 0$ export. Trends are given by the Sen's slope estimator.

PCBs

Trends in annual F_{net} of PCBs during the present climate are negative and significant at the $p < 0.01$ level, and the magnitude of the trend is larger in PCB153 nearly doubling that in PCB28 (Table 2.1). The trend is associated with decreasing net import with F_{net} falling sharply in 1980 (Figure B.4c,e). For the future climate, the trends are of the same sign (being negative) to those found for the present, but the magnitude decreases by one order of magnitude in PCB153 and four orders in PCB28. The negative trend in PCB153 transport leads to a shift in the sign of F_{net}, that is, from positive to negative, in the mid-2070s (Figure B.4d). Looking at contributions of individual flows, it is apparent that while the mean export of PCB153 is always less than the mean import toward the Arctic during the present period (Figure B.5c), the export will become more dominant toward the future (Figure B.5d) which may result from the enhanced volatilization of this species. However, the mean export under the future climate conditions does not show an increasing trend except in two sub-periods, 2075−2080 and 2085−2095. Inherent variability on a decadal scale is still relevant in the future as in the present, and may lead to strong variations of export and import. Nevertheless, PCB153 soil burden in the Arctic is found to increase under future climate conditions (compartmental burdens are listed in Table B.1). For PCB28, the negative trend in F_{net} indicates that net import will likely continue to take place toward the end of 21st century, albeit decreasing in magnitude (Figure B.4f). Mean fluxes from all major import and export gates decrease continuously with the mean import always being greater than the mean export (Figure B.5e,f).

2.3.3 Role of AO and NAO

Table 2.2 presents Pearson correlation coefficients (r) and their p-values (p) between zonal mean F_{net} and AOI and NAOI. Figures 2.2−2.4 presents the spatiotemporal (longitudinal and seasonal) patterns of r and their significance for DDT, PCB153, and PCB28, respectively.

DDT

In the present period, zonal mean F_{net} is only weakly correlated with AOI and NAOI but analysis by season shows that the correlations are positive ($r = 0.33$ and 0.35 with AOI and NAOI, respectively) and statistically significant ($p < 0.01$) in DJF when the atmospheric circulation modes are more dominant (Thompson and Wallace, 1998; Hurrell, 1995; Ambaum et al., 2001). These correlations likely correspond to more imports of DDT when AO+ and NAO+ intensify (Figure B.6a for AO and Figure B.7a for NAO). With regard to AO, correlations between annual F_{net} and the AO index are significant ($p < 0.05$) over specific regions (Figure 2.2a,b): negative over Alaska (163°W−145°W) and Davis Strait−Greenland (60°W−45°W), and positive over Urals−Siberian (70°E−90°E). However, the magnitudes are very small, that is, $|r| = 0.1$−0.2. Note that these regions are considered as major import gates of DDT (Section 2.3.1). Seasonally, F_{net}−AO linkage tends to appear stronger in winter. This is reflected by the total area occupied by positive correlations being larger than that by negative correlations. In particular, a sector of significant negative correlations ($|r| = 0.2$−0.4, $p < 0.05$) is found

Table 2.2: Pearson's correlations between de-trended (raw − KZ-filtered) net meridional mass flux across 65°N, 0−360°E and two large-scale climate indices, that is, Arctic Oscillation Index (AOI) and North Atlantic Oscillation Index (NAOI); Derived from monthly data.[‡]

		Correlation coefficients			
		1970−1999		**2070−2099**	
Substance	**Annual/Season**	**AOI**	**NAOI**	**AOI**	**NAOI**
DDT	ANN	0.18***	0.16***	0.37***	0.37***
	DJF	0.33***	0.35***	0.31***	0.34***
	MAM	0.15	0.16	0.32***	0.30***
	JJA	0.06	−0.04	0.30***	0.46***
	SON	0.16	0.05	0.34***	0.45***
PCB153	ANN	0.28***	0.33***	0.17***	0.12**
	DJF	0.50***	0.61***	0.11	0.10
	MAM	0.30***	0.42***	0.09	0.07
	JJA	0.40***	0.39***	0.20*	0.09
	SON	0.29***	0.30***	0.39***	0.30***
PCB28	ANN	0.22***	0.26***	0.38***	0.35***
	DJF	0.45***	0.51***	0.35***	0.36***
	MAM	0.28***	0.39***	0.41***	0.41***
	JJA	0.46***	0.42***	0.36***	0.44***
	SON	0.17	0.21*	0.28***	0.21*

[‡] The symbols *, **, *** identify statistical significance at $\alpha = 0.10$, 0.05, and 0.01, respectively.

over Alaska−Northwest Territories (155°W−122°W) and Davis Strait−Greenland (65°W−45°W) whereas another sector of opposite correlations is seen over the Denmark Strait−Norwegian Sea (30°W−0°E), Urals−Siberian (75°W−95°W), and Yakutia (115°E−127°E). With regard to NAO, the spatiotemporal patterns are similar to those for AO (Figure 2.2e,f) over Davis Strait−Greenland, Scandinavia and Urals−Siberian. Unlike with AO, however, F_{net} presents significant positive correlations with NAO over the Denmark Strait−Norwegian Sea throughout the year. Also, the relationships to NAO are more prominent than those to AO over Canadian Arctic−Davis Strait (87°W−55°W) in SON and over Yakutia (105°E−140°E) in JJA, when correlations are negative and significant ($|r| = 0.2-0.4$, $p < 0.1$).

Correlations under the future climate are significantly positive at the $p < 0.01$ level, for annual and seasonal values, with r being overall larger than those obtained under the present climate. The linkage of zonal-mean F_{net} to AO is more uniform across seasons ($r = 0.30-0.34$) than the linkage to NAO ($r = 0.30-0.46$). All correlations are higher during SON. The positive correlations in DJF tend to point to higher imports whenever AO+ and NAO+ frequency are high, whereas the opposite signal is present in JJA, that is, higher exports whenever AO− and NAO− frequency are high (Figures B.6b and B.7b). Future changes in the atmospheric circulation patterns result in stronger correlations with DDT transport over a vast region: Davis Strait−Norwegian Sea (60°W−10°E) for AO and the Canadian Arctic−Norwegian Sea (103°W−10°E) for NAO (Figure 2.2c,d,g,h). Within this region, there appear two homogeneous zones of statistically significant correlations ($|r| = 0.2-0.6$, $p < 0.01$), one negative west of and over most of Greenland, and one positive over eastern Greenland. In the first zone, the negative correlations strengthen during MAM, whereas in the second zone the positive correlations strengthen during SON. Higher significant correlations for the future climate are also evident over part of Yakutia (130°E−145°E) for annual and MAM. In contrast, the relationship between AO and NAO weakens or disappears over western Siberia (75°E−90°E).

PCBs

In the present period, zonal-mean F_{net} exhibits statistically significant ($p < 0.01$) positive correlations with AOI and NAOI ($r > 0.2$), annual mean and seasonally (excluding SON). F_{net} links to NAO are generally stronger than to AO, but both teleconnections similarly exert the greatest influence on F_{net} during DJF and the weakest during SON. It was found that the positive correlations in DJF are associated more frequently with higher import fluxes when AO and NAO are more positive, whereas in JJA it is vice versa, higher export fluxes under more negative phases (see Figure B.6c,e for AO and Figure B.7c,e for NAO). Comparing the two congeners, correlations of meridional flux with AO and NAO are higher in PCB153 except during JJA. Figures 2.3 and 2.4 show the spatiotemporal correlation patterns for PCB153 and PCB28, respectively. With regard to F_{net}−AOI, the annual patterns are characterized by the existence of three zones of significant correlations ($p < 0.05$): (1) Baffin Region−Greenland (65°W−45°W) where correlations are negative, (2) Denmark Strait−Norwegian Sea (38°W−10°W), and (3) the Urals (70°E−85°E) where correlations are positive. The correlations are weak ($|r| = 0.1-0.2$, except for western Greenland) but get stronger in MAM for the first zone and in DJF and JJA for

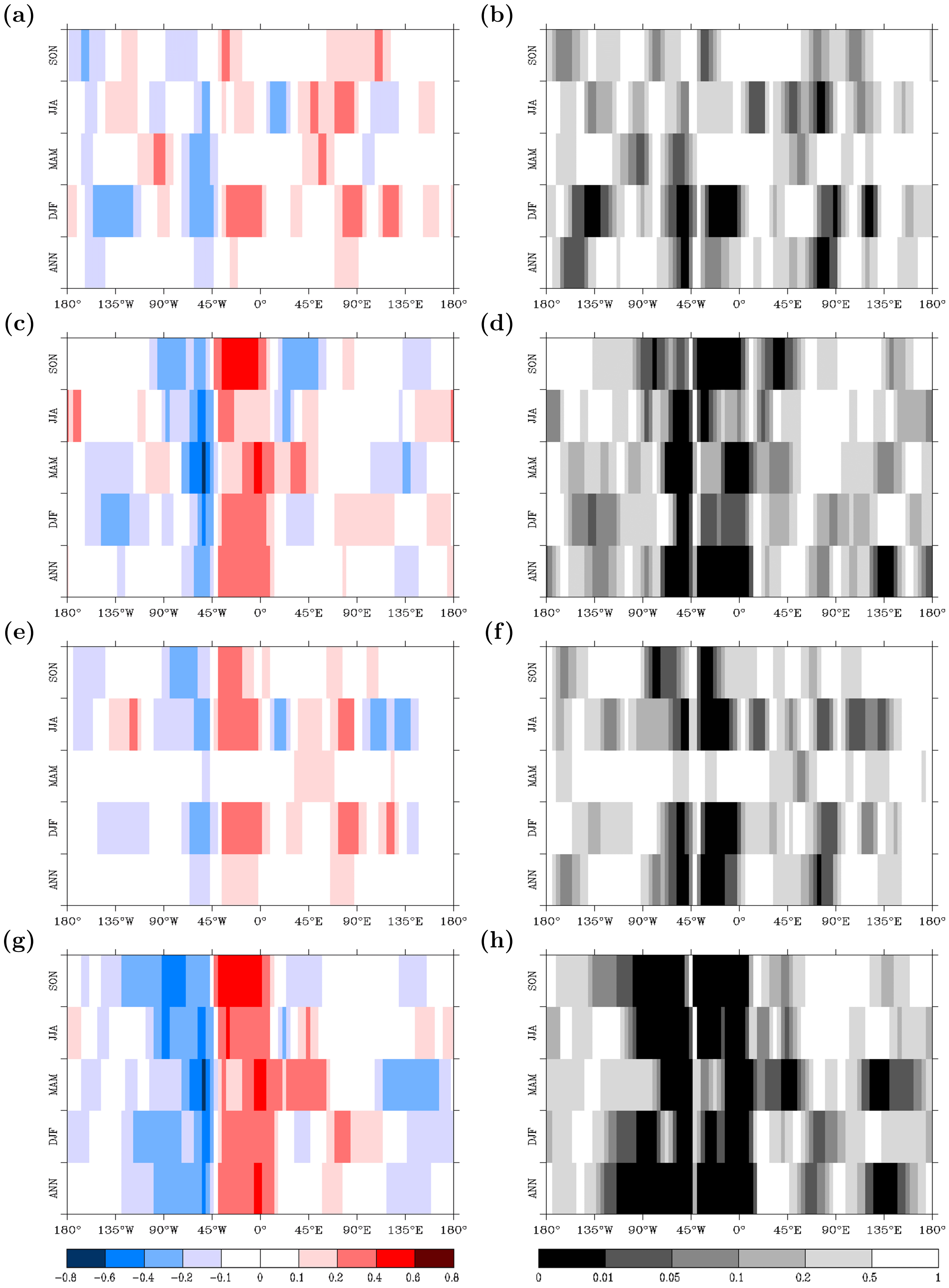

Figure 2.2: Hovmöller plots of Pearson's correlation coefficients (a,c,e,g) and their corresponding two-tailed *t*-test *p*-values (b,d,f,h) between detrended (raw − KZ-filtered) net meridional mass flux of DDT and two large-scale climate indices, that is, (a–d) Arctic Oscillation Index (AOI) and (e–h) North Atlantic Oscillation Index (NAOI), during (a,b,e,f) 1970–1999 and (c,d,g,h) 2070–2099. Monthly data, grouped seasonally or for the whole year.

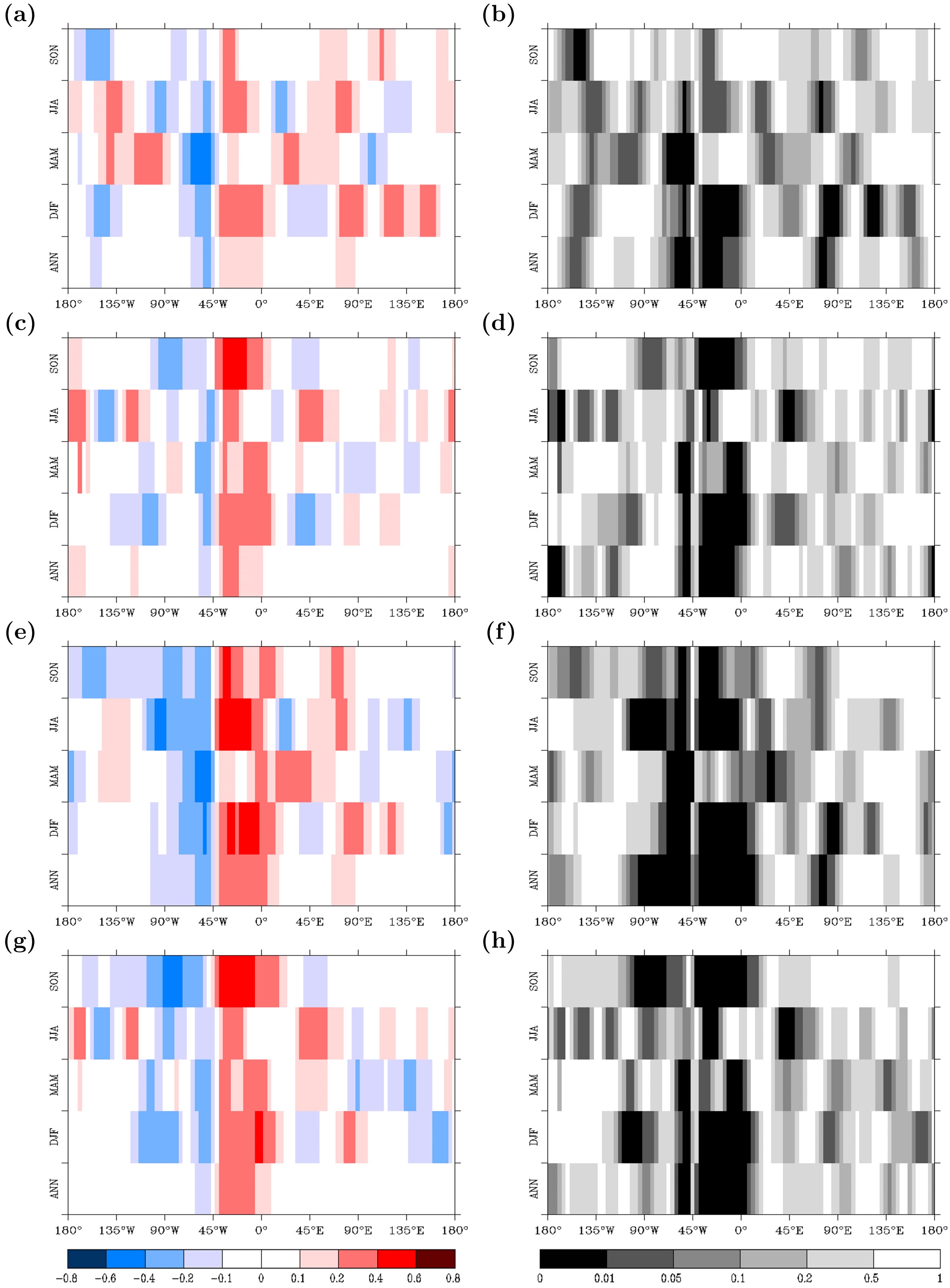

Figure 2.3: Same as Figure 2.2, but for PCB153

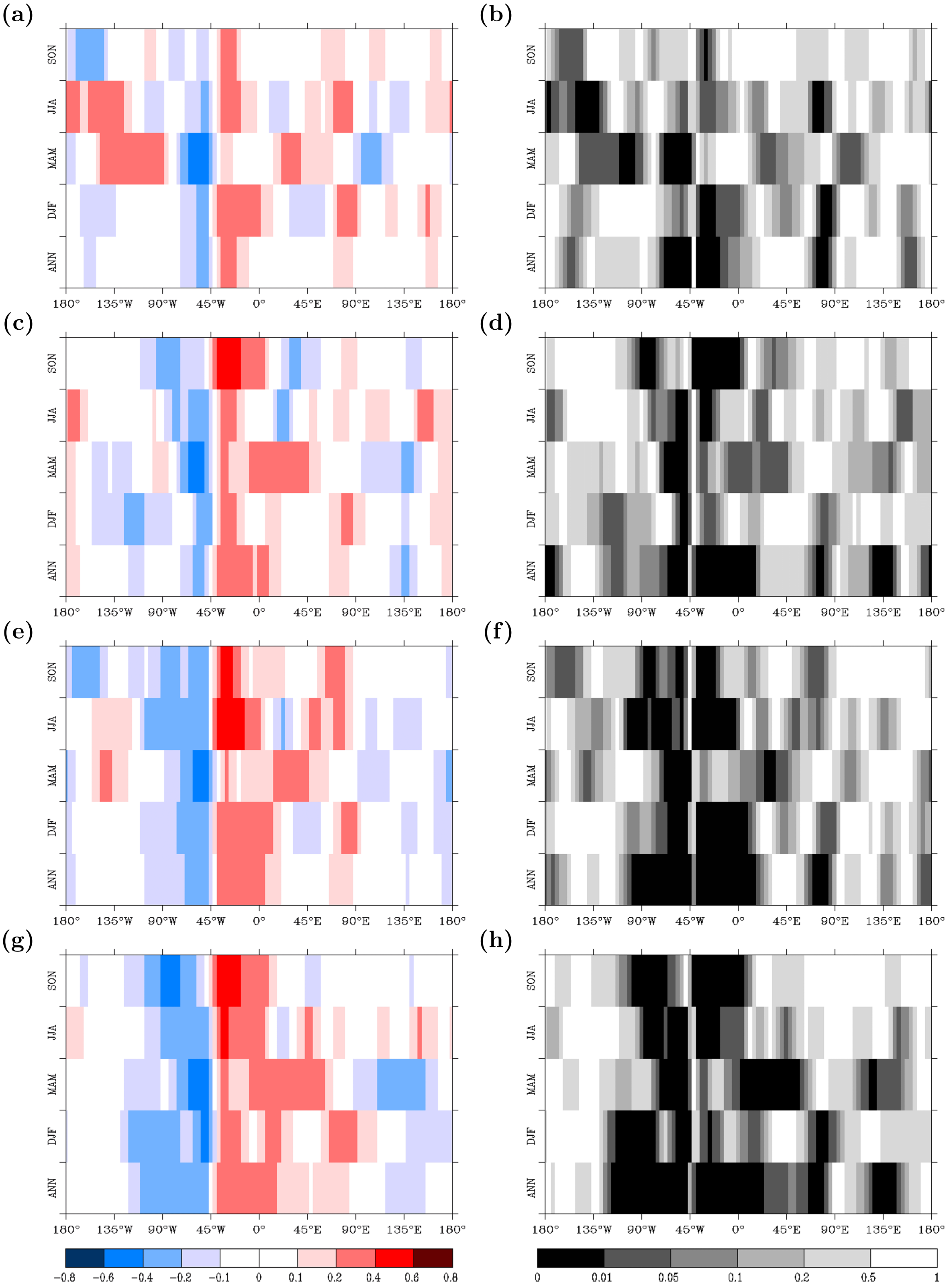

Figure 2.4: Same as Figure 2.2, but for PCB28

the others. In MAM, significant correlations are positive ($r = 0.2{-}0.4$, $p < 0.05$) in a band from the Northwest Territories to the western Canadian Arctic (115°W−95°W) for PCB153 (Figure 2.3a,b) and from eastern Alaska to the Canadian Arctic (145°W−90°W) for PCB28 (Figure 2.4a,b). In SON, significant negative correlations are found over most of Alaska (165°W−150°W) for both congeners. The results for NAO are comparable to those for AO to a limited extent: In particular, the annual F_{net}−NAOI correlation patterns are also characterized by the three zones of significant correlations stated above, but the magnitudes are higher and more significant than with AOI ($|r| = 0.2{-}0.4$, $p < 0.01$) in the first two zones (Figures 2.3e,f and 2.4e,f). Moreover, the west boundary of zone 1 extends to the Canadian Arctic, whereas the east boundary of zone 2 extends to Scandinavia, and for these two zones together (100°W−15°E), larger correlations are typically obtained in JJA (PCB153 and PCB28) and DJF (PCB153).

For PCB153, the future climate leads to decreasing influence of AO and NAO on zonal mean F_{net} for the annual mean and in most seasons, which is obvious as correlations are very small and not significant (Table 2.2). For PCB28, the correlations in the future likely continue to be positive and significant ($r = 0.28{-}0.44$, $p < 0.01$). In DJF, the positive sign corresponds mostly to higher imports going parallel with high AO+ and NAO+ (Figures B.6d,f, and B.7d,f), whereas that in JJA corresponds to the opposite direction, that is, higher exports with low (large absolutes) AO− and NAO−. Despite their discrepancies, the spatiotemporal correlation patterns between PCB153 and PCB28 are largely similar. From Davis Strait to the Norwegian Sea (60°W−5°W, except along 45°W−40°W), significant negative correlations ($p < 0.01$) with annual mean AOI and NAOI dominate in western Greenland, whereas positive correlations dominate in eastern Greenland (Figure 2.3c,d,g,h and Figure 2.4c,d,g,h). Note that the area of negative correlations between PCB28 transport and NAOI extends toward Baffin Region (118°W), whereas the area of positive correlations extends toward Scandinavia (25°E). These correlations results are similar to those obtained under the present climate conditions, except (1) correlations with AOI and NAOI in SON over the Canadian Arctic (90°W−75°W) and Denmark Strait−Iceland (35°W−15°W) would increase ($|r| = 0.2{-}0.6$, $p < 0.05$); (2) from the Canadian Arctic to Greenland (100°W−50°W) the negative correlations between PCB153 transport and NAOI, annual mean and during JJA, weaken or disappear, whereas those in SON strengthen; (3) correlations with NAOI over the central part of Yakutia (125°E−150°E), annual mean and during MAM, would turn negative and significant ($|r| = 0.1{-}0.4$, $p < 0.05$).

2.4 Discussion

Based on a long-term simulation and under a medium greenhouse gas forcing scenario, this study assesses the spatiotemporal features of net meridional transport of POPs into and from the Arctic. Under the present climate, DDT, PCB153, and PCB28 traverse into the Arctic through four major import gates representing separate contributions via (1) Alaska−Northwest Territories (from North America), (2) Greenland, (3) the Norwegian Sea−Northwestern Russia (from Europe), and (4) Urals−Siberian (from Asia). In the case of PCBs, the direction of meridional transports in Asia varies across seasons (largely southward in summer, Figure 2.1). Note that identifying contributions from North America, Europe, and Asia does not imply that the emissions originate in the respective continents because of the influence of intercontinental transports, namely trans-Atlantic, trans-Pacific, and trans-Eurasian transports (Huang et al., 2007; Li et al., 2002; Stemmler and Lammel, 2012). This particularly applies to the Greenland gate with almost no emissions from the island, where transport is likely from stronger meridional advection occurring due to the frequent activity of northward traveling cyclones over Baffin Bay (Stohl, 2006). With regard to export gates, the substances leave the Arctic mainly by passing over the Canadian Arctic and Eastern Russia, possibly facilitated by contributions from anticyclonic activities near the Beaufort and Siberian Highs, respectively.

The meridional component of atmospheric transport is organized by planetary waves leading to meandering circulation in mid to high latitudes. These waves can be highlighted by subtracting the zonal mean pressure from local pressure showing that in winter a planetary wave with wavenumber two is dominating with low pressure (troughs) over the North Atlantic and North Pacific and high pressure over North America and especially over northern Asia (the Siberian High). In summer planetary waves are weaker, less organized and of higher wavenumber, that is, there are more but weaker ridges and troughs. Transport is generally northward at the western (eastern) flank of a ridge (trough). In general, the atmospheric mass fluxes of semi volatiles, which are slowly degrading in ground compartments, are determined by the atmospheric dynamics, by the sinks (photochemistry, wet and dry depositions), and by the secondary emissions from storage in ground compartments (which host $>90\%$ of the total environmental burdens in the case of the substances studied here; Table B.1). As a consequence of its low vapor pressure, DDT is least subject to air−surface exchange. Therefore, the seasonal variation of the atmospheric transport of DDT reflects the seasonality of meteorological conditions rather than the secondary sources (revolatilization from land and sea surfaces). The consequences are apparent in two regions of Eastern Asia: net import over Urals−Siberia is maximal in winter and minimal in summer, whereas net export over Chukotka is maximal in summer and minimal in winter. For PCBs, the seasonality of transport in NH is controlled by the combination of compartmental distribution, removal rates, and photochemistry on the one hand and transport pathways on the other hand (Huang et al., 2007; Stemmler and Lammel, 2012). The combination of both impact factors leads to much stronger zonal variability of the meridional transport and less seasonal differences than would be expected from atmospheric circulation alone.

The spatial distribution of the main transport gates seems to remain unchanged until the end of the 21st century. Obviously, a decline in absolute meridional fluxes is expected as primary emissions will be very weak. Secondary emissions (revolatilization from surfaces) will dominate global atmospheric cycling of POPs. These are fed from storage in ground compartments and are changing over time in strength and distribution, not least by migration (northerly shifts) (Stemmler and Lammel, 2012). The largest reduction is expected for PCB28 (by 4 orders of magnitude), followed by DDT and PCB153 ($\sim$2 orders of magnitude). Long after the cease of primary emissions, PCB153 and DDT in the air are mostly fed by the substance's storage in soils and oceans, whereas PCB28 is significantly less stored in these surface compartments mainly due to its limited lifetime (Lammel and Stemmler, 2012). Interestingly, the decreasing trend of net import of DDT to the Arctic is expected to change to an increasing trend in net import —the second time in history —long after the emission maximum. In contrast, PCB153 is expected to be increasingly exported from the Arctic under future climate conditions.

Under the present climate, for annual and seasonal timescales, all significant correlations between meridional transports and two climate indices are positive and suggest high net zonal mean imports into the Arctic as AO+ and NAO+ frequency increases for DJF and high net exports as AO− and NAO− frequency increases for JJA. Under the future climate, there will be an increasing significance of the correlations for DDT, whereas the linkage of PCB153 meridional fluxes to NH climate indices seems to weaken or be absent, except during fall. Surface exchange (water/air and soil/air) is much more important in PCB153 cycling than in PCB28 cycling (because of short atmospheric lifetimes (Hung et al., 2005b)) and in DDT cycling (because of very low volatility (Stemmler and Lammel, 2009; Lammel and Stemmler, 2012)). Therefore, the variability of atmospheric PCB153 levels is less determined by advection than in PCB28 and DDT. Moreover, based on monitoring in the Arctic atmosphere, it was found that the influence of atmospheric transport is stronger for lower-chlorinated PCB congeners than for the higher ones (Hung et al., 2001). Despite the fact that the zonal-mean fluxes are positively correlated with AO and NAO, the influence of these two modes varies by section of the Arctic Circle —during AO+ and NAO+, net imports via the North American and Greenland gates tend to be lower than normal, whereas net imports via the Asian gate (Urals−Siberian) tend to be higher. AO apparently induces a similar influence on the pollutant transport as NAO over Davis Strait−Greenland, Denmark Strait−Norwegian Sea, and Urals−Siberian. This finding may be related to the fact that temporal coherence between the Arctic and mid-latitude SLP anomalies associated with AO is largest in the Atlantic sector (Deser, 2000). Our results explain why POPs (α-HCH) concentrations in Svalbard (Zeppelin) were found to correlate with AO phases, whereas no correlation was found in Greenland (Alert) (Becker et al., 2008). Surface concentrations at Zeppelin are maintained by F_{net} via the European gate (Figures 2.1 and B.1), positively correlated with AO (Figure 2.2), whereas pollutant levels observed at Alert are subject to outflow via the Canadian Arctic gate (Figures 2.1 and B.1), negatively correlated with AO.

The transport gates and the circulation changes identified and described for POPs could be important for other (conventional) air pollutants, which undergo single-hop atmospheric transport only, depending on their source distributions and source/sink mechanisms. Long-term trends of conventional air pollutants' source distributions, however, are not influenced by migrating secondary emissions. Previous studies concluded that variability in AO and NAO in decadal timescales has become pronounced since 1960 with positive index values getting stronger since 1980 until the mid-1990s (with transient negative values in mid-1980s) (Thompson and Wallace, 1998; Hurrell, 1995). Under future climate conditions, simulations for the period 1850−2100 within the CMIP5 framework (37 AOGCMs covered) suggest that there is an increasing likelihood of modes of high AOI+ and NAOI+ (Gillett and Fyfe, 2013). An increase in the frequency of NAOI+ has also been suggested under the A1B scenario (CMIP3 experiments) (Fan et al., 2014). We can thus expect that transport toward the Arctic under the influence of these modes will be more important than under present-day climate conditions. We interpret the trends of correlations between the zonal-mean meridional transport and AOI and NAOI in the light of this trend: All significant correlations are positive, thus we expect that, depending on season, AO+ and NAO+ go along with high net imports into, or AO− and NAO− go along with high exports out of, the Arctic. Toward the end of this century, the correlations with AO and NAO are increasing for PCB28 and DDT, but decreasing for PCB153. We conclude that under the future climate, which corresponds with more frequent AO+ and NAO+, especially during wintertime when the two climatic patterns are of largest amplitude, net import of DDT will likely increase. Since meridional net fluxes of PCB28 in 2070−2100 into the Arctic are expected to be extremely low (≈1.4 mg s^{-1}), the practical implications of significant correlations are of very limited relevance.

Unlike the here addressed substances, the emissions of other persistent organic pollutants with similar behavior (fate) in the environment and similar global distribution started to decline much later, or no turn has been achieved yet. For example, the productions of the brominated flame retardants pentaBDE (a mixture of polybrominated diphenyl ethers) and hexabromocyclododecane (HBCD), which have been reported in the Arctic atmosphere (Wit et al., 2004; Wit et al., 2010), were around the year 2000 ≈6.5 and ≈13 times, respectively, higher than those of PCB153 in the year of peak production (1970) (Alcock et al., 2003; Breivik et al., 2007; Law et al., 2006). Based on estimates of primary emissions for Europe (Nordic Council of Ministers, 2008; Prevedouros et al., 2004), their global emissions around the year 2000 will have been in the same order of magnitude as the PCB153 emissions (secondary only) (Lammel and Stemmler, 2012), as emission factors are much higher in low latitudes and secondary emissions are significant, too, albeit unknown. PentaBDE, which is emitted mostly in North America, is likely to enter the Arctic via the Alaska−Northwest Territories import gate, whereas HBCD, which is emitted mostly in Europe, is likely to reach the Arctic mostly via the Norwegian Sea−Northwestern Russia and the Urals−Siberian import gates (more likely in the future as correlated with AO+, see above). The long-term accumulation trends in the Arctic of these and other emerging pollutants under a changing climate, however, are subject to the substances' specific behavior and fate in the environment and need to be explicitly studied.

Chapter 3

Development and Evaluation of an ECHAM/MESSy Submodel for the Simulation of Semivolatile Organic Compounds (EMAC-SVOC)

This chapter is comprised of a manuscript by the candidate in preparation for submission to *Geosci. Model Dev.*. The candidate and Gerhard Lammel conceived the study. The candidate designed methods, collected observation data, performed a number of model runs, and conducted data analyses, with input from Gerhard Lammel and support from Holger Tost. The chapter (including its suppplementary materials in Appendices C−I) was written by the candidate with suggestions for improvements from Gerhard Lammel and Holger Tost.

3.1 Introduction

Global and regional studies of the fate and transport of semivolatile organic compounds (SOCs[1]) using three-dimensional Eulerian dynamical models have been performed for more than a decade. To name a few, CanMETOP (Ma et al., 2003b) was developed in North America to investigate the impact of γ-hexachlorocyclohexane (γ-HCH) usage over the Great Lakes region and was modified further to model the transport and outflow of polycyclic aromatic hydrocarbons (PAHs) from China (Zhang et al., 2011b). DEHM-POP (Hansen et al., 2004) was developed to simulate the environmental fate of α-HCH within the Northern Hemisphere with a particular focus on the transport into the Arctic. In Europe, MSCE-POP (Gusev et al., 2005; Shatalov et al., 2005) and CMAQ-BaP (Aulinger et al., 2007; Matthias et al., 2009) were applied to evaluate the spatial distributions of concentrations and deposition of persistent organic pollutants (POPs). The study using AURAMS-PAH by Galarneau et al. (2014) was aimed at understanding the distribution of PAHs in North America whereas similar studies for East Asia have been conducted using

---

[1] Throughout this thesis, the term SOC refers to the group of semivolatile organics rather than SVOC which is used later as a module name coupled to a global atmospheric chemistry−climate model.

RAQM2-POP (Inomata et al., 2013) and WRF-Chem-BaP (Mu et al., 2018). On a global scale, the simulations of large-scale transport, degradation, deposition, and partitioning of SOCs have been implemented using multiple models, for example, MPI-MCTMs (Semeena and Lammel, 2005; Semeena et al., 2006; Guglielmo et al., 2009; Hofmann et al., 2012), GEM/POPs (Gong et al., 2007; Huang et al., 2007), GEOS-Chem PAH (Friedman and Selin, 2012; Friedman et al., 2014; Friedman and Selin, 2016) and CAM5-PAH (Shrivastava et al., 2017).[2] Species that have been simulated include polychlorinated biphenyls (PCBs), dichlorodiphenyltrichloroethanes (DDTs), HCHs and PAHs. Evaluation against observation data have shown that all the models were in reasonable agreement with measurements for spatial and seasonal distributions, but several disagreements were identified and some deficiencies remain associated with model uncertainty and process details. Upon their developments, the models have served a wide range of applications, including studies of intercontinental transport (Huang et al., 2007; Zhang et al., 2011a; Stemmler and Lammel, 2012) and source-receptor relationship (Friedman and Selin, 2012; Inomata et al., 2017), impact of emission and climate changes (Bieser et al., 2012; Friedman et al., 2013; Octaviani et al., 2015), and the assessment of adverse health effects from exposure to ambient SOCs (Zhang et al., 2009; Shen et al., 2014; Shrivastava et al., 2017).

The description of SOC cycling, transport, and chemistry differ among models with regard to the number and dimensionality of environmental compartments and process representations in each compartment. These factors depend on substance studied, spatial resolution, and region of interest. For example, Hansen et al. (2004) excluded the gas−particle partitioning of γ-HCH and simulated the species as a gas-phase tracer. Surface compartments and air−surface exchange processes were not covered in Aulinger et al. (2007), Friedman and Selin (2012), Inomata et al. (2013), and Galarneau et al. (2014) when modeling the environmental fate of PAHs. Furthermore, the simulation of SOC cycling has been found to be sensitive to environmental conditions and chemical properties, particularly to the degradation and partitioning coefficients and their temperature dependencies. Wania (2006) reported that the potential for Arctic accumulation is very sensitive to degradation rate constants in the air except for species that are strongly particle-bound in the atmosphere and for very soluble species. On the other hand, species which partition strongly into the gas phase are less affected by the change in surface degradation rate and usually have a low potential for Arctic accumulation. Schenker et al. (2009) corroborated this finding for DDT and added that the temperature dependence of degradation rate constants and partition coefficients is more critical for concentrations in the Arctic than in temperate regions and is almost negligible in the tropics. To date, there have been a few similar studies aimed at revealing which input parameters and environmental processes have the most substantial influence on model results (e.g., MacLeod et al., 2002; Meyer et al., 2005; Luo and Yang, 2007; Meyer and Wania, 2007; Wöhrnschimmel et al., 2013, and Thackray et al., 2015). Oftentimes however, the

---

[2] CanMETOP: Canadian Model for Environmental Transport of Organochlorine Pesticides; DEHM-POP: Danish Eulerian Hemipsheric Model adapted for POPs; MSCE-POP: Meteorological Synthesizing Centre-East model for POPs; CMAQ-BaP: Community Multiscale Air Quality model adapted for benzo[a]pyrene; AURAMS-PAH: A Unified Regional Air Quality Modeling System model adapted for PAHs; RAQM2-POP: Regional Air Quality Model version 2 adapted for POPs; WRF-Chem-PAH: Weather Research and Forecasting model coupled with chemistry and adapted for PAHs; MPI-MCTM: MPI Multi-Compartmental Transport Model; GEM/POPs: Global Environmental Multiscale model adapted for POPs; GEOS-Chem: Goddard Earth Observing System model with a stand-alone chemical module; CAM5-PAH: Community Atmosphere Model version 5.2 adapted for PAHs

existing studies reported results from the application of multimedia fate models which describe the whole or part of the globe as a few zones of homogeneous climatic characteristics. The 3D dynamical models are computationally less efficient than the multimedia models, but they treat the atmospheric transport and phase partitioning of SOCs more realistically and thus better resolve the spatial and temporal variability of species concentrations. With such models, a limited number of studies have attempted to assess the effect of physicochemical properties and process parameterizations on the fate and distributions of SOCs (Semeena et al., 2006; Sehili and Lammel, 2007; Friedman and Selin, 2012; Galarneau et al., 2014; Thackray et al., 2015). Sehili and Lammel (2007), for instance, suggest that the gas−particle partitioning and particulate-phase oxidation scenarios have significant influences on the long-range atmospheric transport of PAHs. This finding is supported by Friedman and Selin (2012) who also concluded that the effects are higher than those of irreversible partitioning and of increased aerosol concentrations. Other factors that can influence the model output still receive little attention or have not been addressed in the literature.

This study presents a new multicompartment module (namely SVOC) that has been integrated into a global dynamical atmospheric chemistry−climate model through an interface which interconnects various Earth system model components (EMAC model; http://www.messy-interface.org). The model system applies open-source code principles and modular framework, and permits a continual stream of improvements and new developments to maintain the model applicability for a wide variety of scientific needs. SVOC considers main environmental compartments (atmosphere, soil, vegetation, ocean, and snow) and cycling processes (emission, phase partitioning, deposition, degradation, and air−surface exchange). The standard and flexible coding allow EMAC-SVOC to be adaptable to different semivolatile groups and process complexity, and to be efficiently improved for the implementation of new knowledge. In this study, the model was used to simulate four selected PAHs and to investigate the impact on PAH concentrations from changes in four modeling factors: temporal resolution of emissions, particulate-phase representation, gas−particle partitioning, and volatilization from surfaces. The factor separation method (Stein and Alpert, 1993) was applied to isolate the influence of individual factor and the interaction between different factors.

3.2 Model descriptions

3.2.1 ECHAM/MESSy Atmospheric Chemistry−Climate (EMAC) model

The global model applied in this study is the ECHAM/MESSy Atmospheric Chemistry−Climate model (EMAC), a three-dimensional Eulerian model for the simulations of meteorological variables, gaseous, aerosols, clouds, and other climate-related parameters. EMAC combines the general circulation model ECHAM5 (here, version 5.3.02) (Roeckner et al., 2003; Roeckner et al., 2006) with the Modular Earth Submodel System (MESSy version 2.50; Jöckel et al., 2006, 2010). The atmospheric component ECHAM5 derives four prognostic variables, namely, vorticity, divergence, temperature, and the logarithm of surface pressure in truncated series of spherical harmonics, whereas specific humidity, cloud water, and cloud ice are represented in grid point space. MESSy provides a modular framework to define atmospheric dynamics, chemistry, transport, and radiative transfer processes. For a more detailed description of the EMAC model, evaluation and relevant studies, refer to Jöckel et al. (2006, 2010) and http://www.messy-interface.org. List of MESSy process-based modules, hereinafter submodels, applied in the study are summarized in Table 3.1. Descriptions of some of the submodels are discussed in Appendix C.

3.2.2 Semivolatile Organic Compounds submodel SVOC

The new MESSy submodel SVOC for simulating the fate and cycling of semivolatile organics in the global environment is presented. Processes involved in the submodel include gas−particle partitioning, volatilization from the surface, dry and wet depositions, chemical and biotic degradations. These processes are connected to other MESSy submodels. For example, deposition of gas-phase SOCs are calculated by the submodels SCAV and DDEP, aerosol microphysics by GMXe, gas-phase chemistry mechanisms by MECCA, and ocean−air flux exchange by AIRSEA. Figure 3.1 illustrates the EMAC-SVOC structure and SVOC interactions with other MESSy submodels. More details on individual physicochemical process and parameterization are given in the following section. Appendix D provides a guideline for submodel users and the list of input and output parameters.

3.3 Parameterizations of cycling processes in multiple compartments

3.3.1 Representation of SOC in particulate phase

The parameterizations of aerosol microphysical processes for SOCs such as gas-to-particle partitioning and dry and wet deposition depend on the way the particulate phase is represented in the model. Here, there are two approaches employed in the submodel to represent the particulate-phase SOC: 1) it is assumed as a bulk species, or 2) the particle sizes are resolved into n continuous (modal) distributions. The former will be hereinafter referred to as the *bulk* scheme, and the latter referred to as the *modal* scheme. In the *modal* scheme, n is equal to the 7 log-normal modes of the GMXe submodel, four with hydrophilic coating (ns: nucleation soluble, ks: Aitken soluble, as: accumulation soluble, cs: coarse soluble) and three hydrophobic (ki: Aitken insoluble, ai: accumulation insoluble, ci: coarse insoluble) (Pringle et al., 2010 and Appendix C). Each mode is treated as an individual tracer.

3.3.2 Partitioning between gas phase and particulate phase

Gas−particle partitioning is assumed to take place when SOC is at equilibrium between the gas and particulate phases. The concentration of the species that is bound to particles (C_{particle}) is calculated with

$$C_{\text{particle}} = \theta \times (C_{\text{particle}} + C_{\text{gas}}) \ , \tag{3.1}$$

Table 3.1: Summary of MESSy process submodels used in the study

Submodel	Purpose	Reference
AEROPT	Aerosol optical properties	Lauer et al., 2007
AIRSEA	Air−sea exchange	Pozzer et al., 2006
CLOUD	ECHAM5 cloud and precipitation scheme as MESSy submodel	Roeckner et al., 2006 and references therein
CONVECT	Convection parameterizations	Tost et al., 2006a, 2010
CVTRANS	Convective tracer transport	Tost, 2006
DDEP	Dry deposition of gases and aerosols	Kerkweg et al., 2006a
GMXe	Aerosol dynamics and thermodynamics	Pringle et al., 2010
JVAL	Rate of photolysis	based on Landgraf and Crutzen, 1998
LNOX	NO_x production from lightning	Tost et al., 2007
MECCA	Tropospheric and stratospheric chemistry	Sander et al., 2011
OFFEMIS	Offline emissions	Kerkweg et al., 2006b
ONEMIS	Online emissions	ibid.
RAD	ECHAM5 radiation scheme as MESSy submodel	Roeckner et al., 2006; Jöckel et al., 2006
SCAV	Scavenging of gases and aerosols	Tost et al., 2006b
SEDI	Aerosol sedimentation	Kerkweg et al., 2006a

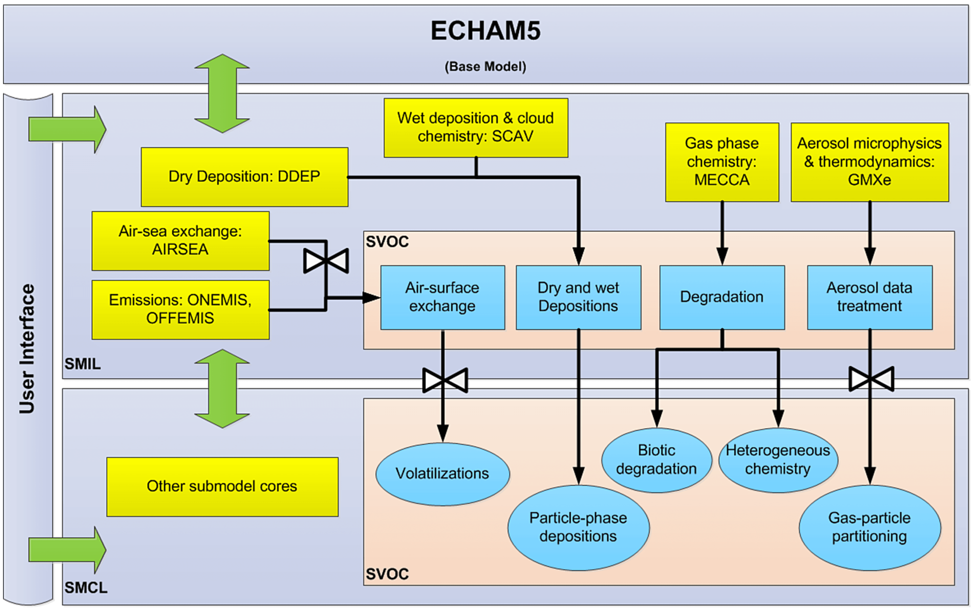

Figure 3.1: Overview of EMAC-SVOC model structure, the cycling processes in SVOC submodel and its interaction with other MESSy submodels. SMIL (submodel interface layer) and SMCL (submodel core layer) are components of MESSy coding standard, see (Jöckel et al., 2006) for further details.

and the particulate mass fraction (θ) is defined as

$$\theta = \frac{C_{\text{particle}}}{C_{\text{particle}} + C_{\text{gas}}} = \frac{K_{\text{p}} \times C_{\text{PM}}}{1 + K_{\text{p}} \times C_{\text{PM}}} = \frac{K_{\text{p}}^{'}}{1 + K_{\text{p}}^{'}} \ , \tag{3.2}$$

where C_{PM} is the concentration of particulate matter or PM (μg m^{-3}), K_{p} is the temperature-dependent particle−air partition coefficient (m^3 μg^{-1}), and $K_{\text{p}}^{'}$ is the dimensionless K_{p}.

In a model configuration using size-resolved particles (viz. the *modal* scheme), each SVOC tracer is introduced in the model as eight different species, seven aerosol particles in *ns*, *ks*, *as*, *cs*, *ki*, *ai*, *ci* modes and one in the gas phase. The particulate fraction of the species in mode i (θ_i) is calculated using Equation 3.2 with C_{PM_i} and K_{p_i} being the PM mass concentration and aerosol−air partition coefficient in the corresponding mode, respectively. The gaseous concentration C_{gas} is calculated using the sum of K_{p} values across modes, as well as total C_{particle} and C_{PM}:

$$C_{\text{gas}} = \frac{\sum\limits_{i=1}^{7} C_{\text{particle}_i} / \sum\limits_{i=1}^{7} C_{\text{PM}_i}}{\sum\limits_{i=1}^{7} K_{\text{p}_i}} \ . \tag{3.3}$$

It is noted that this approach does not hold the constraint of mass consistency, and is thus subject to further corrections. For the current study, the effects from this problem are expected to be minimal, given the fact that PAHs in the particulate phase are mainly distributed in the accumulation mode (Lammel et al., 2010 and references therein).

For K_{p} calculation four options of gas−particle partitioning schemes are available in EMAC-SVOC, they are: (1) a parameterization that is based on adsorption onto aerosol surface (Junge, 1977; Pankow, 1987), (2) absorption into organic matter (Finizio et al., 1997), (3) a combination of two ways of organic matter absorption and black carbon adsorption (Lohmann and Lammel, 2004), and (4) multiple phase of the two-ways sorption system (Goss and Schwarzenbach, 2001; Endo and Goss, 2014; Shahpoury et al., 2016).

Junge−Pankow scheme

This scheme is the first theoretical description of SOCs association with particles, suggested by Junge (1977) and further refined by Pankow (1987). It assumes that SOCs are adsorbed onto aerosol surfaces based on an inverse relationship with the sub-cooled liquid vapor pressure p_{L}^{0}:

$$\theta = \frac{c_{\text{J}} \times \Phi}{c_{\text{J}} \times \Phi + p_{\text{L}}^{0}} \ , \tag{3.4}$$

where Φ is the surface area of particles per unit volume of air (cm^{-1}), and c_{J} is fixed at 17.2 Pa cm. The parameter p_{L}^{0} is the sub-cooled liquid vapor pressure (Pa) at ambient temperature, interpolated from liquid vapor pressure at T_0=298 K ($P_{v(T_0)}$) using the van't Hoff equation that takes the form

$$\ln p_{\mathrm{L}}^0 = \ln P_{v(T_0)} - \frac{\Delta \mathrm{H}_{\mathrm{vap}}}{R}\left(\frac{1}{T} - \frac{1}{T_0}\right) \ , \tag{3.5}$$

The calculated θ is converted to K_{p} by

$$K_{\mathrm{p}} = \frac{\theta}{C_{\mathrm{PM}} \times (1-\theta)} \ . \tag{3.6}$$

The Junge−Pankow adsorption theory neglects the absorptive partitioning potential to organic matter (OM) which has been found from laboratory studies to be relevant mainly for lipophilic compounds (Lohmann and Lammel, 2004 and references therein).

Finizio scheme

An absorptive theory for phase partitioning of SOC is described by Finizio et al. (1997) as a function of octanol−air partition coefficient K_{oa}. This scheme assumes that SOC partition into particles by diffusing through the organic matrix of PM. For this scheme, K_{p} is determined as follows

$$K_{\mathrm{p}} = 10^{-12}\left(f_{\mathrm{OM}} \times \frac{\gamma_{\mathrm{oct}}\ \mathrm{MW}_{\mathrm{oct}}}{\gamma_{\mathrm{OM}}\ \mathrm{MW}_{\mathrm{OM}}\ \rho_{\mathrm{oct}}}\right) K_{\mathrm{oa}} \ , \tag{3.7}$$

where f_{OM} (unitless) is the fraction of organic matter (OM) in PM, ρ_{oct} is the density of octanol (0.82 kg L^{-1}), γ_{oct} and γ_{OM} (unitless) are the activity coefficients of the target compound in octanol and OM, respectively, $\mathrm{MW}_{\mathrm{oct}}$ and $\mathrm{MW}_{\mathrm{OM}}$ (g mol^{-1}) are the molecular weights of octanol and OM, respectively. Harner and Bidleman (1998b) suggested a more general form of the relationship between K_p and K_{oa} for PAHs by assuming that $\frac{\gamma_{\mathrm{oct}}}{\gamma_{\mathrm{OM}}}$ is one and remains constant and that $\mathrm{MW}_{\mathrm{oct}}$ and $\mathrm{MW}_{\mathrm{sOM}}$ are equal. They found that a better agreement between predicted and measured gas−particle partitioning was obtained by applying

$$\log K_{\mathrm{p}} = \log K_{\mathrm{oa}} + \log f_{\mathrm{OM}} - 11.91 \ . \tag{3.8}$$

The K_{oa} value is determined as a function of ambient air temperature using a linear regression relationship defined in Odabasi et al. (2006) with $K_{\mathrm{oa-m}}$ and $K_{\mathrm{oa-b}}$ being the slope and intercept of the temperature regression.

$$\log K_{\mathrm{oa}} = \frac{K_{\mathrm{oa-m}}}{T} + K_{\mathrm{oa-b}} \ . \tag{3.9}$$

Lohmann−Lammel scheme

The Lohmann−Lammel scheme takes into account a parameter that is not considered in the previous schemes, that is, an adsorption onto black carbon (BC) surface in addition to absorption into OM (Lohmann and Lammel, 2004). This dual sorption theory empirically calculates K_p according to the following relation

$$K_\mathrm{p} = 10^{-12} \left(f_\mathrm{OM} \, \frac{\gamma_\mathrm{oct} \, \mathrm{MW}_\mathrm{oct}}{\gamma_\mathrm{OM} \, \mathrm{MW}_\mathrm{OM} \, \rho_\mathrm{oct}} \, K_\mathrm{oa} + f_\mathrm{BC} \, \frac{a_{\mathrm{atm-BC}}}{a_\mathrm{soot} \, \rho_\mathrm{BC}} \, K_\mathrm{sa} \right) \,, \tag{3.10}$$

where ρ_BC is the density of BC (assumed as 1 kg L^{-1}), ρ_oct is the density of octanol (0.82 kg L^{-1} at 20°), K_sa is the partition coefficient between diesel soot and air, $a_{\mathrm{atm-BC}}$ is the available surface of atmospheric BC (m^2 g^{-1}), and a_soot is the specific surface area of diesel soot (m^2 g^{-1}). The adsorptive properties of diesel soot are selected to represent the atmospheric BC because this material is considered the most significant type of BC in polluted air.

The K_sa value is calculated as a function of sub-cooled liquid vapor pressure p_L^0 using an estimate suggested by van Noort (2003),

$$\log K_\mathrm{sa} = -0.85 \log p_\mathrm{L}^0 + 8.94 - \log \left(\frac{998}{a_\mathrm{soot}} \right) \,, \tag{3.11}$$

where a_soot in the model is set as 18.21 m^2 g^{-1}.

Poly-Parameter Linear Free Energy Relationships (ppLFER) scheme

The concept of poly-parameter linear free energy relationships (ppLFER) for the prediction of equilibrium partition coefficients is introduced by Goss and Schwarzenbach (2001), and its application in environmental chemistry has been reviewed by Endo and Goss (2014). This approach can describe a composite of different types of interactions between gas-phase species and aerosols. In contrast, single-parameter LFERs only correlates the partition coefficient to the sub-cooled liquid vapor pressure or the octanol−air partition coefficient of the species, hence only valid within the group of compounds for which they were developed.

In the study, ppLFER scheme is incorporated into EMAC-SVOC in which it defines K_p as the sum of individual partition coefficients representing surface adsorption and bulk-phase absorption processes to inorganic and organic aerosols. The formulation of K_p is adopted from Shahpoury et al. (2016) and is described as follows

$$\begin{aligned} K_{\mathrm{p}} &= \frac{K_{\mathrm{p}}^{'}}{C_{\mathrm{PM}}} \\ K_{\mathrm{p}}^{'} &= K_{\mathrm{EC}} \times a_{\mathrm{EC}} \times C_{\mathrm{EC}} \times 10^{-6} + \\ &\quad K_{(\mathrm{NH_4})_2\mathrm{SO_4}} \times a_{(\mathrm{NH_4})_2\mathrm{SO_4}} \times C_{(\mathrm{NH_4})_2\mathrm{SO_4}} \times 10^{-6} + \\ &\quad K_{\mathrm{NaCl}} \times a_{\mathrm{NaCl}} \times C_{\mathrm{NaCl}} \times 10^{-6} + \\ &\quad K_{\mathrm{DMSO}} \times \frac{C_{\mathrm{WSOM}}}{\rho_{\mathrm{DMSO}}} \times 10^{-6} + \\ &\quad K_{\mathrm{PU}} \times 0.2 \times C_{\mathrm{WIOM}} \times 10^{-12} + \\ &\quad K_{\mathrm{hexadecane}} \times 0.8 \times \frac{C_{\mathrm{WIOM}}}{\rho_{\mathrm{hexadecane}}} \times 10^{-6} \end{aligned} \tag{3.12}$$

where K_{EC}, $K_{(\mathrm{NH_4})_2\mathrm{SO_4}}$, and K_{NaCl} are the substance partition (adsorption) coefficients ($\mathrm{m^3_{air}\ m^{-2}_{surface}}$) for elemental−carbon/diesel soot, ammonium sulfate, and sodium chloride aerosol surface−air systems, respectively. K_{DMSO} is the substance partition (absorption) coefficient for dimethyl sulfoxide−air system ($\mathrm{L_{air}\ L^{-1}_{DMSO}}$). K_{PU} is the substance partition (absorption) coefficient for polyurethane−air system ($\mathrm{m^3_{air}\ kg^{-1}_{PU}}$). $K_{\mathrm{hexadecane}}$ is the substance partition (absorption) coefficient for hexadecane−air system ($\mathrm{L_{air}\ L^{-1}_{hexadecane}}$). a_{EC}, $a_{(\mathrm{NH_4})_2\mathrm{SO_4}}$, and a_{NaCl} are the adsorbent specific surface areas: 18.21, 0.1, and 0.1 $\mathrm{m^2_{surface}\ g^{-1}_{adsorbent}}$, respectively. ρ_{DMSO} and $\rho_{\mathrm{hexadecane}}$ are the dimethly sulfoxide and hexadecane densities: $1.1{\times}10^6$ and $0.77{\times}10^6$ g $\mathrm{m^{-3}}$, respectively. C_{EC}, $C_{(\mathrm{NH_4})_2\mathrm{SO_4}}$, C_{NaCl}, C_{WSOM}, C_{WIOM} are the concentration ($\mu\mathrm{g_{substance}\ m^{-3}_{air}}$) of elemental carbon (here, black carbon), ammonium sulfate, sodium chloride, water-soluble organic matter, and water-insoluble organic matter, respectively.

The ppLFER scheme calculates the sorptive partition coefficient for every aerosol system, as summarized in Table 3.2. Each of the coefficients requires information on system parameters (e, s, a, b, v, l), and the constant c, as shown in Table 3.3. The Abraham solute descriptors (E, S, A, B, V, and L) are substance specific, and for the species selected in this study, refer to Table 3.7.

All the predicted partition constants are adjusted to environmental temperature using the van't Hoff equation

$$\ln K_{(\mathrm{T})} = \ln K_{(\mathrm{T_0})} - \frac{\Delta \mathrm{H}}{R}\left(\frac{1}{\mathrm{T}} - \frac{1}{\mathrm{T_0}}\right) , \tag{3.13}$$

where ΔH is the enthalpy of solvent-air phase transfer in J $\mathrm{mol^{-1}}$. This variable is system specific and calculated by applying the ppLFER equations given in Table 3.4 and input parameters given in Table 3.5.

In EMAC-SVOC, the sequence of K_{p} calculation from ppLFER analysis is illustrated in Figure 3.2.

Table 3.2: Gas−particle partition coefficient for every sorption system in the ppLFER

System	Unit	Equation
NIST diesel soot−air	$\mathrm{m}^{3}_{\mathrm{air}}\ \mathrm{m}^{-2}_{\mathrm{surface}}$	$\log_{10} K_{\mathrm{EC}} = lL + aA + bB + c$
$(NH_4)_2SO_4$−air	$\mathrm{m}^{3}_{\mathrm{air}}\ \mathrm{m}^{-2}_{\mathrm{surface}}$	$\log_{10} K_{(\mathrm{NH_4})_2\mathrm{SO_4}} = lL + aA + bB + c$
NaCl−air	$\mathrm{m}^{3}_{\mathrm{air}}\ \mathrm{m}^{-2}_{\mathrm{surface}}$	$\log_{10} K_{\mathrm{NaCl}} = lL + aA + bB + c$
Dry DMSO−air	$\mathrm{L}_{\mathrm{air}}\ \mathrm{L}^{-1}_{\mathrm{solvent}}$	$\log_{10} K_{\mathrm{DMSO}} = lL + sS + aA + bB + eE + c$
PU−air	$\mathrm{L}_{\mathrm{air}}\ \mathrm{kg}^{-1}_{\mathrm{PU}}$	$\log_{10} K_{\mathrm{PU}} = lL + sS + aA + bB + vV + c$
Wet/dry hexadecane−air	$\mathrm{L}_{\mathrm{air}}\ \mathrm{L}^{-1}_{\mathrm{solvent}}$	$\log_{10} K_{\mathrm{hexadecane}} = lL + sS + aA + bB + eE + c$

Table 3.3: ppLFER system parameters for gas−particle partition coefficients

System	***e***	***s***	***a***	***b***	***v***	***l***	***c***	**$\mathbf{T_0}$ (K)**	**Reference**
NIST diesel soot−air	-	-	2.70	2.45	-	1.09	−8.47	288	Roth et al., 2005
$(NH_4)_2SO_4$−air (20% RH)	-	-	2.46	5.23	-	0.90	−8.47	288	Goss et al., 2003
$(NH_4)_2SO_4$−air (40% RH)	-	-	2.46	5.23	-	0.89	−8.47	288	ibid.
$(NH_4)_2SO_4$−air (60% RH)	-	-	2.13	5.34	-	0.88	−8.47	288	ibid.
NaCl−air (20% RH)	-	-	3.12	4.77	-	0.87	−8.47	288	ibid.
NaCl−air (40% RH)	-	-	2.94	4.82	-	0.86	−8.47	288	ibid.
NaCl−air (60% RH)	-	-	2.86	4.82	-	0.84	−8.47	288	ibid.
Dry DMSO−air	−0.22	2.90	5.04	0.00	-	0.72	−0.56	298	Abraham et al., 2010
PU−air	-	1.69	3.66	0.00	0.36	0.71	−0.15	288	Kamprad and Goss, 2007
Wet/dry hexadecane−air	0.00	0.00	0.00	0.00	-	1.00	0.00	298	Abraham et al., 2010

Table 3.4: Enthalpy of phase transfer for every sorption system in the ppLFER scheme

System	Unit	Equation
NIST diesel soot−air	J mol^{-1}	$\Delta H1 = -\Delta H^{*}_{\mathrm{vap}}$
$(NH_4)_2SO_4$−air	J mol^{-1}	$\Delta H2 = (-10.2 \times \log_{10} K_{(\mathrm{NH_4})_2\mathrm{SO_4}} - 89.6) \times 10^3$
NaCl−air	J mol^{-1}	$\Delta H3 = (-10.2 \times \log_{10} K_{\mathrm{NaCl}} - 89.6) \times 10^3$
Dry DMSO−air	J mol^{-1}	$\Delta H4 = (l'L + s'S + a'A + b'B + v'V + c') \times 10^3$
PU-air	J mol^{-1}	$\Delta H5 = (l'L + s'S + a'A + v'V + c') \times 10^3$
Dry hexadecane−air	J mol^{-1}	$\Delta H6 = (l'L + s'S + a'A + b'B + v'V + c') \times 10^3$

$^{*}\Delta H_{\mathrm{vap}}$ values are given in Table 3.7

Table 3.5: ppLFER system parameters for phase transfer enthalpy

System	e'	s'	a'	b'	v'	l'	c'	Reference
Dry DMSO−air	-	−19.04	−47.80	−5.52	−0.75	−6.19	−2.39	Mintz et al., 2008
PU−air	-	−17.60	−46.60	-	−12.80	−4.30	2.70	Kamprad and Goss, 2007
Dry hexadecane−air	-	−3.20	−1.51	2.58	−10.86	−6.79	−2.97	Abraham et al., 2010

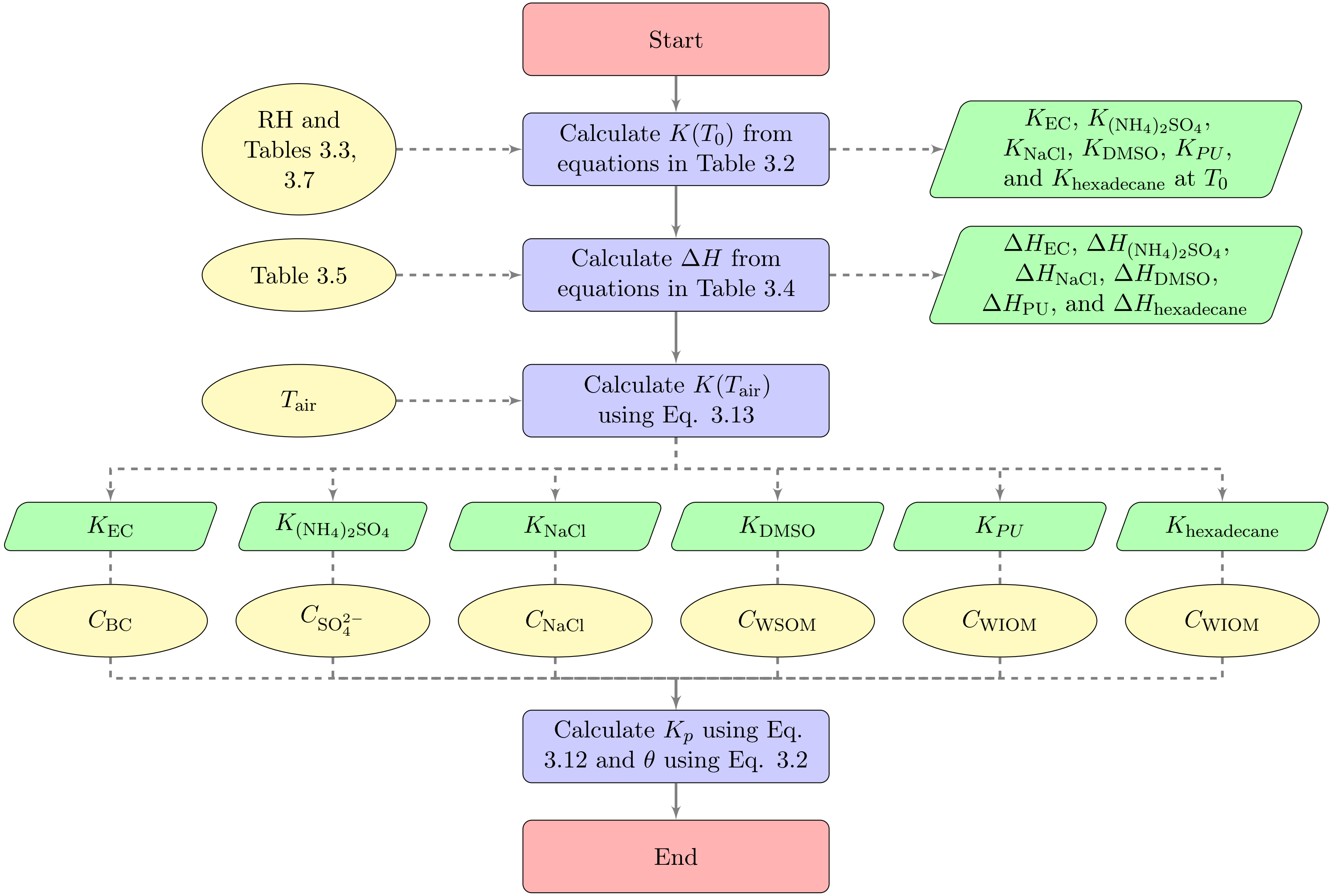

Figure 3.2: Schematic diagram in EMAC-SVOC for the prediction of gas−particle partition coefficient using the ppLFER scheme

3.3.3 Volatilization

Soil

For soil volatilization, two parameterization schemes are implemented in EMAC-SVOC, that is, the Jury scheme (Jury et al., 1983; Jury et al., 1990), and the Smit scheme (Smit et al., 1997).

1. Jury scheme

   This scheme is introduced by Jury et al. (1983) whereby the volatilization process is parameterized in a simplified way (Jury et al., 1990): 1) Only one soil layer is considered hence diffusion and convection within the soil are not accounted for, 2) Only consider volatilization fluxes at the surface with no volatilization from chemicals residing below the soil surface, 3) Assume homogeneous soil properties (constant water content, bulk density, porosity, liquid water flux, and organic carbon fraction), and 4) Two transport processes at the surface (that is, vapor/gaseous and liquid diffusion) are implemented in a two-film model using the diffusion coefficients D_{gas} and D_{wat}.

   The soil-gas diffusion coefficient is derived from multiplying the air gas diffusion coefficient $D_{\mathrm{g}}^{\mathrm{air}}$ with a tortuosity factor. Using the Millington−Quirk tortuosity formula, the diffusion coefficient can be calculated from soil porosity ϕ and volumetric air fraction ψ:

   $$D_{\mathrm{gas}} = D_{\mathrm{g}}^{\mathrm{air}} \, \frac{\psi^{10/3}}{\phi^2} \; . \tag{3.14}$$

   Similarly, the soil−liquid diffusion coefficient is derived from the water−liquid diffusion coefficient $D_{\mathrm{l}}^{\mathrm{wat}}$, soil porosity ϕ and volumetric water fraction φ:

   $$D_{\mathrm{wat}} = D_{\mathrm{l}}^{\mathrm{wat}} \, \frac{\varphi^{10/3}}{\phi^2} \; , \tag{3.15}$$

   where $\varphi = \phi$ - ψ. The representative values of 0.018 $\mathrm{m}^2\ \mathrm{h}^{-1}$ for $D_{\mathrm{g}}^{\mathrm{air}}$ and 0.000018 $\mathrm{m}^2\ \mathrm{h}^{-1}$ for $D_{\mathrm{l}}^{\mathrm{wat}}$ were selected for use based on the compilation of Boynton and Brattain (1929) and Bruins (1929), respectively, which measurements have been made on pesticides.

   According to Jury et al. (1990), the volatilization flux at the top soil layer (J_s in μg m^{-2} s^{-1}), for zero water evaporation and zero boundary layer thickness, can be written as:

   $$J_s = C_0 \exp\left(-k_{\mathrm{sfc}}\ t\right) \sqrt{\left(\frac{D_E}{\pi\ t}\right)} \left[1 - \exp\left(\frac{-L^2}{4 D_E\ t}\right)\right] \; , \tag{3.16}$$

   where C_0 is the concentration of a chemical at the initial time (μg m^{-3}), k_{sfc} is the 1st order biological/chemical degradation rate constant (s^{-1}), t is the experimental run time (s), D_E is the effective diffusion coefficient ($\mathrm{m}^2\ \mathrm{s}^{-1}$), and L is the depth of the contaminated layer (m).

   In the model, k_{sfc} is taken as zero because degradation process is calculated separately (see Section 3.3.7). L is assumed to be 0.1 m for forest and 0.2 m for agricultural land.

For other land use type, L is defined as $f_{\text{forest}} \times 0.1 + (1 - f_{\text{forest}}) \times 0.2$ where f_{forest} is the fraction of forest within a grid cell. The effective diffusion coefficient D_E is diagnostically computed from

$$D_E = \frac{(K_{\text{aw}} D_{\text{gas}} + D_{\text{wat}})}{\rho_{\text{soil}} K_{\text{sl}} + \varphi + \psi K_{\text{aw}}} \ , \tag{3.17}$$

where K_{aw} is the dimensionless air−water partition coefficient, ρ_{soil} is the dry bulk density of soil (kg m^{-3}), and K_{sl} is the solid−liquid partition coefficient (m^3 kg^{-1}). K_{sl} can be set equal to the sorption coefficient to soil organic matter K_{om} times the fraction of organic carbon in soil f_{OM_s}. Since K_{om} is not available, the coefficient for sorption to soil organic carbon K_{oc} was used to estimate K_{sl}:

$$K_{\text{sl}} = 0.56 K_{\text{oc}} f_{\text{OM}_\text{s}} \ , \tag{3.18}$$

Mackay and Boethling (2000) has suggested a reasonably good regression relationship between K_{oc} and octanol−water partition coefficient K_{ow} for PAHs:

$$\log(K_{\text{oc}}/1000) = 0.823 \log(K_{\text{ow}}/1000) - 0.727 \ . \tag{3.19}$$

where the factor of 1000 is needed because K_{oc} and K_{ow} are expressed in m^3 kg^{-1} whereas, in the original regression, they used mL g^{-1}. The air−water partition coefficient K_{aw} is calculated based on the Henry's Law constant:

$$K_{\text{aw}} = 1/\,(H \ R \ T) \ , \text{ and} \tag{3.20}$$

$$H = k_{\text{H}}^{\ominus} \times \exp\left[\frac{-\Delta H_{\text{soln}}}{R}\left(\frac{1}{T} - \frac{1}{T_0}\right)\right] \ , \tag{3.21}$$

where H is the temperature-adjusted Henry coefficient (M atm^{-1}), R is the dry air gas constant (= 8.314 J mol K^{-1}), T is the environment temperature (K), ΔH_{soln} is the enthalpy of dissolution (J mol^{-1}).

2. Smit scheme

This scheme focuses on the volatilization of pesticides from the surface of fallow soils (Smit et al., 1997). The volatilization occurs upon partitioning over three soil phases (solid, gas, and liquid). The concentration of the chemical in the soil system (kg m^{-3}) is formulated as

$$C_{\text{soil}} = Q \times C_{\text{vapor}} \ , \tag{3.22}$$

and the capacity factor Q is given by

$$Q = \psi + \varphi K_{\mathrm{wa}} + \rho_{\mathrm{soil}} K_{\mathrm{wa}} K_{\mathrm{sl}} \ , \tag{3.23}$$

where ψ and φ are the volume fractions of air and moisture, respectively, ρsoil is the soil density, K_{wa} is the water−air partition coefficient where $K_{\mathrm{wa}} = 1/K_{\mathrm{aw}}$ (Equation 3.20), and K_{sl} is the solid−liquid partition coefficient (Equation 3.18). The dimensionless fraction of the chemical in the gas phase F_{gas} is then calculated as

$$F_{\mathrm{gas}} = \frac{\psi}{Q} \ . \tag{3.24}$$

An empirical relation was established between F_{gas} and cumulative volatilization (CV in % of substance deposit). CV was determined based on field and greenhouse experiments with numerous pesticides at 21 days after application. For normal to moist field conditions, CV is expressed as

$$CV = 71.9 + 11.6 \log(100\ F_{\mathrm{gas}}) \ ; \ 6.33 \times 10^{-9} < F_{\mathrm{gas}} \leq 1 \ , \tag{3.25}$$

and for dry field conditions,

$$CV = 42.3 + 9.0 \log(100\ F_{\mathrm{gas}}) \ ; \ 0.2 \times 10^{-6} < F_{\mathrm{gas}} \leq 1 \ . \tag{3.26}$$

Vegetation

Smit et al. (1998) derived an equation for the cumulative volatilization CV from plants against vapor pressure P_v (mPa) at seven days after application based on field and climate chamber experiments of pesticide volatilization (Equation 3.27).

$$CV = 10^{1.528 + 0.466 \log P_v} ; P_v \leq 10.3 \ . \tag{3.27}$$

For compounds with P_v above 10.3 mPa, CV is set at 100 % of deposit. Temperature adjustments were made for P_v using the Clausius−Clapeyron equation:

$$\frac{d(\ln P_v)}{dT} = -\frac{\Delta H_{\mathrm{vap}}}{R\, T^2} \ . \tag{3.28}$$

Snow and glaciers

The parameterization of substance loss by volatilization from snow pack follows Wania (1997) whereby the process is calculated using a consecutive cycle of an equilibrium partitioning among four phases followed by a contaminant loss. The four phases considered are liquid water, organic matter contained in the snowpack, snow pores (air), and an ice−air interface. Fugacity capacity factors for these phases are expressed with the following relations:

air (mol m^{-3} Pa^{-1}) $\quad Z_a = 1/RT$ (3.29a)

water (mol m^{-3} Pa^{-1}) $\quad Z_l = K_{\mathrm{wa}}/RT = K_{\mathrm{wa}}\ Z_a$ (3.29b)

organic carbon (mol m^{-3} Pa^{-1}) $\quad Z_o = Z_l\ 0.41\ K^{'}_{\mathrm{ow}}$ (3.29c)

ice–air interface (mol m^{-2} Pa^{-1}) $\quad z_i = K_{\mathrm{ia}}/RT = K_{\mathrm{ia}}\ Z_a$ (3.29d)

where R is the dry air gas constant (8.312 J mol^{-1} K^{-1}), T is the air temperature (K), K_{wa} is the water−air partition coefficient (unitless), $K^{'}_{\mathrm{ow}}$ is the dimensionless octanol−water partition coefficient, and K_{ia} is the ice surface−air partition coefficient (m). K_{ia} at 20°C is estimated using K_{wa} and water solubility C^s_w (mol m^{-3}),

$$\log K_{\mathrm{ia}}\,(20°\mathrm{C}) = -0.769 \log C^s_w - 5.97 + \log K_{\mathrm{wa}}\ , \tag{3.30}$$

and further extrapolated to other temperatures using enthalpy of condensation of solid (ΔH_{subl} in J mol^{-1}),

$$\log K_{\mathrm{ia}}(T) = \log K_{\mathrm{ia}}\,(20°\mathrm{C}) + \frac{0.878\ \Delta H_{\mathrm{subl}}}{2.303\ R}\left(\frac{1}{T} - \frac{1}{293}\right)\ . \tag{3.31}$$

An equilibrium fugacity f_s is thereby determined by

$$f_s = \frac{M_{\mathrm{sp}}}{Z_a\ v_a + Z_l\ v_l + z_i\ A_{\mathrm{snow}}\ \rho_{\mathrm{mw}} + Z_o v_o}\ , \tag{3.32}$$

where M_{sp} is the amount of chemical contained in snowpack (the model here applies snow burden of the chemical in kg m^{-2}), v_a, v_l, and v_o is the volume fraction of air, liquid water, and organic matter in snowpack (m^3 m^{-3}). For this study, v_a and v_l values are set to 0.3 and 0.1, respectively, whereas v_o is zero assuming no polluted snow. A_{snow} is the specific snow surface area (m^2 g^{-1}). In Daly and Wania (2004), a value of 0.1 m^2 g^{-1} for A_{snow} was used for snow accumulation period and a linear decrease from 0.1 to 0.01 m^2 g^{-1} was used during the snowmelt period. In EMAC-SVOC, a value of 0.025 m^2 g^{-1} is adopted for A_{snow} to represent fairly aged snowpack. ρ_{mw} is the density of snowmelt water and here is taken as 7×10^5 g m^{-3}.

Volatilization rate (kg m^{-2} s^{-1}) is calculated by applying

$$\frac{dM_{\mathrm{sp}}}{dt} = \frac{1}{\frac{1}{U_7\ Z_a} + \frac{1}{U_5\ Z_l\ +\ U_6\ Z_a}} \times \frac{f_s}{h_s}\ , \tag{3.33}$$

where h_s is the snow depth (m), U_5 is the snow−water phase diffusion mass transfer coefficient (m h^{-1}), U_6 is the snow−air phase diffusion mass transfer coefficient (m h^{-1}), and U_7 is the snow−air boundary layer mass transfer coefficient (m h^{-1}). U_5 and U_6 are calculated from molecular diffusivities in air and water (Equations 3.34 and 3.35), whereas a typical value of 5 m h^{-1} is adopted for U_7.

$$U_5 = B_w\ \frac{v_l^{10/3}/(v_a + v_l)^2}{\ln\ 2h_s}\ , \tag{3.34}$$

$$U_6 = B_a \, \frac{v_a^{10/3}/(v_a + v_l)^2}{\ln \; 2h_s} \; , \tag{3.35}$$

where B_w and B_a are the molecular diffusivities (m^2 h^{-1}) in water and air respectively. In the model, B_a is derived from the molecular weight (MW) as $B_a = \frac{1.55}{\mathrm{MW}^{0.65}}$ cm^{2}s^{-1}, whereas B_w is set as $1{\times}10^4$ less than B_a, following Schwarzenbach et al. (2005).

It is noted that the same parameterization is applied to volatilization from ice sheets and glaciers.

Ocean

In the study, the ocean is treated as a two-dimensional compartment (no vertical layer). The flux of chemicals from the ocean to the atmosphere is parameterized based on the two-film model of Liss and Slater (1974) and is calculated within the AIRSEA submodel (Pozzer et al., 2006 and see Appendix C). Note that no ocean and sea-ice dynamics were included in the simulations.

3.3.4 Dry deposition

Dry deposition is simulated using deposition velocities. For gas-phase SOCs, the velocities are calculated by the DDEP submodel (Kerkweg et al., 2006a and see Appendix C), whereas particulate-bound SOCs are assumed to deposit at similar rates to other aerosols whose velocities are also computed by DDEP. If the *modal* scheme is selected (see Section 3.3.1), the particle deposition velocity v_d^{SOC} at mode i is equal to the aerosol deposition velocity v_d^{aer} at the respective mode. On the other hand, for the *bulk* scheme, v_d^{SOC} is computed as a weighted average of v_d^{aer} from the four BC modes (*ki*, *ks*, *as*, and *cs*) where the weight is the surface area of BC.[3] The above relations are formulated as follows

$$\textit{modal}\text{ scheme:} \qquad v_{d,i}^{\mathrm{SOC}} = v_{d,i}^{\mathrm{aer}} \tag{3.36a}$$

$$\textit{bulk}\text{ scheme:} \qquad v_{d,\mathrm{bulk}}^{\mathrm{SOC}} = \frac{\sum\limits_{i=1}^{4} S_{\mathrm{BC}_i} \times v_{d,i}^{\mathrm{aer}}}{\sum\limits_{i=1}^{4} S_{\mathrm{BC}_i}} \tag{3.36b}$$

and the BC surface area per unit volume S_{BC} (cm^2 cm^{-3}) is given by

$$S_{\mathrm{BC}_i} = 4\pi \left[r_i \exp\left(\ln^2 \sigma_{g_i}\right)\right]^2 N_i \times \frac{C_{\mathrm{BC}_i}}{C_{\mathrm{aer}_i}} \; , \tag{3.37}$$

where N_i is the number concentration for mode i (cm^{-3}), r_i is the number radius (cm), σ_{g_i} is the geometric standard deviation, C_{BC_i} is the BC concentration (μg m^{-3}) in mode i, and C_{aer_i} is the sum of aerosol concentrations in the same mode (μg m^{-3}).

---

[3] This method is most relevant for PAHs as they are assumed to be predominantly transported by sorption to BC.

3.3.5 Wet deposition

Wet deposition is applied to both gas and particulate SOCs. The gaseous fraction is scavenged into cloud and rain droplets according to diffusion limitation, Henry's law equilibrium, and accommodation coefficient, and this process is parameterized and solved empirically in the SCAV submodel (Tost et al., 2006b and see Appendix C). Particulate-phase SOCs are scavenged in convective updrafts, rainout and washout, and cloud evaporation, with the rate proportional to BC wet scavenging^3; hence the change in SOC concentration is described as

$$\textit{modal}\text{ scheme:} \qquad \frac{\Delta C_{\mathrm{SOC}_i}}{\Delta t} = \frac{\mu_{\mathrm{SOC}_i}}{\mu_{\mathrm{BC}_i}} \times \frac{\Delta C_{\mathrm{BC}_i}}{\Delta t} \tag{3.38a}$$

$$\textit{bulk}\text{ scheme:} \qquad \frac{\Delta C_{\mathrm{SOC}}}{\Delta t} = \frac{\mu_{\mathrm{SOC}}}{\sum\limits_{i=1}^{4} \mu_{\mathrm{BC}_i}} \times \sum_{i=1}^{4} \frac{\Delta C_{\mathrm{BC}_i}}{\Delta t} \tag{3.38b}$$

where μ is the particle volume mixing ratio ($\mathrm{mol}_{\mathrm{SOC/BC}}\ \mathrm{mol}_{\mathrm{air}}^{-1}$) and Δt is the model time step (s). Note that Equation 3.38a imposes a restrictive prerequisite, namely, BC and the particle-bound SOC have similar size distributions. When this condition is not met, there is a high possibility of an artificial mass being produced, usually in the largest aerosol mode. To solve this problem, a correction factor is applied and defined as a function of the ratio of positive fluxes to negative fluxes integrated across levels and modes.

3.3.6 Atmospheric degradation

The atmospheric degradation of SOCs in the gas phase as well as within aerosol particles are explicitly treated in EMAC-SVOC. The gas-phase chemical mechanism is calculated within the MECCA submodel (Sander et al., 2011). SOC gaseous degradation is from photochemical reactions with OH, NO_3, and O_3 radicals which follow a 2nd-order transformation, with the rate constants $k^{(2)}$ obtained from laboratory studies. $k^{(2)}_{\mathrm{OH}}$ value is typically higher, suggesting that oxidation with OH radical is the dominant loss pathway.

Most models do not consider oxidation rate of particulate-phase SOCs as experimental aerosols studied in laboratory cover only a small part of atmospheric relevant aerosols. For PAHs, such as benzo[a]pyrene which stays mostly in the particulate phase, the degradation is more efficient by surface reactions with O_3 (Shiraiwa et al., 2009 and references therein) with the rate depending on the substrate. In this work, EMAC-SVOC includes degradation process of PAHs on aerosol particles from the O_3 reaction with one assumption, that is, the heterogeneous reaction does not lead to a change in the oxidant concentration. Due to a limited number of kinetic studies of heterogeneous reactions of PAHs, only two species are considered (phenanthrene and benzo[a]pyrene). Nevertheless, the submodel structure provides a relatively straightforward approach to allow more species in the future.

The reaction rate coefficient for particulate-phase PHE with O_3 at aerosol surfaces was derived from laboratory experiments using chemically unspecific model aerosol (silica) with PAH surface coverage of less than a monolayer (Perraudin et al., 2007). To this end, the second order rate coefficient, $k^{(2)}$, in $\mathrm{cm}^4\ \mathrm{molec}^{-1}\ \mathrm{s}^{-1}$ was derived from the reported PHE decay kinetics,

$k^{(2)}_{\mathrm{O_3,het}}$ (cm^3 molec^{-1} s^{-1}), as $k^{(2)} = k^{(2)}_{\mathrm{O_3,het}}/\left(\frac{S}{V}\right) = (6.2 \pm 4.8) \times 10^{-17}$ cm^4 molec^{-1} s^{-1}, with $\frac{S}{V}$ (cm^{-1}) being the experimental aerosol surface concentration (0.56 ± 0.43 cm^{-1} in Perraudin et al., 2007). In the submodel, $k^{(2)}_{\mathrm{O_3,het}}$ (cm^3 molec^{-1} s^{-1}) is calculated using the ambient aerosol surface concentration. As for BaP, the pseudo-first-order rate coefficient, $k^{(1)}_{\mathrm{O_3,het}}$ in s^{-1}, was derived from surface-adsorbed BaP reaction with O_3 on solid organic and salt aerosols following the Langmuir−Hinshelwood mechanism (Kwamena et al., 2004).

3.3.7 Biotic and abiotic degradations

Biotic and abiotic processes in surface compartments contribute to the degradation of chemicals and are strongly dependent on local environmental conditions, for example, nutrient contents, water, temperature, PH, and light. In EMAC-SVOC, these factors are not explicitly quantified. The degradation is alternatively described as following a first-order decay law (Equation 3.39), and the rate is assumed to double for every 10 K warming (Equation 3.40).

$$\frac{\partial C_{\mathrm{SOC_s}}}{\partial t} = -k_{\mathrm{sfc}} \times C_{\mathrm{SOC_s}} \ , \tag{3.39}$$

$$k_{\mathrm{sfc}(T)} = k_{\mathrm{sfc}(T_{\mathrm{ref}})} \times 2^{\frac{T-T_{\mathrm{ref}}}{10}} \ , \tag{3.40}$$

where $C_{\mathrm{SOC_s}}$ is the substance concentration (kg m^{-3}) in surface compartments (that is, soil, vegetation, or ocean) and k_{sfc} is the first-order decay rate (s^{-1}). T_{ref} is the reference temperature, that is, 298 K for soil and 273 K for ocean. Note that the degradation in vegetation is calculated assuming the same k_{sfc} for the soil compartment.

3.4 Data

3.4.1 Kinetic and physicochemical properties

The model simulations were performed for four PAH species: phenanthrene (PHE), pyrene (PYR), fluoranthene (FLT), and benzo[a]pyrene (BaP). To simulate the fate and environmental distribution of these species, the model requires some physicochemical properties (Table 3.6). These include equilibrium partition coefficients and their related energies of phase transfer. The characteristics from PHE to BaP are indicated by decreasing volatility (as molar mass increases), increasing K_{oa} and K_{ow}, and decreasing water solubility (as C^s_w and Henry's coefficients decrease). The properties also include the second-rate coefficients for homogeneous oxidation with OH, O_3, and NO_3 except for BaP where the gaseous reaction is switched off. Heterogeneous oxidation by O_3 is simulated only for PHE and BaP.

Besides the above properties, the model also requires compound solute parameters for simulations using the ppLFER gas−particle partitioning scheme. These values are summarized in Table 3.7.

Table 3.6: Physicochemical properties of selected PAHs

Parameter*	**Unit**	**PHE**	**PYR**	**FLT**	**BaP**	**Reference**
MW	g mol^{-1}	178.2	202.3	202.3	252.3	Finlayson-Pitts and Pitts, 2000
MV	cm^3 mol^{-1}	199.2	213.8	217.3	262.9	Mackay et al., 2006
$k_{\mathrm{OH}}^{(2)}$	cm^3 molec^{-1} s^{-1}	$2.7\times10^{-11\,(a)}$	$5.0\times10^{-11\,(b)}$	$1.1\times10^{-11\,(a)}$	-	$^{(a)}$Brubaker and Hites, 1998; $^{(b)}$Finlayson-Pitts and Pitts, 2000
$k_{\mathrm{NO_3}}^{(2)}$	cm^3 molec^{-1} s^{-1}	1.2×10^{-13}	1.6×10^{-27} [NO$_2$]	5.1×10^{-28} [NO$_2$]	-	Finlayson-Pitts and Pitts, 2000
$k_{\mathrm{O_3}}^{(2)}$	cm^3 molec^{-1} s^{-1}	4.0×10^{-19}	-	-	-	ibid.
$k_{\mathrm{O_3,het}}^{(2)}$	cm^3 molec^{-1} s^{-1}	$6.2\times10^{-17}\ \frac{S}{V}$	-	-	-	Perraudin et al., 2007
$k_{\mathrm{O_3,het}}^{(1)}$	s^{-1}	-	-	-	$\frac{1.68\times10^{-16}}{(1/[O_3]+2.8\times10^{-15})}$	Kwamena et al., 2004
k_{soil}	s^{-1}	5.17×10^{-7}	3.125×10^{-8}	2.08×10^{-8}	2.55×10^{-8}	Park et al., 1990
k_{ocean}	s^{-1}	5.4×10^{-8}	2.8×10^{-9}	4.2×10^{-9}	1.3×10^{-9}	BioHCWin v1.01, 2008
C_w^s	mg L^{-1}	1.10	0.132	0.26	0.0038	Finlayson-Pitts and Pitts, 2000
P_{sat}	Pa	$7.0\times10^{-2\,(a)}$	$6.0\times10^{-4\,(b)}$	$1.24\times10^{-3\,(b)}$	$1.22\times10^{-5\,(a)}$	$^{(a)}$Yamasaki et al., 1984; $^{(b)}$Wasik et al., 1983
ΔH_{soln}	kJ mol^{-1}	34.81	35.44	39.83	50.6	Mackay et al., 2006
ΔH_{vap}	kJ mol^{-1}	78.3	89.4	87.1	116.7	Roux et al., 2008
ΔH_{subl}	kJ mol^{-1}	92.1	100.3	101.2	120.5	ibid.
$\log K_{\mathrm{ow}}$	-	4.47	5.01	4.97	6.05	Ma et al., 2010
$K_{\mathrm{oa-m}}$	K	3293.$^{(a)}$	3985.$^{(b)}$	3904.$^{(a)}$	5382.$^{(a)}$	$^{(a)}$Odabasi et al., 2006; $^{(b)}$Harner and Bidleman, 1998a
$K_{\mathrm{oa-b}}$	-	$-3.37^{(a)}$	$-4.56^{(b)}$	$-4.34^{(a)}$	$-6.50^{(a)}$	ibid.
$\mathrm{k}_{\mathrm{H}}^{\ominus}$	M atm^{-1}	$2.4\times10^{1\,(a)}$	$5.9\times10^{1\,(a)}$	$5.2\times10^{1\,(a)}$	$2.2\times10^{3\,(b)}$	$^{(a)}$Bamford et al., 1999; $^{(b)}$ten Hulscher et al., 1992
$\frac{\Delta H_{\mathrm{soln}}}{R}$	K	6000.$^{(a)}$	5500.$^{(a)}$	4900.$^{(a)}$	4700.$^{(b)}$	ibid.
ρ_{p}	kg m^{-3}	1174.	1271.	1252.	1351.	Mackay et al., 2006

*Notes: MW: Molecular weight; MV: Molecular volume at boiling point; $k_{\mathrm{OH}}^{(2)}$: 2nd-order rate constant for gas-phase reaction with OH; $k_{\mathrm{NO_3}}^{(2)}$: 2nd-order rate constant for gas-phase reaction with NO$_3$; $k_{\mathrm{O_3}}^{(2)}$: 2nd-order rate constant for gas-phase reaction with O$_3$; $k_{\mathrm{O_3,het}}^{(2)}$: 2nd-order rate constant for heterogeneous oxidation with O$_3$; $k_{\mathrm{O_3,het}}^{(1)}$: Pseudo-1st-order rate constant for heterogeneous oxidation with O$_3$; $\frac{S}{V}$: Surface area of aerosols per unit volume of air (cm^2 cm^{-3}); k_{soil}: 1st-order rate constant for biotic and abiotic decay in soil; k_{ocean}: 1st-order rate constant for biotic and abitoc decay in ocean; C_w^s: Water solubility at 298.15 K; P_{sat}: Saturation vapor pressure at 298.15 K; ΔH_{soln}: Enthalpy of solution at 298.15 K; ΔH_{vap}: Enthalpy of vaporization at 298.15 K; ΔH_{subl}: Enthalpy of condensation of sub-cooled liquid at 298.15 K; K_{ow}: Octanol−water partition coefficient; K_{oa}: Temperature-dependent octanol−air partition coefficient; $\mathrm{k}_{\mathrm{H}}^{\ominus}$: Henry's Law coefficient at 298.15 K; R: Gas constant (8.314 J mol^{-1} K^{-1}); ρ_{p}: Density of particulate-phase SOC.

Table 3.7: Abraham solute descriptors for selected PAHs

	E	*S*	*A*	*B*	*V*	*L*	Reference
PHE	1.92	1.28	0.00	0.29	1.45	7.71	Ariyasena and Poole, 2014
PYR	2.81	1.71	0.00	0.28	1.59	8.83	Sprunger et al., 2007
FLT	2.38	1.55	0.00	0.24	1.59	8.83	ibid.
BaP	3.02	1.85	0.00	0.42	1.95	11.54	Ariyasena and Poole, 2014

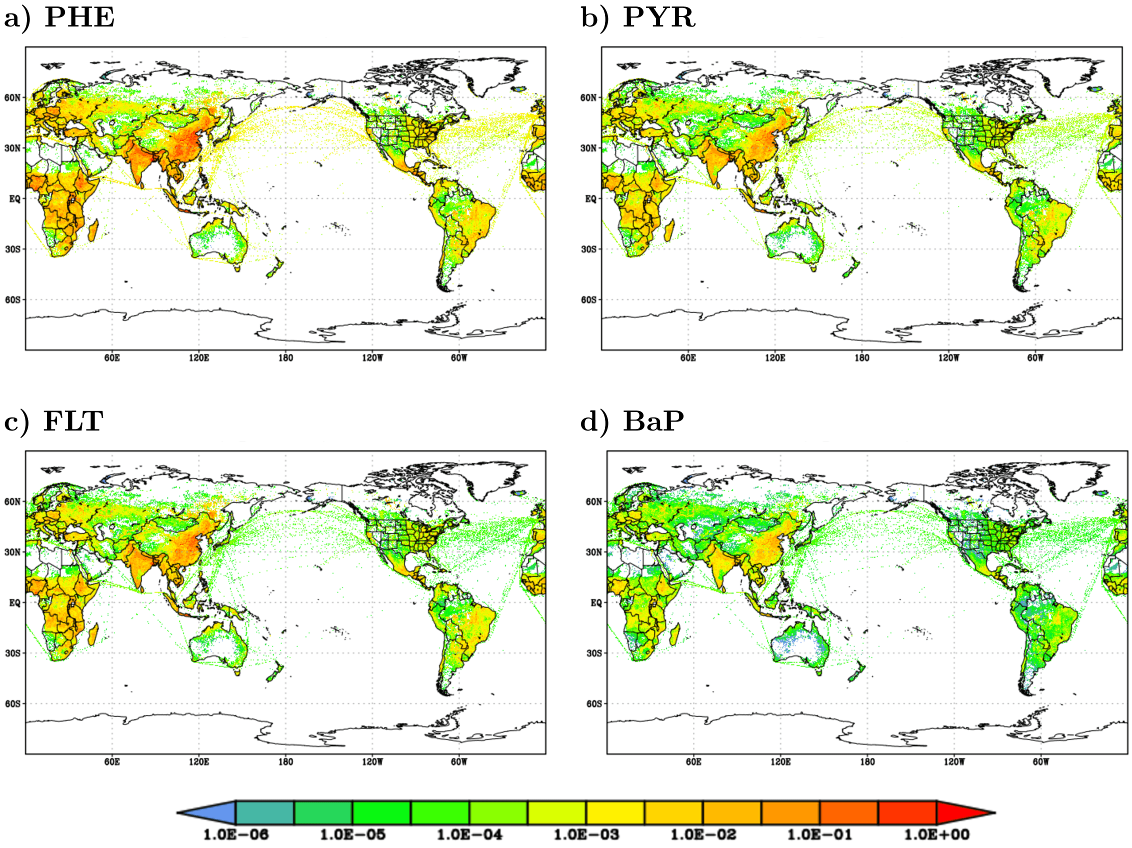
a) PHE
b) PYR
c) FLT
d) BaP

Figure 3.3: Annual emissions (ng m^{-2} s^{-1}) of PHE, PYR, FLT, BaP for 2008 from Shen et al. (2013)

3.4.2 Emissions and other model input

As model input, several emission datasets were employed in the study. Emission estimates for PAHs were obtained from the annual mean inventory of Shen et al. (2013) for the year 2008. They applied regression and technology split methods to construct country-level emissions for six categories (coal, petroleum, natural gas, solid wastes, biomass, and an industrial process category) or six sectors (energy production, industry, transportation, commercial/residential sources, agriculture, and deforestation/wildfire) before further regridding the emissions to a $0.1° \times 0.1°$ grid. Figure 3.3 presents the total estimates of global PAH emissions from all sectors or categories.

Emissions of aerosol species such as organic carbon (OC), black carbon (BC), mineral dust (DU), and sea salt (SS) were included. For BC and OC, the Representative Concentration Pathway (RCP) 6.0 emission scenario of the IPCC (Intergovernmental Panel on Climate Change) (Vuuren et al., 2011) was used and accessible via ftp://ftp-ipcc.fz-juelich.de/pub/emissions/gridded_netcdf. Emissions are calculated for anthropogenic, biomass burning, ship, and aircraft. The RCP database provides a seasonality only for the biomass burning and ship emissions. In this study, seasonal scale factors were applied to the anthropogenic emission whereby the seasonality was based upon the monthly variation of the Hemispheric Transport of Air Pollutants (HTAP) v2.2 anthropogenic emission inventory (Janssens-Maenhout et al., 2015). BC emissions from all sectors were assumed to be hydrophobic. For OC, it was assumed to be 65% hydrophilic and 35% hydrophobic upon biomass burning emissions and to be 100% hydrophobic upon anthropogenic and ship emissions. Both OC and BC were emitted at Aitken mode which spans the size range from about 5 to 50 nanometer in diameter. A factor of 1.724 was used to scale the OC emissions to primary organic matter (OM).

DU and SS emissions were computed online by the ONEMIS submodel (Kerkweg et al., 2006b). DU emission flux is calculated based on wind speed at 10 m altitude and soil parameters (Schulz et al., 1998). The emission of SS particles by bubble bursting is described as wind-speed dependent particle mass and number fluxes at accumulation (50−500 nm) and coarse (>500 nm) modes. In ONEMIS, the fluxes are determined from pre-calculated lookup tables following the Guelle et al. (2001) parameterization. SVOC submodel accounts for OM fraction in the SS mass fluxes (J_{SS}), and the fraction is estimated using a 10 m wind (v_{10})-dependent empirical relationship derived from Figure 2a in Gantt et al. (2011). Equation 3.41 below is used to calculate the OM mass fluxes, J_{OM}, in kg m^{-2} s^{-1}.

$$J_{\mathrm{OM}} = J_{\mathrm{SS}} \times \frac{1}{2}\left(\frac{0.78}{1+0.03\exp\left(0.48 v_{10}\right)} + \frac{0.24}{1+0.05\exp\left(0.38 v_{10}\right)}\right) . \tag{3.41}$$

Emissions of other gases including volatile organic species (SO_2, CO, NH_3, NO, CH_4, and NMHC) were prescribed using the IPCC RCP6.0 dataset (Vuuren et al., 2011). The model also requires soil properties data (i,e, dry bulk density and organic matter content) and ocean mixed layer depths (Boyer Montégut et al., 2004).

3.4.3 Observations

The observation data used for model performance evaluation were collected from several surface monitoring networks: the European Monitoring and Evaluation Programme (EMEP) (Tørseth et al., 2012), the Arctic Monitoring and Assessment Program (AMAP) (Hung et al., 2005a), the Great Lakes Integrated Atmospheric Deposition Network (IADN) (IADN, 2014), the Department for Environment, Food & Rural Affairs (DEFRA) UK-AIR (Air Information Resource) program (DEFRA, 2010), and the MONitoring NETwork in the African continent (MONET-Africa) (Klánová et al., 2008). These data were screened and quality controlled according to the description in Appendix E. Final stations with reliable monthly data are depicted in Figure 3.4 wherein shows 3 stations in the Arctic, 19 in the northern mid-latitudes, and 6 in the tropics. The availability of data differs by station, species, and variable of interest; see the site-specific information in Table 3.8 for total concentration and Table 3.9 for particulate mass fraction (θ).

The study also compared simulated concentrations in the marine atmosphere to two ship cruise measurement campaigns: 1) on a West to East transect across the tropical Atlantic Ocean (Lohmann et al., 2013), and 2) along the Asian marginal seas, the Indian, and the Pacific Oceans (Liu et al., 2014). The monthly mean modeled values were compared to daily measurements at each sampling points.

3.5 Experiment designs

3.5.1 Model configuration

The model was run on a spectral T42 grid in the horizontal (approximately 2.8° in a lat−lon grid) and 19 unevenly distributed layers in the vertical with the top level at 10 hPa. The vertical layers are discretized using a hybrid coordinate (the lowest level follows the terrain and becomes surfaces of constant pressure in the stratosphere). All simulations were run for a three-year period (i.e., 2007−2009), with a one-year spin-up (i.e., 2006), and nudged toward the European Centre for Medium-range Weather Forecasts (ECMWF) reanalysis data (Dee et al., 2011). Note that the simulation period was selected based on the representative year of PAH emissions (i.e., 2008) and the availability of reliable observation data (see Appendix E).

3.5.2 Sensitivity to the temporal resolution of emissions and process parameterizations

This study quantitatively evaluated the sensitivity of model output to components of model input and physics configurations through factor separation analysis (Stein and Alpert, 1993) described below. The total (gas + particle) concentration at the lowest model level was selected for its higher relevance with all the factors (compared to, e.g., atmospheric burden) and to facilitate direct comparison with observations. The model components (hereinafter, factors) of interest are as follows:

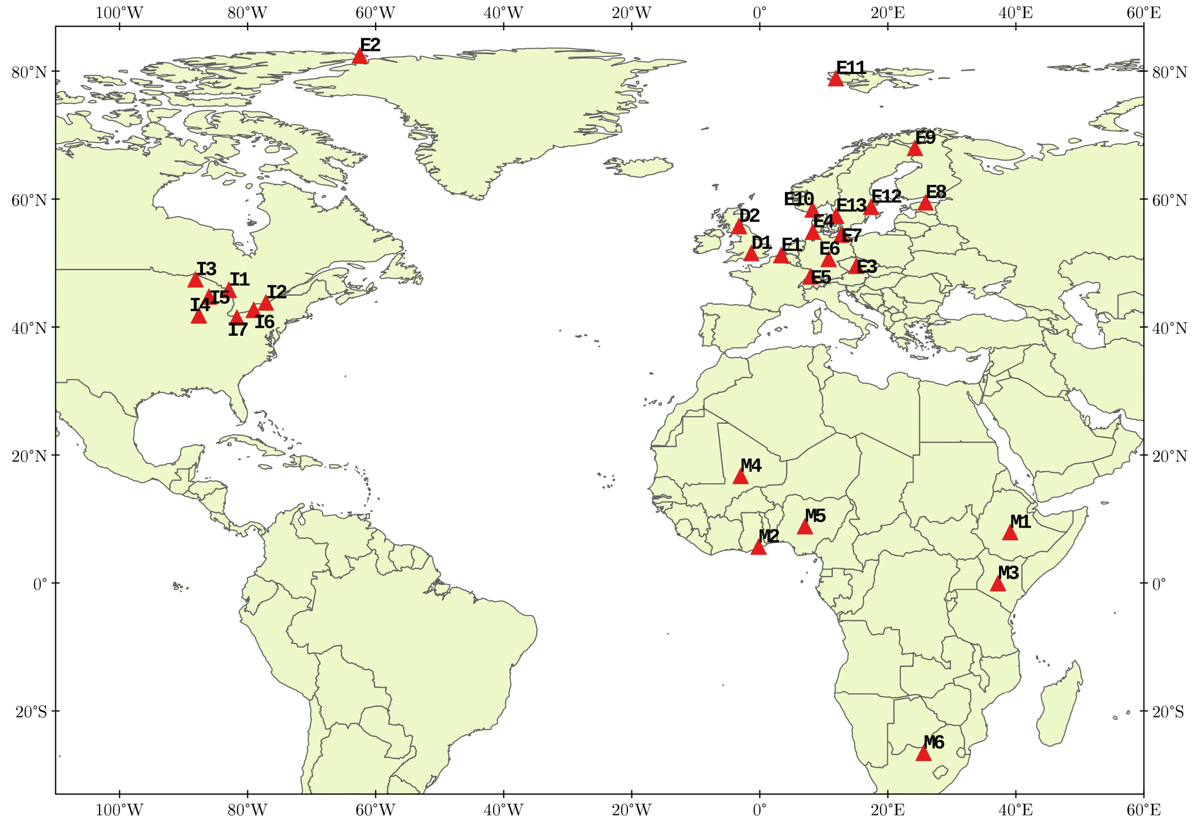

Figure 3.4: Locations of monitoring stations used in the study. The initial letter of each station ID refers to the individual monitoring network (E: EMEP & AMAP; D: DEFRA, I: IADN, M: MONET-Africa)

Table 3.8: **Monitoring stations used in the study and the availability of monthly concentration data in each year**

ID	Location	Lat.	Lon.	Data Availability		
				2007	**2008**	**2009**
			DEFRA†			
D1	Harwell, UK	51.6	-1.3	-	All	All
D2	Auchencorth Moss, UK	55.8	-3.2	-	All	All
			EMEP and AMAP†			
E1	Houtem, Belgium	51.3	3.4	-	-	PYR, FLT, BaP
E2	Alert, Canada	82.5	-62.5	All	All	All
E3	Kosetice, Czech Republic	49.6	15.1	All	All	All
E4	Westerland, Germany	54.9	8.3	All	All	All
E5	Schauinsland, Germany	47.9	7.9	All	All	All
E6	Schmücke, Germany	50.7	10.8	All	All	All
E7	Zingst, Germany	54.4	12.7	All	All	All
E8	Lahemaa, Estonia	59.5	25.9	BaP	BaP	BaP
E9	Pallas, Finland	24.2	68.0	All	All	-
E10	Birkenes, Norway	58.4	8.3	-	All	All
E11	Spitsbergen/Zeppelinfjell, Norway	78.9	11.9	All	PHE, PYR, FLT	All
E12	Aspvreten, Sweden	58.8	17.4	-	-	PYR
E13	Råö, Sweden	57.4	11.9	All	All	-
			IADN†			
I1	Burnt Island, Canada	45.8	-82.9	All	All	All
I2	Point Petre, Ontario Canada	43.8	-77.2	All	All	All
I3	Eagle Harbor, Michigan US	47.5	-88.1	PHE, FLT, BaP	-	PHE, FLT, BaP
I4	IIT Chicago, Michigan US	41.8	-87.6	PHE, FLT, BaP	PHE, FLT, BaP	PHE, FLT, BaP

continued ...

Table 3.8: continued

				Data Availability		
ID	**Location**	**Lat.**	**Lon.**	**2007**	**2008**	**2009**
I5	Sleeping Bear Dunes, Michigan US	44.8	−86.1	PHE, FLT, BaP	-	PHE, FLT, BaP
I6	Sturgeon Point, New York US	42.7	−79.1	PHE, FLT, BaP	-	-
I7	Cleveland, Ohio US	41.5	−81.7	PHE, FLT, BaP	PHE, FLT, BaP	-
MONET-Africa[‡,§]						
M1	Asela, Ethiopia	7.9	39.1	-	PHE, PYR, FLT	-
M2	Kwabenya, Ghana	5.7	−0.2	-	PHE, PYR, FLT	-
M3	Mt. Kenya, Kenya	−0.03	37.2	-	PHE, PYR, FLT	-
M4	Tombouctou, Mali	16.7	−3.0	-	PHE, PYR, FLT	-
M5	Sheda, Nigeria	8.9	7.1	-	PHE, PYR, FLT	-
M6	Molopo Nature Reserve, South Africa	−26.5	25.6	-	PHE, PYR, FLT	-

[†] Mid-latitude stations, except E2, E9, and E11 are the Arctic stations

[‡] Tropic stations

[§] Only concentration in the gas phase

Table 3.9: Same as Table 3.8 but for monthly particulate mass fraction data

	Data Availability		
Station ID	**2007**	**2008**	**2009**
E3	All	All	-
I1	All	All	All
I2	All	All	All
I3	BaP	-	BaP
I4	-	FLT	FLT
I5	FLT, BaP	-	FLT, BaP
I6	FLT, BaP	-	-
I7	FLT, BaP	FLT, BaP	-

1. Temporal resolution of emissions (hereinafter, *fac1*)
   The PAH emission inventory of Shen et al. (2013) was based on 2008 annual emission totals from all sectors (see Section 3.4.2). The emissions were divided over the year using monthly factors derived from BC anthropogenic emissions. Two sets of simulations were carried out to test the sensitivity of model output to the seasonal profile of emission. The first set used constant emissions throughout the simulations and the second was done with monthly emission interval.
2. The representation of particulate-phase PAHs (hereinafter, *fac2*)
   The two options for this factor was tested: *bulk* versus *modal* (Section 3.3.1). Note that with regards to BaP, 95% of the emissions were assumed to be in particulate phase and for the *modal*-scheme scenario, all of the emitted particles are treated as the hydrophobic Aitken (*ki*) tracers.
3. The choice of gas−particle partitioning scheme (hereinafter, *fac3*)
   Among the four options available (see Section 3.3.2), the present study focuses on the comparison between the Lohmann−Lammel and ppLFER schemes.
4. The influence of volatilization (hereinafter, *fac4*)
   Model runs with volatilization process switched off are compared to those runs which have volatilization switched on. In the case of the latter, the Smit scheme (Smit et al., 1997) was used for soil volatilization.

Factor separation analysis

The factor separation (FS) analysis is introduced by Stein and Alpert (1993) to assess the contributions of each factor, as well as interactions among factors, to a particular output variable. This method has been applied in many numerical studies (e.g., Romero et al., 1997; Carvalho et al., 2006; Lynn et al., 2009; and Torma and Giorgi, 2014) and is employed here to quantify the sensitivity of total concentration to changes in emission and physics parameterizations selected above. Following Stein and Alpert (1993), the effects of individual and interactive/synergistic changes are defined by:

$$\hat{f}_1 = f_1 - f_0 \tag{3.42a}$$

$$\hat{f}_2 = f_2 - f_0 \tag{3.42b}$$

$$\hat{f}_3 = f_3 - f_0 \tag{3.42c}$$

$$\hat{f}_4 = f_4 - f_0 \tag{3.42d}$$

$$\hat{f}_{12} = f_{12} - (f_1 + f_2) + f_0 \tag{3.43a}$$

$$\hat{f}_{13} = f_{13} - (f_1 + f_3) + f_0 \tag{3.43b}$$

$$\hat{f}_{14} = f_{14} - (f_1 + f_4) + f_0 \tag{3.43c}$$

$$\hat{f}_{23} = f_{23} - (f_2 + f_3) + f_0 \tag{3.43d}$$

$$\hat{f}_{24} = f_{24} - (f_2 + f_4) + f_0 \tag{3.43e}$$

$$\hat{f}_{34} = f_{12} - (f_3 + f_4) + f_0 \tag{3.43f}$$

$$\hat{f}_{123} = f_{123} - (f_{12} + f_{13} + f_{23}) + (f_1 + f_2 + f_3) - f_0 \tag{3.44a}$$

$$\hat{f}_{134} = f_{134} - (f_{13} + f_{14} + f_{34}) + (f_1 + f_3 + f_4) - f_0 \tag{3.44b}$$

$$\hat{f}_{124} = f_{124} - (f_{12} + f_{14} + f_{24}) + (f_1 + f_2 + f_4) - f_0 \tag{3.44c}$$

$$\hat{f}_{234} = f_{234} - (f_{23} + f_{34} + f_{24}) + (f_2 + f_3 + f_4) - f_0 \tag{3.44d}$$

$$\begin{aligned} \hat{f}_{1234} =& f_{1234} - (f_{134} + f_{134} + f_{124} + f_{234}) + \\ & (f_{12} + f_{13} + f_{14} + f_{23} + f_{24} + f_{34}) - \\ & (f_1 + f_2 + f_3 + f_4) + f_0 \end{aligned} \tag{3.45}$$

where f_0 is the concentrations from a *base* simulation, $\hat{f}_1$ is the concentration changes influenced directly by the 1st factor (in this study is the temporal emission variation), $\hat{f}_2$ is by the 2nd factor (particulate-phase representation), $\hat{f}_3$ is by the 3rd factor (the choice of gas−particle partitioning scheme), and $\hat{f}_4$ is by the 4th factor (volatilization). $\hat{f}_{ij}$ gives information related to the non-linear interaction of 2 factors together (i and j) on the concentrations, $\hat{f}_{ijk}$ is from 3-factor interactions, and $\hat{f}_{1234}$ is from all factor interactions.

Accordingly, a total of 16 (or 2^n) simulations are necessary to get a complete solution. Figure 3.5 shows the list of experiments conducted for the FS-based sensitivity study. The ABLN experiment is designed to be the *base* simulation (f_0), in which annual emission (A), the *bulk* scheme (B), the Lohmann−Lammel scheme (L), and no-volatilization (N) were applied. SMPW is referred to as the *target* simulation (f_{1234}) in which the four factors were changed, and here they are expected to improve process representations relative to the *base* simulation.

A new method to simplify the FS solution has been proposed by Schär and Kröner (2017), namely, the sequential factor separation (SFS). The basis of SFS is to focus on the main influences of selected factors using only $2n$ simulations (eventually, 8 simulations for $n = 4$ factors). The method provides an error measure to quantify the strength of any possible interaction and the root-mean-square average to represent overall uncertainty. Schär and Kröner (2017) argue that when the uncertainty is not significant, this method leads to similar results as in FS. Summary of the SFS methodology and some selective results from this study are presented in Appendix F. It is found that the effect of each of the four factors on the PAH concentrations is not independent of their interactions. For this reason, the classical FS method was applied.

In this study, we have chosen to focus on interpreting the direct effects of individual factor ($\hat{f}_i$) and the effects of total interactions between the corresponding factor and all other factors ($\sum\limits_{j} \hat{f}_{ij} + \sum\limits_{j,k} \hat{f}_{ijk} + \hat{f}_{1234} \ , \quad j \neq k \neq i$). Our main aims are to see if the interactions have the effects of strengthening or buffering the direct effects and examine the magnitude of the

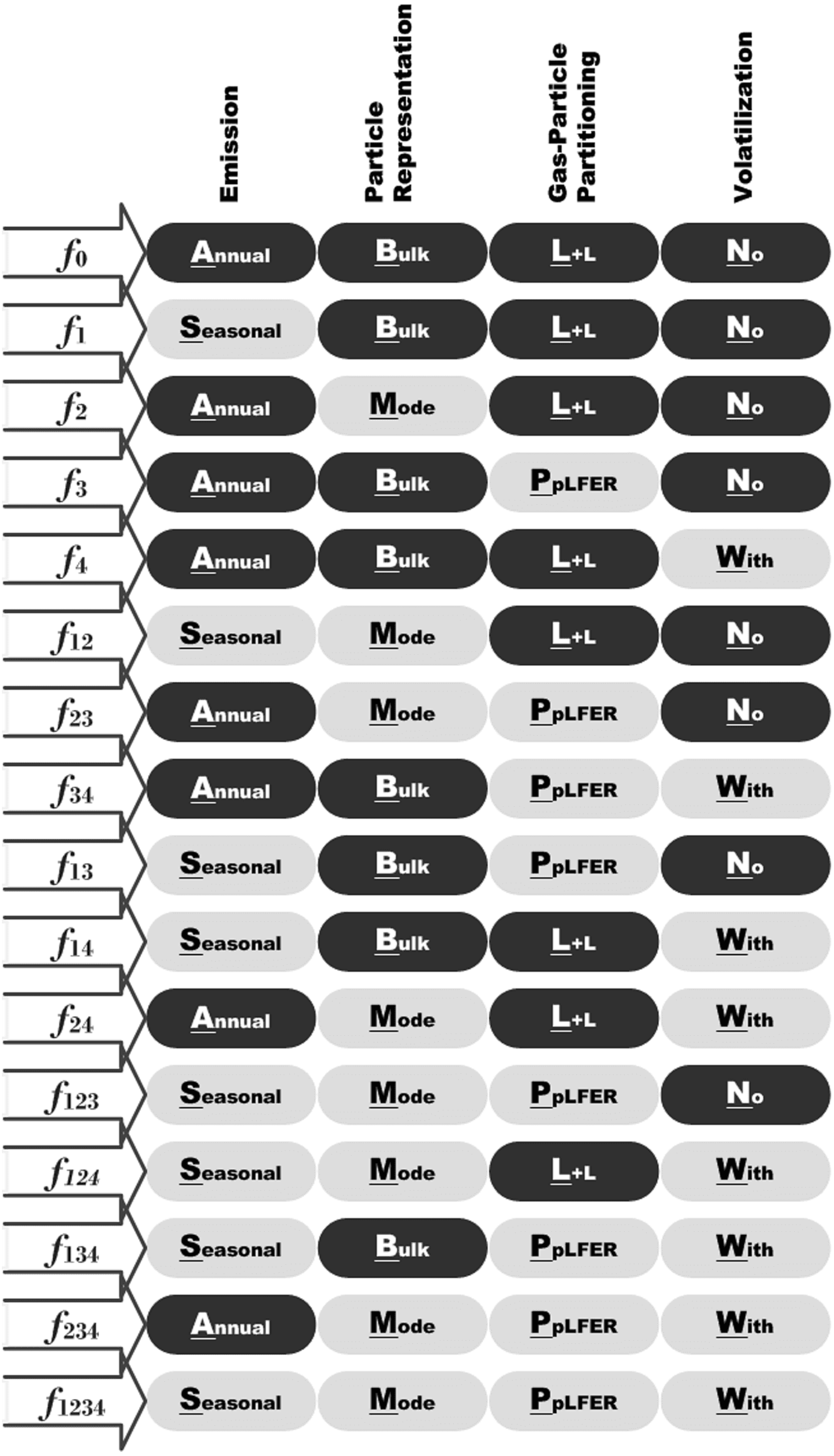

	Emission	Particle Representation	Gas-Particle Partitioning	Volatilization
f_0	Annual	Bulk	L+L	No
f_1	Seasonal	Bulk	L+L	No
f_2	Annual	Mode	L+L	No
f_3	Annual	Bulk	PpLFER	No
f_4	Annual	Bulk	L+L	With
f_{12}	Seasonal	Mode	L+L	No
f_{23}	Annual	Mode	PpLFER	No
f_{34}	Annual	Bulk	PpLFER	With
f_{13}	Seasonal	Bulk	PpLFER	No
f_{14}	Seasonal	Bulk	L+L	With
f_{24}	Annual	Mode	L+L	With
f_{123}	Seasonal	Mode	PpLFER	No
f_{124}	Seasonal	Mode	L+L	With
f_{134}	Seasonal	Bulk	PpLFER	With
f_{234}	Annual	Mode	PpLFER	With
f_{1234}	Seasonal	Mode	PpLFER	With

Figure 3.5: List of experiments performed for the factor separation analysis to study sensitivity to temporal variation in emission and process parameterizations (particulate-phase representation, gas−particle partitioning scheme, and volatilization). L+L: Lohmann−Lammel, ppLFER: Poly Parameter Linear Free Energy Relationships.

interactions relative to its associated direct effects.

3.5.3 Statistical indicators for model evaluation

Multiple performance indicators were applied for model evaluation (see Table 3.10) and the inherent limitations of each were recognized. The first comparison is based on the descriptive statistics of both observed and predicted concentrations, represented by the arithmetic mean ($\overline{O}$ or $\overline{M}$), median (Q_{2O} or Q_{2M}) and standard deviation (SD_O or SD_M). The geometric mean (GM_O or GM_M) is additionally used considering the distribution of air pollutant concentrations is mostly close to log-normal; hence GM treats extreme high and low equally.

Following the works of Chang and Hanna (2004), Yu et al. (2006), Galarneau et al. (2014) and many others, the simulation-to-observation comparison focuses on the mean bias (MB), root mean square error (RMSE), normalized mean bias (NMB), normalized mean bias factor (NMBF), fractions of predictions within a factor of 2 or 10 of observations (FAC2 and FAC10, respectively), and correlation coefficient (r). MB describes a general tendency of bias, but individual positive and negative errors tend to compensate each other. RMSE helps characterize the spread of individual bias and indicate any large outliers. Relative measures in NMB and NMBF are useful to compare the model performance for different substances in which concentrations can be largely different. The normalization of the difference in NMB leads to an asymmetry problem, that is, overpredictions are artificially unbounded whereas underpredictions are bounded by -100%. To overcome this issue, the study adopted NMBF introduced by Yu et al. (2006) by which the index is defined individually when $\overline{M} \geq \overline{O}$ and when $\overline{O} \leq \overline{M}$. It is also easy to interpret the index. If NMBF is positive (negative), the model overestimates (underestimates) the observations by a factor of NMBF $+1$ ($1 -$ NBMF). For example, if NMBF $= -2$, the model underestimates by a factor of 3. The last parameters, FAC2 and FAC10, give a simple measure of scattering that is less influenced by outliers, whereas r reflects the linear relationship between two datasets.

Although all of the above measures were computed and examined, most of the discussions were based on selected indices for simplicity. Note that prior to the model evaluation, predicted values at the model grid were bilinearly interpolated to each station location.

3.6 Analysis of factor separation results

The analysis of the factor separation results is given below. For each factor, the analysis includes the assessment of direct effects ($\hat{f}_i$) and total interaction effects ($\Sigma\hat{f}_{ij} + \Sigma\hat{f}_{ijk} + \hat{f}_{1234}$) on near-surface PAH concentrations in two seasons, i.e., December−January−February (DJF) and June−July−August (JJA). Figure 3.6 shows the respective effects for all factors as relative to the seasonal means of the *base* experiment (f_0). A positive value indicates a concentration increase with respect to f_0, whereas a negative indicates a decrease. The spatial distributions of f_0 seasonal mean concentrations for the four species are shown in Appendix G, Figure G.1. We studied the relative effects in five climatic regions, two over high ($> 60°$; *Arc.* & *Ant.*) and middle (*N.Mid* & *S.Mid*) latitude zones of each hemisphere, and

Table 3.10: List of performance indicators used in model evaluation

Metrics	Formula*	Ideal Value	Range
Arithmetic mean	$\overline{x} = \frac{\sum_{i=1}^{N} x_i}{N}$	$\overline{M} = \overline{O}$	$[0, +\inf)$
Median	$\mathrm{Q2}_x = x_i$, where $i = \frac{(N+1)}{2}$	$\mathrm{Q2}_M = \mathrm{Q2}_O$	$[0, +\inf)$
Standard deviation	$\mathrm{SD}_x = \sqrt{\frac{1}{N}\sum_{i=1}^{N}(x_i - \overline{x})^2}$	$\mathrm{SD}_M = \mathrm{SD}_O$	$[0, +\inf)$
Geometric mean	$\mathrm{GM}_x = \left(\prod_{i=1}^{N} x_i\right)^{\frac{1}{N}} = \exp\left[\frac{1}{N}\sum_{i=1}^{N}\ln x_i\right]$	$\mathrm{GM}_M = \mathrm{GM}_O$	$[0, +\inf)$
Mean bias	$\mathrm{MB} = \frac{\sum_{i=1}^{N}(M_i - O_i)}{N}$	0.0	$\left[-\overline{O}, +\inf\right)$
Root mean square error	$\mathrm{RMSE} = \sqrt{\frac{\sum_{i=1}^{N}(M_i - O_i)^2}{N}}$	0.0	$[0, +\inf)$
Normalized mean bias	$\mathrm{NMB} = \frac{\mathrm{MB}}{\overline{O}} \times 100\%$	0.0	$[-100\%, +\inf)$
Normalized mean bias factor	$\mathrm{NMBF} = S\left[\exp\left(\left\|\ln\frac{\overline{M}}{\overline{O}}\right\|\right) - 1\right]$, where $S = \frac{\overline{M}-\overline{O}}{\left\|\overline{M}-\overline{O}\right\|}$	0.0	$(-\inf, +\inf)$
Factor of 2	$\mathrm{FAC2} = \frac{1}{N}\sum_{i=1}^{N} n_i$, with $n_i = \begin{cases} 1, & \text{if } 0.5 \leq \frac{M_i}{O_i} \leq 2 \\ 0, & \text{otherwise} \end{cases}$	1.0	$[0, 1]$
Factor of 10	$\mathrm{FAC10} = \frac{1}{N}\sum_{i=1}^{N} n_i$, with $n_i = \begin{cases} 1, & \text{if } 0.1 \leq \frac{M_i}{O_i} \leq 10 \\ 0, & \text{otherwise} \end{cases}$	1.0	$[0, 1]$
Correlation coefficient	$r = \frac{\sum_{i=1}^{N}\left(M_i - \overline{M}\right)\left(O_i - \overline{O}\right)}{\sqrt{\sum_{i=1}^{N}\left(M_i - \overline{M}\right)^2}\sqrt{\sum_{i=1}^{N}\left(O_i - \overline{O}\right)^2}}$	1.0	$[-1, 1]$

*Notes: x: Modeled/Simulated (M) or Observed (O) data; N: Number of monthly data or monthly pairs one encompassing the tropical belts (30°N – 30°S; *Trop.*). The global distributions of the relative effects are presented in Figures G.2−G.9. In addition, Figures G.10−G.17 present the relative interaction effects from the individual combination of factors. In the following, we do not look to interpret concentration responses to each interaction term. Reasons for this are that (1) accounting for all such interactions is complicated given the number of factors and (2) higher-order interactions (combinations of more than two factors) is hard to physically justify.

3.6.1 Effects of emission interval

Figure 3.6a shows that using monthly emissions increases PAH concentrations in DJF and decreases the concentrations in JJA over the areas from the middle to high latitudes of NH. This result is expected and is attributed to emissions during the northern winter (summer) are higher (lower) than annual means and photochemistry being less (more) active. Over the Arctic, the relative changes ($\hat{f}_1/f_0$) in DJF show a median increase of 30% for PHE, PYR and FLT, and 7% for BaP, whereas $\hat{f}_1/f_0$ in JJA are weaker in magnitude for PHE and PYR (−16%) but comparable for FLT (−28%) and BaP (−5%). In general, $\hat{f}_1/f_0$ becomes smaller over *N.Mid* by around half. The upper (lower) quartile of $\hat{f}_1/f_0$ in DJF (JJA) indicates about one-quarter areas of the temperate and polar regions experience at least 40% of an increase (decrease), most were located in northeastern Eurasia (see the left panels of Figures G.2 and G.3). Note $\hat{f}_1/f_0$ over the tropics are small-to-negligible (±1%) mainly due to little variation in emissions from anthropogenic sectors. PAH concentrations may be higher in dry season due to increased amounts of biomass burning, but they are poorly represented in the current inventory. In *S.Mid* and *Ant.*, the direct effects of emission change are substantially opposite in sign to the effects seen in the northern latitudes, being negative in DJF (median ranges from −4% to −32%) and positive in JJA (7%−25%).

The total interactions between *fac1* and other factors generally produce opposite signals to $\hat{f}_1$ over middle and high latitudes in the two seasons. This result indicates that the changes in other factors tend to buffer the influence of monthly emission on increasing or decreasing f_0 concentrations. Some exceptions are seen over parts of East Asia in DJF for all species (Figures G.2, right panels) and over the Southern Ocean in JJA for BaP (G.3, right panels) where the interactions work to reinforce the direct effects. In DJF, the degree of interactions is smaller or comparable to the size of $\hat{f}_1$ for the *Arc.* and *N.Mid* but becomes stronger by at least double for *Ant.* The opposite tendency is seen in JJA but only applies to PYR and FLT. In agreement to $\hat{f}_1$, the interaction effects are less apparent over the tropics. Note that the positive effects in $\hat{f}_{14}$ during local summer tend to be more dominant than the effects in other combinations for PHE, PYR, and FLT (Figures G.14-G.16). In the simulation, the presence of volatilization in summer tends to suppress $\hat{f}_1$ by promoting more gases available for long-range transport, thus implies a negative feedback.

3.6.2 Effects of particulate-phase representation

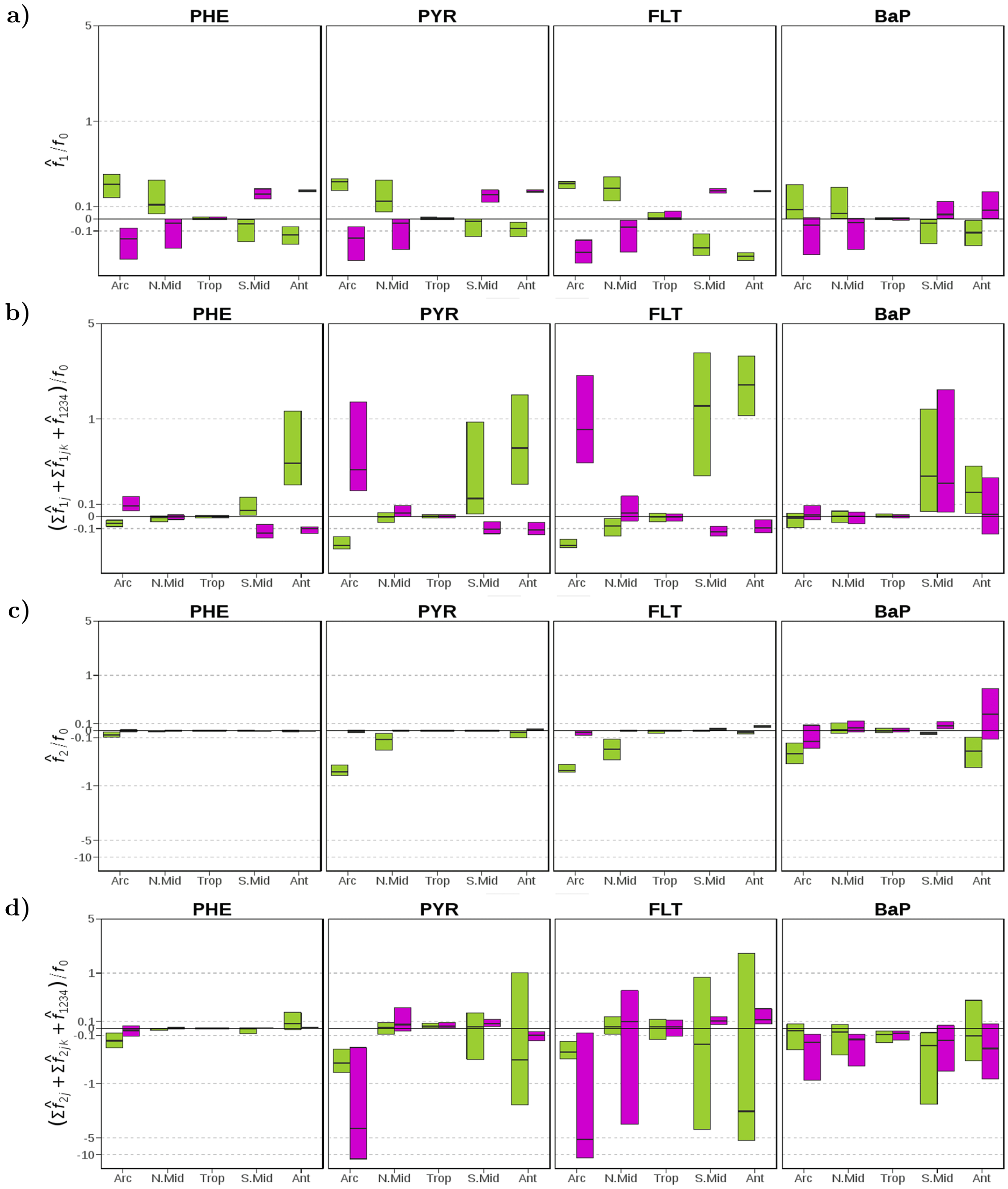

Figure 3.6: Direct and interaction effects on seasonal-mean near-surface PAH concentrations of (a,b) monthly emissions ($i = 1$), (c,d) the *modal* scheme ($i = 2$), (e,f) the ppLFER scheme ($i = 3$), and (g,h) volatilization ($i = 4$). The direct effects (a,c,e,g) are expressed as the difference between two distributions ($\hat{f}_i = f_i - f_0$) whereas the interaction effects (b,d,f,h) are expressed as the sum of two ($\Sigma\hat{f}_{ij}$, $i \neq j$), three ($\Sigma\hat{f}_{ijk}$, $i \neq j \neq k$), and all ($\hat{f}_{1234}$) factor interactions. They are presented as relative to concentrations from the *base* (f_0) simulation. The figures display the median, 25th and 75th percentiles of the relative effects over each of five main climatic regions. Note the inverse hyperbolic sine function has been used in scaling the y axes.

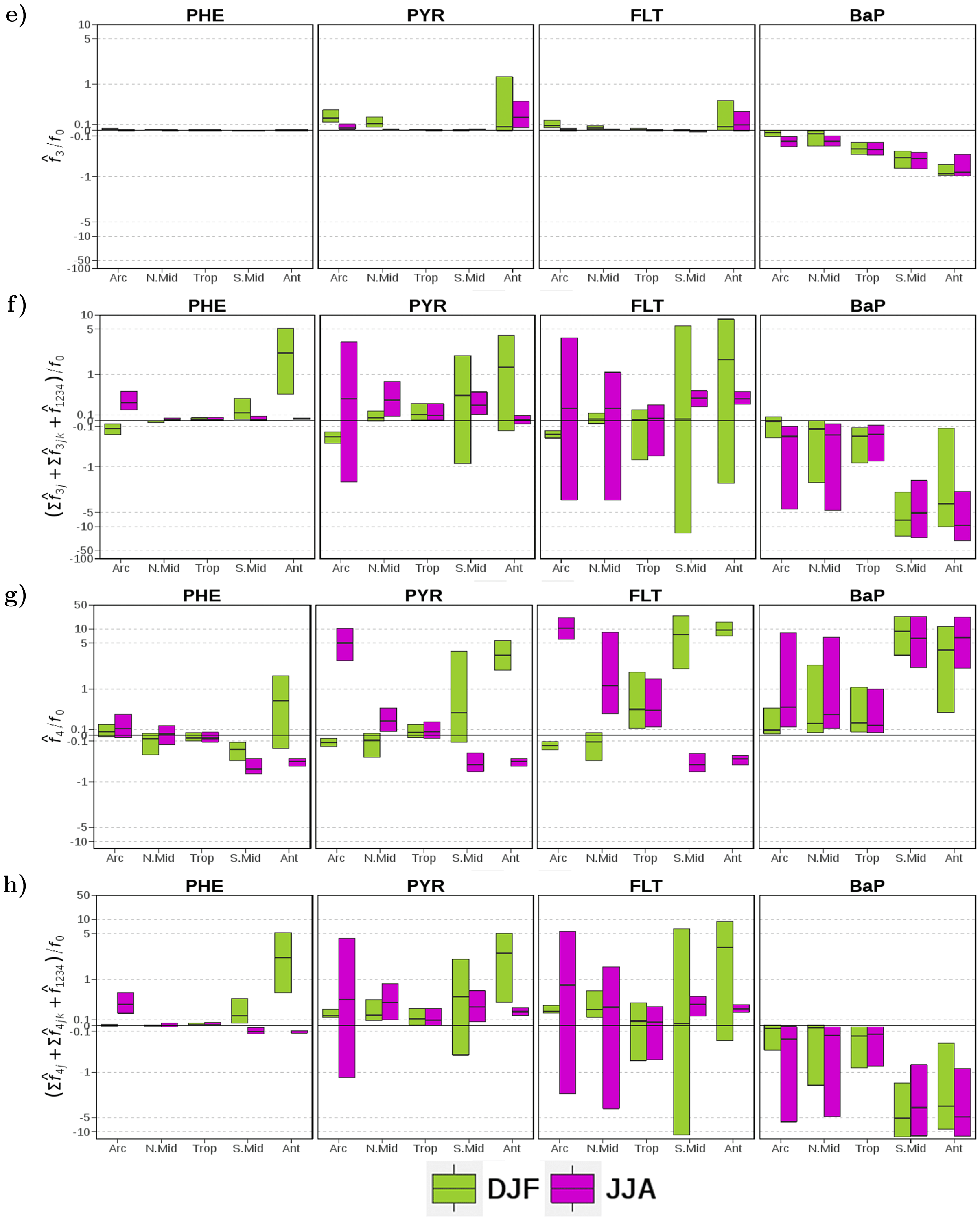

Figure 3.6: continued

The direct effects of the *modal* scheme ($\hat{f}_2$) vary among species (Figure 3.6c). $\hat{f}_2$ is almost absent for PHE as the species resides almost completely in the gas phase. For PYR and FLT, $\hat{f}_2$ is negative in DJF over *N.Mid* ($\hat{f}_2/f_0$ quartiles range from −5% to −30%) and *Arc.* (−50% to −75%) whereas it is hardly visible in JJA or over other regions. Further analysis reveals stronger particle deposition results when the aerosol phase is discretized into different modes (not shown). In long-range transport under modal aerosol representation, the aerosols are more associated with larger particles hence particle deposition becomes more effective. For BaP, the *modal* scheme generally decreases the Arctic concentrations (as median, −35% in DJF and −15% in JJA) and increases (approx. 5%) those over mid- and low-latitude landmass (Figures G.4d and G.5d, left panels).

As is the case for the direct effects, the interaction contributions are peculiar to individual species (Figure 3.6d). For PHE, the interaction effects in DJF are reflected in negative concentration responses over *Arc.* (18%) and positive over *Ant.* (7%), in contrast to relatively mild influences over other regions or in JJA. For PYR and FLT, the effects are negative over the Arctic both in DJF (quartiles vary from −20% to −75%) and in JJA (−6% to −120%). It is interesting to note that the joint effect between the *modal* and ppLFER schemes has a major influence on the negative contributions (Figures G.11, G.12, G.15, G.16), suggesting that the decrease in simulated concentration associated with the change from *bulk* to *modal* could be intensified when the ppLFER scheme is used. In the remaining areas, the interaction effects vary in sign spatially as illustrated in the right panels of Figures G.4b,c−G.5b,c. Nevertheless, it shows for both species that maximum influences occur over the Southern Ocean in DJF (where the effects may reach two orders of magnitude) and mid-latitude landmass in JJA (more than a factor of five). As for BaP, the median effects are negative (−7% to −30%) in both seasons, although some positive signals are apparent in parts of high latitudes while the tropical oceans bear small synergistic effects. Similar to other species, the degree of interactions are stronger than $\hat{f}_2$ by more than a factor of three for the majority of grid cells (Figures G.4d−G.5d, right panels). The large fractions of the effects are dominated by two-factor and three-factor combinations related to the interaction with the ppLFER scheme and/or volatilization (Figures G.13, G.17).

3.6.3 Effects of the choice of gas−particle partitioning scheme

Figure 3.6e shows that the direct effects of the ppLFER scheme ($\hat{f}_3$) show little spatial heterogeneities in both seasons and for all species. The effects are barely important for PHE due to low gas−aerosol partition constant (Kp). $\hat{f}_3$ is positive for PYR and FLT over polar regions and *N.Mid* especially in local winter when low temperature favors partitioning to aerosols (higher Kp). The median of $\hat{f}_3/f_0$ varies from 1% to 25% with some parts of *Ant.* showing an increase larger than 50%. For BaP, the effects are overall negative (by at least −5%) with $\hat{f}_3/f_0$ reflecting a positive north−south gradient (increasing from *Arc.* to *Ant.*), associated in part with stronger signals over oceans (Figures G.6d and G.7d, left panels). The application of ppLFER increases Kp as this module is calculated from not only interaction with BC and OM (as in Lohmann−Lammel scheme) but also with some other aerosol matrices. Higher Kp indicates higher particle mass fraction. For PYR and FLT, this leads to an increase in total atmospheric lifetime as the aerosol phase is not degraded, and can, therefore, be transported over a larger distance. For BaP, the additional particles are subject to depositions and heterogeneous oxidation by ozone, particularly in regions away from sources. The factor influence is notably too small for PHE as oxidations occur in both phases.

The effects from *fac3* interactions vary by region and are relatively stronger than $\hat{f}_3$ (Figure 3.6f). This finding is common to all species and seasons. The degree of effects is weaker for PHE compared to that for other species. However, the interactions increase polar concentrations in local summer, by 20% to a factor of five, mainly associated with the coupled effect of ppLFER and volatilization ($\hat{f}_{34}$, Figures G.10 and G.14). For PYR and FLT, there is a high spatial variability over extratropical regions in local summer, as indicated by the interquartile range (distance between the 3rd and 1st quartiles). With regard to synergistic terms, ppLFER interactions with the *modal* scheme and volatilization, in two- or three-factor combinations, are more important than other contributions (Figures G.11−G.12 and G.15−G.16). For BaP, the interaction effects show negative signals similar to $\hat{f}_3$, suggesting a positive feedback. The interactions exert a stronger influence on the concentrations of the oceans than on that of land, except for the tropical region (Figure G.6d and G.7d, right panels). The median of relative effects ranges from −1% to a factor of −10, minimum (maximum) in the northern (southern) extratropics. Two second-order interactions likely make major contributions, that is, $\hat{f}_{34}$ which dominates the response over oceans, and $\hat{f}_{23}$ which dominates over land (Figures G.13 and G.17).

3.6.4 Effects of volatilization

The direct effects of volatilization ($\hat{f}_4$) are illustrated in Figure 3.6g. $\hat{f}_4$ is positive over *Trop.* in both seasons, with the median $\hat{f}_4/f_0$ ranging from 5% to 50%. Intensive volatilization in this region would increase net surface fluxes, thereby increasing concentrations, and seasonal temperature has a little influence in comparison with that in other regions. Nevertheless, it is found that the positive $\hat{f}_4$ values for PHE are more localized over the tropical landmass, while the negative $\hat{f}_4$ values are predicted over the tropical ocean (Figures G.8a and G.9a; left panels). The positive (negative) effects over land (ocean) areas are also apparent at higher latitudes during most of the year. This reflects the fact that the negative effects on marine air concentrations act contrary to the positive effects on net surface fluxes, mainly caused by the non-linear relationships of air−sea gas exchange (deposition and volatilization), air and surface burden, atmospheric oxidation, and emissions. For PYR and FLT, a positive signal is apparent over the high and middle latitudes during local summer in contrast to a negative signal during local winter (Figure 3.6g). Similar to PHE, the negative signal is confined over oceans (Figures G.8b−c and G.9b−c; left panels). The summer increases are stronger (20% to a factor of ten) than the winter decreases (−10% to −60%) and the magnitudes are higher in FLT than in PYR. For BaP, $\hat{f}_4$ is positive consistently across regions and seasons ($\hat{f}_4/f_0$ ranges from 20% to a factor of ten), with substantial effects occurring over oceans (Figures G.8*d*−G.9d; left panels). The simulations show the seasonality in concentration increase over land areas tends to be proportional to the seasonality in volatilization fluxes, albeit weak. During winter months volatilization fluxes are generally very low or even absent whereas during summer months higher temperature enhances volatilization fluxes from land surfaces. It should be noted, however, that the parameterization adopted here to describe volatilization from soils (the Smit scheme) is relatively simple and derived from an experimental study, there is a need to improve the parameterization for a better representation of temperature influence.

The interactions generally point toward positive effects for the high-to-medium volatility species (Figure 3.6h), despite some negative effects present over parts of the southern (northern) oceans in DJF (JJA) (Figures G.8−G.9; right panels). As for BaP, the effects are uniformly negative, inferring the interactions work in opposition to $\hat{f}_4$. The negative response is almost entirely caused by the negative $\hat{f}_{34}$, that is, the two-factor interaction between volatilization and the ppLFER scheme (Figures G.13,G.17). Compared to $\hat{f}_4$, the degree of interactions are weaker for PHE, except in polar regions during local summer where the interactions could amplify $\hat{f}_4$. The above implies that $\hat{f}_4$ may point in the right direction regardless of the influences from other factor changes. On the contrary, the degree of interactions is overall comparable to $\hat{f}_4$ for the other species.

3.7 Evaluation of model predicted near-surface concentrations and particulate mass fraction

As previously discussed, the results from the factor separation method demonstrate that the direct effects of some factors can be overridden by their interactions and such responses are species-specific, hence it is crucial to decompose the contributions of both effects for determining the potential of model input and physical schemes to influence predicted concentrations. We further investigate the impact on model performance due to changes in the four factors, individually or simultaneously, by comparing the predictions from 16 sensitivity experiments against observation data, focusing on the general characteristics of seasonal mean concentrations and mean bias in two regions (the Arctic and NH mid-latitude). The findings are presented in Appendix H.

A more detailed evaluation of model performance from the *target* experiment SMPW (i.e., Seasonal emission + *Modal* scheme + ppLFER scheme + With volatilization) is presented below. Two predicted variables are evaluated, that is, total (gas+particle) concentrations and particulate mass fraction at the lowest model level.

3.7.1 Near-surface air concentration

Comparison to land monitoring stations

Central tendency. Table 3.11 shows statistical indices for near-surface concentrations of atmospheric PAHs from observations and simulations and their comparisons, averaged across stations in the Arctic, NH mid-latitudes, and the tropics. We can see that mean observed concentrations are higher for PHE and smaller for BaP over all regions. Furthermore, the Arctic concentrations are lower than those in the NH mid-latitudes by a factor of around 20 and those

Table 3.11: Statistics comparison of model simulation and observations of total (gas+particle) concentrations of PAHs from stations in the Arctic, northern mid-latitudes and tropics. N: Number of observed-simulated monthly data pairs; $\overline{x}$: Mean; Q2_x: Median; SD_x: Standard deviation; GM_x: Geometric mean; x: Simulated (M) or Observed (O) data; MB: Mean bias; RMSE: Root mean square error; NMB: Normalized mean bias; NMBF: Normalized mean bias factor; FAC2: Factor of 2; FAC10: Factor of 10; r: Correlation coefficient.

		Arctic				**NH mid-latitudes**				**Tropics**		
Metrics	**Unit**	**PHE**	**PYR**	**FLT**	**BaP**	**PHE**	**PYR**	**FLT**	**BaP**	**PHE**	**PYR**	**FLT**
N	months	89	89	89	46	361	328	372	405	34	34	34
$N_{<\text{LOQ}}$	months	0	0	0	30	0	0	0	0	0	0	0
$\overline{O}$	ng m^{-3}	0.107	0.024	0.039	0.007	2.193	0.408	0.803	0.141	11.818	6.431	6.843
Q2_O	ng m^{-3}	0.034	0.014	0.012	0.002	1.301	0.194	0.360	0.037	3.608	2.106	2.181
SD_O	ng m^{-3}	0.162	0.027	0.054	0.015	2.956	0.582	1.135	0.253	16.598	10.141	10.217
GM_O	ng m^{-3}	0.051	0.014	0.018	0.003	0.968	0.221	0.383	0.046	3.733	1.369	1.726
$\overline{M}$	ng m^{-3}	0.046	0.025	0.079	5.2E−4	2.270	1.086	1.670	0.059	4.966	2.005	3.400
Q2_M	ng m^{-3}	0.010	0.007	0.034	1.9E−5	0.840	0.500	0.736	0.022	4.274	1.236	2.012
SD_M	ng m^{-3}	0.089	0.040	0.099	6.5E−4	2.955	1.225	2.007	0.085	3.897	2.019	3.462
GM_M	ng m^{-3}	0.012	0.008	0.041	3.4E−5	1.144	0.635	0.913	0.028	2.816	1.038	1.788
MB	ng m^{-3}	−0.060	0.001	0.040	−0.006	0.077	0.679	0.867	−0.083	−6.851	−4.426	−3.443
RMSE	ng m^{-3}	0.118	0.038	0.099	0.016	3.564	1.404	2.383	0.279	16.005	10.631	10.392
NMB	-	−0.56	0.06	1.04	−0.92	0.04	1.66	1.08	−0.58	−0.58	−0.69	−0.50
NMBF	-	−1.30	0.06	1.04	−12.17	0.04	1.66	1.08	−1.40	−1.38	−2.21	−1.01
FAC2	-	0.20	0.28	0.30	0.17	0.40	0.39	0.30	0.31	0.26	0.24	0.29
FAC10	-	0.82	0.90	0.94	0.33	0.90	0.84	0.83	0.79	0.97	0.79	0.85
r	-	0.83	0.42	0.42	0.16	0.27	0.23	0.09	0.01	0.63	0.33	0.29

in the tropics by approx. two orders of magnitude. The model captures well these species and regional variations, but the magnitudes are both under- and over-estimated. In the Arctic, it underestimates PHE (MB = −0.060) and BaP (MB = −0.006) concentrations but overestimates PYR (MB = 0.001) and FLT (MB = 0.04). In the NH mid-latitudes, the model overestimates the three species predominantly occur in the gas phase (MB = 0.077−0.867) but underestimates BaP (MB = −0.58). Negative bias is seen in the tropics for three PAHs (MB = −3.443 to −6.851). Nevertheless, the comparison of model and observations at individual monitoring station can be different from the regional mean statistics, as described in Appendix I. Comparing all four PAHs, a larger degree of bias is found for BaP which increases from the northern mid-latitudes (NMB = −0.58, NMBF = −1.40, FAC2 = 0.31, FAC10 = 0.79) to the Arctic (NMB = −0.92, NMBF = −12.17, FAC2 = 0.17, FAC10 = 0.33).

Dispersion of monthly concentrations. In the following, the coefficient of variation (CoV) is used to compare the dispersion of concentrations among species of different ranges. CoV was calculated by dividing standard deviation (SD) of all data points by its mean value ($\overline{x}$). The observations show high variability (CoV $>$ 1) with CoV ranging between 1.12 and 2.14. The simulated concentrations appear to be less dispersed than the observations (CoV = 0.78−1.93) except for the Arctic PHE and PYR concentrations. The degree of underestimation is larger in the tropics with CoV being 30%−50% smaller than the observations. Furthermore, correlations between predicted and observed concentrations are weaker than those in other regions where r varies between 0.29−0.63 (the model reproduces 8%−40% of the variance in observed concentrations). Comparing the four species, the simulated BaP shows greater underpredictions of the variability where CoV values are less than half of those observed and correlations are less than 0.2 (accounting not over than 4% of observed variance). Higher variability in BaP measurements (than in model results) can be influenced by strongly varying emissions in source regions that are not reflected in emission inventory (Matthias et al., 2009).

Seasonal variation. Figure 3.7 compares simulated and observed seasonal cycle of average concentrations for different species and regions. The observed mean concentrations are largest in winter and lowest during summer because of less emission and the strong presence of OH for oxidation. The winter maximum to summer minimum ratio (amplitude) is more pronounced (by more than a factor of two) in the Arctic than that in the NH mid-latitudes. The seasonality between model and observations is in a qualitative agreement, particularly over the Arctic (except in summer) and mid-latitudes. In the Arctic, the model overestimates the seasonal amplitude of PHE and BaP and underestimates their mean concentrations. The contrast is seen for PYR and FLT. FLT concentration is overestimated up to a factor of three in summer while PYR is quite well predicted. In the NH mid-latitudes, the model underestimates the amplitude but overestimates the concentrations of PHE, PYR, and FLT (by typically a factor of two), whereas a systematic negative bias is found for BaP. In the tropics, both the amplitude and magnitude are too low in the model (for magnitude, by a factor of 2−5).

Intermodel comparison. A comparison of simulated PAH concentrations from EMAC-SVOC for the year 2007−2009 and from GEOS-Chem model for 2005−2009 (Friedman and Selin, 2012) revealed that both models overall overestimate observed PHE and PYR over mid-latitudes

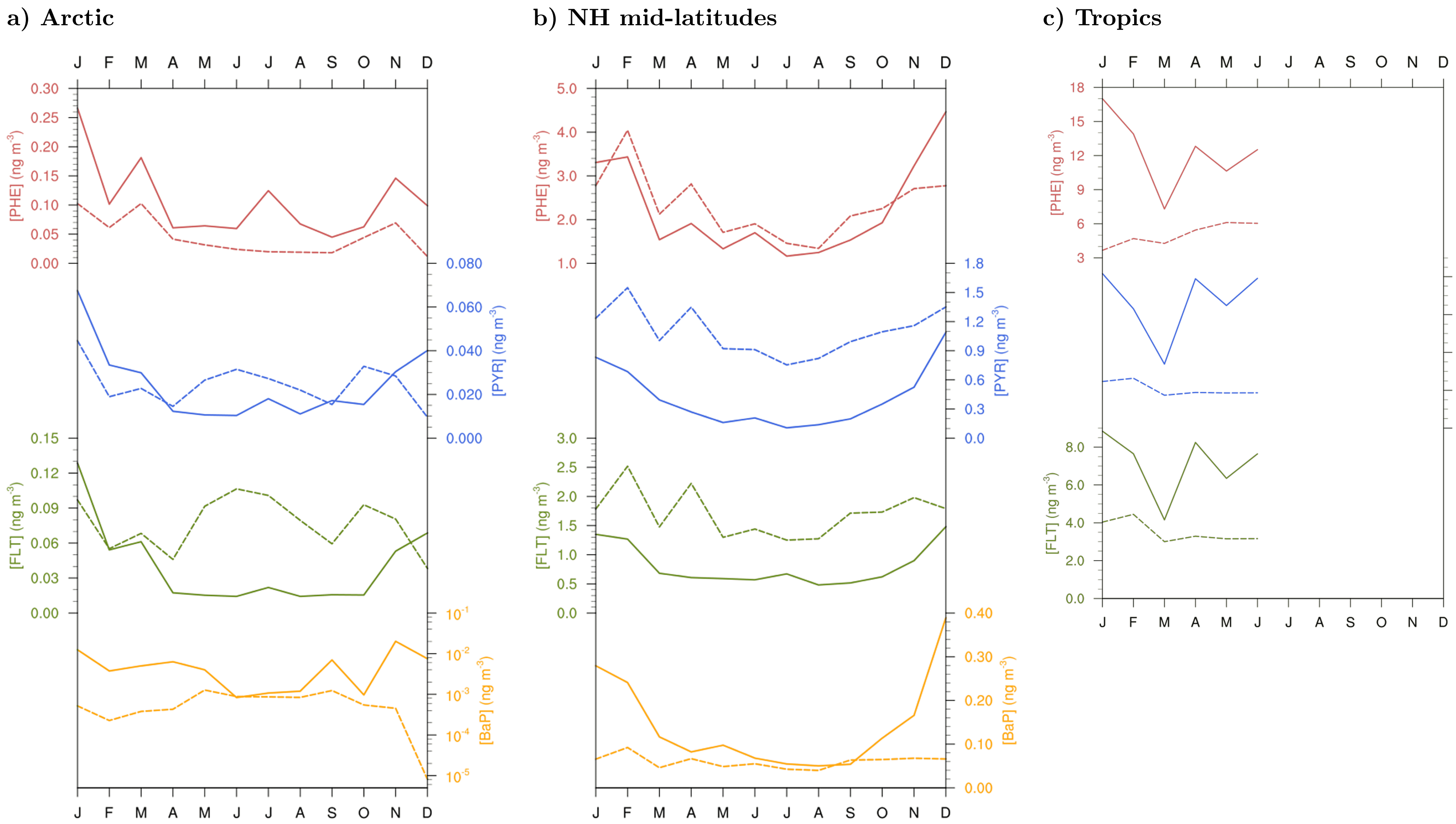

Figure 3.7: Seasonal mean total (gas+particle) concentrations of PAHs (ng m^{-3}) from observations (solid lines) and simulations (dashed lines) averaged over all stations in the (a) Arctic, (b) northern mid-latitudes, and (c) tropics. Note that logarithmic scale has been used for BaP concentrations in the Arctic.

whereas the Arctic concentrations for both species are underestimated by EMAC-SVOC but overestimated by GEOS-Chem in winter. The discrepancies are more likely to be caused by different emission inventory and by high spatial variability in the emissions which results in changes in PAH concentrations on scales not captured by both GCMs with a grid spacing of >100 km. It is also noteworthy that the simulation carried out with GEOS-Chem differs in complexity to EMAC-SVOC, that is, the model neglected volatilization and seasonal variation in emissions and applied a dual BC adsorption and OM absorption gas−particle partitioning. Nevertheless, both models systematically underestimate the BaP concentrations over all regions, reflecting a difficulty in modeling the behavior of this species. Model bias is usually larger for the Arctic sites than for the mid-latitude sites and the agreement with observations is more satisfactory in summer. BaP underestimation in remote regions has also been reported in other global modeling studies (Sehili and Lammel, 2007; Shrivastava et al., 2017). Despite uncertainties in the emissions, which seasonality has been taken into account in the EMAC-SVOC simulation, this finding suggests that current models underestimate the role of temperature for the long-range transport of BaP. A GEOS-Chem configuration which neglected heterogeneous oxidations for BaP yielded predicted concentrations higher than measurements over NH mid-latitudes but rather in a good agreement over the Arctic (Friedman and Selin, 2012), suggesting a strong dependence of BaP long-range transport on the temperature sensitivity of particulate-phase oxidation. Similarly, agreement/overprediction of BaP was found using ECHAM/HAM model (Lammel et al., 2009) when setting $k^{(2)}_{\mathrm{O_3,het}}$ to zero (BAPOB scenario; agreement for the Zeppelin station, overestimation for the Alert station). In addition, the latest global BaP modeling study carried out with CAM5 model (Shrivastava et al., 2017) also found that temperature and humidity are important factors to affect heterogeneous oxidation kinetics of BaP and influence the long-range transport. Their default simulation underestimates observed BaP concentrations by approximately 77% whereas the predictions improved when the model assumed that BaP underwent a complete shielding by highly viscous organic aerosols under cool/dry conditions. It is important to understand further the effect of the variation of temperature and humidity on reactive rate constants of the heterogeneous oxidations during the long-range transport. This topic is discussed in details in Mu et al. (2018) and Chapter 4 of this thesis.

Comparison to ship cruise measurements

Measurements of PHE, PYR, and FLT concentrations over the Atlantic Ocean were taken during a cruise in July 2009 (Lohmann et al., 2013). Figure 3.8 shows the ship sample concentrations overlaying the simulated PAH concentrations. Sample arithmetic (geometric) means during the whole cruise transect are 322 (209), 95 (88), and 128 (111) pg m^{-3} for PHE, PYR, and FLT respectively. The model poorly reproduces the remote marine environments and overall underestimates the observations, except at 3 locations along the North American coast. The simulated means across sampling positions are 23 (7), 20 (3), and 39 (2) pg m^{-3} respectively and the underestimation ranges from a factor of 2 to 1000. The degree of bias is most apparent over the tropical South Atlantic at latitude bands 5°S-15°S.

a) PHE

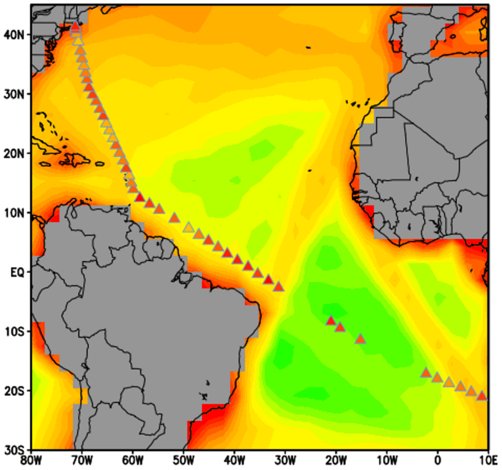

b) PYR

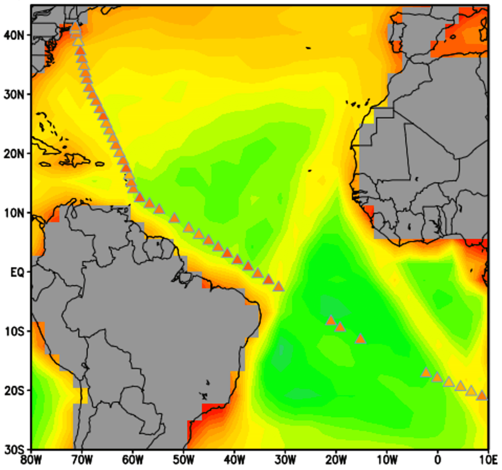

c) FLT

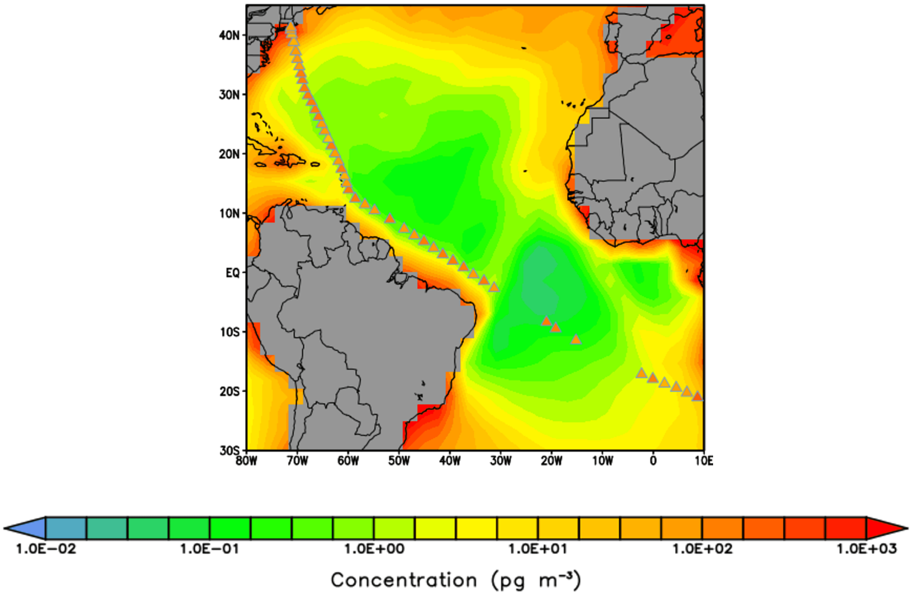

Figure 3.8: Simulated concentrations of PHE, PYR, and FLT (pg m^{-3}) over the Atlantic ocean overlaid with concentrations from a ship cruise measurement campaign during July 2009 (triangles). Land grid cells are depicted in gray shades.

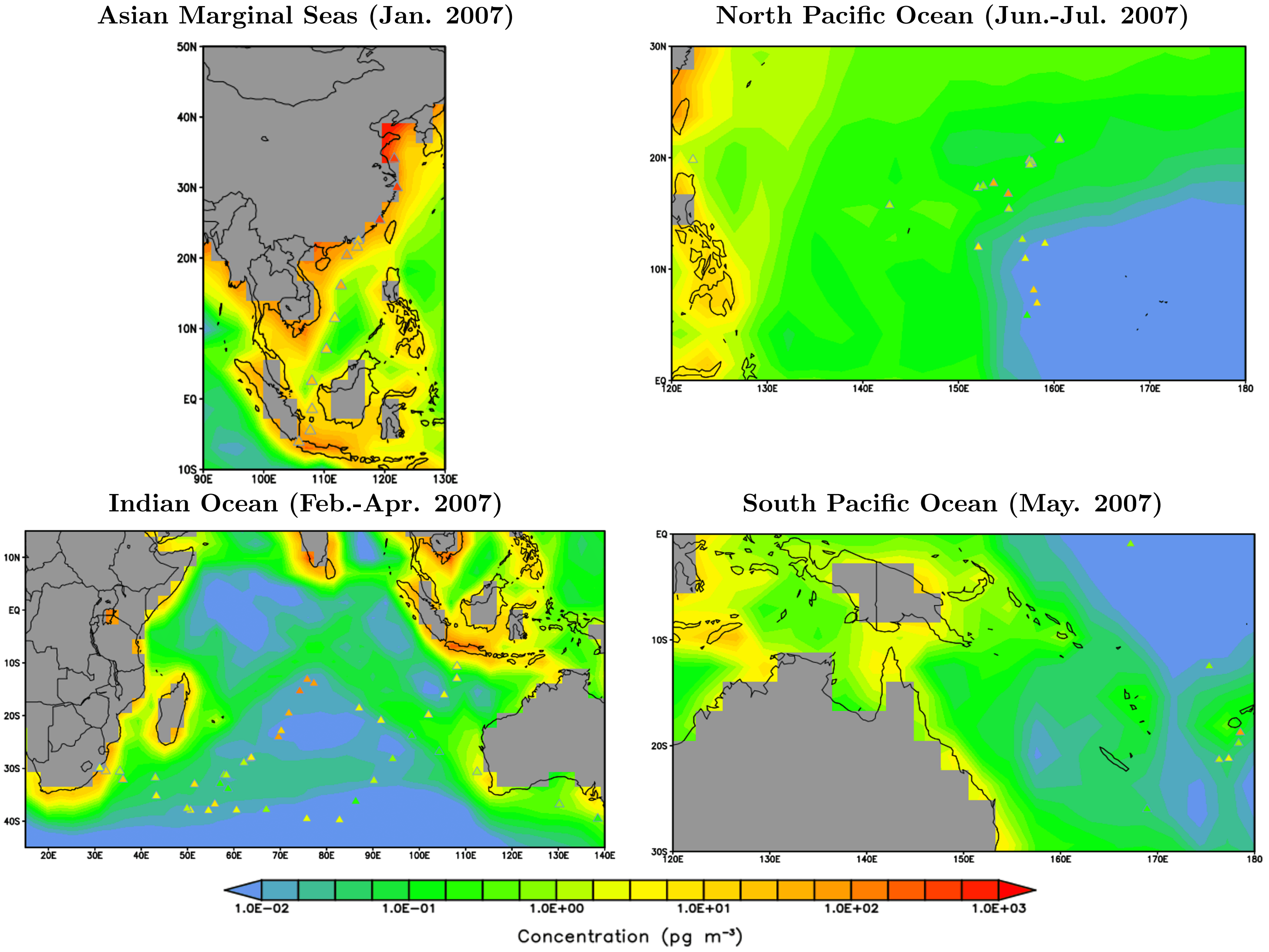

Asian Marginal Seas (Jan. 2007)

North Pacific Ocean (Jun.-Jul. 2007)

Indian Ocean (Feb.-Apr. 2007)

South Pacific Ocean (May. 2007)

Figure 3.9: Simulated BaP concentrations (pg m^{-3}) over the four ocean margins overlaid with concentrations from a ship cruise measurement campaign (triangles). Land grid cells are depicted in gray shades.

As reported in Liu et al. (2014), the measured concentrations of BaP over the Asian marginal seas, the Indian Ocean, the South and North Pacific Oceans are 131 (45), 14 (3), 9 (2), and 8 (3) pg m^{-3}, respectively, for the arithmetic (geometric) means of all samples. Similar to other species, the model also underestimates the BaP concentrations with mean values being 75 (15), 4 (0.05), 0.09 (0.03), and 0.2 (0.06) pg m^{-3}, respectively. The discrepancy appears relatively smaller over the Asian marginal seas as compared to other locations (Figure 3.9). A substantial degree of bias is seen over the Indian Ocean covering approximately the area bounded by 70°E−90°E and 10°S−30°S, with simulated values being more than two orders of magnitude smaller than the observed.

The model tendency to underestimate the marine air concentrations may likely be due to several factors: (a) The grid resolution is not sufficient to reproduce fine-scale processes at the grid points close to shipping tracks; (b) Great uncertainties associated with the air−sea gas exchange parameterizations still exist, most notably in the estimation of gas transfer velocity; (c) The global inventory (Shen et al., 2013) may significantly underestimate emissions from ocean shipping and do not well characterize the spatial and temporal variability of biomass burning plumes as another potential origins of pollutans in the marine air (Nizzetto et al., 2008); (d) PAH concentration over remote oceans is controlled by atmospheric components (e.g., temperature, wind speed, boundary layer height, photochemical degradation) and the dynamical and biogeochemical components of the ocean. However, the ocean components have not been covered in the simulation; (e) The particulate-bound PAHs may undergo too fast heterogeneous oxidation (most relevant for BaP), leading to short atmospheric lifetimes and weaker long-range transport.

3.7.2 Particulate mass fraction

Measurements of particulate mass fraction (θ) were available only from E3 station in Europe and IADN stations (I1-I7) in North America (see Table 3.9). Table 3.12 presents summary statistics on monthly mean θ from observations and simulations including some performance metrics. The observed mean θ is smaller for PHE (0.051 ± 0.035) and higher for BaP (0.949 ± 0.067). This result is expected as volatility decreases (hence θ increases) from (lighter) PHE to (heavier) BaP. The θ values for PYR and FLT are larger by over five times than those for PHE and lower by around one-third than those for BaP. The model reproduces well the distinct differences among species but underestimates the observed θ for PHE, PYR and FLT. The degree of negative bias is relatively large in PHE (NMB $= -0.910$ and NMBF $= -10.145$), whereas for the isomer pair of PYR and FLT, the model exhibits a similar performance with a slight improvement in PYR (NMB $= -0.410$ and NMBF $= -0.694$). With regard to BaP, there is a satisfactorily small bias (MB $= 0.015$, RMSE $= 0.074$, NMB $= 0.016$, and NMBF $= 0.016$) although the observed and simulated values have a very weak correlation ($r = 0.03$).

Figure 3.10 shows the seasonal mean θ averaged over three years for all PAHs. Observations show that θ for BaP varies less than those for 3−4 ring PAHs. Although the model adequately reproduces this feature as well as seasonal variation of individual species, the simulated θ of PHE, PYR, and FLT are generally lower than the observations (except for PYR in winter). For BaP, differences between model and observations are less than 10% in all months. EMAC-SVOC describes the gas−particle partitioning of atmospheric SOCs as a function of temperature and aerosol phase composition. The underestimation might be related to the fact that the model assumes the particle to be fully in equilibrium with the gas phase at all times. It neglects kinetic limitations of molecular diffusivity that could lead to the trapping of particles inside viscous (or semisolid) organic aerosol coating. This shielding effect increases equilibration times of the particles, thereby reducing part of θ from the mass available for gas−particle partitioning. Deviations from measurements can also be partly attributed to the locations of some stations that are within, or close to, residential and industrial area (namely, I4, I6, and I7) where the scale and gradient in anthropogenic emissions are not resolved by the model grid resolution nor represented by the emission inventory.

Table 3.12: Statistics comparison of model simulation and observations of particulate mass fraction (θ) from a subset of surface stations, as listed in Table 3.9. N: **Number of observed-simulated monthly data pairs;** $\overline{x}$: **Mean;** SD$_x$: **Standard deviation;** x: **Simulated (**M**) or Observed (**O**) data;** MB: **Mean bias;** RMSE: **Root mean square error;** NMB: **Normalized mean bias;** NMBF: **Normalized mean bias factor;** FAC2: **Factor of 2;** FAC10: **Factor of 10;** r: **Correlation coefficient.**

Metrics	PHE	PYR	FLT	BaP
N	63	63	99	93
$\overline{O}$	0.051	0.359	0.268	0.949
SD$_O$	0.035	0.150	0.162	0.067
$\overline{M}$	0.005	0.212	0.106	0.964
SD$_M$	0.005	0.138	0.086	0.027
MB	−0.046	−0.147	−0.162	0.015
RMSE	0.057	0.214	0.225	0.074
NMB	−0.910	−0.410	−0.604	0.016
NMBF	−10.145	−0.694	−1.523	0.016
FAC2	0.00	0.56	0.30	1.00
FAC10	0.38	1.00	0.94	1.00
r	0.42	0.42	0.33	0.03

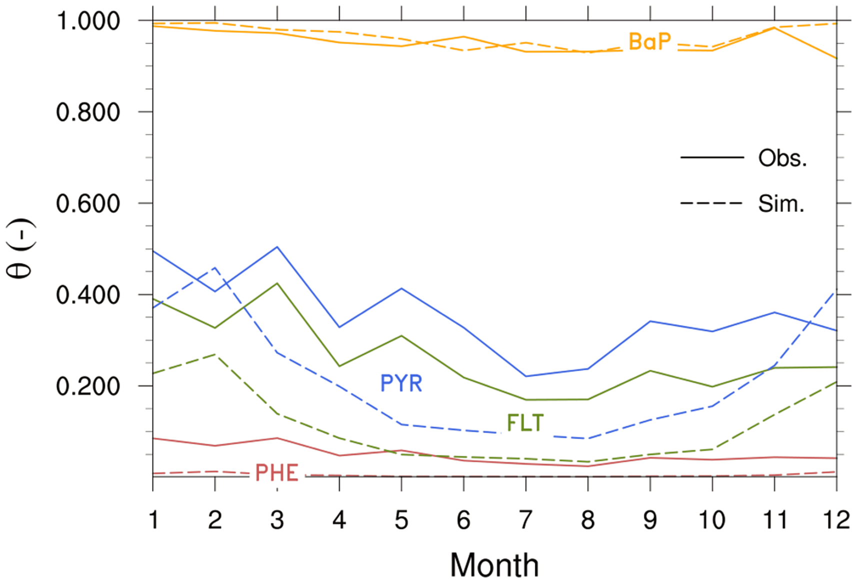

Figure 3.10: Seasonal mean particulate mass fraction (θ; unitless) from observations (solid lines) and simulations (dashed lines)

Chapter 4

Temperature Effect on Phase State and Reactivity Controls Atmospheric Multiphase Chemistry and Transport of PAHs

This chapter is comprised of the article "Temperature effect on phase state and reactivity controls atmospheric multiphase chemistry and transport of PAHs" by Qing Mu, Manabu Shiraiwa, Mega Octaviani, Nan Ma, Aijun Ding, Hang Su, Gerhard Lammel, Ulrich Pöschl, and Yafang Cheng published in *Sci. Adv.*, 2018, 4: 3 (DOI: 10.1126/sciadv.aap7314). Y.C., H.S., U.P., and G.L. conceived the study. M.S., Y.C., H.S., and U.P. developed the temperature-dependent ROI-T scheme for model implementation. Q.M. incorporated new PAH module into the regional model WRF-Chem and performed the model simulation and data analyses. M.O. (candidate) incorporated new PAH module into the global model EMAC and performed the model simulation and data analyses. Y.C., H.S., and Q.M. analyzed and interpreted results. N.M. contributed to data analysis and visualization. A.D. contributed to the transport process analysis and relevant discussion in supplementary materials. All coauthors discussed the results. The article was written by H.S., Y.C., and Q.M. with input from all coauthors. The postprint version of the article was incorporated into this chapter whereas its supplementary materials was incorporated into Appendix J.

For this study, the candidate applied EMAC-SVOC model to simulate four simulations representing different multiphase degradation scenarios. The global model output have been used for two purposes: the evaluation of model performance and the identification of meridional long-range transports. The candidate collected and quality screened observation data in the Arctic and mid-latitude sites for comparison with simulated results from each scenario. Furthermore, the candidate designed two variables, that is, net meridional mass flux and vertical center of column mass, to help investigate differences among scenarios with regard to mass transports to the Arctic. Only simulated results from two scenarios (Kwamena and ROI-T) were shown in the original article. To complement the study, the remaining results from the other scenarios are shown in Appendix K of this thesis.

4.1 Introduction

Polycyclic aromatic hydrocarbons (PAHs) are derived from combustion processes. High health risks are associated with exposure to PAHs, among which benzo(a)pyrene (BaP) is one of the most carcinogenic species (Perera, 1997; Boffetta et al., 1997). Since BaP resides almost entirely in the particulate phase, the distribution and long-range atmospheric transport of BaP are largely controlled by its multiphase degradation, mainly the reaction of particulate BaP with gaseous ozone (Keyte et al., 2013). Laboratory studies showed rapid BaP degradation on the surface of soot, ammonium sulfate and organic aerosol (OA) particles (Pöschl et al., 2001; Kwamena et al., 2004; Zhou et al., 2012), whereas atmospheric observations revealed a much longer lifetime and persistence of BaP especially toward remote and polar regions (Halsall et al., 1997; Schauer et al., 2003). Recent laboratory and kinetic studies have shown that OA coatings can effectively shield BaP from oxidants and that the OA phase state may strongly influence the rate of degradation (Shiraiwa et al., 2011a; Berkemeier et al., 2016; Zhou et al., 2013; Shiraiwa et al., 2017; Koop et al., 2011). However, key factors controlling the multiphase degradation and the fate of BaP in aerosols under real atmosphere conditions are still not resolved (Shrivastava et al., 2017). In particular, the laboratory-derived degradation schemes of BaP that have been applied in previous model studies (Figure 4.1A, Table J.1 of Appendix J) (Shrivastava et al., 2017; Matthias et al., 2009; Aulinger et al., 2011; Friedman and Selin, 2012; San José et al., 2013; Friedman et al., 2014; Friedman et al., 2013; Efstathiou et al., 2016) do not fully account for the dependency on environmental conditions/parameters.

Temperature (T) and relative humidity (RH) in the atmosphere cover a wide range, which influence not only the phase state and diffusivity of OA (Shiraiwa et al., 2017) but also the chemical reactivity of organic compounds. Because most modeling studies used degradation rates determined at room temperature (that is, 296−298 K) in laboratory experiments, they may overestimate degradation rates when applied in a colder atmospheric environment. On the basis of the study of Zhou et al. (2013), Shrivastava et al. (2017) introduced a threshold temperature below which the OA coating was assumed to shut off the multiphase degradation of BaP. This shielding effect improved agreement between model predictions and observations and was very sensitive to the choice of the threshold temperature. A simple threshold value, however, does not resolve the actual temperature dependence of multiphase reactions because both the molecular diffusivity and the chemical reactivity of BaP are expected to exhibit a continuous change in response to changing temperature rather than following a step function (Koop et al., 2011).

Moreover, the effects of diffusion and reaction on the particle bulk are not well characterized in earlier studies. For example, most laboratory experiments (Pöschl et al., 2001; Kwamena et al., 2004; Zhou et al., 2013; Kahan et al., 2006) were carried out under excessively high ozone concentrations (up to three orders of magnitude above tropospheric levels), and often, surface reaction rate equations were used to extrapolate the laboratory results for application in atmospheric models. The use of surface reaction rate equations without considering bulk processes, however, can result in inconsistent dependencies of BaP degradation rates on RH and ozone concentration (see Section J.1).

In this study, we use an advanced kinetic model framework to develop an elaborate kinetic scheme for better representation of multiphase degradation of BaP in regional and global models. This new scheme has incorporated three major improvements compared to previous schemes: (i) considering the formation of reactive oxygen intermediates (ROI); (ii) including temperature and humidity effects on phase state of OA and temperature-dependent chemical reactivity; and (iii) using a model framework that considers both bulk diffusion/reaction and surface reaction to interpret laboratory results for application in models and comparison to field measurements. We find that the new ROI-T scheme can be a good predictor of BaP concentrations from regional to global scales. Our results highlight the importance of temperature in BaP multiphase degradation from a kinetic view and demonstrate a universal scheme that can be applied to various atmospheric conditions and geolocations. Due to the common existence of OA coating, similar temperature effects are expected for other multiphase reactions, which can be determined from laboratory studies by the general modeling framework and approaches proposed here.

4.2 Materials and methods

4.2.1 Model setup

The ROI-T scheme was incorporated as a look-up table (Table J.3) into two state-of-the-art models with BaP extension for further application.

Regional model

The open-source community model WRF-Chem (Weather Research and Forecasting model coupled with Chemistry), an “online” regional model with coupled meteorology and chemistry (Grell et al., 2005; Peckham et al., 2014), has higher spatial resolution and advantages in determining the fine structures of transport process, especially the vertical transport within and out of the boundary layer. The PAH extension was based on the model version 3.6.1.

The physics schemes of the regional WRF-Chem model used here were as follows (Peckham et al., 2014): microphysics and cumulus parameterizations followed the Purdue−Lin scheme and the Grell 3D ensemble scheme, respectively. The longwave and shortwave radiation were calculated by the online rapid radiative transfer model and the Goddard scheme, respectively. The planetary boundary layer was based on the Mellor−Yamada−Janjic scheme, along with the Eta Similarity surface layer scheme. The implemented air−soil gas exchange was coupled with the Noah Land Surface Model. Photolysis rates used the Fast-J photolysis scheme. As for the chemistry schemes, the Regional Atmospheric Chemistry Mechanism (RACM) was used for homogeneous gas-phase reactions. The aerosol module included the inorganic fraction Modal Aerosol Dynamics Model for Europe (MADE) and organic fraction Secondary Organic Aerosol Model (SORGAM).

Global model

The global model EMAC (ECHAM/MESSy Atmospheric Chemistry) covered intercontinental transport, such as from source areas to the Arctic. It was a combination of the ECHAM5 general circulation model (Roeckner et al., 2003) and MESSy (Modular Earth Submodel System, version 2.50) (Jöckel et al., 2010). MESSy provided infrastructure to couple the base model ECHAM5 and different components (or submodels) that represent various processes of the Earth system.

The model simulations included the following MESSy submodels (Jöckel et al. (2010) and references therein): CLOUD described cloud scheme and precipitation. Convection parameterization and radiation were in submodels CONVECT and RAD. Air−sea exchange was parameterized by AIRSEA. Wet and dry depositions were described by SCAV and DDEP. Prescribed emissions were calculated by OFFEMIS, whereas online emissions were calculated by ONEMIS. As for chemistry, MECCA was responsible for gas-phase chemistry, JVAL took care of photolysis rate, and GMXe was the submodel for aerosol microphysics and semivolatile inorganic partitioning.

Simulation

We performed regional (global) simulations at a grid spacing of 27 km × 27 km ($\approx 2.8^\circ$) with 39 (19) vertical levels from the surface to 100 hPa (10 hPa). Simulations were conducted during 11 to 22 July 2013 for Xianghe case and 14 to 25 February 2003 for Gosan case over East Asia domain (15°N to 55°N, 95°E to 155°E) by the regional model, and 2007−2009 for mid-latitude and Arctic sites by the global model, respectively.

4.2.2 BaP extension

The following processes of BaP were included: emission, gas−particle partitioning, gas phase and multiphase reactions, air−soil gas exchange, and wet and dry depositions[1].

Emissions

Anthropogenic BaP emissions were regridded from a $0.1^\circ \times 0.1^\circ$ global annual PAH emission inventory, with 69 detailed source types (Shen et al., 2013). Monthly variation was based on BC emission seasonality of HTAP_v2.2 (Janssens-Maenhout et al., 2015). For regional simulations, annual scaling factors (Shen et al., 2013) and diurnal cycle (following BC) of the PAH emissions are also applied. Biogenic contributions to PAH emission have been neglected.

Gas−particle partitioning

Gas−particle partitioning of BaP used in the regional model followed an equilibrium partitioning expression that accounted for the absorption into organic matter and adsorption onto BC

---

[1] Refer to Chapter 3 Section 3.3 for more details

(Lohmann and Lammel, 2004; Galarneau et al., 2014). In the global model, the poly-parameter linear free energy relationships were applied, which accounted for BaP absorption into organic matter and adsorption to soot and inorganic salts (Shahpoury et al., 2016).

Gas-phase reaction

The second-order rate coefficients for reactions of gaseous BaP with OH, NO_3, and O_3 are 1.5×10^{-10}, 5.4×10^{-11} and 2.6×10^{-17} cm^3 $molec^{-1}$ s^{-1}, respectively (Klöpffer et al., 2008).

Wet/dry depositions

The original regional/global model routines have been adapted to include the deposition of gas-phase and particulate-phase BaP using corresponding deposition parameterizations.

Air−soil gas exchange

Air−soil gas exchange of BaP was parameterized (Jury et al., 1983) on the basis of air/soil concentrations and properties of BaP. The concentrations of BaP in soil were initialized by the global multicompartmental model ECHAM5-HAM: BaP has been simulated globally over 10 years with 2.8° × 2.8° horizontal resolution (Lammel et al., 2009). A steady state of BaP concentrations in the soil compartment was safely reached.

4.2.3 KM-SUB model

The KM-SUB model treats mass transport and chemical reactions at the surface and in the particle bulk (Shiraiwa et al., 2010). KM-SUB was composed of the following compartments: gas phase, near-surface gas phase, sorption layer, quasi-static surface layer, near-surface bulk layer, and a number of bulk layers. The model resolved the following processes explicitly: gas-phase diffusion, reversible adsorption of O_3, surface reaction involving decomposition of O_3 and formation of long-lived ROIs, bulk diffusion of O_3 and BaP in OA coating, and bulk reaction between O_3 and BaP. Note that heat transfer was not treated in the model because heat released by trace gas uptake and reactions can be efficiently buffered by the ambient gas and did not lead to a substantial increase of particle-surface temperature (Shiraiwa et al., 2012). KM-SUB can simulate the evolution of species at the particle surface and in the particle bulk, along with surface concentrations and gas uptake coefficients. Core-shell morphology was assumed with an organic phase embedding BaP as particle shell and an inorganic phase as particle core (Shiraiwa et al., 2013). The required kinetic parameters were summarized in Table J.2, and the values were on the basis of previous studies of KM-SUB applications to experimental data of Zhou et al. (2013).

The ROI-T considered the temperature dependence of bulk diffusivity and chemical reactivity. The diffusion coefficients of O_3 and PAH were assumed to decrease by one order of magnitude upon a decrease of temperature by 10°C based on the Vogel−Fulcher−Tamman approach (Arangio et al., 2015; Berkemeier et al., 2014). Temperature-dependence of rate coefficients k was considered by the Arrhenius equation using the activation energies of surface reactions as listed in Table J.2. KM-SUB simulations were conducted in the temperature range of $-20°$ to $40°C$ with gas-phase O_3 concentrations of 0 to 200 parts per billion (ppb). The obtained first-order decay rate of PAH was then fitted with the Hill equation as shown in Table J.3, so that the parameterizations can be efficiently incorporated in regional and global transport models.

4.2.4 Observational data of BaP

The near-source observation data of BaP were collected at the Xianghe Atmospheric Observatory (39.80°N, 116.96°E). The Xianghe site is a sub-urban site locating 45 km southeast of Beijing and 70 km northwest of Tianjin. Particulate- and gas-phase samples were collected for daytime (8:00 to 18:00 local time) and nighttime (20:00 to 6:00 local time), respectively, during 11 to 22 July 2013.

The outflow observation data of BaP was measured at the Gosan site (33.28°N, 126.17°E) on Jeju Island. The site was 72 m above sea level and about 100 km south of the Korean peninsula. Gosan is a representative background station in East Asia to study outflow of air pollutants from land to ocean. Intensive daily measurements (8:00 to 8:00 local time in the following morning) of particulate-phase BaP were carried out during a pollution period 14 to 25 February 2003. Details of sampling and analysis methods were given in the study of Kim et al. (2012).

The mid-latitude observation data of BaP were taken from 18 stations of the European Monitoring and Evaluation Programme (EMEP) (Tørseth et al., 2012), the Integrated Atmospheric Deposition Network (IADN) (Galarneau et al., 2006), and Arctic Monitoring and Assessment Programme (AMAP) (Hung et al., 2010). Three Arctic sites (that is, north of 66.5°N) are Alert in Canada (AMAP; 62.3°W, 82.5°N), Spitsbergen in Norway (EMEP; 11.9°E, 78.9°N) and Pallas in Finland (EMEP; 24.3°E, 68.0°N). The concentration of BaP during 2007−2009 was averaged over all months, with at least one weekly measurement reported.

4.3 Results

4.3.1 BaP degradation kinetic scheme

In the new kinetic scheme ROI-T, the multiphase degradation of BaP with ozone is treated in multiple compartments as shown in Figure 4.1B, which has not yet been fully considered by previous schemes. The reaction involves the decomposition of surface ozone and formation of ROI (Shiraiwa et al., 2011b). To account for mass transport and reactions of gaseous and particle-bound chemical species at the surface and in the bulk phase, we apply the kinetic multi-layer model of aerosol surface and bulk chemistry (KM-SUB) (Shiraiwa et al., 2010) (see Section 4.2.3) which is based on the Pöschl−Rudich−Ammann framework (Pöschl et al., 2007). Secondary OA (SOA) formed from α-pinene oxidation is chosen to represent the OA coating (Zhou et al., 2013). With the kinetic parameters in Table S2, the new kinetic scheme ROI-T can effectively explain the kinetics of multiphase degradation of BaP and successfully reproduce the

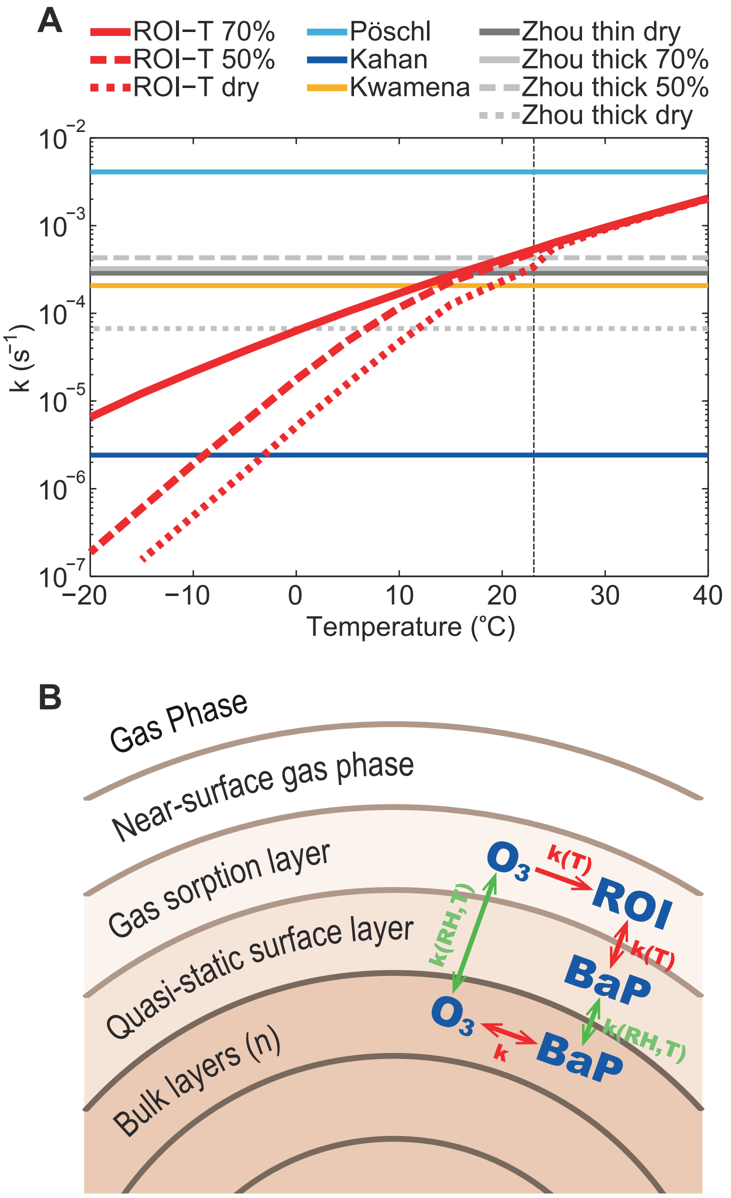

Figure 4.1: Kinetic scheme ROI-T. (A) First-order multiphase degradation rate coefficient *k* (s^{-1}) for laboratory schemes of Pöschl et al. (2001), Kahan et al. (2006), Kwamena et al. (2004), and Zhou et al. (2013) (Table J.1) and the kinetic scheme ROI-T at 50 ppb O_3. Vertical dashed line denotes 23°C. (B) Model framework of the multilayer kinetic scheme ROI-T. Red arrows show the reactions: O_3 is decomposed and forms ROI in the gas sorption layer, BaP reacts with ROI between gas sorption and surface layer, and BaP reacts with O_3 in the bulk. Green arrows show the RH/T-dependent mass transport: O_3 from gas sorption to bulk layer, BaP from bulk to surface layer.

results of the Zhou's experimental data (Zhou et al., 2013) for both thin and thick coating cases (8 nm and 40 nm) at different RH (that is, dry, 50% and 70%). In further regional/global model applications, the thick coating scenario is adopted, because the global simulation has found that the OA shielding on BaP is generally thick (Shrivastava et al., 2017). As shown in Figure 4.1A, rather than a fixed degradation rate, the rate coefficients of the ROI-T scheme show a monotonic increase with increasing temperature and systematically smaller degradation rate of BaP at lower RH.

The temperature and RH dependence of diffusivity and BaP chemical reactivity both control the degradation rate of BaP. In the new ROI-T scheme, on the one hand, temperature influences OA diffusivity and its phase state, that is, the diffusion coefficients of ozone and BaP are assumed to decrease by one order of magnitude upon a temperature decrease of 10°C (Arangio et al., 2015) (see Section 4.2.3). On the other hand, temperature influences the chemical reactivity of BaP with ROI following the Arrhenius equation (see Section 4.2.3). Considering both effects, the degradation rates of BaP at 253 K are three to four orders of magnitude smaller than those at 313 K (Figure 4.1A).

To demonstrate the advantage of the new ROI-T scheme, we have also included other commonly used degradation schemes of BaP: Kwamean (Kwamena et al., 2004), Kahan (Kahan et al., 2006), and Pöschl (Pöschl et al., 2001) schemes refer to ozonolysis of uncoated BaP on azelaic acid, liquid substrates, and soot, respectively; the Zhou (Zhou et al., 2013) scheme refers to ozonolysis of OA-coated BaP. As shown in Figure 4.1A, these schemes show different degradation rates due to the substrate and shielding effects as summarized in Table J.1.

4.3.2 Model versus observation

Other BaP degradation schemes provide reliable predictions only at specific characteristic distances from sources or geolocations but are less at others. For example, the Kwamena scheme shows the best agreement with observations at mid-latitude, whereas the optimum scheme for the Arctic is the scheme that predicts the slowest degradation rates, that is, the Kahan scheme (Figure 4.1A) (Friedman and Selin, 2012; Friedman et al., 2014). The ROI-T scheme, on the contrary, can account for the different temperature/RH regimes at different locations and transport distances.

In Figure 4.2A, we compare the performance of the kinetic ROI-T scheme and the most commonly used Kwamena scheme (Matthias et al., 2009; San José et al., 2013; Efstathiou et al., 2016; Aulinger et al., 2007) in multiscale model simulations (see Sections 4.2.1 and 4.2.2). The model results from the Pöschl scheme (the fastest) and the Kahan scheme (the slowest) (Figure 4.1A) are also included as references. The observational data used for model evaluation cover a wide range of source/receptor sites over a large span of latitudes (33°N−83°N; see Section 4.2.4). Compared with other schemes, the ROI-T scheme consistently provides better predictions at all types of sites, from near-source, mid-latitude, remote background sites to the Arctic (Table J.4). It improves the BaP simulation most significantly at the Arctic sites, where air masses underwent the longest and coldest transport processes. For example, simulated BaP levels at the

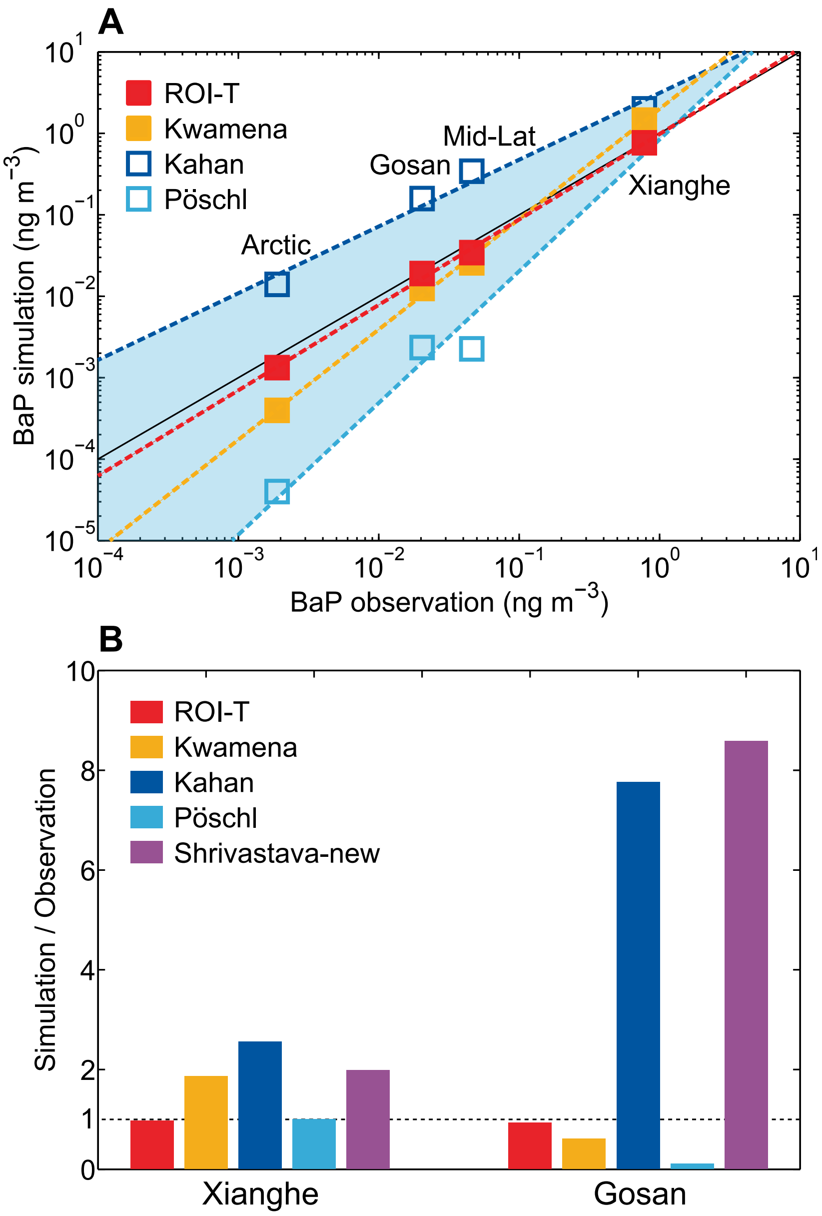

Figure 4.2: Comparisons of the ROI-T scheme and previous laboratory-derived schemes with observations. (A) Simulated concentrations of BaP (ng m^{-3}) by the ROI-T, Kwamena, Kahan, and Pöschl schemes at the Xianghe site, the Gosan site, other mid-latitude sites, and the Arctic sites[2]. The solid black line is a 1:1 line of simulation and observation. The dashed lines are fitted by respective simulations. The shaded area is constrained by the Pöschl and Kahan schemes. (B) The ratios of simulated and observed BaP concentrations with different schemes at the Xianghe site and the Gosan site.

---

[2] Box-and-whisker plots showing the distributions of monthly BaP concentration across the Arctic and mid-latitude sites are shown in Appendix K, Figure K.1. In addition, seasonal mean BaP concentrations averaged all sites over the two respective regions are shown in Figure K.2.

Alert and Spitsbergen sites are improved by more than one order of magnitude with the ROI-T scheme compared with the Kwamena scheme (Table J.4A).

To further elucidate the advantage of the ROI-T scheme, we focus on two cases with contrasting temperature/RH conditions (Figure 4.2B): a near-source site Xianghe (39.80°N, 116.96°E, 45 km southeast of Beijing, China), representing the local surface transport in hot/humid environment in July, and a remote background site Gosan (33.28°N, 126.17°E, on the Jeju Island, about 100 km south of the Korean peninsula), representing long-range transport in cold/dry air in February. The results show that it is impossible to reproduce observations for both cases by a fixed degradation rate. The Kwamena scheme is either too slow for the Xianghe summer case or too fast for the Gosan winter case, suggesting strong temperature and humidity effects on the diffusivity and reactivity. The model performance cannot be improved by simply changing for another degradation rate, because a higher (lower) degradation rate will reduce (increase) the BaP concentrations at both sites. As shown in Figure 4.2 (A and B), a scheme with faster degradation rates, such as Pöschl scheme, reduces the BaP concentration to the same level as observations for the Xianghe case but shows a larger underestimation for the Gosan case. We also test the step function setting of the Zhou scheme as in Shrivastava et al. (2017). It cannot reproduce BaP observations over both cases either, with a very similar performance as the Kahan scheme (the slowest) (Figure 4.2B).

By unifying the impact of temperature and RH on diffusivity and reactivity under an elaborate kinetic framework (Figure 4.1B), the ROI-T scheme solves the problem with changing BaP degradation rates in response to the changes of environmental conditions (Figure 4.1A). Under the new scheme, the hot/humid conditions increase the diffusivity/reactivity and the BaP degradation rate, whereas it is the other way around in the cold/dry environment. Compared with the Kwamena scheme, our ROI-T scheme leads to reduced BaP concentrations at the Xianghe site and elevated BaP concentration at the Gosan site, finally showing good agreements for both cases. The changes in both diffusivity and chemical reactivity contribute to the changes of degradation rate in the new ROI-T scheme. To decouple their effects, we perform sensitivity studies by turning on/off temperature/RH dependence of diffusivity. At the Gosan site, a fixed degradation rate in ROI-T scheme at room temperature 296 K leads to an underestimation of BaP concentration by a factor of 3. Further tests show that the temperature/RH-induced change of diffusivity would account for ~50% of the improvement in the predicted BaP concentrations whereas the change of reactivity further contributes to the rest of the ~50% (as shown by the comparison between "ROI-T at 296 K" and "ROI-T with fixed diffusivity" cases in Figure J.1).

4.3.3 East Asia outflow

As one of the largest source regions, the outflow of BaP from East Asia to the downwind regions and the remote Pacific Ocean is of international concern (Zhang et al., 2011a; Zhang et al., 2011b). Figure 4.3 (A and B) shows a typical outflow transport of BaP from East Asia in winter (24 February 2003). With the Kwamena scheme, most BaP is bounded in the boundary layer due to fast degradation with an average lifetime of ~2 to 3 hours throughout the whole domain (Figure

J.2), resulting in very low concentrations above 1 km (Figure 4.3A). However, the decrease of degradation rate, which results from the change in temperature and RH during air mass rising (see temperature and RH distribution in Figure J.3), is not accounted for. Even when BaP is able to escape out of the boundary layer by large-scale advections associated with cyclones or by convections in mid-latitudes (that is, 35°N to 45°N), fast degradation limits dispersion and transport of BaP to the vicinity of the source region. Thus, the transport of BaP with the Kwamena scheme is constrained within the boundary layer, and the long-range transport impacts are limited.

The ROI-T scheme shows a different spatial distribution and transport pathway of BaP, with more BaP distributed at higher altitude. This is because low temperature reduces OA diffusivity and reaction rate of BaP with ROI ["freezing effect"; see three-dimensional (3D) degradation rate k in Figure J.2] and thus leads to a much longer lifetime of BaP above 1 km ($\sim$2 to 3 hours to more than 20 days; Figure J.2), making transport in the free troposphere an efficient pathway. Compared with the Kwamena scheme, 15 times more BaP is lifted by frontal activities and convection to the middle troposphere, where strong westerlies/jets cause a fast transport of the plumes to downwind areas (Figures J.5 and J.6 and Section J.2) and toward the polar region, resulting in much stronger global impacts. At the cross section of 126°E (Figure 4.3, A and B), the BaP outflow toward the ocean shows a maximum zonal net flux of $\sim$35 ng m^{-2} s^{-1} in the ROI-T scheme but only $\sim$10 ng m^{-2} s^{-1} in the Kwamena scheme (Figure J.4, A and B). It is also clear that the vertical center of the BaP column mass in the ROI-T scheme is higher than that in the Kwamena scheme, that is, $\sim$0.6 km and 0.3 km, respectively (Figure J.4, C and D).

4.3.4 Transport to the Arctic

BaP emitted in source regions can undergo intercontinental transport, allowing them to distribute and accumulate even in the polar regions (Halsall et al., 1997; Hoyau et al., 1996). The concentration level of BaP in the Arctic arouses high interest, because BaP is not only a good indicator of human contamination (Hoyau et al., 1996) but also responsible for the severe bioconcentrate effect in the Arctic (Macdonald and Bewers, 1996) where the ecosystem is most vulnerable, bioaccumulation along marine and terrestrial food chains (Macdonald and Bewers, 1996; Achazi Rudolf and Van Gestel Cornelis, 2003; Meador et al., 1995). As shown in the East Asia outflow case, the "freezing effect" may make the intercontinental transport of BaP from source regions to the Arctic at high-altitude or low-temperature region more efficient than previously thought.

As shown in Figure 4.3 (C and D), BaP in the Arctic is mainly transported from Europe, North America and Asia, similar to long-lived halogenated pollutants (Octaviani et al., 2015). The 2007−2009 average total meridional net flux of BaP toward the Arctic (integrated over 1000 to 10 hPa at 65°N) is 1.97 ng m^{-2} s^{-1} with the ROI-T scheme, but only 0.12 ng m^{-2} s^{-1} with the Kwamena scheme (Figure J.4E), which is about 16 times lower. The larger fluxes of BaP with the ROI-T scheme can be attributed to a longer lifetime of BaP caused by the "freezing effect" (Figure J.2), as the pollutant is transported significantly higher. The average vertical center of the BaP column mass transported across 65°N during 2007−2009 is 2 km for

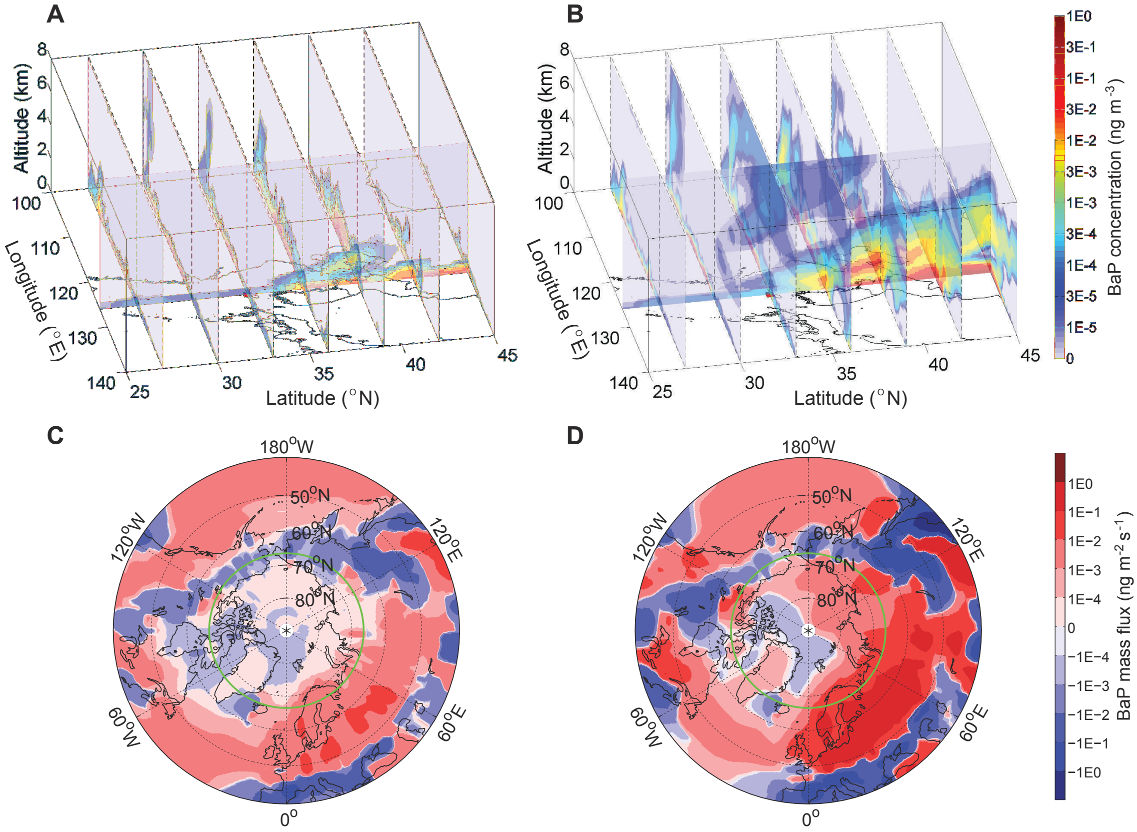

Figure 4.3: Implications on the transports. Average concentrations of BaP (ng m^{-3}) in a strong East Asia outflow episode on 24 February 2003 are shown for the (A) Kwamena scheme and the (B) ROI-T scheme. Longitude cross section locates at 126°E. BaP net meridional mass flux (ng m^{-2} s^{-1}) averaged over the years 2007−2009 are shown for the (C) Kwamena scheme and the (D) ROI-T scheme[3]. Northward has positive values (red), and southward has negative values (blue). Green circle marks the Arctic Circle at 66.5°N.

---

[3] The mean BaP net meridional mass fluxes for the Pöschl and Kahan schemes are shown in Figure K.3.

the ROI-T scheme but only 0.5 km for the Kwamena scheme (Figure J.4F), showing a more prominent difference in height than that in the East Asian outflow case.

4.4 Discussion

The strong temperature/RH effects on fate and global transport of BaP advance the understanding and challenge the traditional view of modeling the multiphase degradation of reactive pollutants (such as BaP) in OAs. In warm/humid environments (for example, tropical rainforests), aerosol particles tend to be liquid, whereas in cold environments, aerosols are found to be in an amorphous solid phase, most probably glassy state (Shiraiwa et al., 2017). The phase state and degradation rate of BaP may vary largely depending on temperature/RH and hence the season (summer vs. winter), altitude (surface vs. high altitude) and latitude (tropical vs. polar) (Figure 4.4). It also emphasizes the importance of higher altitude or cold season/region pathway for the long-range transport, that is, the low temperature helps OA and reactive compounds within it survive from the multiphase chemistry, remaining undegraded and being transported further.

The ROI-T scheme is based on the kinetic data observed on the ozonolysis of BaP coated by α-pinene SOA. Recent studies have revealed that α-pinene SOA is less viscous than aromatic SOA and is more viscous than isoprene SOA (Berkemeier et al., 2014; Song et al., 2015). SOA particles are also often internally mixed with inorganic components, which may affect particle phase state, non-ideal mixing and morphology and hence the multiphase reaction rates (Shiraiwa et al., 2013). Therefore, the effects of different SOA precursors and inorganic interactions should be further explored. Partitioning of PAHs to other OAs, such as bioparticles, is less efficient than partitioning to liquid and semisolid SOA (Shahpoury et al., 2016). The presence of more viscous bioparticles will lead to less reactive PAHs and therefore an even higher long-range transport potential.

The large impact of temperature/RH on the diffusivity/reactivity is not limited to the degradation of BaP but has general implications for all kinds of multiphase reactions in aerosols, clouds, and fog droplets relevant for atmospheric chemistry and transport (Shiraiwa et al., 2011a, 2017; Cheng et al., 2015, 2016). The impact is particularly important for the northern hemisphere where efficient large-scale advection/convection associated with cyclones and strongest anthropogenic emissions exist. Our results demonstrate that it is important to perform laboratory kinetic studies on the large temperature/RH span relevant for atmospheric conditions. Our modeling scheme provides an advanced physicochemical-based framework for the representation of multiphase reaction in atmospheric models and can be readily modified to include other hazardous air pollutants and OA species once the kinetic data are available.

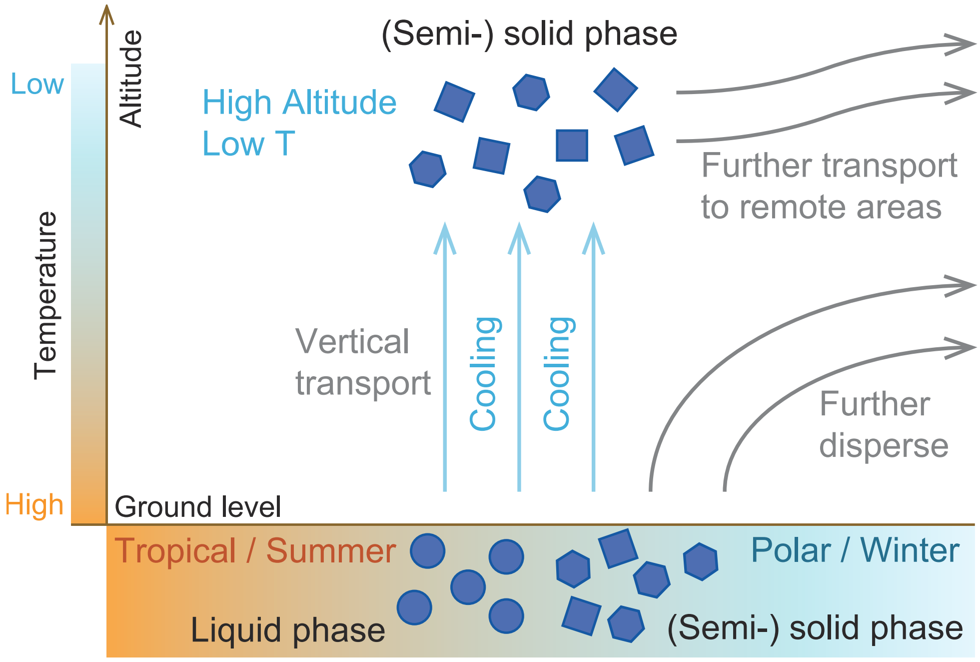

Figure 4.4: Diagram of temperature/RH effects on BaP transport in ambient air. OA diffusivity and chemical reactivity are both reduced in response to changes in season (summer to winter), latitude (tropical to polar), and altitude (surface to high altitude), when OA phase state also changes from liquid to (semi-) solid phase. With a slower degradation rate and hence prolonged lifetime, BaP can be further dispersed and transported.

Chapter 5
Summary and Outlook

This doctoral study aims to investigate the global transport and chemistry of SOCs, specifically those defined as persistent organic pollutants, by means of dynamical multi-compartment models. The first part of the study focused on investigating the influence of a changing climate on the meridional transport of DDT and PCBs and their correlations with AO and NAO. The MPI-MCTM model was used and run for a continuous long-term period to cover the present-day (1970−1999) and future (2070−2099) climates. Regions of import and export maxima into the Arctic are identified along the Arctic Circle. It is found that the net export of PCB153 out of the Arctic will increase under future climate conditions. The meridional net flux pattern of this substance is expected to become independent of AO and NAO. For DDT, a trend of decreasing net Arctic import will reverse to an increasing trend 100 years after peak emission, which is partly due to more frequent AO and NAO positive phases. It is concluded that the long-term accumulation trends in the Arctic of other persistent pollutants, including so-called emerging pollutants, are subject to the substances' specific behavior and fate in the environment and need to be studied specifically.[1]

The second part of the study is devoted to the development of SVOC submodel for extending the EMAC model application to SOC simulation. The EMAC-SVOC model herein includes more up-to-date physics parameterizations compared to their predecessors (including MPI-MCTM). It also offers flexible complexities of model configuration and facilitates a continuous improvement through its straightforward modeling framework and coding technique. In this first development, the focus was set on the predictions of four PAHs (PHE, PYR, FLT, and BaP). The initial model application was aimed to test some novel features (or factors) in PAH modeling efforts, including seasonality in emissions, the *modal* scheme for particle representation, the ppLFER scheme for gas−particle partitioning, and volatilization from ocean, land, vegetation, and snow surfaces. In order to understand how these factors influence the simulated near-surface concentrations and model performance, the factor separation technique was applied to isolate the individual effects of each factor and the nonlinear interactions among the different factors.

Results indicate that using seasonal emission acts to increase PAH concentrations in winter and to decrease them in summer, particularly over temperate and polar regions. These lead

---

[1] This paragraph contains an excerpt from the abstract of Octaviani et al. (2015).

to improved model biases in predicted PHE concentrations. The simulations, where the size of PAH particles was discretized into series of lognormal modes, yield smaller concentrations compared to those that applied the default *bulk* representation. However, the differences are only apparent for semi and less volatile PAHs. The effects of the ppLFER scheme are likely to increase the concentrations of PYR and FLT and to decrease the BaP concentrations but are of less significance for PHE. Revolatilization process has an overall positive influence on concentrations, particularly during summer, that results in a pronounced overestimation in the predicted PYR and FLT concentrations.

The effects of interactions could reinforce (hence, positive feedback) or suppress (hence, negative feedback) each factor's effects. One example of a negative feedback is seen from the interactions between seasonal emission and other factors which contribute to a concentration change in the opposite direction to the respective pure contribution. In contrast, the combined effects from the *modal* scheme interactions work to amplify the negative signal of its direct effects. The ppLFER scheme interactions do not show a consistent concentration response but the degree of contribution exceeds that of the pure contribution. The effects from volatilization interactions point toward a concentration decrease for BaP (negative feedback) yet a general increase for other species (positive feedback).

In a model configuration where all the new features were taken into account, the comparison of simulation results against observation data indicates the following. For near-surface concentrations, the model is able to capture observed seasonality although it generally overestimates the seasonal amplitude (maximum to minimum). In terms of magnitude, model bias varies by region and/or species, being negative (positive) in the Arctic for PHE and BaP (PYR and FLT), positive in the northern mid-latitudes for most species but BaP, and negative in the Tropics. The model also suffers from negative biases for marine boundary layer air concentrations, substantially over remote marine areas. With regard to particulate mass fraction (θ), the model adequately reproduces observed seasonal variation but the predictions of θ for high-to-medium volatility species are lower than the observations.

The above findings revealed that the model produces a systematic underestimation of BaP concentrations, particularly over regions away from sources. This species in the atmosphere is mainly sorbed to particulate matter and degraded through a multiphase reaction with O_3. Earlier modeling studies used reaction rate coefficients determined in laboratory experiments at room temperature, which may overestimate/underestimate degradation rates when applied under atmospheric conditions. Moreover, the effects of diffusion in the particle bulk are neglected, leading to large discrepancies between model results and observations. The last part of this thesis is aimed to study how regional and global distributions and transport of BaP can be explained by a new kinetic scheme that provides a realistic description of the temperature and humidity dependence of phase state, diffusivity, and reactivity of BaP-containing particles. Low temperature and humidity can substantially increase the lifetime of BaP and enhance its atmospheric dispersion through both the planetary boundary layer and the free troposphere. The new scheme (ROI-T) greatly improves the performance of multiscale models, leading to a better agreement with observed BaP concentrations in both source regions and remote regions (Arctic), which cannot be achieved by less-elaborate degradation schemes (deviations by multiple orders of magnitude). The results highlight the importance of considering temperature and humidity effects on both the phase state of aerosol particles and the chemical reactivity of particulate air pollutants. The ROI-T scheme can be readily modified to include other organic aerosol species once kinetic data from laboratory studies are available.[2]

The EMAC-SVOC applications have currently been limited to the simulations of a few PAH species. A follow-up study is underway to address global characteristics of the four PAHs (compartmental distributions, persistence, and long-range transport potential) and source−receptor relationships. A brief description and selected preliminary results are presented in Appendix L. Further investigations may study secondary PAHs that are formed by the oxidation of their parent species. More pronounced adverse health effects may be attributed to the first-generation products, e.g., some nitro-PAHs and oxy-PAHs, than to their precursors. Other groups of SOCs with similar or distinct range of volatility and degradability from PAHs, e.g., PBDE, PCDD/Fs, and other emerging pollutants, also remain an important area of future research. Nevertheless, modeling the PAH derivatives and other SOC species could be heavily constrained by the availability of input data on atmospheric chemistry and emissions.

Further improvements to modeling SOCs by EMAC-SVOC could be achieved in several ways depending on future needs. For instance, the coupling of EMAC-SVOC with a 3D dynamical ocean model and a marine biogeochemistry module is important to study the long-term effects of persistent compounds since the present application does not allow for horizontal and vertical transports in the deep ocean. For the same reason, contaminant remobilization within soil, sea-ice, and inland ice should also be incorporated. To study the size distribution of particulate-phase PAHs, aerosol microphysics needs to be taken into account along with emissions and removal processes. This can be done by integrating these tracers into the aerosol submodel GMXe (Pringle et al., 2010). Doing so will also resolve the issue of BC-dependent wet removal rate (see Section 3.3.5 of Chapter 3). In the current parameterization, the wet scavenging of particle-bound PAHs was calculated under an assumption that BC is the dominant sorbent. Accounting for other strong sorbents (e.g., OM) would be reflected in a change of the PAH deposition rate.

In order to improve predictions of θ, the model should consider the diffusion limitation of the particulate-phase SOCs to repartition into the gas phase. At present, the treatment of gas−particle partitioning in EMAC-SVOC relies on a reversible equilibrium assumption within each time step. Friedman et al. (2014) compared the instantaneous gas−particle equilibrium with a configuration where PAHs are trapped within primary OM/BC aerosols upon emissions and subsequently slowly evaporated. The former underpredicts PYR particulate mass fraction (as is the case in this study) whereas the latter gives the best agreement between observed and simulated results. In addition, Zelenyuk et al. (2012) suggested, based on their experimental data, that when PAHs are trapped inside the bulk of secondary organic aerosols (SOA) during particle formation and growth, they evaporate at least one order of magnitude slower than those predicted by equilibrium-based partitioning models.

---

[2] This paragraph contains an excerpt from the abstract of Mu et al. (2018).

Finally, it is noteworthy that the model simulations have neglected the formation of SOA in the atmosphere, leading to the underestimation of overall OA atmospheric burden. There is a need for describing SOA in modeling SOCs as they play an important role in the predictions of phase partitioning and heterogeneous oxidations (such as the BaP$-$O$_3$ reaction in Chapter 4). A recent MESSy submodel ORACLE has been dedicated for the simulations of SOA (Tsimpidi et al., 2014) based on lumping organic species in logarithmically-spaced volatility bins. ORACLE is an efficient MESSy submodel to describe the composition and evolution of SOA in the atmosphere. It takes into account the SOA formation from the condensation of volatile organic compound (VOC) oxidation products and from semivolatile compounds, as well as the gas$-$particle partitioning processes and photochemical aging reactions. Accordingly, this submodel should be coupled to EMAC-SVOC in order to better resolve gas$-$particle distributions of SOCs.

Appendix A
POP Simulations with MPI-MCTM: Process Parameterizations, Input Data and Model Evaluation

A.1 Parameterizations of POP Cycling

Persistent Organic Pollutants (POPs) are cycling in the atmosphere, ocean, soil, vegetation, and land snow. Cycling processes include phase partitioning, mass exchange, and degradation. These parameterizations were presented and described in Semeena et al. (2006), Guglielmo et al. (2009), and Hofmann et al. (2012).

Atmosphere

Gas−particle partitioning is parameterized using the octanol−air partition coefficient (K_{oa}) according to Finizio et al. (1997). Chemical degradation is controlled by reaction with OH during daytime and $\mathrm{NO_3}$ during nighttime. The reaction rate constants, k_{OH} and $k_{\mathrm{NO_3}}$, are temperature dependent and are formulated following the Aarhenius equation. Dry deposition flux is calculated using the concentration in the lowest atmospheric layer and dry deposition velocity (v_d). v_d of gaseous species follows the "big-leaf" approach (Hicks et al., 1987) with a series of resistances for different surface types (Ganzeveld and Lelieveld, 1995), whereas a v_d model adopted in Ganzeveld et al. (1998) is used for particulate phase. The scavenging of gaseous substances is based on the fraction of the total substance dissolved in cloud water, which is derived from Henry's law (Seinfeld and Pandis, 1998). Wet deposition for particles is based on a composition-dependent scavenging coefficient (solubility).

Ocean

The phases in seawater systems are a bulk water phase and four organic phases, that is, sinking and colloidal detritus, phytoplankton, and zooplankton. The fractions of chemicals sorbed to the organic phases are a function of the amount of organic matter associated with each phase and calculated from the organic carbon partitioning coefficient (K_{oc}) which is estimated from the octanol−water partitioning coefficient (K_{ow}) (Ilyina et al., 2013). Air−sea gas exchange is assumed to follow a fugacity-based approach as in Mackay (2010). Chemical degradation and microbial decay are described as a first-order decay law and double per 10 K of temperature increase. In addition to advection and diffusion, particulate substances are subject to gravitational settling.

Soil and vegetation

The soil is represented in a single layer. Partitioning of POPs in top soils between organic matter, pore air, and pore water is described according to Smit et al. (1997). Volatilization from soil and vegetation is parameterized based on saturation vapor pressure and water solubility (Smit et al., 1997, 1998). Biological and chemical degradations are described as a first-order process and assumed to double per 10 K of temperature increase. Degradation in vegetation uses the same rate coefficient as in soil.

Land snow

Gaseous POPs entry into falling snow through in-cloud and below-cloud scavenging based on the air−water partition coefficient (K_{aw}, gas). Particulate-phase POPs entry following a fixed scavenging ratio ($W_p = 1\times10^{-4}$ for rain and 5×10^{-3} for snowfall). In the gaseous dry deposition, the surface resistance for snow depends on the ice−air interfacial partitioning coefficient (K_{ia}) (Wania, 1997). A fugacity-based parameterization (Wania, 1997) is adopted for volatilization, but substances are first partitioned among three snow pack components, namely, ice−air interface, liquid inner water, and air in pore space (Hoff et al., 1995). Substance loss due to melting is considered as a function of snow covered area fraction.

A.2 Substance properties and emissions

The following emission inventories were used as input. DDT emissions from 1950 to 1990 were based on the annual application in agriculture compiled by Semeena and Lammel (2003). The data were derived from country reports made available by the UN Food and Agricultural Organization (FAO) and they were distributed to a 1°×1° grid resolution using global cropland information. For the period 1990−2020, country-wise emissions were developed via linear interpolation based on annual estimates of amounts applied in public health programs in 2000−2010 (Pacyna et al., 2010), and were scaled to a 1°×1° population grid. Primary DDT emissions were set to zero beyond 2010. PCB28 and PCB153 emissions for 1950−2100 were taken as identical employing the 1°-resolution emission inventory of PCB153 from Breivik et al. (2007). All the emission data were re-gridded onto the model grid (that is, T31). The temporal evolution of emissions during 1970−1999 reflects a decline in primary emissions, most pronounced during the 1970s for DDT and 1980s for PCBs.

Table A.1: Physicochemical properties of selected substances

Property	Unit	DDT	PCB153	PCB28
Saturation vapor pressure (P_{sat})	Pa	2.5×10^{-5}(a,c)	1.01×10^{-4}(b,d)	1.306×10^{-2}(b,d)
Water solubility at 298 K (C_w^s)	g L^{-1}	0.149(d)	1.11×10^{-3}(d)	0.23(d)
Enthalpy of vaporization (ΔH_{vap})	kJ mol−1	118(e)	103.5(f)	89.3(g)
Enthalpy of solution (ΔH_{soln})	kJ mol^{-1}	27(e)	27(e)	27(e)
Octanol−air partition coefficient ($\log K_{\mathrm{oa}}$) at 298 K	-	9.73(h)	9.44(i)	8.06(i)
OH gas-phase rate coefficient ($k_{\mathrm{OH}}^{(2)}$) at 298 K	10^{-12} cm^3 molec^{-1} s^{-1}	0.5(e)	0.164(j)	1.06(j)
OH particulate-phase rate coefficient ($k_{\mathrm{OH,het}}^{(2)}$)	10^{-12} cm^3 molec^{-1} s^{-1}	0(e)	0(e)	0(e)
$\frac{\Delta E_a}{R}$ of OH reaction	K^{-1}	−1300(e)	−1400(e)	−800(e)
Degradation rate constant in soil (k_{soil})	s^{-1}	4.05×10^{-9}(c)	3.50×10^{-10}(k)	1.93×10^{-8}(k)

(a)at 293 K; (b)at 298 K; (c)Hornsby et al. (1996); (d)Li et al. (2003); (e)estimated; (f)Puri et al. (2001); (g)Puri et al. (2002); (h)Shen and Wania (2005); (i)$K_{\mathrm{oa}} = \frac{K_{\mathrm{ow}}}{K_{\mathrm{aw}}}$ from Li et al. (2003), K_{aw} is based on C_w^s and P_{sat}; (j)Anderson and Hites (1996); (k)adopted from Wania and Daly (2002).

Table A.2: Observed minimum− maximum atmospheric concentrations (pg m^{-3}) of POPs for 1993−1999 and (in brackets) their seasonal variations at the Arctic stations Alert (AL), Storhofdi (ST), Zeppelin (ZE), and Pallas (PA). Seasonal variation is defined as the concentration ratio $\frac{C_{\mathrm{JJA}}}{C_{\mathrm{DJF}}}$. NA = no data available.

Station	DDT[a]	PCB153[b]	PCB28[c]
AL	0.1−0.2 (2.0−5.5)	0.1−0.4 (2.2−11.0)	NA
ST	0.4−1.1 (1.5−5.3)	0.1−0.7 (2.5−27.0)	0.1−1.0 (NA)
ZE	0.2−0.9 (1.5−15.0)	0.3−1.8 (4.5−7.3)	1.0−15.0 (6.0−10.0)
PA	0.1−0.4 (1.6−12.0)	0.2−0.9 (2.2−6.5)	NA

[a] Observed data based on Figure 4d of Hung et al. (2010), temporal coverage varies by station

[b] Observed data based on Figure 3c of Hung et al. (2010), temporal coverage varies by station

[c] Observed data based on Figure S6 of Lamon et al. (2009b), for 1998−1999

A.3 Model evaluation

Meridional winds

While a comprehensive evaluation of the model performance is not part of our main objectives (see in-depth studies: Hagemann et al. (2013), Notz et al. (2013), and references therein), we attempted to examine the model's ability to simulate the associations between meridional winds at 850 hPa and the SLP based indices prior to the analysis. The National Centers for Environmental Prediction−National Center for Atmospheric Research (NCEP−NCAR) meteorological reanalysis dataset (Kalnay et al., 1996) was used to validate the model predictions for present-day climate. The results are presented in Figures A.1−A.2. In terms of correlations with AOI (Figure A.1a,c), the model agrees reasonably well with the reanalysis, and the regression coefficients (Figure A.1b,d) are consistent with the patterns of correlations. The correlations with NAOI and their regression coefficients (Figure A.2a−d) also show similar patterns and amplitudes of both datasets, except in some parts of Canada and Siberia where the model fails to simulate negative correlations over the Canadian Arctic and positive correlations over Siberia. Also, negative correlations in the Gulf of Alaska are overestimated. Despite the presence of biases in the simulated results, the overall findings confirm the suitability of the model for the evaluation of the relation between F_{net} variability and the two large-scale climate indices.

Atmospheric concentrations

The model results of near-ground concentrations (Figure S3) are compared against observation data reported in the literature (Hung et al., 2010; Lamon et al., 2009b) (Table A.2) for four monitoring stations: Alert, Canada (AL; 62.3°W, 82.5°N); Storhofdi, Iceland (ST; 20.3°W, 63.4°N); Zeppelin, Svalbard (ZE; 11.9°E, 78.9°N); and Pallas, Finland (PA; 24.3°E, 68.0°N), averaged for 1993−1999. Simulated concentrations exceed the observations by typically a factor of 3−10, even higher for DDT. The seasonality tends to be underestimated for DDT, whereas for PCBs the model captures seasonality relatively well at AL and slightly underestimates the observed concentrations at the stations in the European Arctic (ST, ZE, and PA). Becker et al. (2008) reported that POP concentration's seasonality is less pronounced in AO+ phases compared to AO− phases. The years 1993−1999 were mostly under AO+, but the simulated years were equally under AO+ and AO−. For this study (Chapter 2), there is no direct basis for the climate index comparison as our simulation is not nudged with reanalysis data. Therefore, modeled AO phases are not in phase with historic AO.

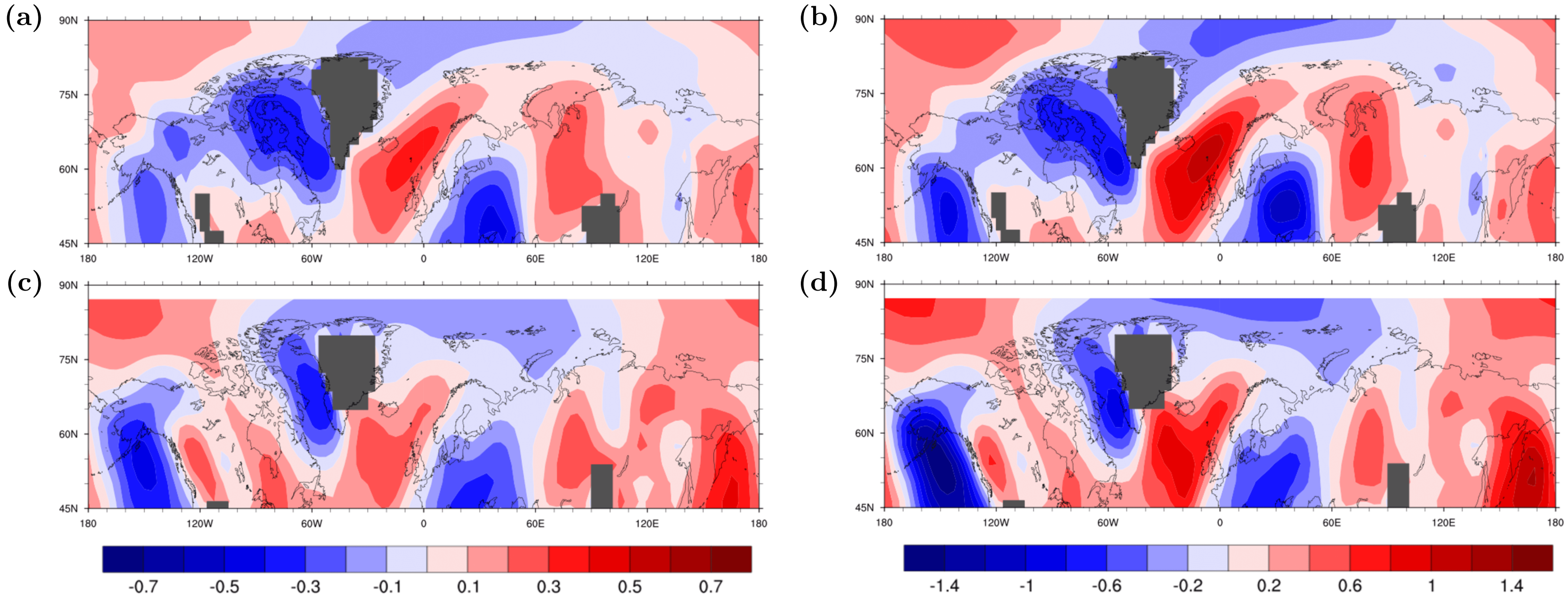

Figure A.1: (a,c) Correlations and (b,d) regression coefficients for meridional wind component at 850 hPa versus the Arctic Oscillation Index (AOI) from (a,b) NCEP-NCAR reanalysis and (c,d) MPI-MCTM simulation. Monthly data, 1970–1999.

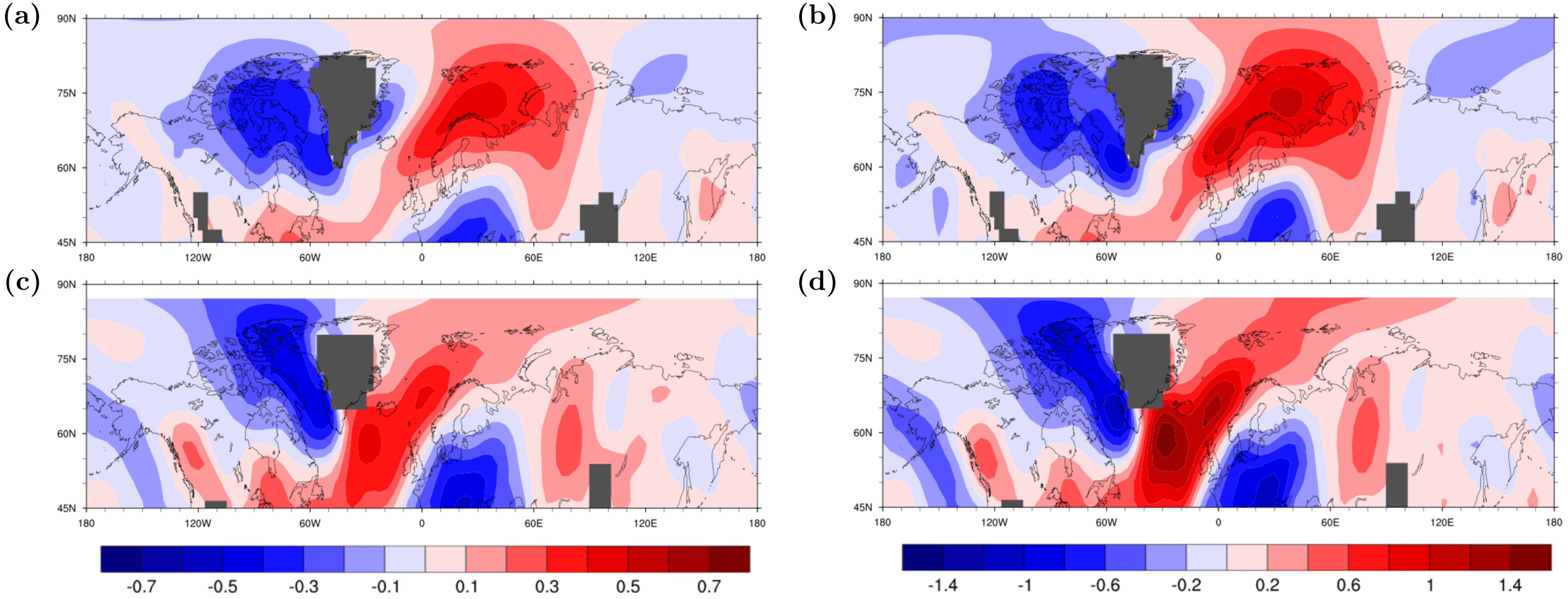

Figure A.2: Same as Figure A.1, but for meridional wind component at 850 hPa versus the North Atlantic Oscillation Index (NAOI)

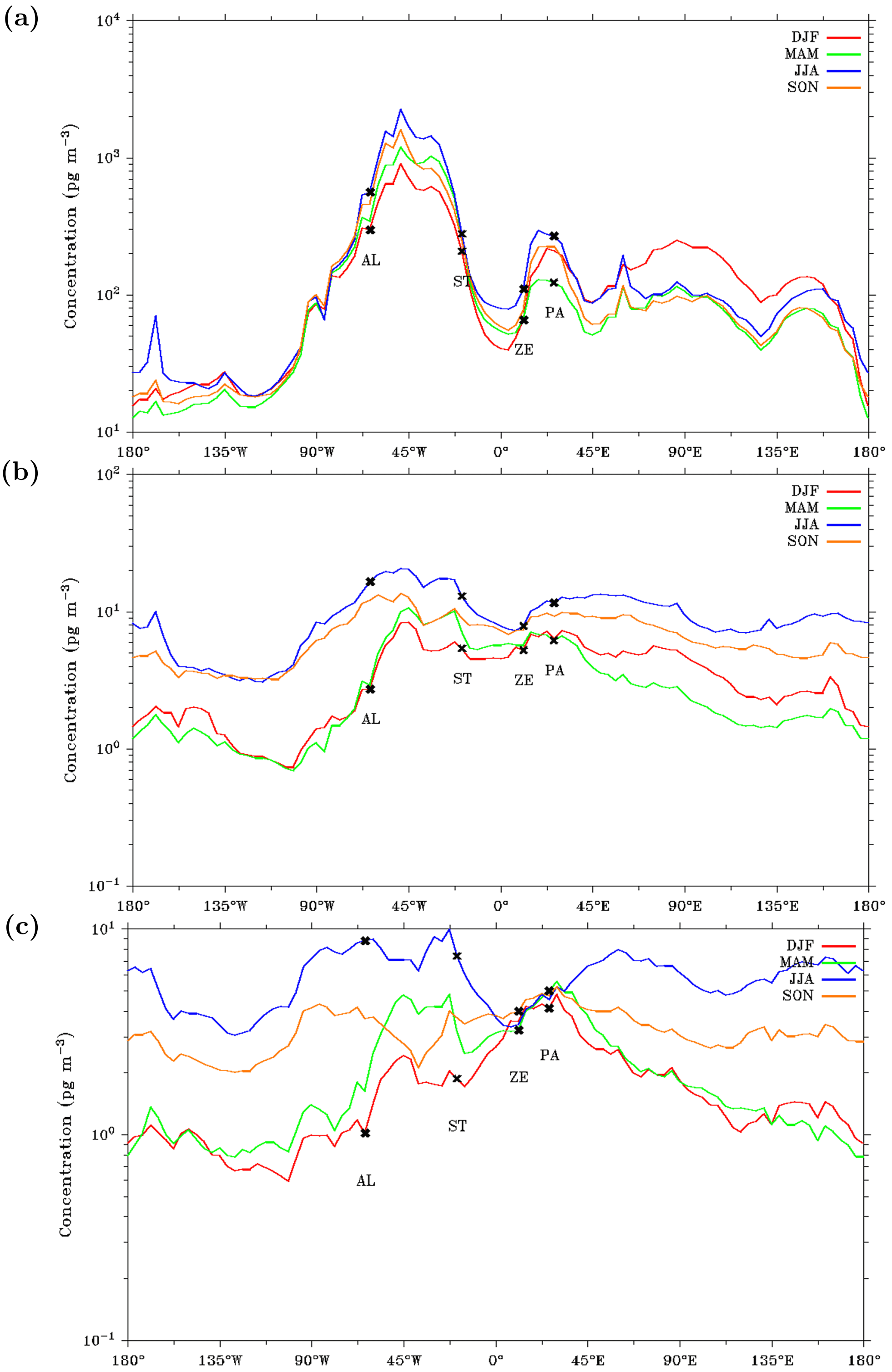

Figure A.3: Longitudinal profile of seasonal mean concentrations (pg m^{-3}) of (a) DDT, (b) PCB153, and (c) PCB28 around the polar circle (60°–80°N), averaged for 1993–1999. Asterisks denote the minimum and maximum predicted concentrations at the stations Alert (AL), Storhofdi (ST), Zeppelin (ZE), and Pallas (PA).

Appendix B
POP Simulations with MPI-MCTM: Additional Results from Meridional Transport Analysis

Table B.1: Compartmental burden (tonnes, 30-year means) of DDT, PCB153, and PCB28 in the Arctic

		Burden (tonnes)			
Substance	**Period**	**Atmosphere**	**Soil**	**Vegetation**	**Ocean & sea ice**
DDT	1970–1999	1.10×10^{2}	8.60×10^{4}	3.31×10^{3}	7.12×10^{4}
	2070–2099	1.85	1.73×10^{3}	1.09×10^{1}	3.60×10^{4}
PCB153	1970–1999	8.52×10^{-1}	2.02×10^{2}	5.90	3.38×10^{1}
	2070–2099	5.41×10^{-2}	2.45×10^{2}	1.51×10^{-1}	3.23
PCB28	1970–1999	5.46×10^{-1}	1.06×10^{1}	2.91	3.81
	2070–2099	3.91×10^{-5}	4.00×10^{-4}	7.64×10^{-5}	1.20×10^{-4}

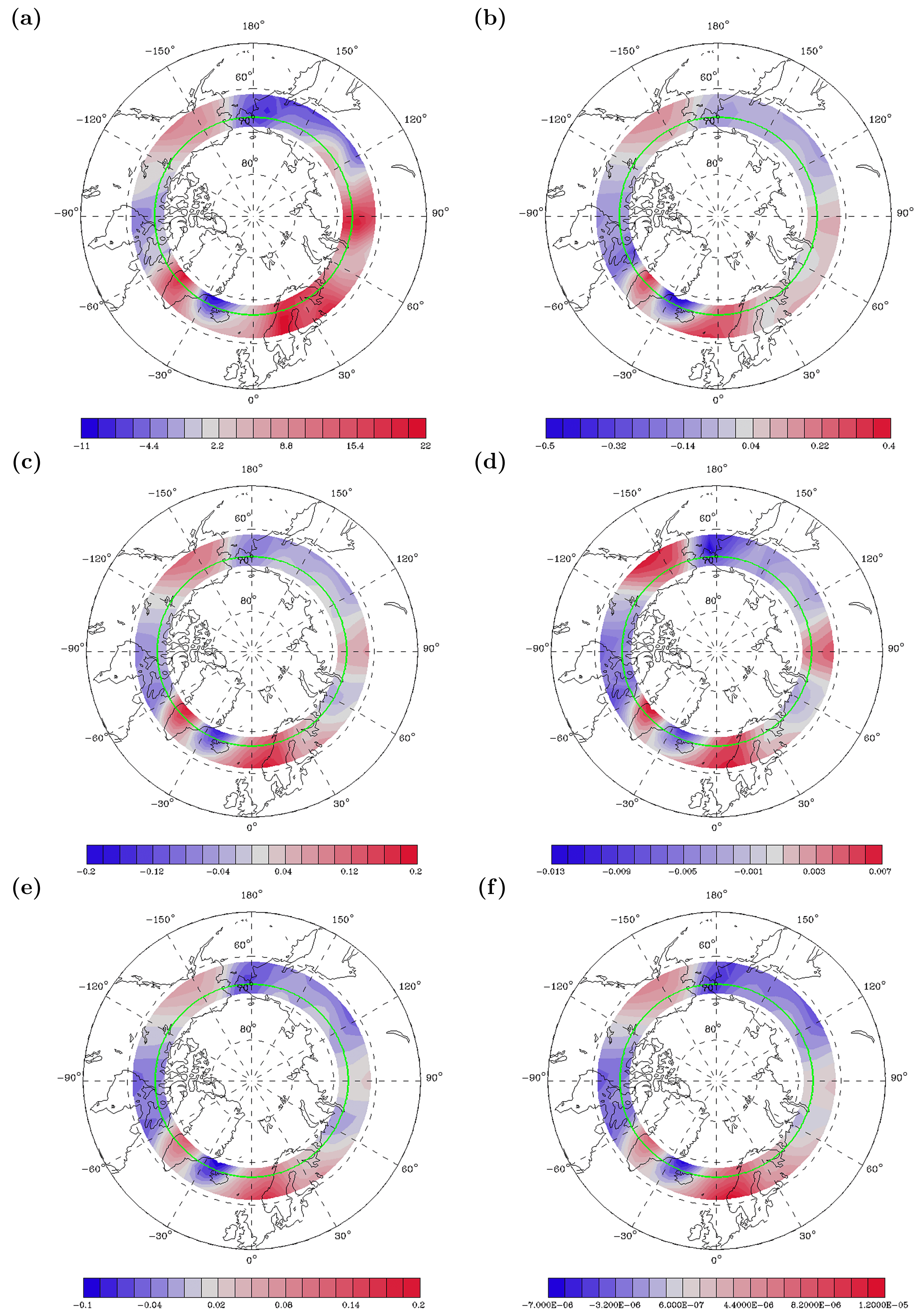

Figure B.1: Simulated annual mean net meridional mass flux F_{net} (ng m^{-2} s^{-1}) of (a,b) DDT, (c,d) PCB153, and (e,f) PCB28 close to the polar circle (60°−70°N) for (a,c,e) 1970−1999 and (b,d,f) 2070−2099. Green line shows the Arctic Circle.

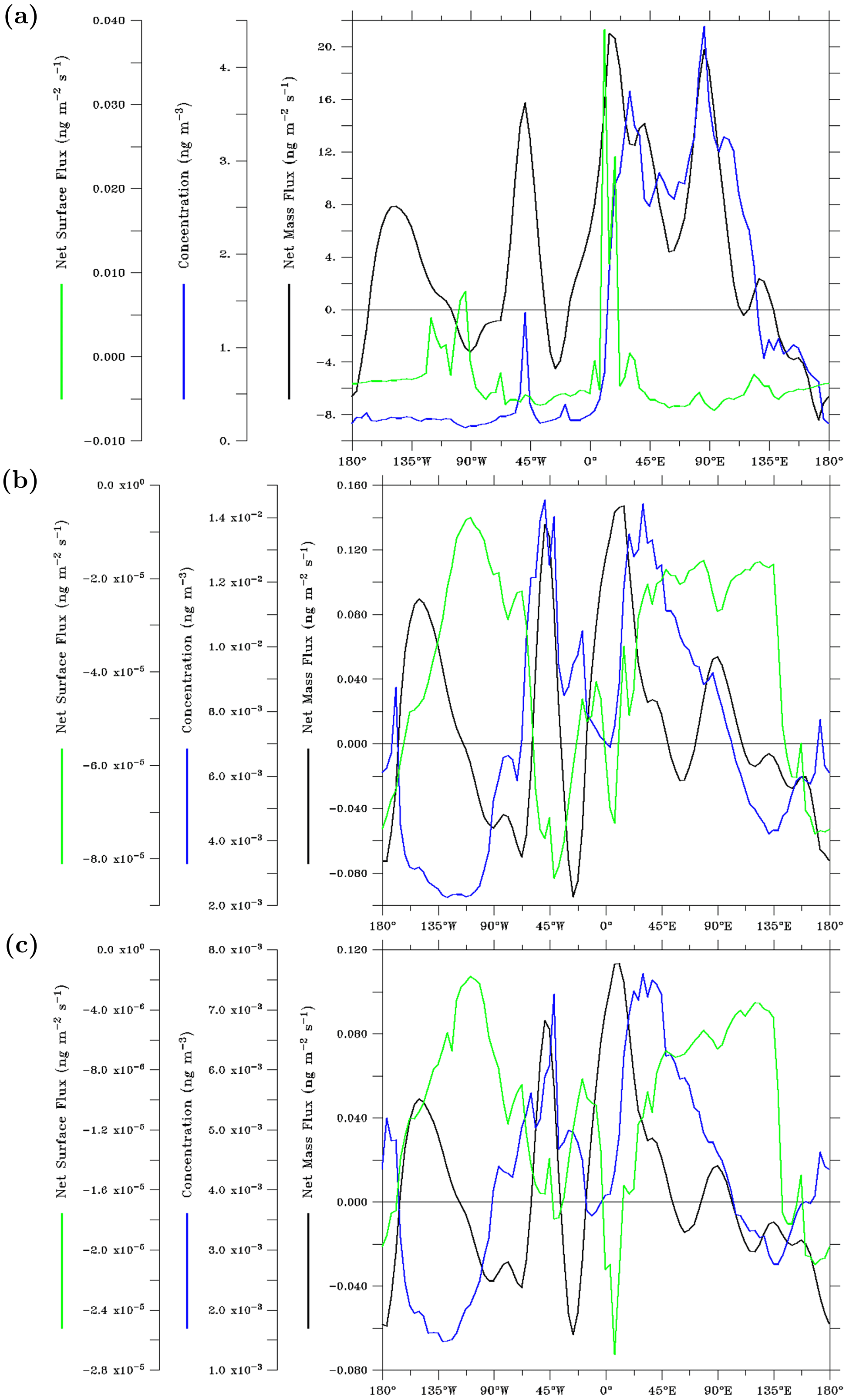

Figure B.2: Annual mean of net meridional mass flux F_{net} (black, ng m^{-2} s^{-1}) at 65°N, low-level concentration (blue, ng m^{-3}) at 65°N, and net surface flux $F_{\text{net,surf}}$ (green, ng m^{-2} s^{-1}) over 45°–65°N for (a) DDT, (c) PCB153, and (e) PCB28; mean of 1970–1999.

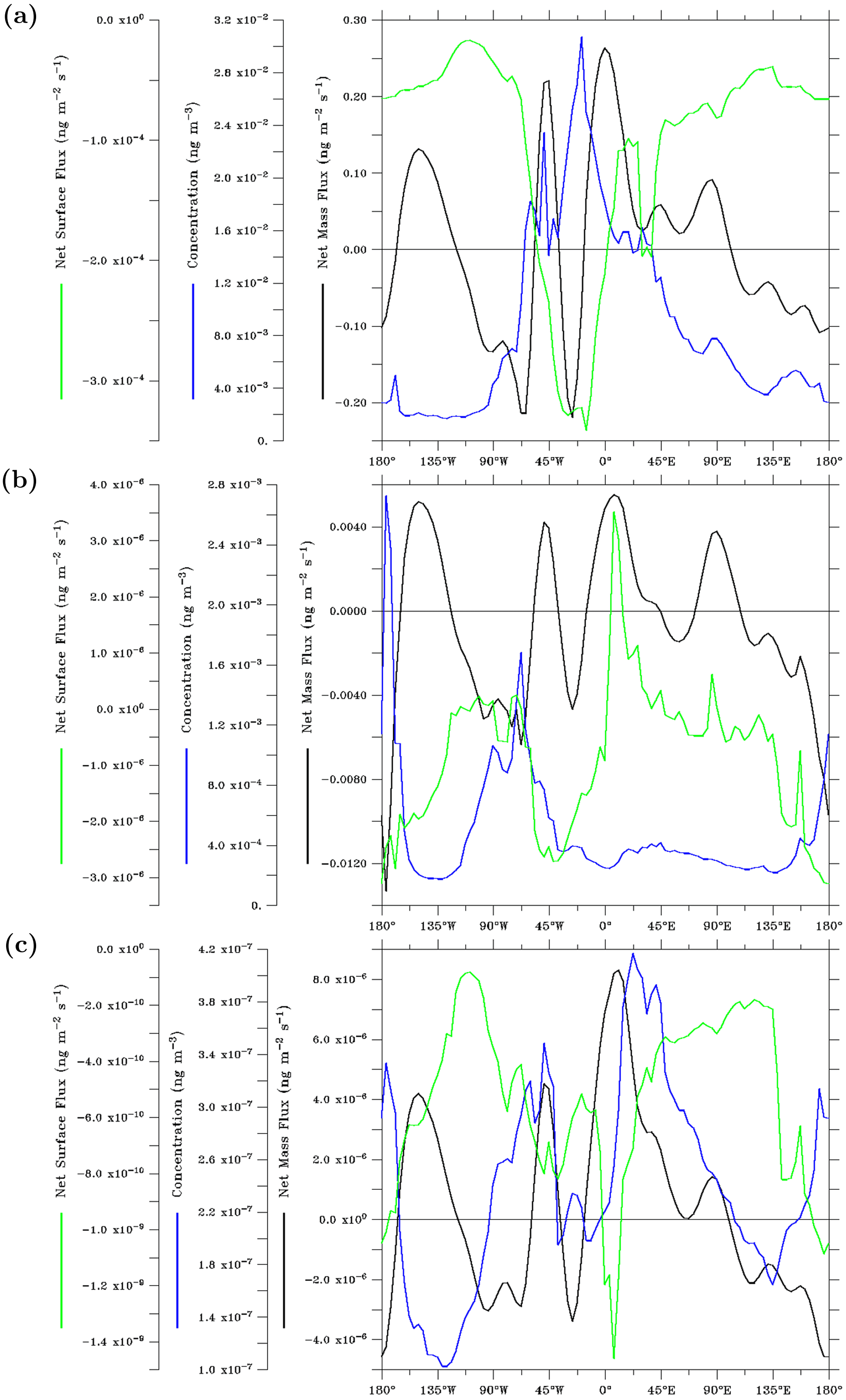

Figure B.3: Same as Figure B.2, but for mean of 2070−2099

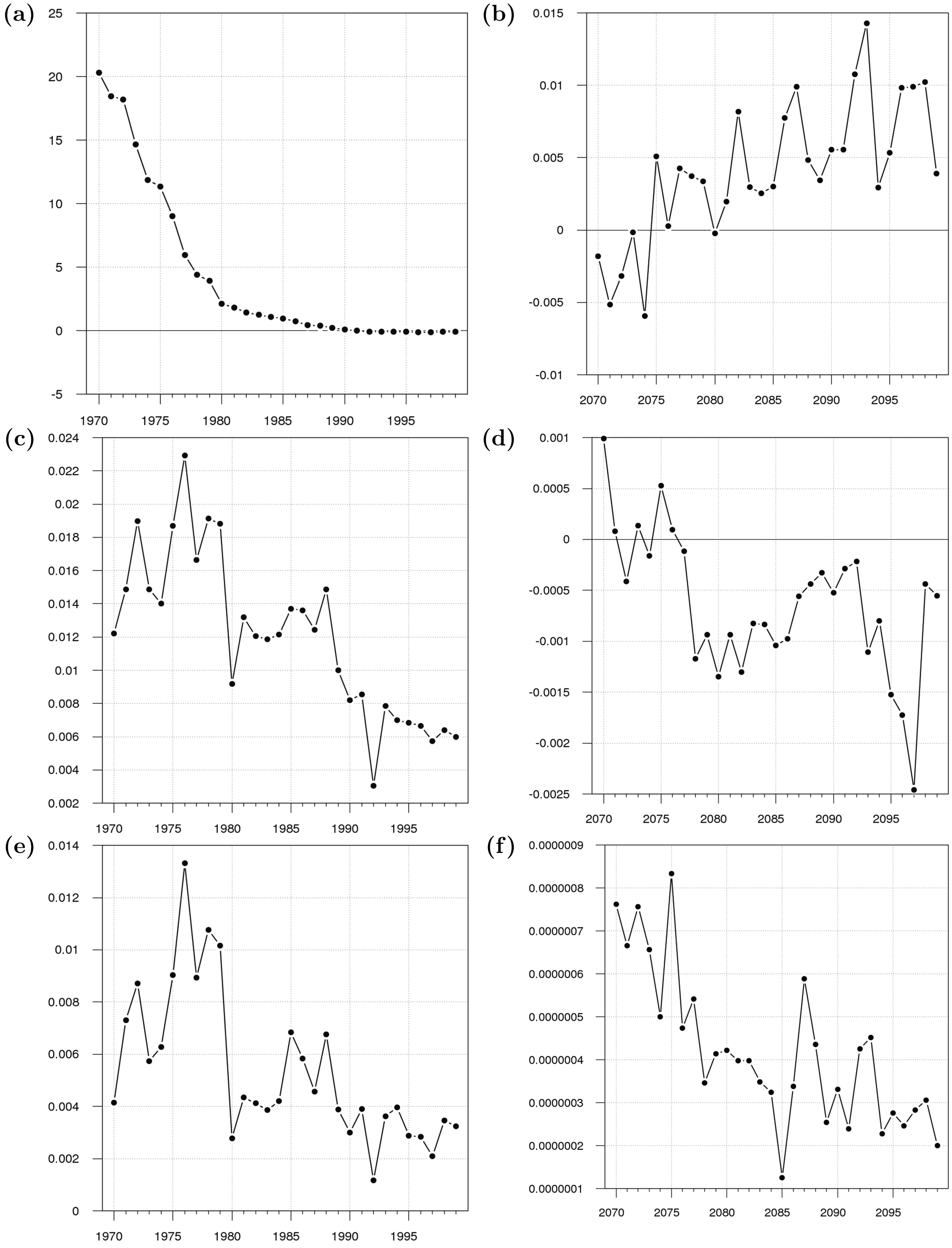

Figure B.4: Annual series of (KZ-filtered) net meridional mass flux F_{net} (ng m^{-2} s^{-1}) across 65°N, 0°−360°E of (a,b) DDT, (c,d) PCB153, and (e,f) PCB28 for (a,c,e) 1970−1999 and (b,d,f) 2070−2099.

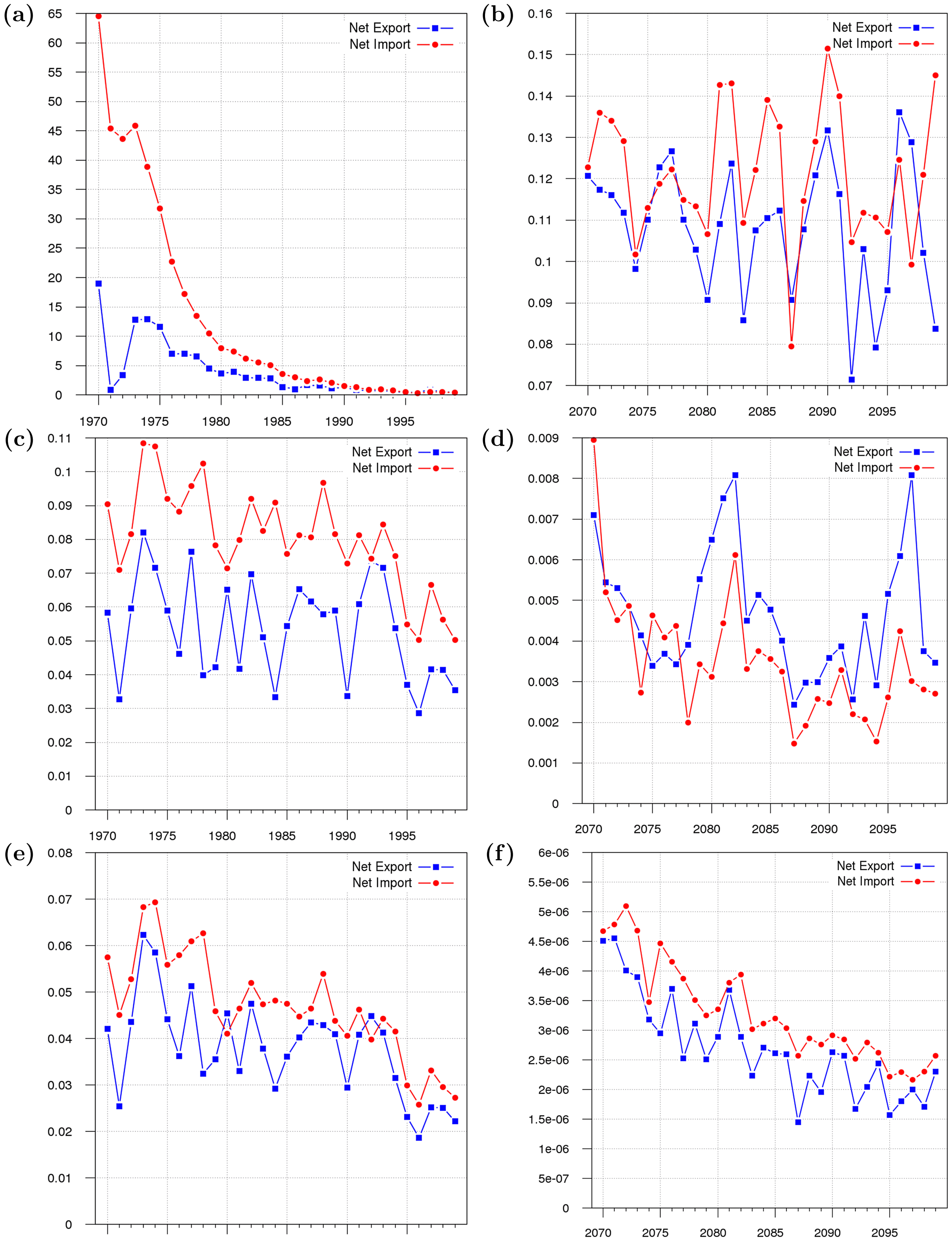

Figure B.5: Annual series of (KZ-filtered) net export (blue line) and import (red line) F_{net} (ng m^{-2} s^{-1}) of (a,b) DDT, (c,d) PCB153, and (e,f) PCB28, averaged across respective gates (see Section 2.3.1) and over the period (a,c,e) 1970−1999 and (b,d,f) 2070−2099.

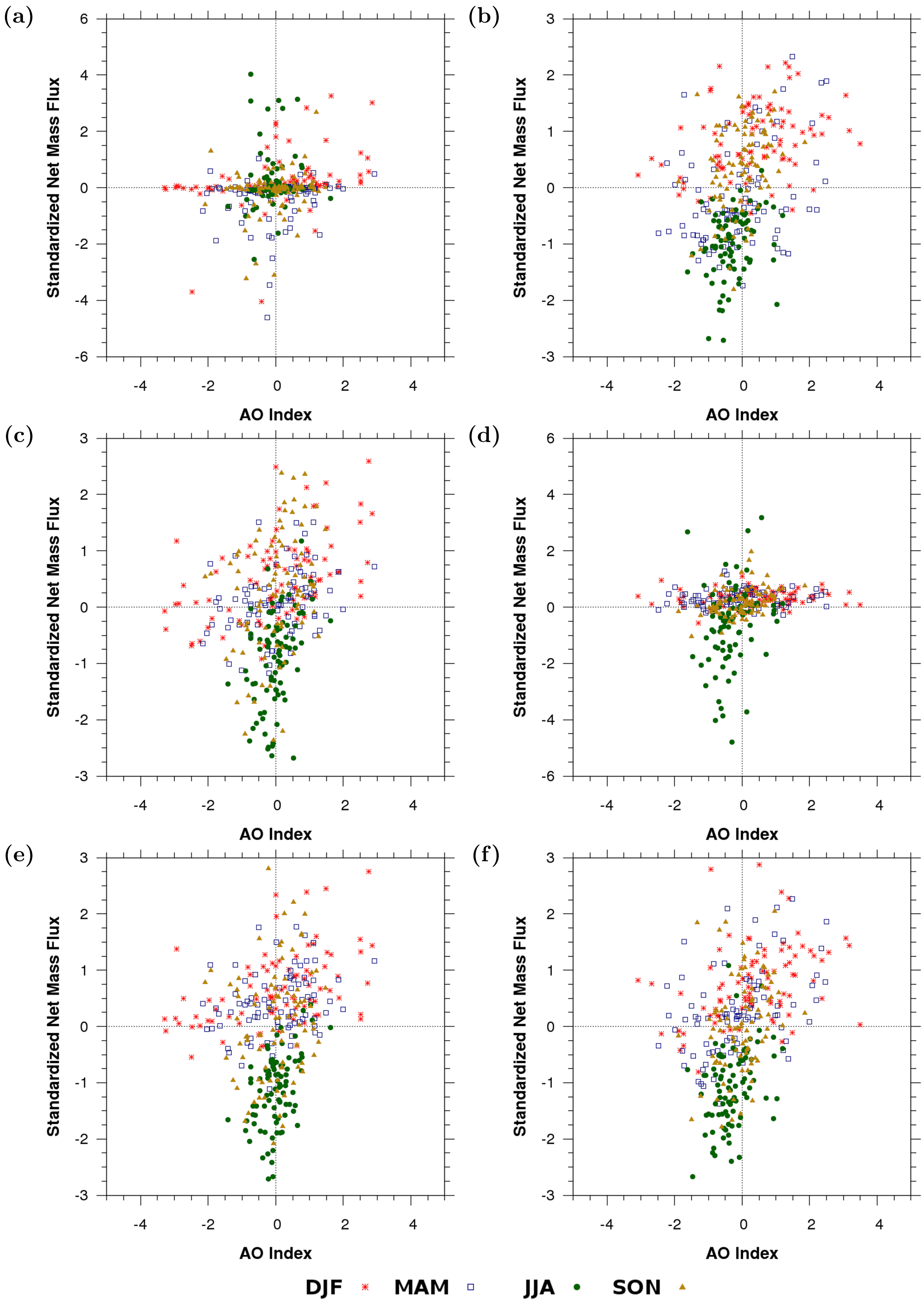

Figure B.6: Scatter plots of monthly Arctic Oscillation Index (x axes) and standardized monthly detrended (raw − KZ-filtered) net meridional mass flux F_{net} (y axes) of (a,b) DDT, (c,d) PCB153, and (e,f) PCB28 during (a,c,e) 1970−1999 and (b,d,f) 2070−2099.

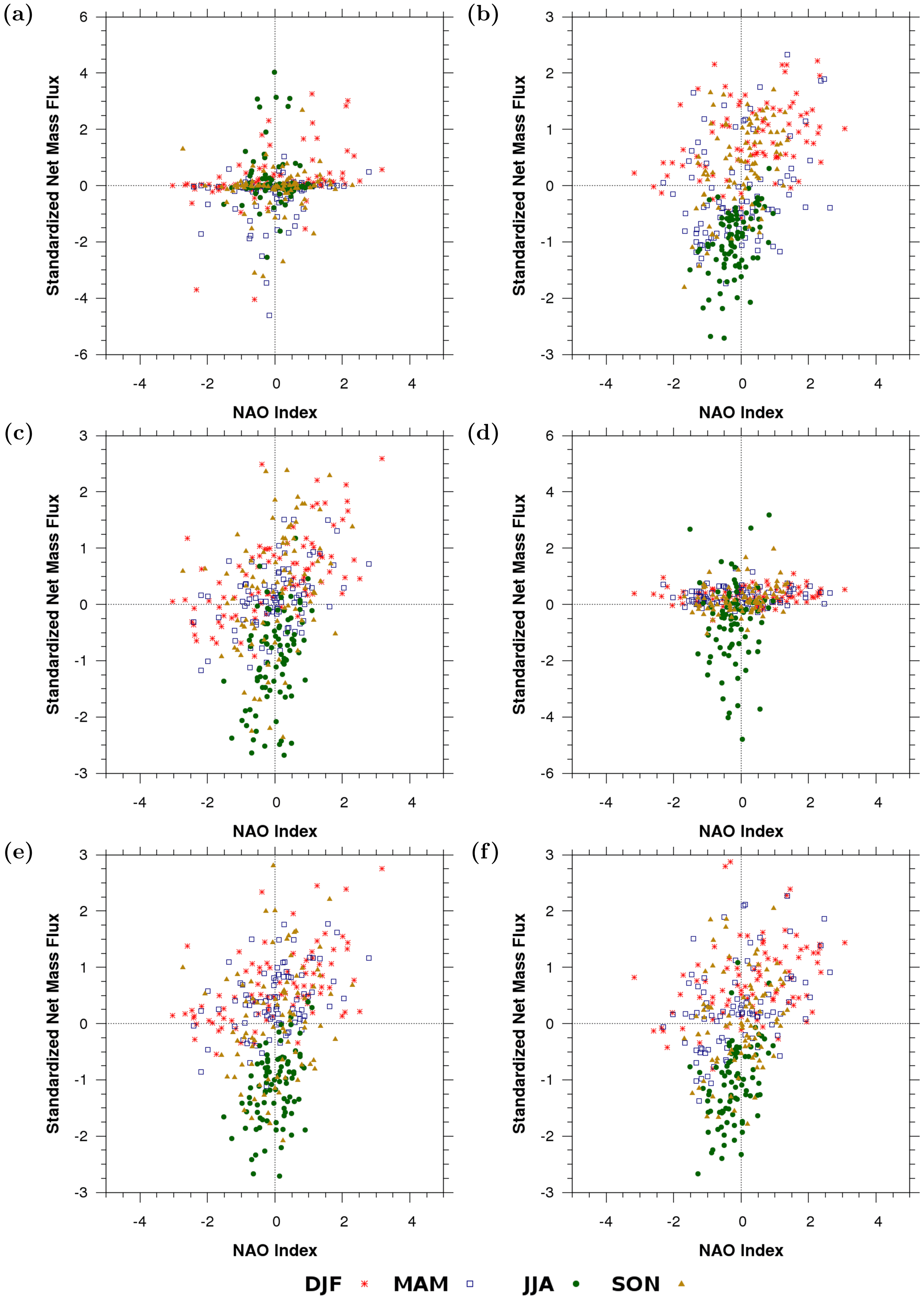

Figure B.7: Same as Figure B.6, but the x axes are the North Atlantic Oscillation Index

Appendix C
ECHAM/MESSy Submodels

In the following, four submodels that are essential to the EMAC-SVOC run are introduced and some parameterizations of main interest are briefly described.

Aerosol microphysics and thermodynamics (GMXe)

The aerosol submodel GMXe simulates ambient aerosol distributions (mass and number) and their chemical compositions (Pringle et al., 2010). The atmospheric aerosol size spectrum is described in terms of log-normal distributions for seven aerosol modes. The modes are composed of four hydrophilic modes (namely: nucleation, Aitken, accumulation, and coarse) and three hydrophobic modes (namely: Aitken, accumulation, and coarse) with distinct chemical compositions (except for bulk species). GMXe treats bulk species (such as BC, OM, DU, and SS), as well as aerosol ions and molecules (such as SO_4^{2-}, NO_3^-, Cl^-, NH_4^+, and Na^+). The submodel also offers flexibility to include more aerosol species. The aerosol size, mass, and number concentration are prognostically calculated and transported as tracers. The aerosol size distribution is described with

$$n(\ln r) = \sum_{i=1}^{7} \frac{N_i}{\sqrt{2\pi} \ln \sigma_i} \exp\left[-\frac{(\ln r - \ln \overline{r}_i)^2}{2 \ln^2 \sigma_{g_i}} \right] \ , \tag{C.1}$$

where N_i is the number concentration for mode i, $\overline{r}_i$ is the number mean radius, and σ_i is the geometric standard deviation. Following Vignati et al. (2004), σ_g of each aerosol mode is prescribed, that is, $\sigma_g = 2.0$ for coarse hydrophobic mode, $\sigma_g = 2.2$ for coarse hydrophilic mode, and $\sigma_g = 1.69$ for the other modes.

Within each mode, aerosol species are internally well mixed, and the composition can be modified by aerosol dynamics (for example, coagulation), thermodynamical processes (for example, nucleation and condensation of sulfate), and cloud processing. Across modes, the aerosols are treated as an external mixture. For the mass transfer from hydrophobic to hydrophilic mode, GMXe implements a monolayer approach (Vignati et al., 2004; Stier et al., 2005) to express the aging of hydrophobic particles into hydrophilic modes. When a hydrophobic particle has sufficient hydrophilic material associated with it such that "n" monolayers of hydrophilic material could be created, the material is moved to the hydrophilic mode. GMXe applies n=5 monolayers based on comparison with observational data limited to BC and dust aerosols.

Air−sea gas exchange (AIRSEA)

This submodel applies the two-film model of Liss and Slater (1974) whereby the air-sea flux parameterization is based on the assumption that the exchange is only driven by molecular diffusion. The flux $F_{\text{air-sea}}$ (mol m^{-2} s^{-1}) across the interface follows an empirical relation with a positive sign indicating sea-to-air direction:

$$F_{\text{air-sea}} = k_{\text{tot}} \left(C_w - H p_g \right) \ , \tag{C.2}$$

where C_w is the tracer concentration in uppermost ocean layer (mol m^{-3}), H is the Henry's Law coefficient (mol m^{-3} Pa^{-1}), p_g is the partial pressure (Pa) of the gas in air over the water surface, and k_{tot} is the transfer velocity (m s^{-1}). The transfer velocity is determined from individual transfer velocities in the gas phase and water phase, k_g and k_w, respectively:

$$k_{\text{tot}} = \left(\frac{1}{\alpha k_w} + \frac{HRT}{k_g} \right)^{-1} \ , \tag{C.3}$$

α is the fractional increase in k_w due to the species reaction in solution (dimensionless), R is the gas constant (8.314 J mol^{-}1 K^{-1}), and T is the temperature (K).

Variables affecting k_{tot}, namely, wind speed, the Schmidt number, atmospheric stability, salinity, and the presence of rain and bubbles, are accounted for (or optionally included) through their effects on both k_g and k_w. More details on the implementation of the air−sea exchange mechanism are found in Pozzer et al. (2006) and references therein.

Dry deposition (DDEP)

Dry deposition processes of gases and aerosols are calculated in this submodel (Kerkweg et al., 2006a). The dry deposition flux F_{dep} (kg m^{-2} s^{-1}) of species x is given by

$$F_{\text{dep}}(x) = \mu_g(x) \, \frac{\text{MW}(x)}{\text{MW}_{\text{air}}} \, \frac{\Delta p}{g \, \Delta z} \, v_d(x) \ , \tag{C.4}$$

where μ_g is the trace gas or the aerosol compound mixing ratio (mol mol^{-1}), MW is the molecular weight (g mol^{-1}), $\frac{\Delta p}{g \, \Delta z}$ is the air density (kg m^{-3}), and v_d is the dry deposition velocity (m s^{-1}). The algorithm used for v_d is adopted from Ganzeveld and Lelieveld (1995) and Ganzeveld et al. (1998).

For a trace gas, the dry deposition velocity, $v_{d,g}$, is defined as the inverse of the sum of atmospheric and surface resistances:

$$v_{d,g}(x) = \frac{1}{R_a + R_{qbr}(x) + R_s(x)} \ , \tag{C.5}$$

where R_a, R_{qbr}, and R_s are the aerodynamic resistance (s m^{-1}), the quasi-laminar boundary layer resistance (s m^{-1}), and the surface resistance (s m^{-1}), respectively. Each term is parameterized differently in the submodel (Kerkweg et al., 2006a). The aerodynamic resistance (R_a) describes turbulent processes over the surface and is independent of the species. This term is calculated from the Monin−Obukhov similarity theory, friction velocity, and von-Karman constant. For the boundary-layer resistance R_{qbr}, it is controlled by molecular diffusion through the surface layer. The surface resistance (R_s) contains different resistances depending on surface type and tracer properties. It is estimated using solubility and reactivity of a tracer relative to those of ozone and sulfur dioxide whose dry deposition velocities are relatively well known, following an approach suggested by Wesely (1989). It is worth noting that for tracers whose air−sea exchanges are resolved by AIRSEA, the calculated $v_{d,g}$ values over ocean grid cells are set to zero within DDEP.

For aerosol particles, the dry deposition velocity $v_{d,p}$ is calculated as follows

$$v_{d,p}(x) = \left(\frac{R_a}{100} + \frac{1}{v_{kd,p}} \right)^{-1} \ . \tag{C.6}$$

R_a is calculated the same way as in the gas-phase dry deposition scheme, whereas the calculation of $v_{kd,p}$ (specific dry deposition velocity in m s^{-1}) depends on the surface type, particle radius, density, and standard deviation of each aerosol mode distribution.

Scavenging and cloud chemistry (SCAV)

This submodel takes into account soluble gas and aerosol scavenging mechanisms and chemistry (Tost et al., 2006b). SCAV works on a vertical water column where the rainwater that enters a grid cell from above affects the scavenging in that particular layer as well as the layers below. For a trace gas, the transfer rate coefficient for cloud droplets, k_{mt} (s^{-1}), is limited by the diffusivity of the respective gas in air (D_g in m^2 s^{-1}) and the transfer velocity across the droplet surface (v_t in m s^{-1}). k_{mt} is determined by

$$k_{mt} = \frac{3D_g}{2r^2} \left(2 + 0.6\sqrt{\frac{2ru}{v}} \left(\frac{v}{D_g} \right)^{1/3} \right) \ , \tag{C.7}$$

where r is the droplet radius (m), u is the terminal velocity of the falling droplets (m s^{-1}), and v is the kinematic viscosity of air (m^2 s^{-1}). k_{mt} has to be multiplied by the liquid water content (LWC in $\mathrm{m}^3_{\mathrm{water}}\ \mathrm{m}^{-3}_{\mathrm{air}}$) for the forward reaction (uptake of gas from cloud or rain droplets) and by the dimensionless temperature-dependent Henry's Law constants (H_x) for the backward reaction (release of gas).

$$k_{\mathrm{exf:f}} = k_{mt} \times \mathrm{LWC} \ , \tag{C.8}$$

$$k_{\mathrm{exf:b}} = k_{mt} \times H_x \ . \tag{C.9}$$

For aerosol particles, different parameterizations are implemented for nucleation and impaction scavenging. The former takes into account the Brownian motion and nucleation of cloud droplets, whereas the latter considers the Brownian motion, interception, and impaction. The concentration of aerosol species follows an exponential approach:

$$C(t_0 + \Delta t) = C(t_0) \times \exp(-\Lambda \ \Delta t) \ , \tag{C.10}$$

where Λ is the scavenging coefficient (s^{-1}), and Δt is the model time step (s^{-1}). The parameterizations for Λ due to the effects of Brownian motion and impaction follow Pruppacher and Klett (2010) and Seinfeld and Pandis (1998). The empirical function for the nucleation of cloud droplets is applied differently, using only the aerosol radius r_{aer} (m), where

$$C(t_0 + \Delta t) = C(t_0) \times \left[1 - \arctan\left(\left(5.0 \times 10^6 r_{\mathrm{aer}}\right)^6\right) 2\pi\right] \ . \tag{C.11}$$

The scavenging process is calculated individually for convective and large-scale precipitation. At the end of each time step, all species which have not been removed will be released through droplet evaporation. The evaporation rate is based on LWC, that is, when LWC is below a threshold value, all non-volatile species and ions are transferred to aerosol species in the largest available mode. For volatile species, their fate is determined according to the Henry's law for equilibrium.

Appendix D
User Guide for SVOC Submodel

SVOC is a new MESSy submodel to simulate tracers in the semivolatile organic group. All important cycling processes including emission, gas−particle partitioning, air−surface exchange, deposition, and degradation are calculated in the submodel through the calling sequence of process subroutines illustrated in Figure D.1. A number of process parameterizations in the areas of gas−particle partitioning, soil volatilization, and the heterogeneous chemistry of benzo[a]pyrene (BaP) are available for use. Specifically, gas−particle partitioning is computed using one of four schemes: (1) Junge−Pankow (Junge, 1977; Pankow, 1987), (2) Finizio (Finizio et al., 1997), (3) Lohmann−Lammel (Lohmann and Lammel, 2004), and (4) Poly-parameter linear free energy relationships (ppLFER) (Goss and Schwarzenbach, 2001; Endo and Goss, 2014; Shahpoury et al., 2016). The soil volatilization is implemented using one of two parameterizations: the Jury scheme (Jury et al., 1983; Jury et al., 1990) and the Smit scheme (Smit et al., 1997). For BaP heterogeneous oxidation by O_3, four options are available for calculating the reaction rate: (1) Pöschl scheme (Pöschl et al., 2001), (2) Kwamena scheme (Kwamena et al., 2004), (3) Kahan scheme (Kahan et al., 2006), and (4) ROI-T scheme (Mu et al., 2018).

(Intentionally left blank)

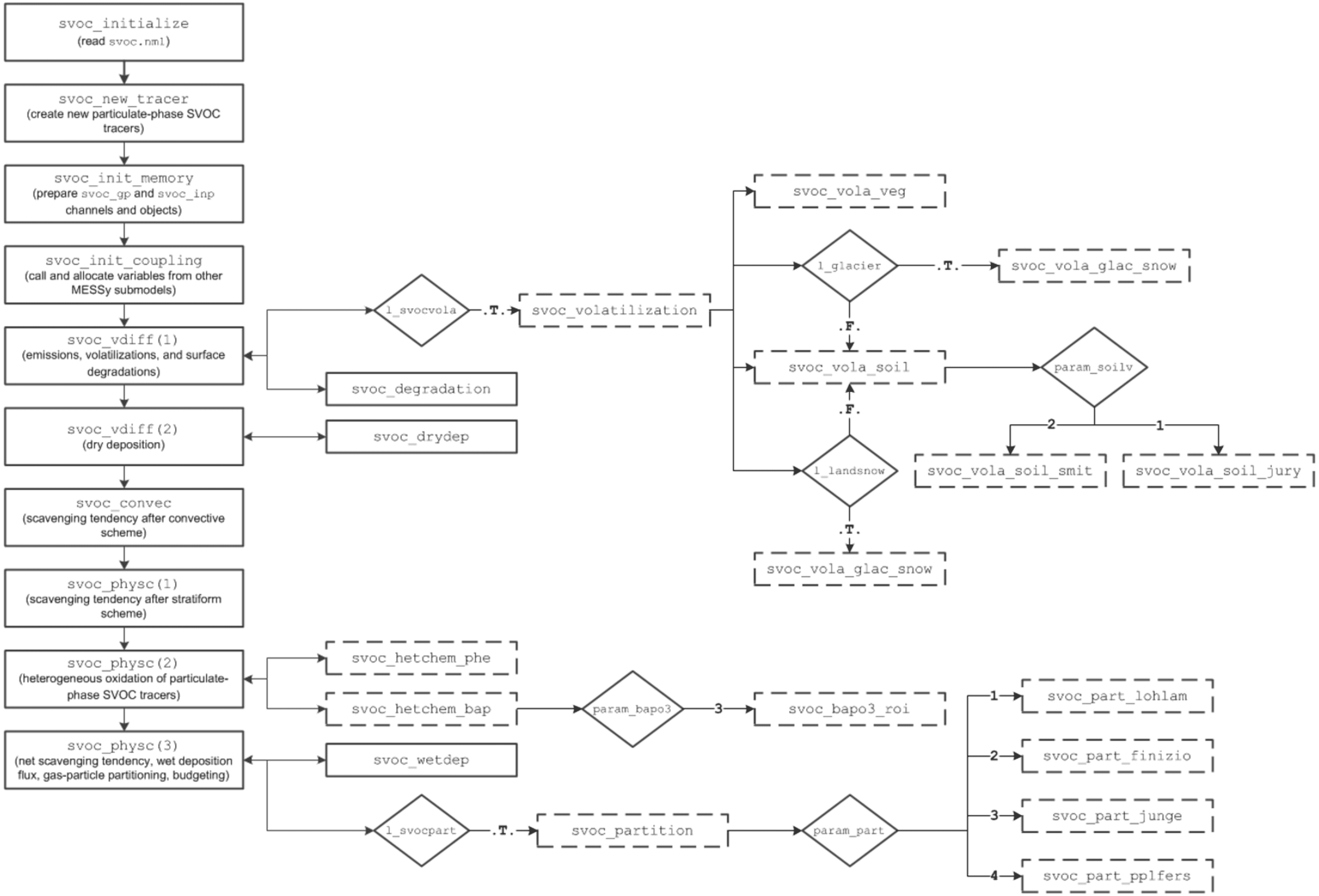

Figure D.1: Calling sequence of process subroutines in SVOC submodel

The following information lists major components in SVOC version 1.0, to be implemented within the ECHAM_v.5.3.0/MESSy_v2.50 model.

Namelist

The first step before running the submodel involves defining several input parameters in `svoc.nml` file. The template for this file can be seen in Figure D.2.

1. Process switches:
   - `L_GP`: Switch to determine whether the calculations are for grid point (GP) tracers.
   - `L_LG`: Switch to determine whether the calculations are for Lagrangian (LG) tracers. The current SVOC version only works for grid-point representation (hence, `L_GP` should always be `.TRUE.`, and `L_LG` should be `.FALSE.`).
   - `l_svocpart`: Switch for gas−particle partitioning calculation. Default: `.TRUE.`
   - `l_svocvola`: Switch for volatilization from the surface. If this process is switched off, the AIRSEA submodel should also be turned off. Default: `.TRUE.`
   - `l_glacier`: Switch to include glacier compartment. Default: `.FALSE.`
   - `l_landsnow`: Switch to include snow compartment. Default: `.FALSE.`
   - `l_mode_partition`: If set to `.TRUE.`, the particulate-phase SVOC tracers will be discretized into the 7 aerosol modes applied in the GMXe and M7 submodels (*ns*: nucleation soluble, *ks*: Aitken soluble, *as*: accumulation soluble, *cs*: coarse soluble, *ki*: Aitken insoluble, *ai*: accumulation insoluble, and *ci*: coarse insoluble). Default: `.FALSE.` (the particle is treated as bulk species).
2. Physics and chemistry parameters:
   - `param_part`: Gas−particle partitioning scheme; 1=Lohmann−Lammel (default), 2=Finizio, 3=Junge-Pankow, or 4=ppLFER.
   - `param_soilv`: Soil volatilization scheme; 1=Smit (default), 2=Jury.
   - `param_bapo3`: Heterogeneous BaP oxidation with O_3; 1=Pöschl (default), 2=Kwamena, 3=ROI-T, or 4=Kahan.
   - `aermod_str`: MESSy submodel for aerosol microphysics (GMXe or M7).
3. Channel and object names to access input data
   - `imp_ss_as_flux`: Sea salt in aitken-soluble mode
   - `imp_om_soil`: Fraction of organic matter in soil
   - `imp_rho_soil`: Soil density
   - `imp_mld_oce`: Ocean mixed layer depth
4. Tracer properties

   Table D.1 lists all the required physicochemical properties for SVOC tracers, including tracer names, molecular weights, partition coefficients, Henry's law constants, and so forth. It also shows a subroutine name to denote which process utilizes the respective properties.

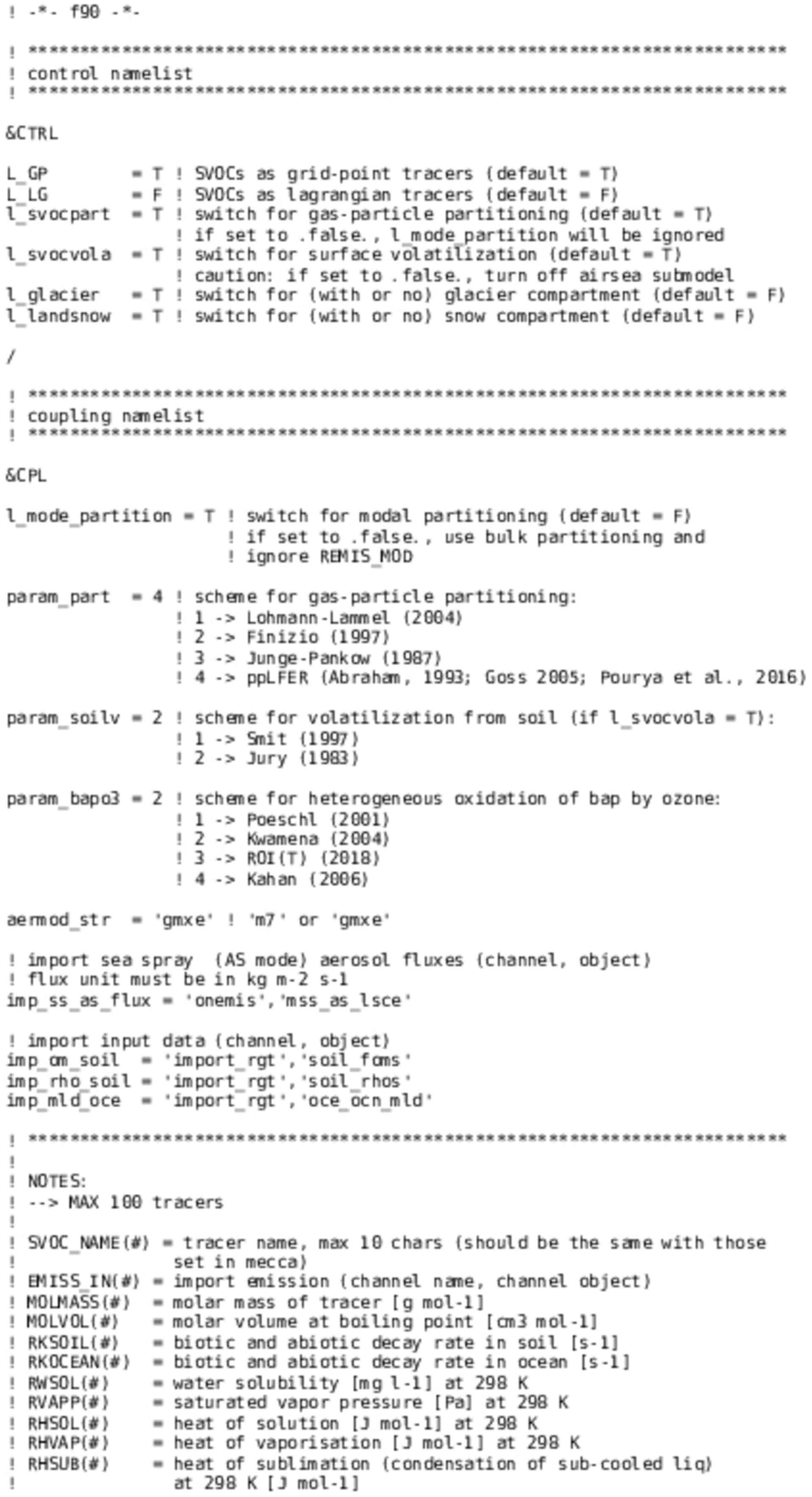

```
! -*- f90 -*-

! *************************************************************************
! control namelist
! *************************************************************************

&CTRL

L_GP        = T ! SVOCs as grid-point tracers (default = T)
L_LG        = F ! SVOCs as lagrangian tracers (default = F)
l_svocpart  = T ! switch for gas-particle partitioning (default = T)
                ! if set to .false., l_mode_partition will be ignored
l_svocvola  = T ! switch for surface volatilization (default = T)
                ! caution: if set to .false., turn off airsea submodel
l_glacier   = T ! switch for (with or no) glacier compartment (default = F)
l_landsnow  = T ! switch for (with or no) snow compartment (default = F)

/

! *************************************************************************
! coupling namelist
! *************************************************************************

&CPL

l_mode_partition = T ! switch for modal partitioning (default = F)
                     ! if set to .false., use bulk partitioning and
                     ! ignore REMIS_MOD

param_part  = 4 ! scheme for gas-particle partitioning:
                ! 1 -> Lohmann-Lammel (2004)
                ! 2 -> Finizio (1997)
                ! 3 -> Junge-Pankow (1987)
                ! 4 -> ppLFER (Abraham, 1993; Goss 2005; Pourya et al., 2016)

param_soilv = 2 ! scheme for volatilization from soil (if l_svocvola = T):
                ! 1 -> Smit (1997)
                ! 2 -> Jury (1983)

param_bapo3 = 2 ! scheme for heterogeneous oxidation of bap by ozone:
                ! 1 -> Poeschl (2001)
                ! 2 -> Kwamena (2004)
                ! 3 -> ROI(T) (2018)
                ! 4 -> Kahan (2006)

aermod_str  = 'gmxe' ! 'm7' or 'gmxe'

! import sea spray  (AS mode) aerosol fluxes (channel, object)
! flux unit must be in kg m-2 s-1
imp_ss_as_flux = 'onemis','mss_as_lsce'

! import input data (channel, object)
imp_om_soil  = 'import_rgt','soil_foms'
imp_rho_soil = 'import_rgt','soil_rhos'
imp_mld_oce  = 'import_rgt','oce_ocn_mld'

! *************************************************************************
!
! NOTES:
! --> MAX 100 tracers
!
! SVOC_NAME(#) = tracer name, max 10 chars (should be the same with those
!                set in mecca)
! EMISS_IN(#) = import emission (channel name, channel object)
! MOLMASS(#)  = molar mass of tracer [g mol-1]
! MOLVOL(#)   = molar volume at boiling point [cm3 mol-1]
! RKSOIL(#)   = biotic and abiotic decay rate in soil [s-1]
! RKOCEAN(#)  = biotic and abiotic decay rate in ocean [s-1]
! RWSOL(#)    = water solubility [mg l-1] at 298 K
! RVAPP(#)    = saturated vapor pressure [Pa] at 298 K
! RHSOL(#)    = heat of solution [J mol-1] at 298 K
! RHVAP(#)    = heat of vaporisation [J mol-1] at 298 K
! RHSUB(#)    = heat of sublimation (condensation of sub-cooled liq)
!               at 298 K [J mol-1]
```

Figure D.2: SVOC namelist example

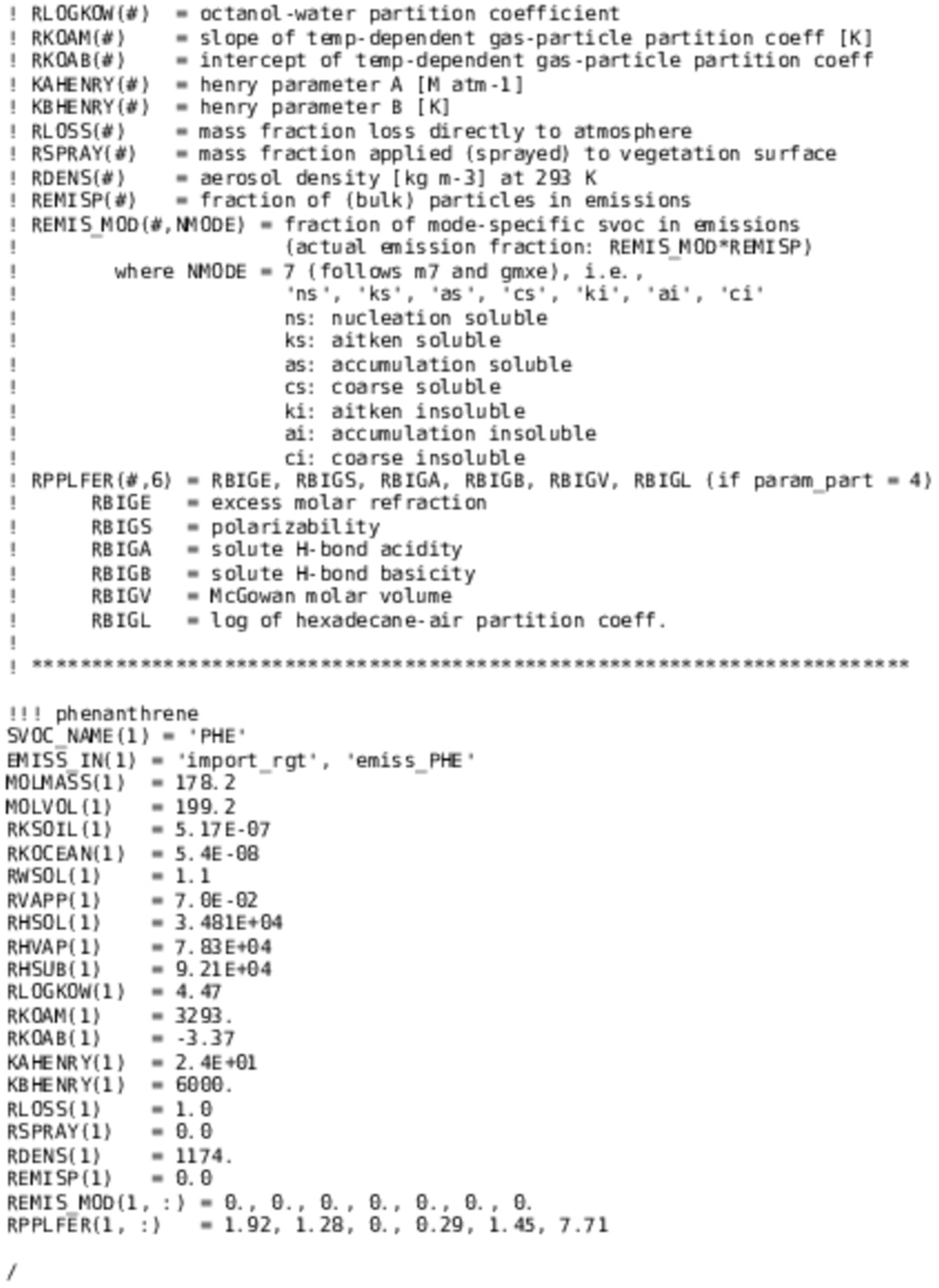

```
! RLOGKOW(#)  = octanol-water partition coefficient
! RKOAM(#)    = slope of temp-dependent gas-particle partition coeff [K]
! RKOAB(#)    = intercept of temp-dependent gas-particle partition coeff
! KAHENRY(#)  = henry parameter A [M atm-1]
! KBHENRY(#)  = henry parameter B [K]
! RLOSS(#)    = mass fraction loss directly to atmosphere
! RSPRAY(#)   = mass fraction applied (sprayed) to vegetation surface
! RDENS(#)    = aerosol density [kg m-3] at 293 K
! REMISP(#)   = fraction of (bulk) particles in emissions
! REMIS_MOD(#,NMODE) = fraction of mode-specific svoc in emissions
!                      (actual emission fraction: REMIS_MOD*REMISP)
!        where NMODE = 7 (follows m7 and gmxe), i.e.,
!                      'ns', 'ks', 'as', 'cs', 'ki', 'ai', 'ci'
!                      ns: nucleation soluble
!                      ks: aitken soluble
!                      as: accumulation soluble
!                      cs: coarse soluble
!                      ki: aitken insoluble
!                      ai: accumulation insoluble
!                      ci: coarse insoluble
! RPPLFER(#,6) = RBIGE, RBIGS, RBIGA, RBIGB, RBIGV, RBIGL (if param_part = 4)
!       RBIGE   = excess molar refraction
!       RBIGS   = polarizability
!       RBIGA   = solute H-bond acidity
!       RBIGB   = solute H-bond basicity
!       RBIGV   = McGowan molar volume
!       RBIGL   = log of hexadecane-air partition coeff.
!
! ************************************************************************

!!! phenanthrene
SVOC_NAME(1) = 'PHE'
EMISS_IN(1) = 'import_rgt', 'emiss_PHE'
MOLMASS(1)  = 178.2
MOLVOL(1)   = 199.2
RKSOIL(1)   = 5.17E-07
RKOCEAN(1)  = 5.4E-08
RWSOL(1)    = 1.1
RVAPP(1)    = 7.0E-02
RHSOL(1)    = 3.481E+04
RHVAP(1)    = 7.83E+04
RHSUB(1)    = 9.21E+04
RLOGKOW(1)  = 4.47
RKOAM(1)    = 3293.
RKOAB(1)    = -3.37
KAHENRY(1)  = 2.4E+01
KBHENRY(1)  = 6000.
RLOSS(1)    = 1.0
RSPRAY(1)   = 0.0
RDENS(1)    = 1174.
REMISP(1)   = 0.0
REMIS_MOD(1, :) = 0., 0., 0., 0., 0., 0., 0.
RPPLFER(1, :)   = 1.92, 1.28, 0., 0.29, 1.45, 7.71

/
```

Figure D.2: continued

Table D.1: List of input parameters for tracer properties defined in `svoc.nml` file

Parameter	Description	Unit	Related subroutine(s)
`SVOC_NAME`	Tracer name		`svoc_new_tracer`
`EMISS_IN`	Import emission data (channel, object)		`svoc_init_coupling`
`MOLMASS`	Molecular mass	g mol^{-1}	`svoc_new_tracer`
`MOLVOL`	Molar volume	cm^{3} mol^{-1}	not used in SVOC, but needed in AIRSEA
`RKSOIL`	1st order degradation rate in soil	s^{-1}	`svoc_degradation`
`RKOCEAN`	1st order degradation rate in ocean	s^{-1}	`svoc_degradation`
`RWSOL`	Water solubility	mg L^{-1}	`svoc_vola_glac_snow`
`RVAPP`	Saturated vapor pressure	Pa	`svoc_vola_veg`, `svoc_vola_glac_snow`, `svoc_part_lohlam`, `svoc_part_junge`
`RHSOL`	Heat of solution	J mol^{-1}	`svoc_vola_glac_snow`
`RHVAP`	Heat of vaporization	J mol^{-1}	see `RVAPP`, `svoc_part_pplfers`
`RHSUB`	Heat of condensation of sub-cooled liquid	J mol^{-1}	`svoc_vola_glac_snow`
`RLOGKOW`	Octanol−water partition coefficient	-	`svoc_vola_soil_smit`, `svoc_vola_soil_jury`
`RKOAM`	Slope of temperature-dependent octanol−air partition coefficient (K_{oa})	-	`svoc_part_lohlam`, `svoc_part_finizio`
`RKOAB`	Intercept of temperature-dependent K_{oa}	-	see `RKOAM`
`KAHENRY`	Henry coefficient at 25°C	M atm^{-1}	`svoc_drydep`, `svoc_vola_glac_snow`, `svoc_vola_soil_jury`, `svoc_vola_soil_smit`
`KBHENRY`	Constant for the temperature-correction of Henry coefficient		see `KAHENRY`
`RLOSS`	Fraction of emission release to the atmosphere	-	`svoc_vdiff(1)`
`RSPRAY`	Fraction of emission applied (sprayed) to surface	-	`svoc_vdiff(1)`
`RDENS`	SVOC particle density	kg m^{-3}	`svoc_new_tracer`
`REMISP`	Fraction of emission emitted as particles	-	`svoc_vdiff(1)`
`REMIS_MOD`	Fraction of `REMISP` assigned into each aerosol mode (7 comma-separated values)	-	`svoc_vdiff(1)`
`RPPLFER`	Solute descriptors for ppLFER (6 comma-separated values)		`svoc_part_pplfers`

Coupling with other MESSy submodels

For its computations, SVOC requires some variables from other MESSy submodels:

- Dry deposition velocities of aerosol and gas-phase SVOC tracers from DDEP (Kerkweg et al., 2006a).
- Aerosol wet radius from either GMXe (Pringle et al., 2010) or M7 (Vignati et al., 2004). If GMXe is used, SVOC will also import aerosol number concentration.
- Wet deposition fluxes of gas-phase and liquid-phase SVOC tracers and scavenging tendencies of black carbon (BC) from SCAV (Tost et al., 2006b). To import the wet deposition fluxes, apply `out_string` = ”`[SVOC_NAME];[SVOC_NAME]_l`” in `scav.nml`, whereas for the BC scavenging tendencies, apply `te_string` = ”`BC_ks;BC_as;BC_cs;BC_ki`”.
- Air−sea exchange fluxes of SVOC tracers from AIRSEA (Pozzer et al., 2006). To let AIRSEA calculate these fluxes, prepare all the necessary information in `airsea.nml`: tracer name, molar volume, Henry's law constants, and tracer concentration over the surface water. The last parameter is obtained from one of SVOC output variables (Table D.3); hence user should set `WATER_CON_CHN(#)` = ”`svoc_gp`”,”`CWAT_[SVOC_NAME]`” in `airsea.nml`.

Starting a simulation

To prepare an EMAC-SVOC run, activate the submodel (set `USE_SVOC = .TRUE.` in `switch.nml`), fill in all input parameters in `svoc.nml` and other namelists, and setup the gaseous and liquid chemistry of SVOC tracers in MECCA and SCAV (more details in the manual of each submodel, Sander et al. (2011) and Tost et al. (2006b), respectively).

Input and output

The following input data should be available in their desirable units: (a) Emission fluxes in kg m^{-2} s^{-1}, (b) soil density in kg m^{-3}, and (c) ocean mixed layer depth in m. Running EMAC-SVOC generates two output files in addition to other standard MESSy output: (a) `[EXP_NAME]___________yyyymmmddd_hhmm_svoc_inp` which stores the three input data after regridding, unit conversion, and other treatment (see Table D.2), and (b) `[EXP_NAME]___________yyyymmmddd_hhmm_svoc_gp` which stores some diagnostic quantities, refer to the list in Table D.3.

Table D.2: List of variables in `svoc_inp` channel

Variable	Definition	Unit
`appl_[SVOC_NAME]`	Application/emissions	$\mathrm{mol_{tr}\ mol_{air}^{-1}\ kg_{air}\ m^{-2}\ s^{-1}}$
`rhos`	Soil density	$\mathrm{kg_{solid}\ m^{-3}}$
`foms`	Fraction of organic matter in soil	$\mathrm{kg_{OM}\ kg_{solid}^{-1}\ m^{-3}}$
`ocn_mld`	Ocean mixed layer depth	m

Table D.3: List of variables in `svoc_gp` channel

Variable	Definition	Unit	Dimension	Note
`Kp_[SVOC_NAME]`	Gas−particle partition coefficient (bulk)	$\mathrm{m^3\ \mu g^{-1}}$	`LON, LAT, LEV`	
`Kp_[SVOC_NAME]_[cm]`	Gas−particle partition coefficient at mode `cm` (namely, `ns`, `cs`, `as`, `ks`, `ki`, `ai`, `ci`)	$\mathrm{m^3\ \mu g^{-1}}$	`LON, LAT, LEV`	
`THETA_[SVOC_NAME]`	Particulate mass fraction (bulk)	-	`LON, LAT, LEV`	
`THETA_[SVOC_NAME]_[cm]`	Particulate mass fraction at mode `cm` (namely, `ns`, `cs`, `as`, `ks`, `ki`, `ai`, `ci`)	-	`LON, LAT, LEV`	
`BURD_[SVOC_NAME]`	Tracer burden in environmental compartments	$\mathrm{kg_{tr}\ m^{-2}}$	`LON, LAT, LEV`	`LEV` (bottom to top): 1=soil, 2=vegetation, 3=ocean, 4=snow, 5=glacier, 6=atmosphere
`VOLA_[SVOC_NAME]`	Volatilization flux from surface compartments	$\mathrm{kg_{tr}\ m^{-2}\ s^{-1}}$	`LON, LAT, LEV`	`LEV` (bottom to top): 1=soil, 2=vegetation, 3=ocean, 4=snow, 5=glacier
`DEPO_[SVOC_NAME]`	Deposition fluxes	$\mathrm{kg_{tr}\ m^{-2}\ s^{-1}}$	`LON, LAT, LEV`	`LEV` (bottom to top): 1=dry, 2=wet, 3=total
`DEGR_[SVOC_NAME]`	Biotic degradation rate	$\mathrm{kg_{tr}\ m^{-2}\ s^{-1}}$	`LON, LAT, LEV`	`LEV` (bottom to top): 1=soil, 2=vegetation, 3=ocean
`CWAT_[SVOC_NAME]`	Tracer concentration in the ocean	$\mathrm{kmol\ m^{-3}}$	`LON, LAT`	

Appendix E
Observation Data Screening

Measured PAH concentration data have been collected from multiple monitoring networks (Table E.1) where the locations of observation sites are distributed over the Arctic, mid-latitudes, and Tropics (Figure E.1). Observations were used to assess the performance of EMAC-SVOC to simulate total concentrations and particulate mass fraction, and to help select simulation period. For these purposes, the data were investigated carefully for suitability of use in this study using a sequence of data screening and quality checking illustrated in Figure E.2. Tables E.2 and E.3 show the number of stations with reliable total concentration and particulate mass fraction data, respectively, for every PAH species and over each year from 2002 to 2014. It is found that the years 2007 to 2009 had sufficient quality-controlled data on the two variables, hence was deemed a suitable simulation period.

(Intentionally left blank)

Table E.1: Summary of observation networks for simulation period selection

Network	Data Availability	Variables	Reported Value	Data Source
EMEP & AMAP[a]	2002-2014	gas, particles, total	daily, weekly, monthly	EBAS NILU, 2012
DEFRA[b]	2008-2010	total	monthly	DEFRA, 2010
IADN[c]	2002-2010	gas, particles	daily	IADN, 2014
MONET-Africa[d]	2008	gas	monthly	Klánová et al., 2008

[a] EMEP: European Monitoring and Environment Program; AMAP: Arctic Monitoring and Assessment Program

[b] DEFRA: Department for Environment, Food & Rural Affairs, UK

[c] IADN: Integrated Atmospheric Deposition Network

[d] MONET-Africa: The MONitoring NETtwork program in Africa

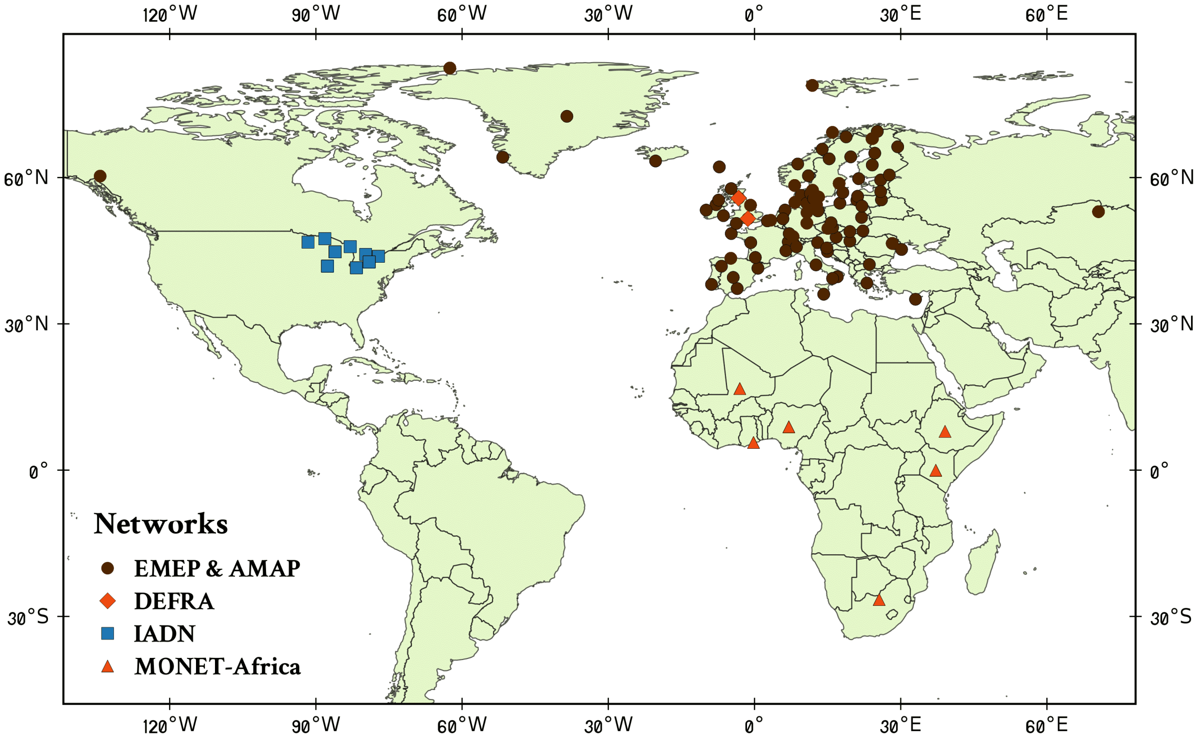

Figure E.1: Available monitoring stations from all networks

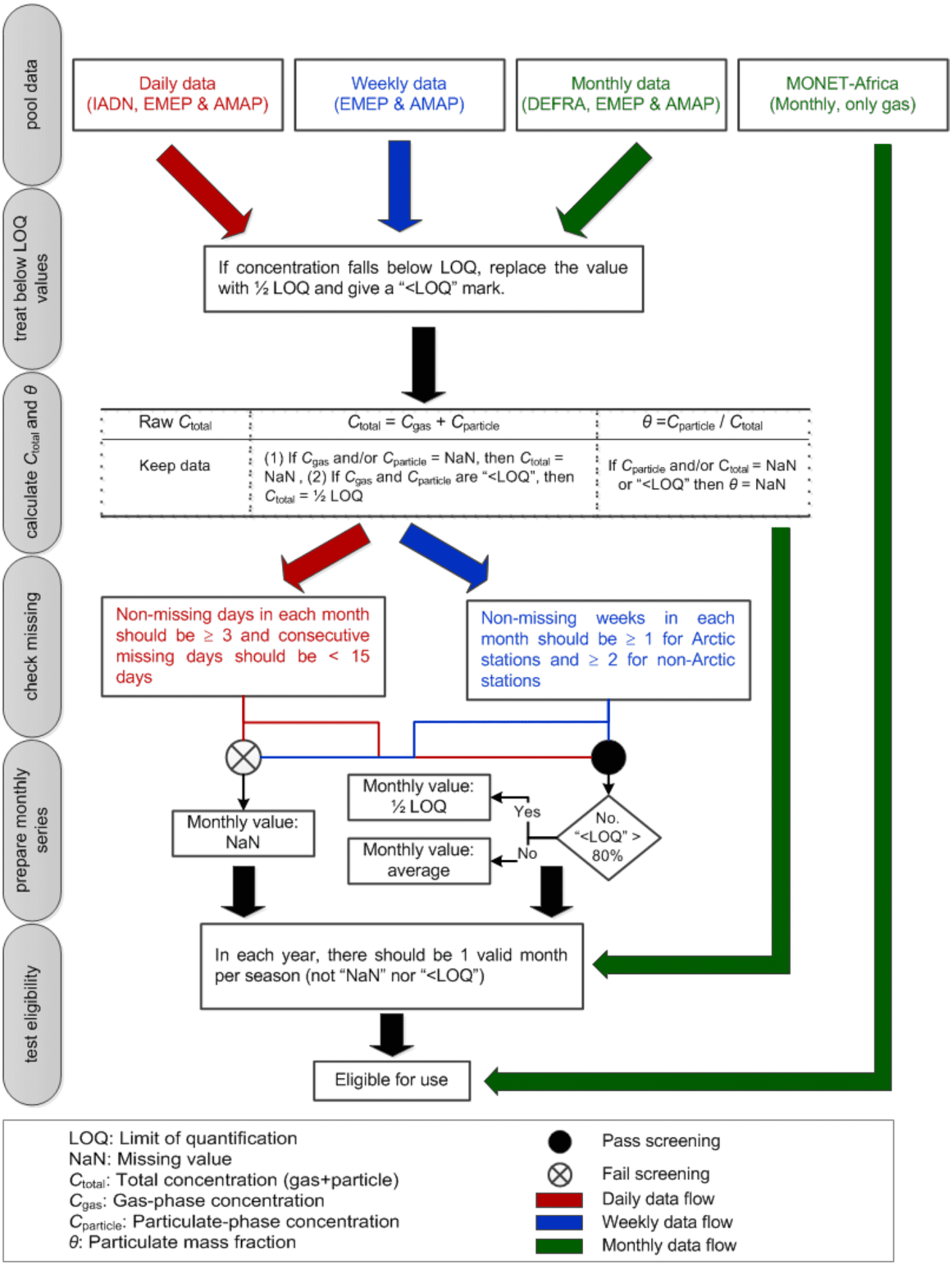

Figure E.2: Flowchart of observation data screening and station selection strategy

Table E.2: Number of stations each year that pass quality screening for total concentration data

	Network																		
	EMEP & AMAP				DEFRA				IADN				MONET-Africa			Total			
Year	PHE	PYR	FLT	BaP	PHE	PYR	FLT	BaP	PHE	PYR	FLT	BaP	PHE	PYR	FLT	PHE	PYR	FLT	BaP
2002	5	5	5	6	-	-	-	-	7	3	7	4	-	-	-	12	8	12	10
2003	5	5	5	5	-	-	-	-	7	3	7	4	-	-	-	12	8	12	9
2004	5	5	5	5	-	-	-	-	7	3	7	4	-	-	-	12	8	12	9
2005	5	5	5	5	-	-	-	-	6	3	6	3	-	-	-	11	8	11	8
2006	5	5	5	5	-	-	-	-	8	3	8	5	-	-	-	13	8	13	10
2007	9	9	9	10	-	-	-	-	7	2	7	7	-	-	-	16	11	16	17
2008	10	10	10	10	2	2	2	2	4	2	4	4	6	6	6	22	20	22	16
2009	8	10	9	10	2	2	2	2	5	2	5	5	-	-	-	15	14	16	17
2010	12	13	13	13	1	1	1	1	7	2	7	7	-	-	-	20	16	21	21
2011	5	9	6	6	-	-	-	-	-	-	-	-	-	-	-	5	9	6	6
2012	6	15	7	7	-	-	-	-	-	-	-	-	-	-	-	6	15	7	7
2013	9	10	10	10	-	-	-	-	-	-	-	-	-	-	-	9	10	10	10
2014	2	3	2	2	-	-	-	-	-	-	-	-	-	-	-	2	3	2	2

Table E.3: Same as Table E.2 but for particulate mass fraction

	Network											
	EMEP & AMAP				IADN				Total			
Year	PHE	PYR	FLT	BaP	PHE	PYR	FLT	BaP	PHE	PYR	FLT	BaP
2002	-	-	-	-	7	3	6	4	7	3	6	4
2003	-	-	-	-	6	3	7	4	6	3	7	4
2004	-	-	-	-	6	3	6	4	6	3	6	4
2005	-	-	-	-	6	3	6	3	6	3	6	3
2006	-	-	-	-	5	3	7	5	5	3	7	5
2007	1	1	1	1	4	2	5	7	5	3	6	8
2008	1	1	1	1	4	2	4	4	5	3	5	5
2009	-	-	-	-	4	2	4	5	4	2	4	5
2010	-	-	-	-	5	2	4	7	5	2	4	7

Appendix F

EMAC-SVOC Sensitivity Study: Sequential Factor Separation Analysis

The sequential factor separation (SFS) method of Schär and Kröner (2017) is an alternative approach to the classical factor separation (FS) of Stein and Alpert (1993) (see Section 3.5.2). SFS is designed in principle to address the influences of individual factor of modeling systems and the strength of possible interactions among different factors. It also accounts for the overall uncertainty of the method. One major advantage is that in the case of n factors, SFS requires only $2n$ simulations compared to the 2^n simulations needed for FS.

The principal design of SFS simulations for $n = 4$ factors is shown in Figure F.1. The order of simulations on the left-hand side of Figure F.1 is obtained by replacing one factor at a time with its surrogate starting from f_0 as the *base* simulation. This yields the simulations f_1, f_{12}, f_{123}, and f_{1234}. The set of simulations on the right-hand side is obtained by sequentially retracting the factors starting from the *target* simulation f_{1234}; hence yields f_{234}, f_{34}, and f_4. A preliminary investigation was carried out to test the suitability of this technique for the study of model sensitivity to different factors of model input and physics parameterizations. The factors of interest are 1) the temporal resolution of emissions (annual vs. monthly), 2) the representation of aerosol-phase PAHs (*bulk* vs. *modal* scheme), 3) the choice of gas−particle partitioning scheme (Lohmann−Lammel vs. ppLFER), and 4) volatilization (on vs. off); refer to Chapter 3, Section 3.5.2 for more details. A total of eight simulations was therefore needed. They are denoted by f terms in Figure F.1 and their model configurations are presented in Figure 3.5. The SFS formulation for four factors and a summary of selected results are discussed in the following.

Formulation

Based on SFS, the effect of each factor ($\hat{F}$) is defined as an arithmetic average of two differences (Equations F.1), one derived from the set of simulations $f_0 \rightarrow f_{1234}$ (left-hand side of Figure F.1) and the other from $f_{1234} \rightarrow f_0$ (right-hand side of Figure F.1).

$$\hat{F}_1 = \frac{1}{2}\left[(f_1 - f_0) + (f_{1234} - f_{234})\right] \tag{F.1a}$$

$$\hat{F}_2 = \frac{1}{2}\left[(f_{12} - f_1) + (f_{234} - f_{34})\right] \tag{F.1b}$$

$$\hat{F}_3 = \frac{1}{2}\left[(f_{123} - f_{12}) + (f_{34} - f_4)\right] \tag{F.1c}$$

$$\hat{F}_4 = \frac{1}{2}\left[(f_{1234} - f_{123}) + (f_4 - f_0)\right] \tag{F.1d}$$

The main objective of FS and SFS is to determine the total effect ($target - base$) of all factors considered. In FS, this term is defined as the sum of 15 $\hat{f}$ terms (Equations 3.42–3.45), whereas in SFS, this is obtained by taking the sum of $\hat{F}_i$:

$$f_{1234} - f_0 = \sum_{i=1}^{n} \hat{F}_i = \hat{F}_1 + \hat{F}_2 + \hat{F}_3 + \hat{F}_4 \ , \tag{F.2}$$

thus enables the quantification of the percentage contribution of the four factors, which is not possible from FS. To analyze the degree of dependence of the individual factor, SFS uses the differences between the two estimates from $f_0 \rightarrow f_{1234}$ and $f_{1234} \rightarrow f_0$ as an error measure, yielding

$$\Delta\hat{F}_1 = \frac{1}{2}\left[(f_1 - f_0) - (f_{1234} - f_{234})\right] \tag{F.3a}$$

$$\Delta\hat{F}_2 = \frac{1}{2}\left[(f_{12} - f_1) - (f_{234} - f_{34})\right] \tag{F.3b}$$

$$\Delta\hat{F}_3 = \frac{1}{2}\left[(f_{123} - f_{12}) - (f_{34} - f_4)\right] \tag{F.3c}$$

$$\Delta\hat{F}_4 = \frac{1}{2}\left[(f_{1234} - f_{123}) - (f_4 - f_0)\right], \tag{F.3d}$$

and by definition the sum of all terms in F.3 is zero ($\sum \Delta\hat{F}_i = 0$).

Note that if the SFS approach is valid, the two estimates in Equations F.1 can be used to quantify the effect of the individual factor and should lead to similar results. For instance, $f_1 - f_0 \approx f_{1234} - f_{234}$ and $f_{12} - f_1 \approx f_{234} - f_{34}$. This indicates that synergistic interactions among factors are too weak to distort the separation of the effects. We may further interpret that the left-hand side of Equations F.3 is near zero if no important interactions occur. To represent the overall uncertainty of the methodology, the root-mean-square average (RMS) is used and is given by

$$\text{RMS} = \left(\frac{1}{n}\sum_{i=1}^{n} \Delta\hat{F}_i^2\right)^{1/2} \ . \tag{F.4}$$

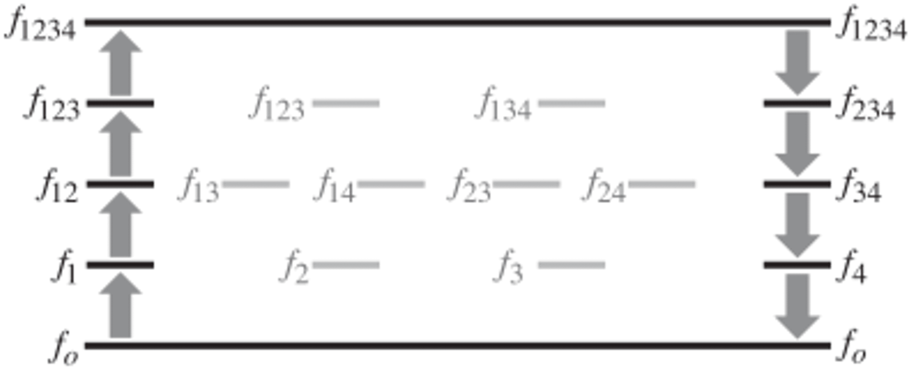

Figure F.1: Sequential factor separation (SFS) for four factors, adopted from Figure 3 of Schär and Kröner (2017). Black bars indicate simulations required for SFS and gray bars additional simulations needed for the complete factor separation (FS) method. For the present study, the f notations refer to the experiments listed in Figure 3.5 of this thesis.

Discussion

The discussion below serves to 1) verify the SFS approach to disentangle the effects of each factor and 2) identify the strength of interactions.

Total effect ($\sum \hat{F}_i$) from all factors to the seasonal-mean (December−January−February, DJF) near-surface concentrations of FLT is computed and presented in Figure F.2a. The distribution of concentration change (*target* − *base*) shows a clear north−south contrast, that is, a decrease over the Arctic and a somewhat homogeneous increase in other regions with an apparent land−sea gradient. In Figure F.2b the influences of emission change ($\hat{F}_1$), particle representation ($\hat{F}_2$), gas−particle partitioning ($\hat{F}_3$) and volatilization ($\hat{F}_4$) are presented. Overall it is evident that the imposed concentration decrease over the Arctic relates strongly to $\hat{F}_2$, that is, the prescribed change from *bulk* to *modal*, yet this effect is weakened by changes in emission ($\hat{F}_1$). The negative signal seen in $\hat{F}_2$ also extends toward the middle latitudes (except over East Asia) and most of the oceans. On the other hand, the results show that volatilization effect explains the distinct pattern of concentration increase shown in Figure F.2a. In particular, over North America $\hat{F}_4$ leads to an increase that is generally higher than the total and those introduced by $\hat{F}_2$ and $\hat{F}_3$. Over East Asia, changes in all factors make a relatively uniform contribution. Over the tropical landmass, $\hat{F}_4$ yields higher increases than the combined effect of $\hat{F}_2$ and $\hat{F}_3$ by more than one order of magnitude whereas $\hat{F}_1$ brings an opposite influence albeit weakly. One particular exception is found for Antarctica and parts of South Pacific Ocean where the concentration increase is not reflected in $\hat{F}_4$ but rather in other factors' effects.

Figure F.2c shows the total uncertainty of the SFS methodology (RMS) and Figure F.2d shows the individual error measure ($\Delta\hat{F}_i$). It is noted that when RMS is large, the separation of the effects would be relative to the design of the *base* and *target* experiments and interactions among factors would play an important role that distorts the inference of main effects (Schär and Kröner, 2017). Overall the results show that 1) the degree of RMS ranges from 30% to 50× higher than $\sum \hat{F}_i$, and 2) $\Delta\hat{F}_i$ terms are of comparable magnitude to their respective $\hat{F}_i$. It is thus concluded that SFS is not suitable for the case considered since the concentration responses are inherently dependent on the factor interactions. Accordingly, the main effects described above may not be valid. Although the current analysis restricted attention to the concentration of FLT, the results for other species and seasons lead to the same conclusions. For this reason, this study applied the original FS technique for sensitivity analysis to allow computing the interaction effects and thus provide a quantitative measure of nonlinearity.

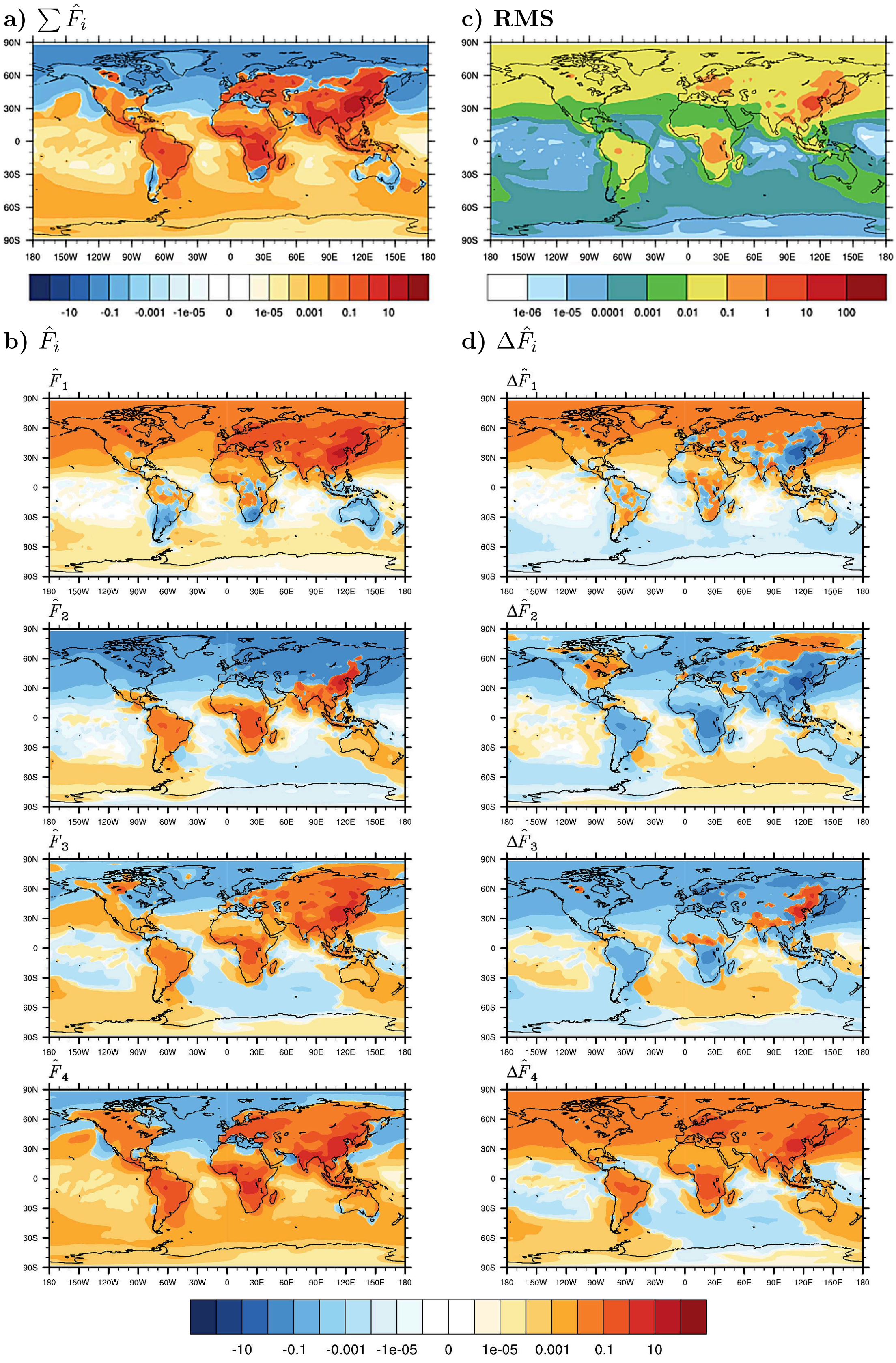

Figure F.2: a) Total effect of four factors ($\sum \hat{F}_i$) on FLT concentrations averaged over December–January–February 2007–2009, b) the overall uncertainty of the SFS method (RMS), c) the four main effects ($\hat{F}_i$), and d) their respective error measures ($\Delta \hat{F}_i$). All units are in ng m^{-3}. Factor i refers to the temporal emission variation ($i = 1$), particulate-phase representation ($i = 2$), the choice of gas–particle partitioning scheme ($i = 3$), and volatilization ($i = 4$).

Appendix G
EMAC-SVOC Sensitivity Study: Direct and Interaction Effects of Factors on Predicted Near-Surface PAH Concentrations

(Intentionally left blank)

a) PHE

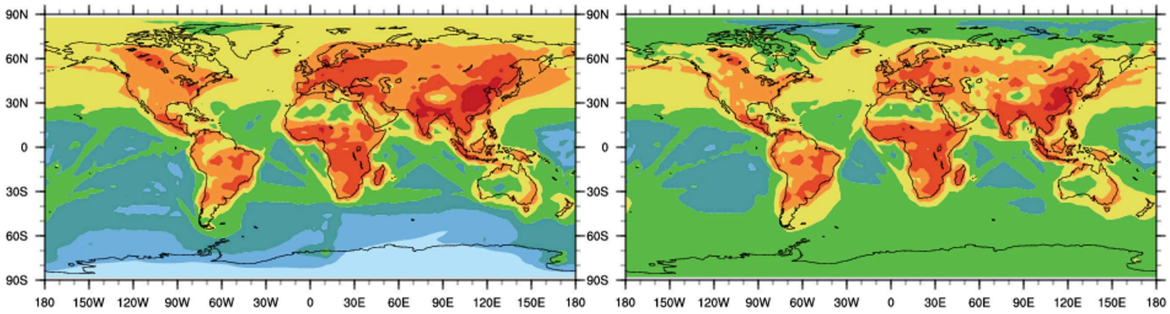

b) PYR

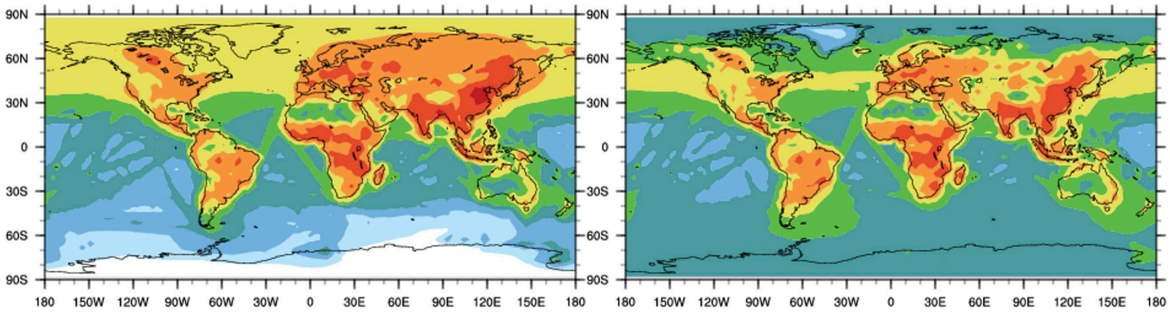

c) FLT

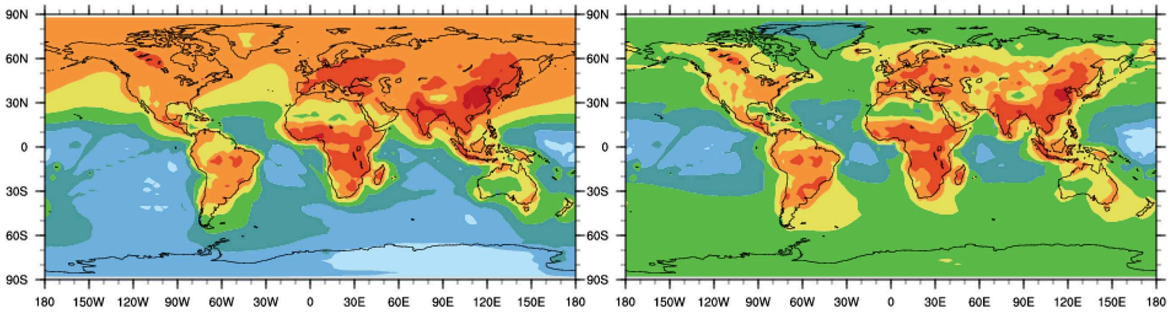

d) BaP

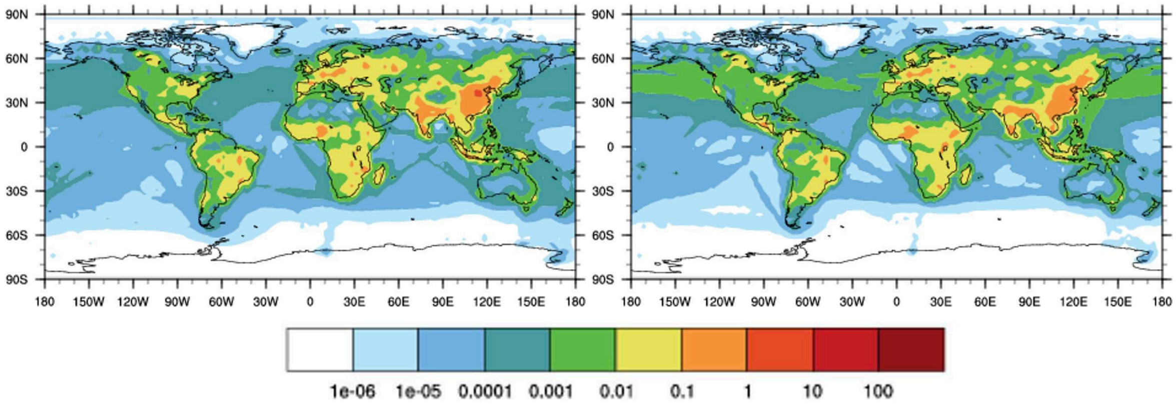

Figure G.1: Seasonal mean near-surface PAH concentrations (ng m^{-3}) from the *base* simulation (f_0) for December–January–February (left panels) and June–July–August (right panels) 2007–2009. Here, f_0 represents a simulation applying annual emissions, the *bulk* scheme, the Lohmann–Lammel partitioning scheme, and no volatilization.

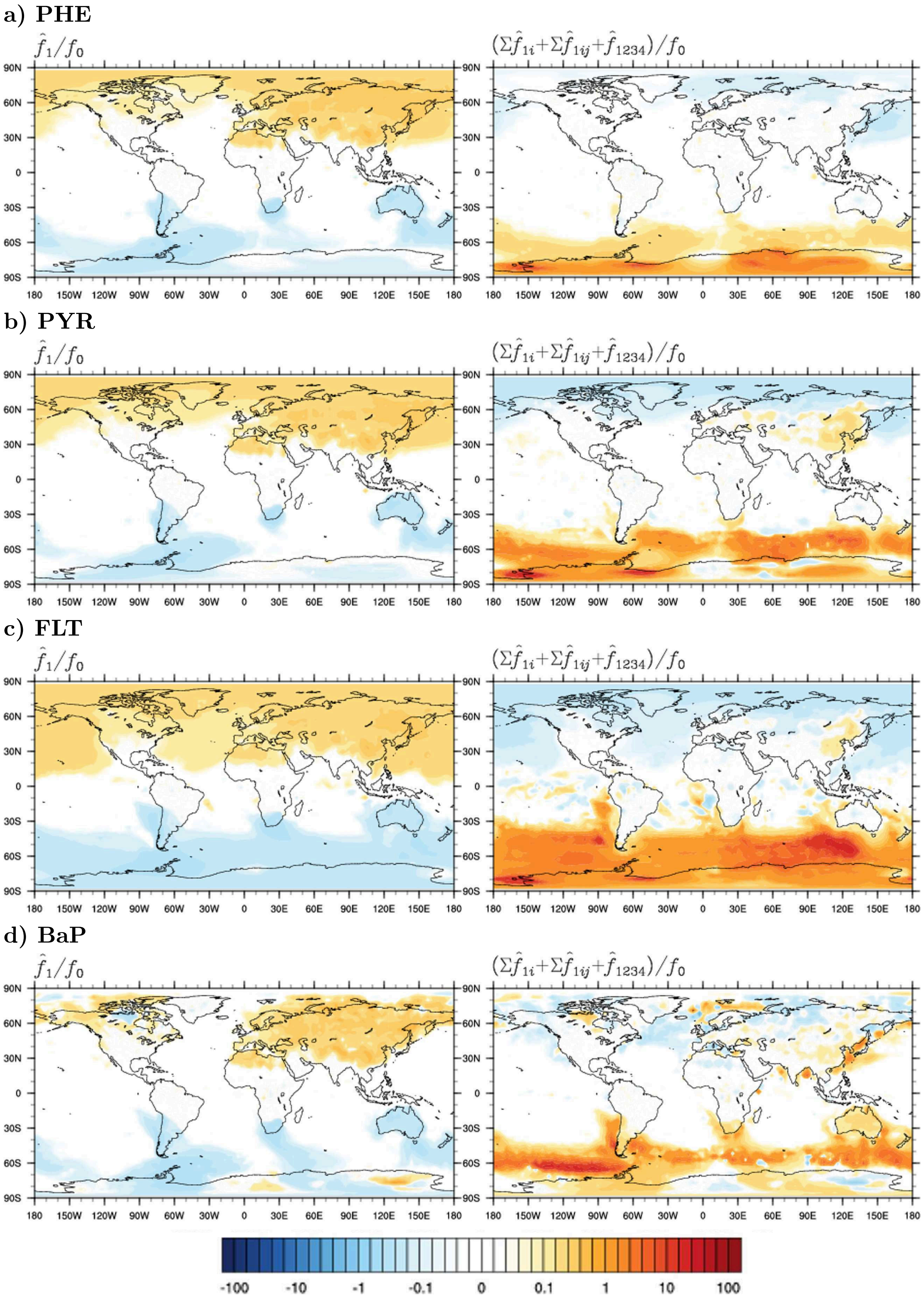

Figure G.2: The effects of monthly emissions (in place of annual emissions) on near-surface PAH concentrations relative to concentrations from the base simulation (f_0), averaged over December−January−February 2007−2009: (left panels) direct effects ($\hat{f}_1$), expressed as the difference between two distributions: $\hat{f}_1 = f_1 - f_0$; (right panels) interaction effects, expressed as the sum of two ($\Sigma\hat{f}_{1j}$, $j \neq 1$), three ($\Sigma\hat{f}_{1jk}$, $j \neq k \neq 1$), and four ($\hat{f}_{1234}$) factor interactions.

a) PHE

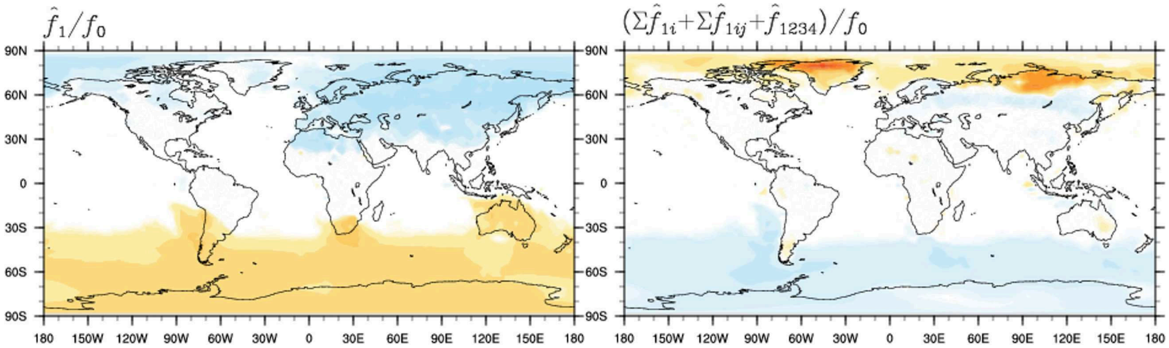

b) PYR

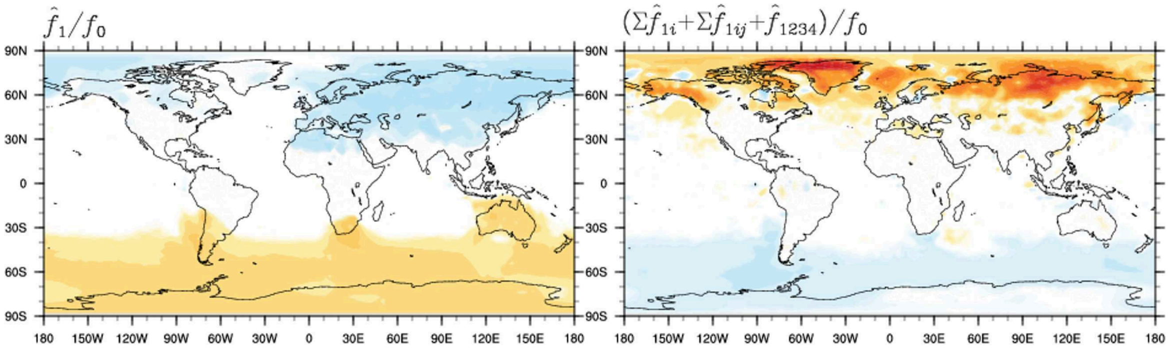

c) FLT

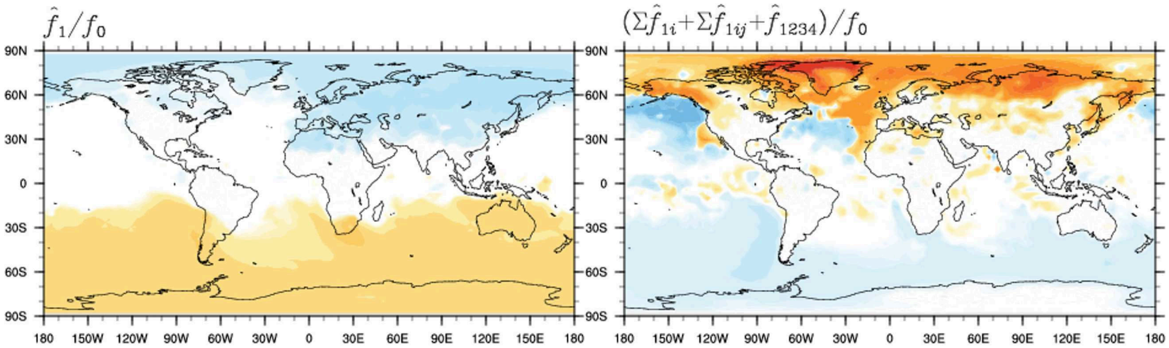

d) BaP

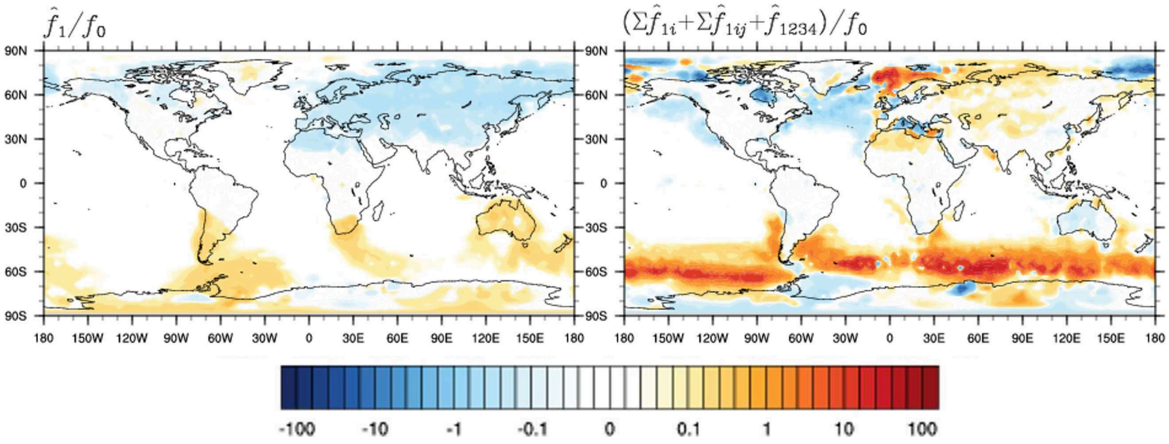

Figure G.3: Same as Figure G.2, but averaged over June–July–August 2007–2009

a) **PHE**

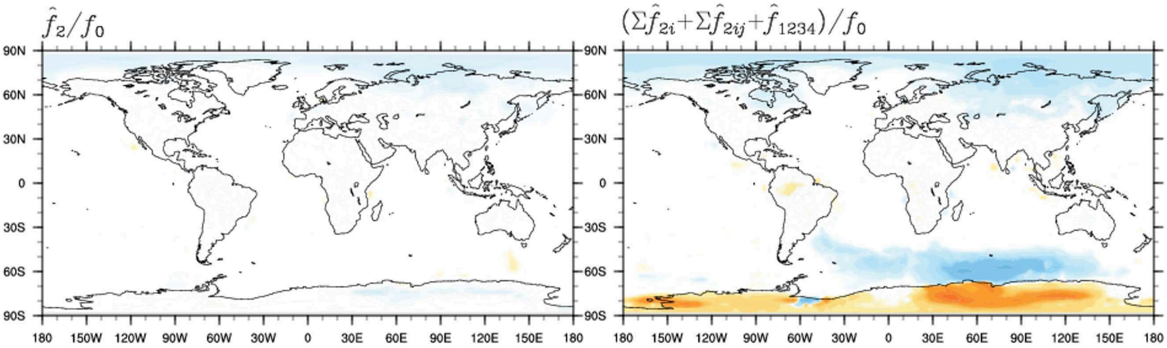

b) **PYR**

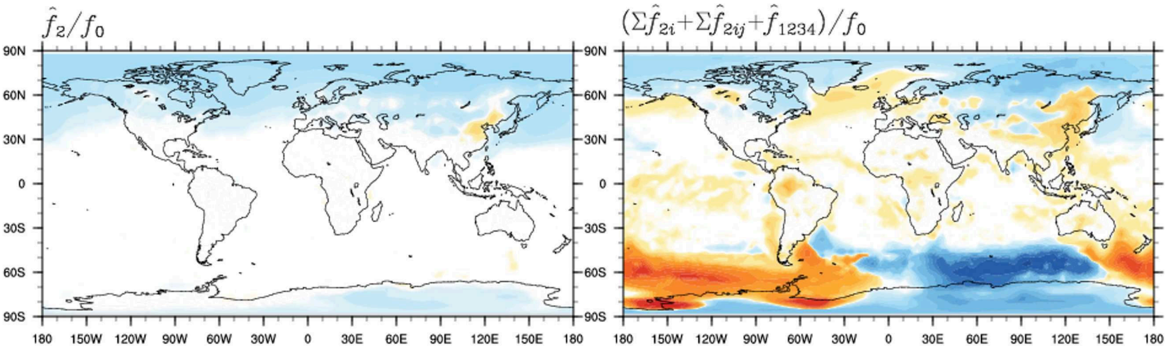

c) **FLT**

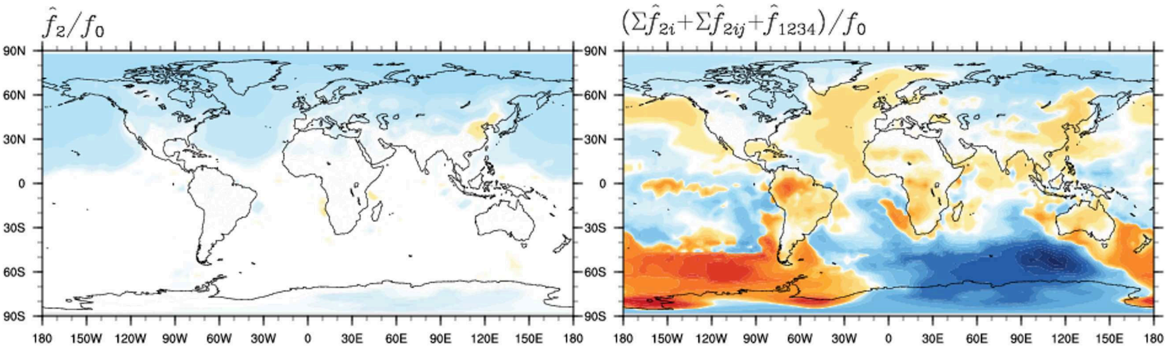

d) **BaP**

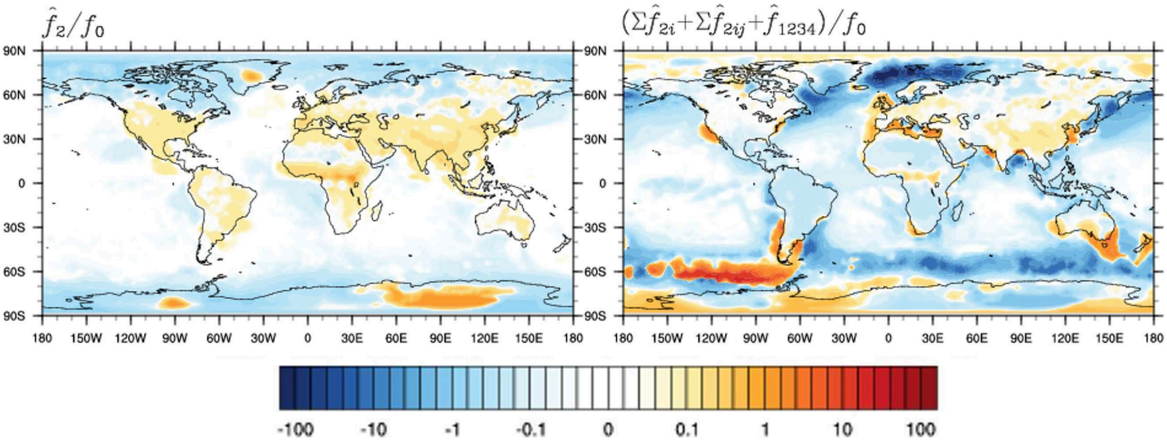

Figure G.4: The effects of the *modal* scheme (in place of the *bulk* scheme) for particulate-phase representation on near-surface PAH concentrations relative to concentrations from the base simulation (f_0), averaged over December–January–February 2007–2009: (left panels) direct effects ($\hat{f}_2$), expressed as the difference between two distributions: $\hat{f}_2 = f_2 - f_0$; (right panels) interaction effects, expressed as the sum of two ($\Sigma\hat{f}_{2j}$, $j \neq 2$), three ($\Sigma\hat{f}_{2jk}$, $j \neq k \neq 2$), and four ($\hat{f}_{1234}$) factor interactions.

a) **PHE**

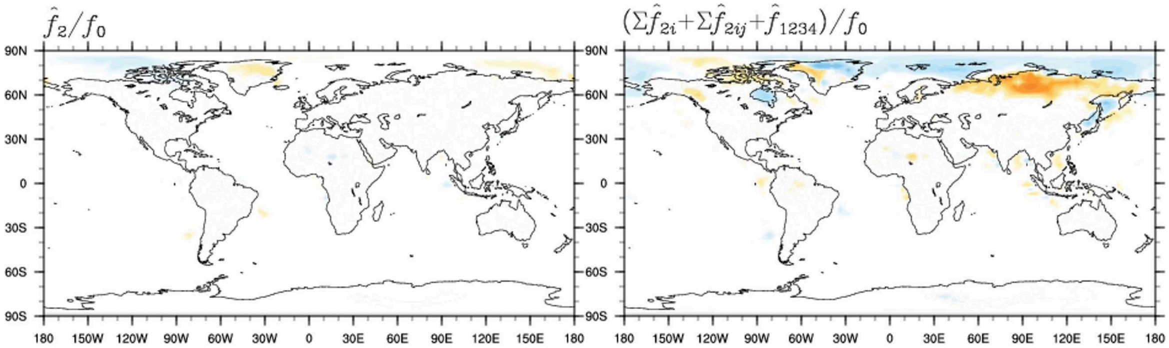

b) **PYR**

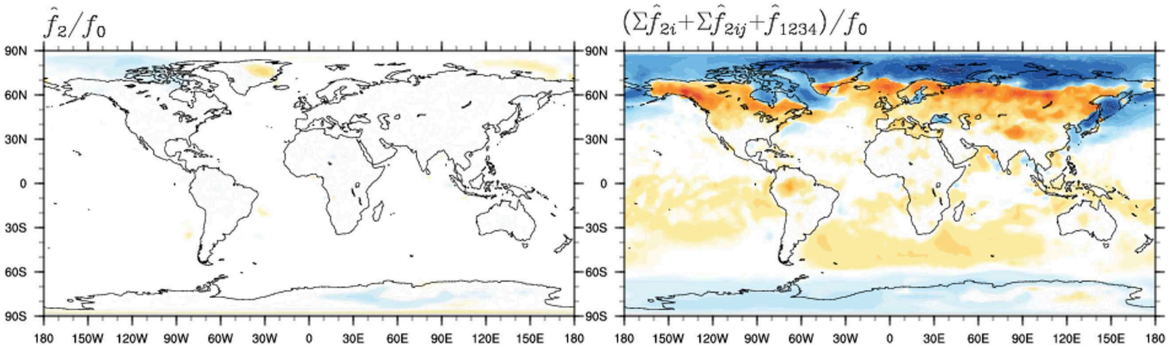

c) **FLT**

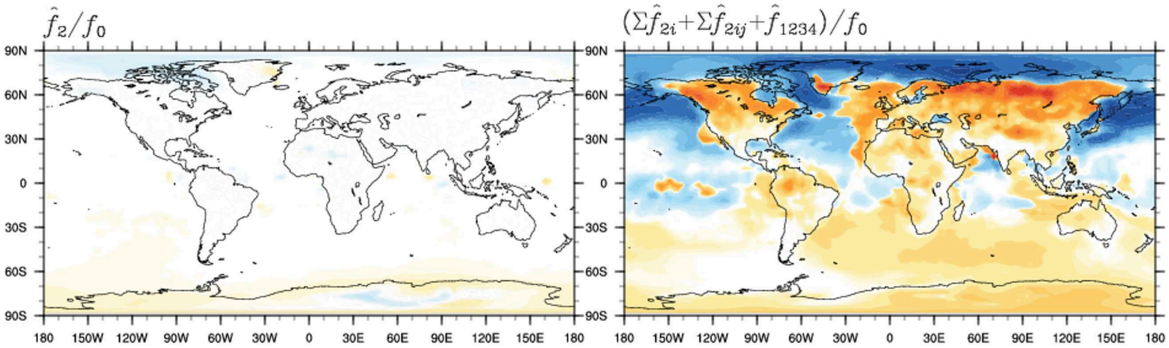

d) **BaP**

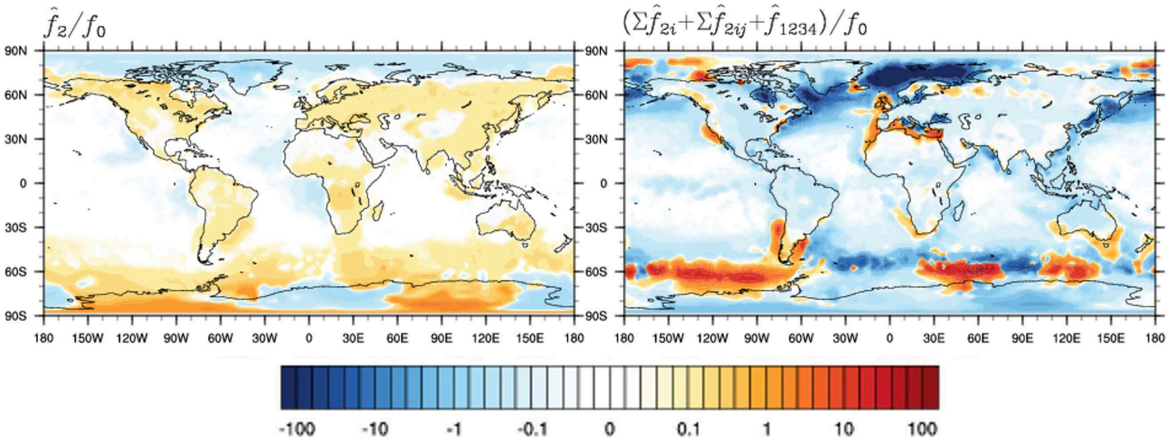

Figure G.5: Same as Figure G.4, but averaged over June–July–August 2007–2009

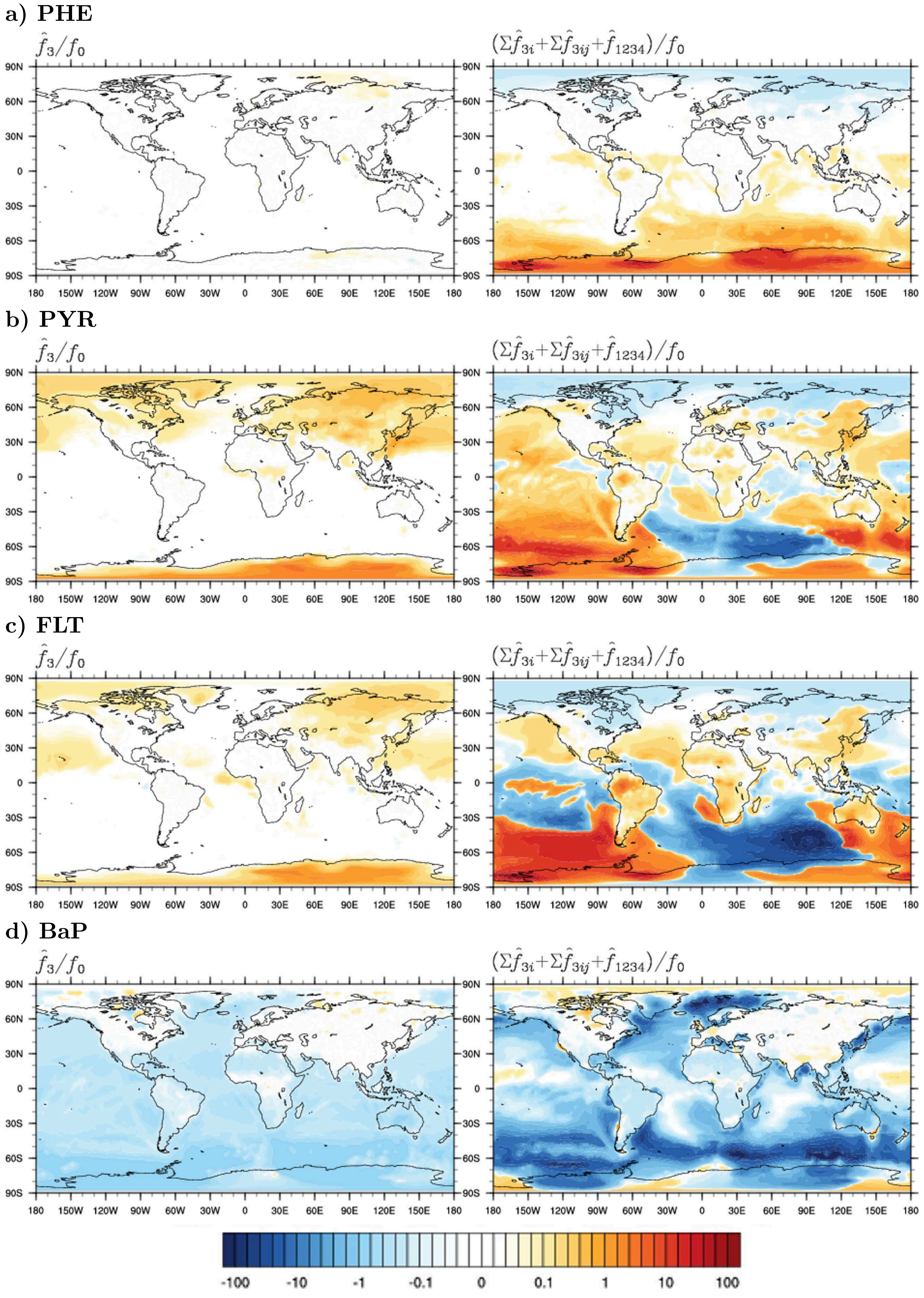

Figure G.6: The effects of ppLFER scheme (in place of Lohmann−Lammel scheme) for gas−particle partitioning on near-surface PAH concentrations relative to concentrations from the base simulation (f_0), averaged over December−January−February 2007−2009: (left panels) direct effects ($\hat{f}_3$), expressed as the difference between two distributions: $\hat{f}_3 = f_3 - f_0$; (right panels) interaction effects, expressed as the sum of two ($\Sigma\hat{f}_{3j}$, $j \neq 3$), three ($\Sigma\hat{f}_{3jk}$, $j \neq k \neq 3$), and four ($\hat{f}_{1234}$) factor interactions.

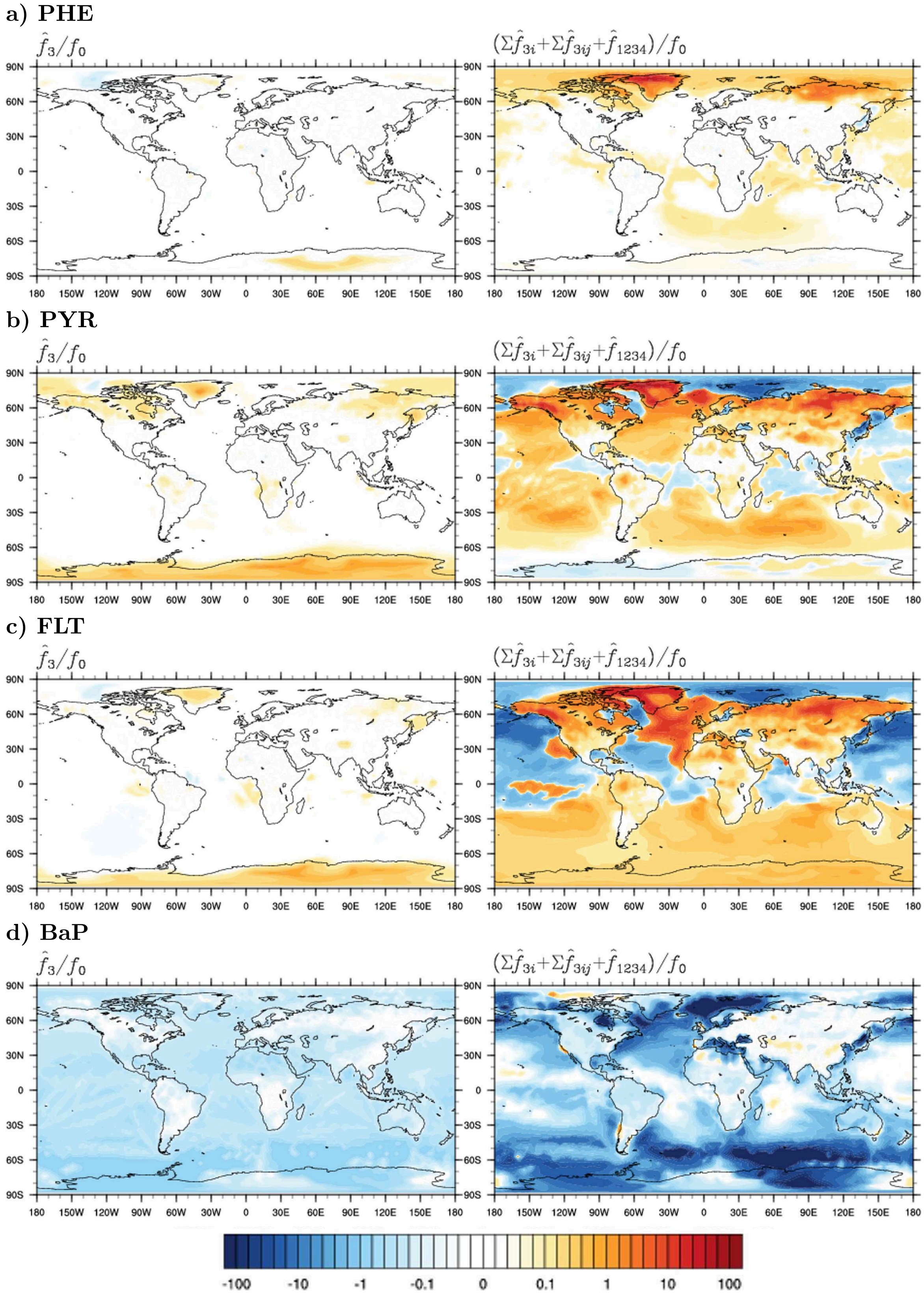

Figure G.7: Same as Figure G.6, but averaged over June–July–August 2007–2009

a) PHE

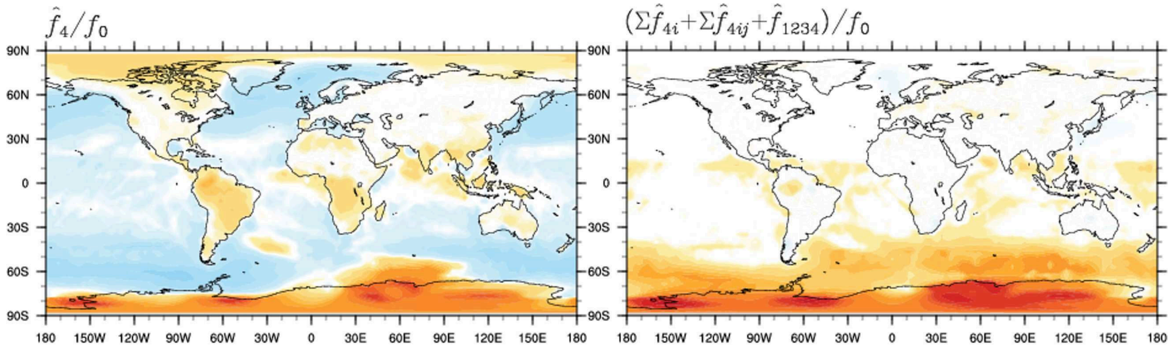
$\hat{f}_4/f_0$

$(\Sigma\hat{f}_{4i}+\Sigma\hat{f}_{4ij}+\hat{f}_{1234})/f_0$

b) PYR

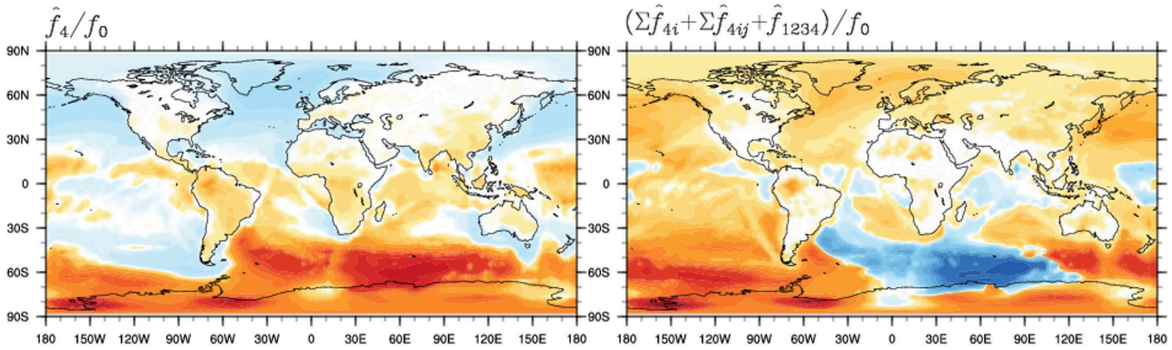
$\hat{f}_4/f_0$

$(\Sigma\hat{f}_{4i}+\Sigma\hat{f}_{4ij}+\hat{f}_{1234})/f_0$

c) FLT

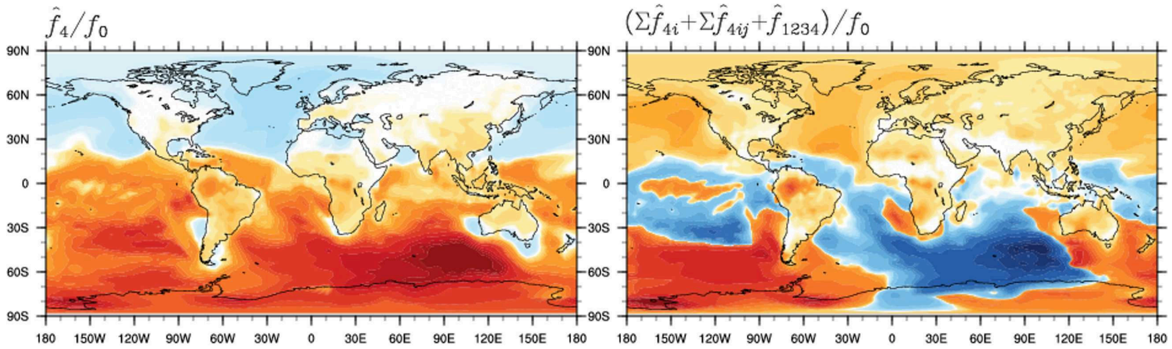
$\hat{f}_4/f_0$

$(\Sigma\hat{f}_{4i}+\Sigma\hat{f}_{4ij}+\hat{f}_{1234})/f_0$

d) BaP

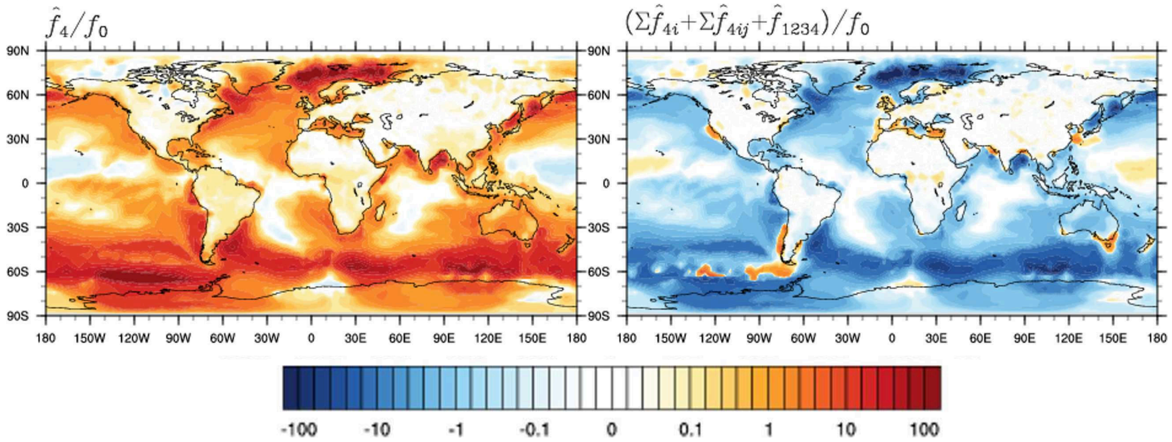
$\hat{f}_4/f_0$

$(\Sigma\hat{f}_{4i}+\Sigma\hat{f}_{4ij}+\hat{f}_{1234})/f_0$

Figure G.8: The effects of volatilization on near-surface PAH concentrations relative to concentrations from the base simulation (f_0), averaged over December–January–February 2007–2009: (left panels) direct effects ($\hat{f}_4$), expressed as the difference between two distributions: $\hat{f}_4 = f_4 - f_0$; (right panels) interaction effects, expressed as the sum of two ($\Sigma\hat{f}_{4j}$, $j \neq 4$), three ($\Sigma\hat{f}_{4jk}$, $j \neq k \neq 4$), and four ($\hat{f}_{1234}$) factor interactions.

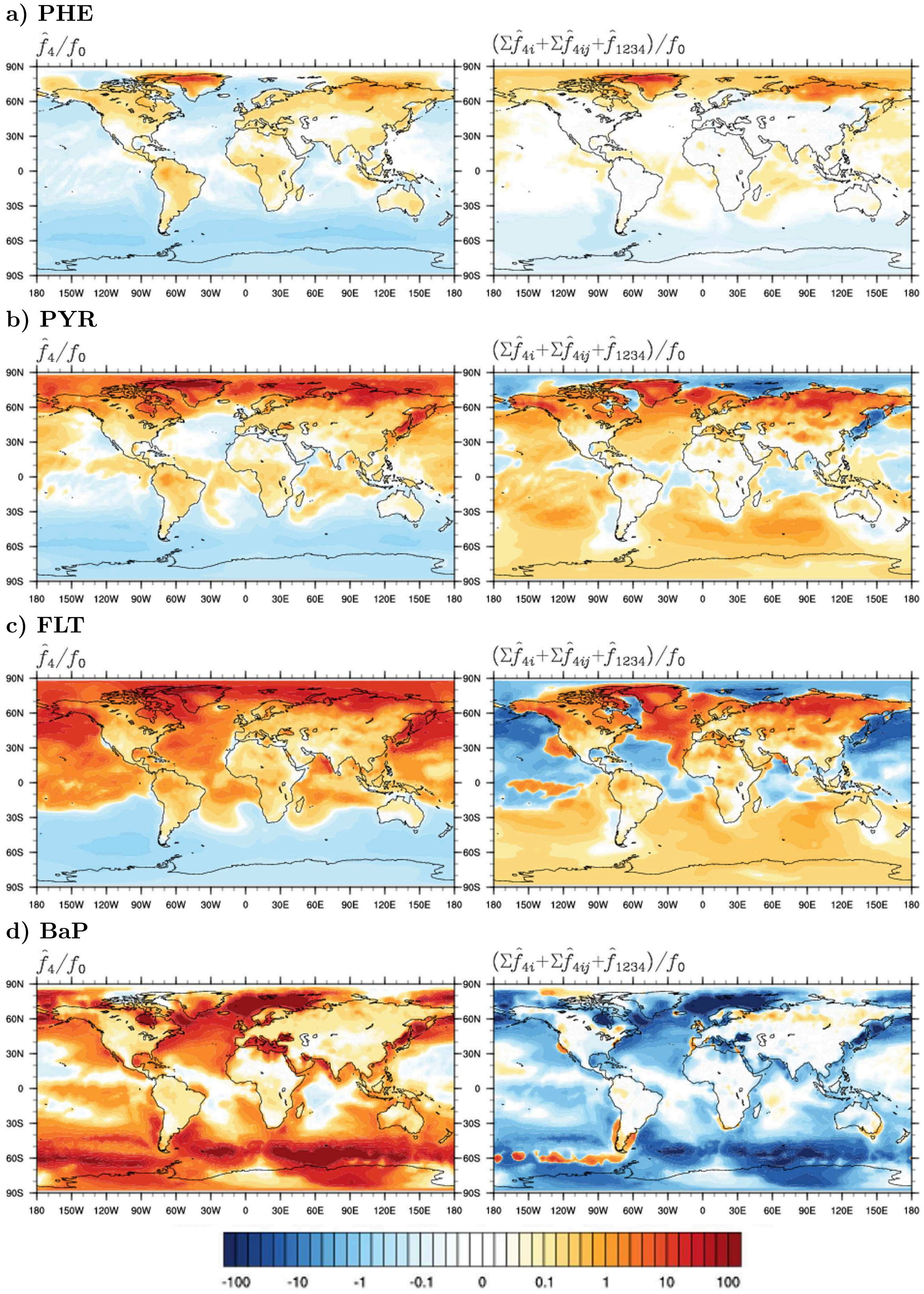

Figure G.9: Same as Figure G.8, but averaged over June–July–August 2007–2009

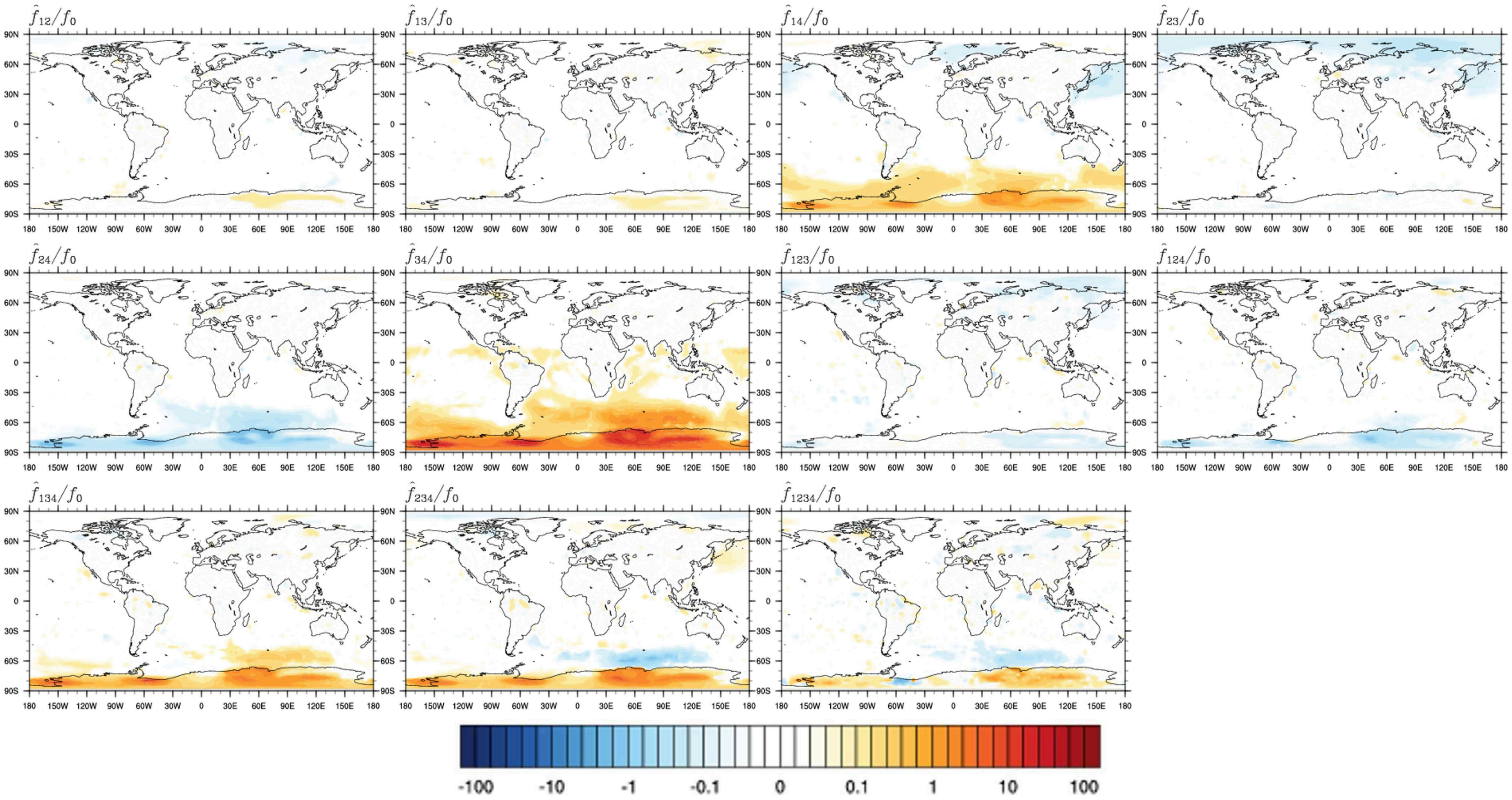

Figure G.10: Average effects on near-surface PHE concentrations relative to concentrations from the base simulation (f_0) from interactions between two ($\hat{f}_{ij}$), three ($\hat{f}_{ijk}$), and four different factors ($\hat{f}_{1234}$); means of December–January–February 2007–2009.

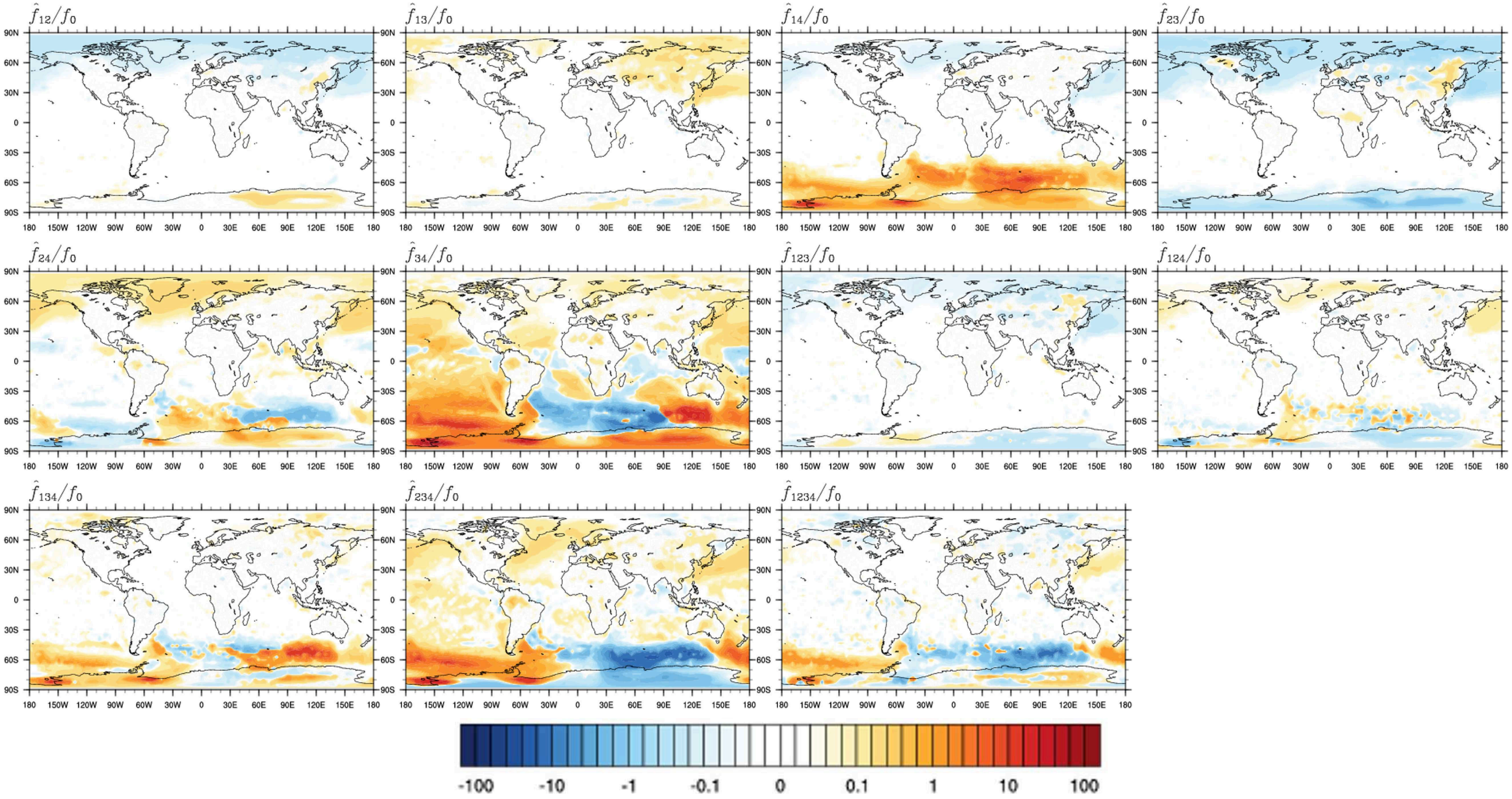

$\hat{f}_{12}/f_0$ $\hat{f}_{13}/f_0$ $\hat{f}_{14}/f_0$ $\hat{f}_{23}/f_0$

$\hat{f}_{24}/f_0$ $\hat{f}_{34}/f_0$ $\hat{f}_{123}/f_0$ $\hat{f}_{124}/f_0$

$\hat{f}_{134}/f_0$ $\hat{f}_{234}/f_0$ $\hat{f}_{1234}/f_0$

Figure G.11: Same as Figure G.10, but for PYR

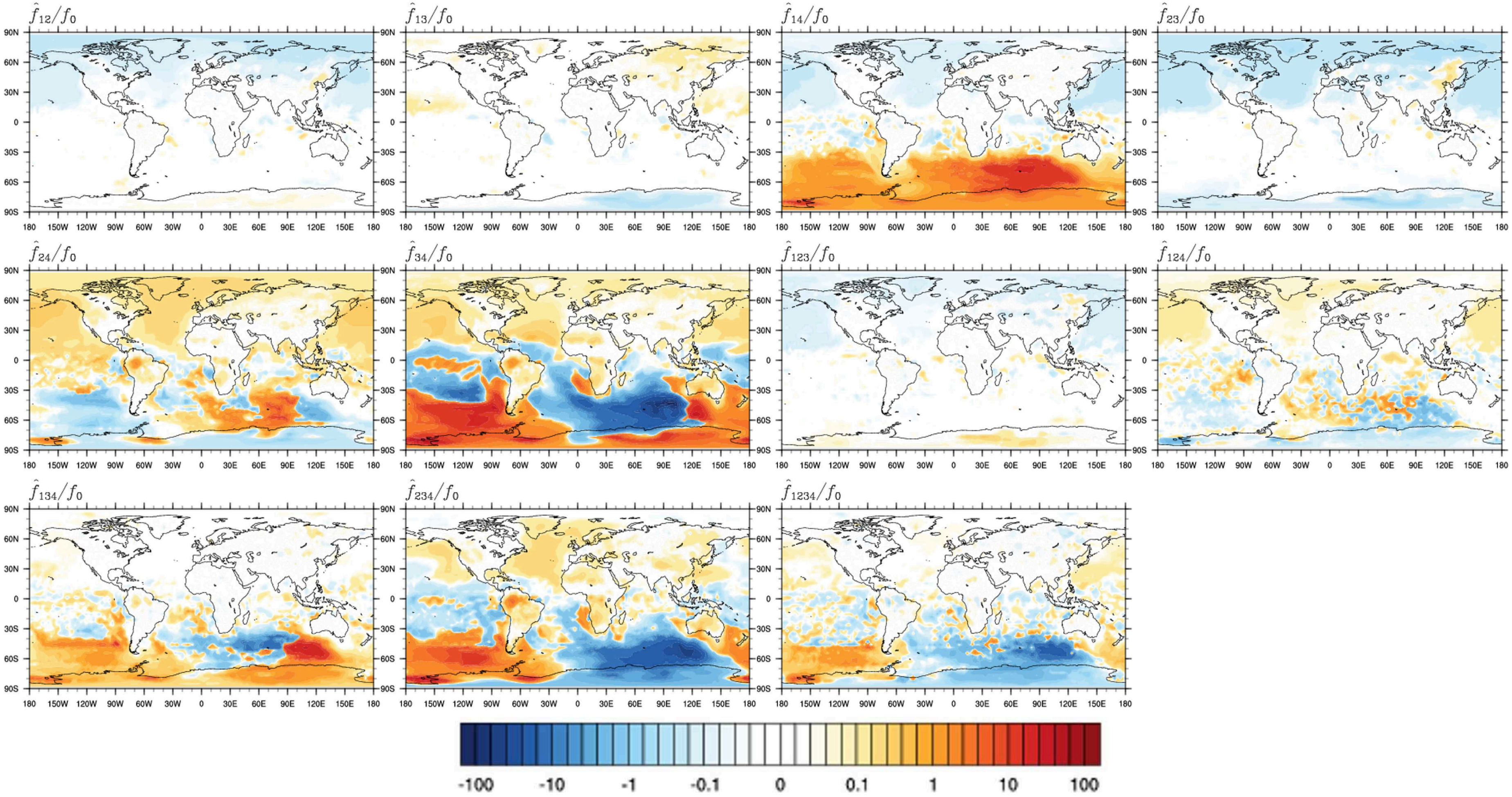

Figure G.12: Same as Figure G.10, but for FLT

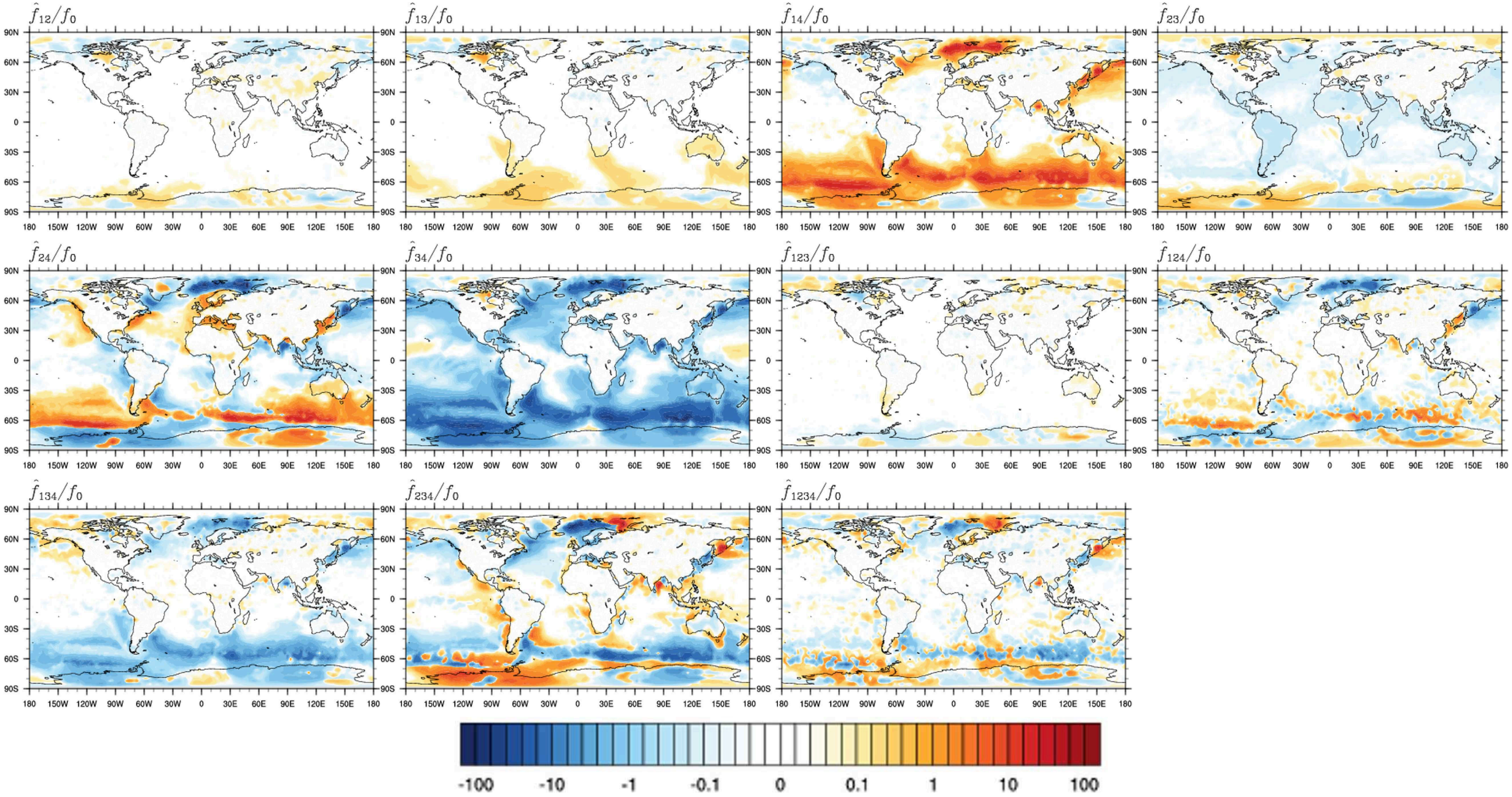

Figure G.13: Same as Figure G.10, but for BaP

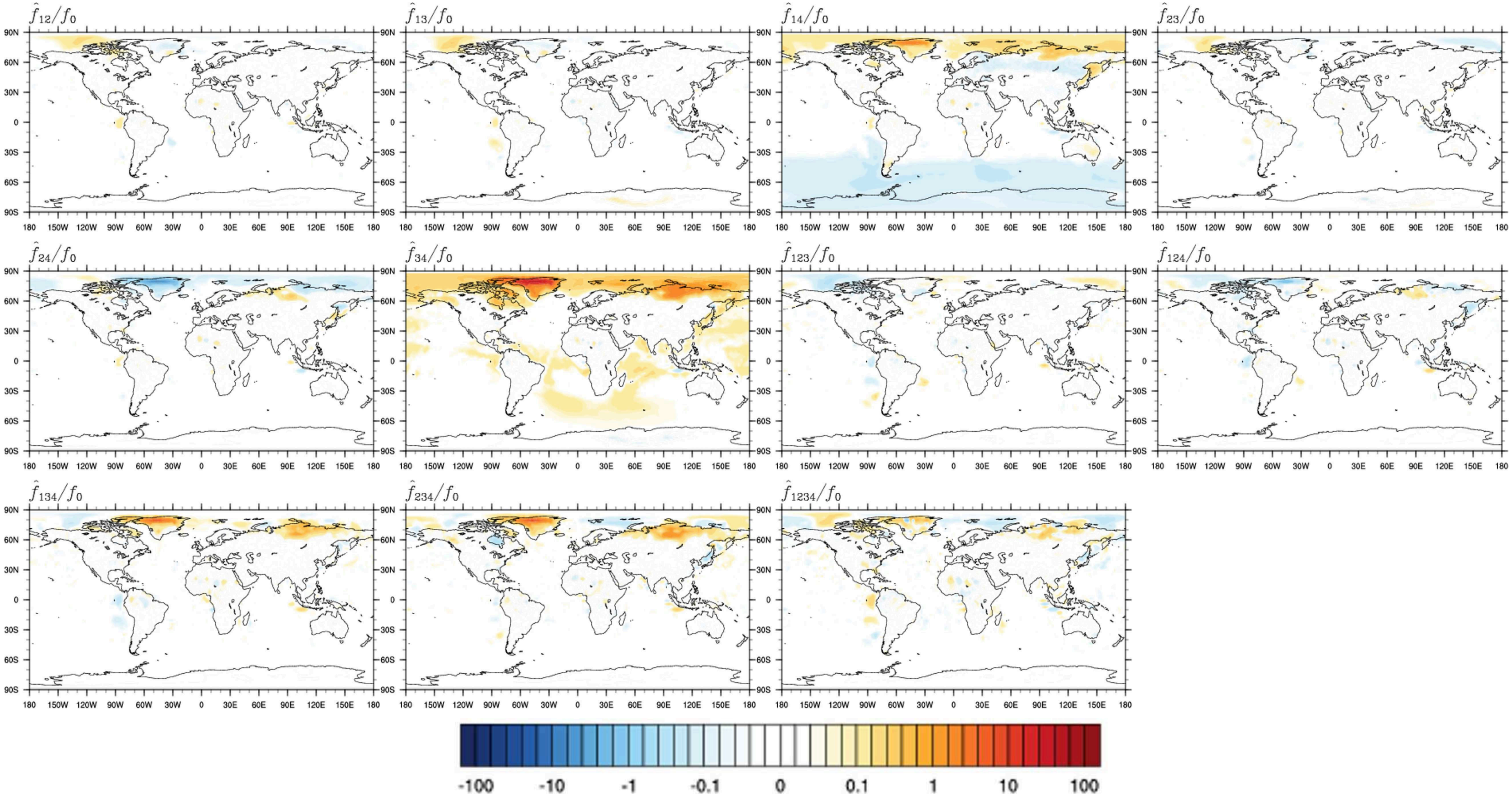

Figure G.14: Average effects on near-surface PHE concentrations relative to concentrations from the base simulation (f_0) from interactions between two ($\hat{f}_{ij}$), three ($\hat{f}_{ijk}$), and four different factors ($\hat{f}_{1234}$); means of June–July–August 2007–2009.

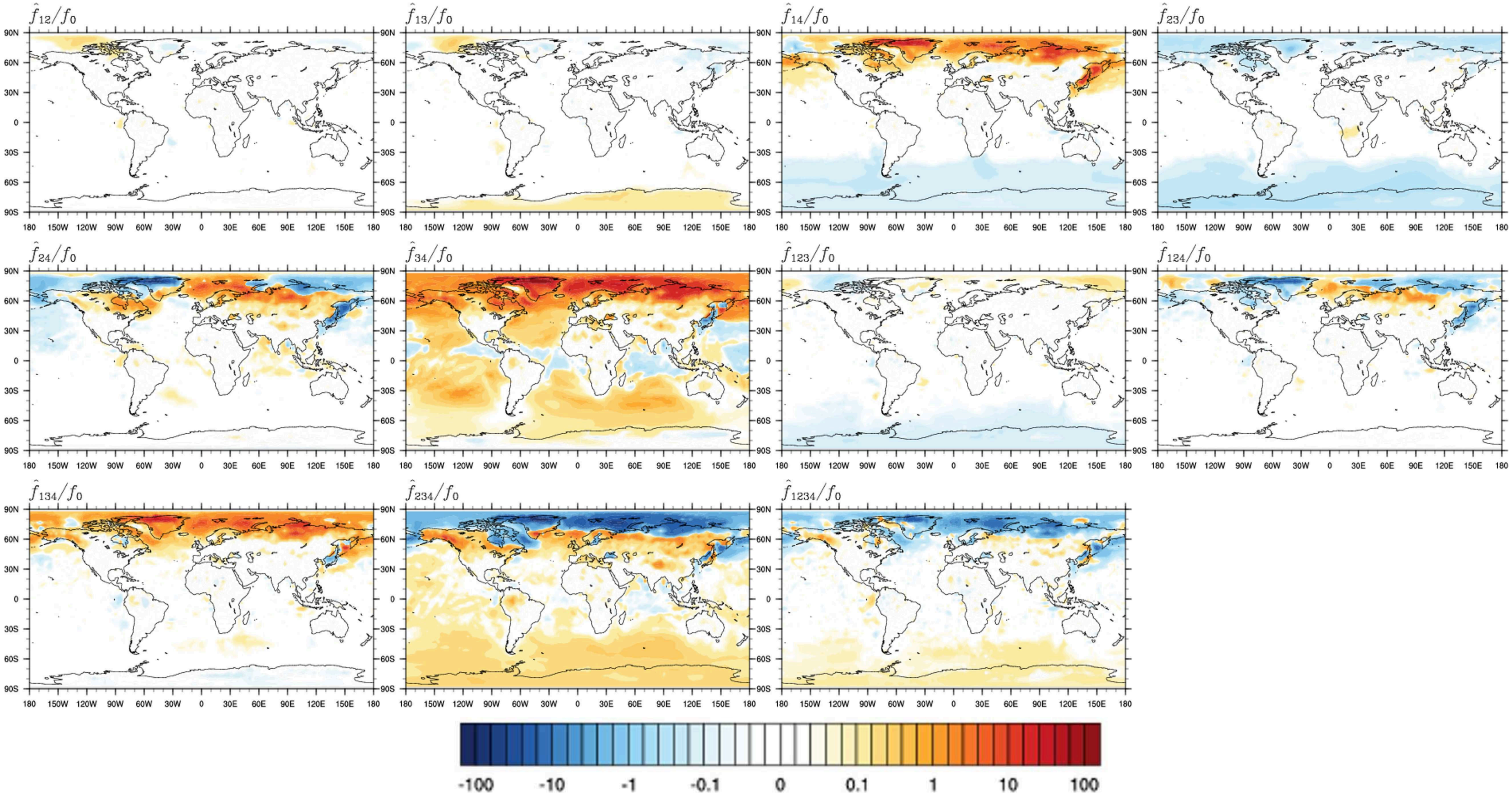

Figure G.15: Same as Figure G.14, but for PYR

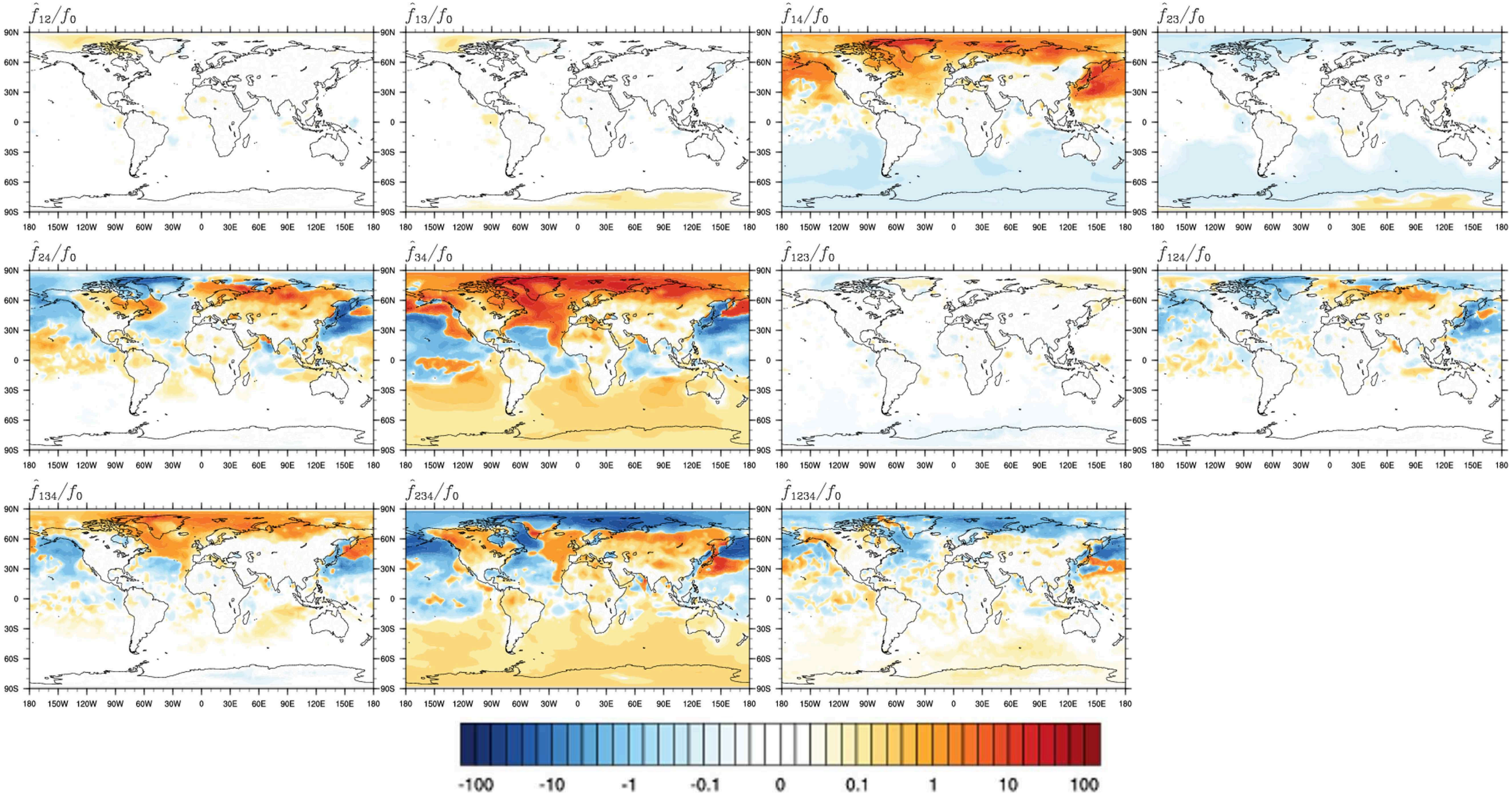

Figure G.16: Same as Figure G.14, but for FLT

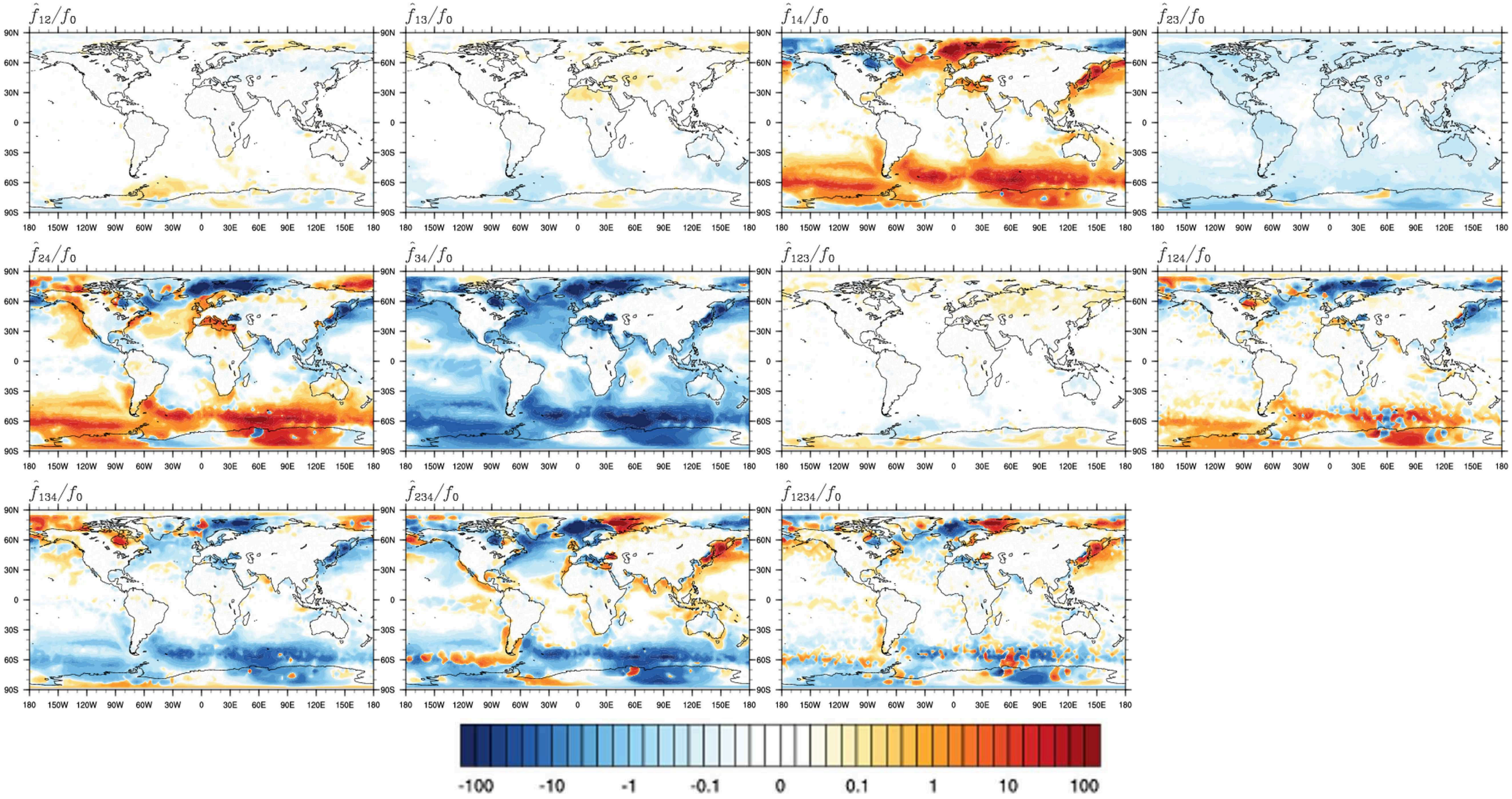

Figure G.17: Same as Figure G.14, but for BaP

Appendix H
EMAC-SVOC Sensitivity Study: Effects of All Factors Combination on Model Performance

In the following, simulated outputs from 16 sensitivity experiments are compared against observation data for two seasons (DJF and JJA) and two regions (Arctic and NH mid-latitudes). Note that while results from factor separation analysis express the effects of each selected factor (see Chapter 3, Section 3.5.2) relative to a reference (i.e., f_0), the discussion below focuses on how the factors affect EMAC-SVOC performance in general. Here, the mean concentration difference (hereinafter, ΔConc) across all possible combinations of two experiments is used, where only one of the four factors is different between the two experiments. For example, the effect of emission seasonality (*fac1*) will be represented as mean of SBLN – ABLN, SBLW – ABLW, SBPN – ABPN, SBPW – ABPW, SMLN – AMLN, SMLW – AMLW, SMPN – AMPN, and SMPW – AMPW (refer to Figure 3.5 for the acronyms). Note that if the mean difference from the first four pairs is different with that from the last four, it indicates that the *fac1* interaction with *fac2* (particulate-phase representation) plays an important role in the model performance.

Phenanthrene

Figure H.1 displays the seasonal mean values and mean bias (MB) of PHE concentrations averaged across monitoring stations in the Arctic and NH mid-latitudes. As shown, all experiments underestimate the seasonal concentrations over the Arctic, suggesting an inherent model bias. It is also apparent that the model is most sensitive to the change in emission interval (*fac1*). One can see that concentration increases in DJF (hence, MB improves) and decreases in JJA (hence, MB deteriorates) when monthly emission is applied in the simulations. This result is expected and is attributed to the seasonal cycle of emissions over NH. On average, ΔConc is 0.009 ng m^{-3} in DJF and -0.007 ng m^{-3} in JJA. Volatilization (*fac4*) appears as the second dominant factor as it contributes to decrease PHE concentrations in DJF and to increase them in JJA, an effect opposite to that of *fac1*. The degree of *fac4* effect is four times smaller than

a) Arctic

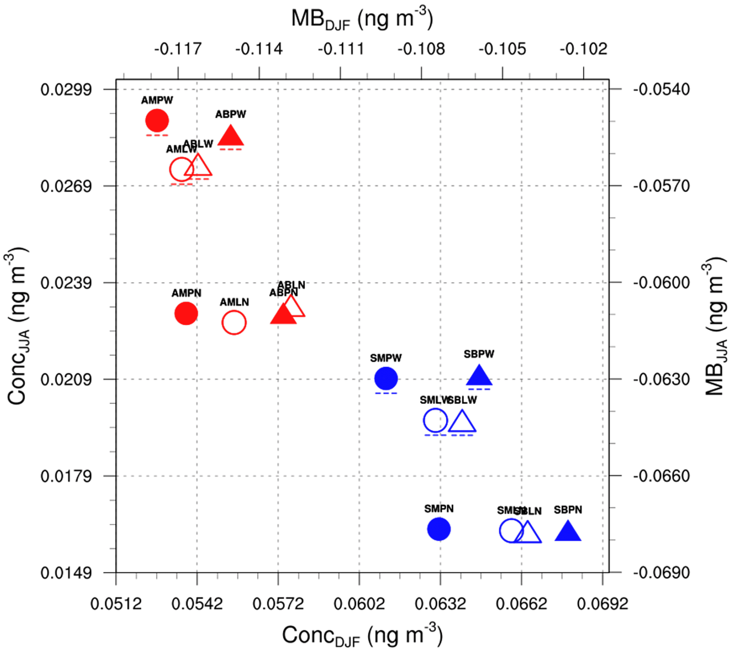

b) NH mid-latitudes

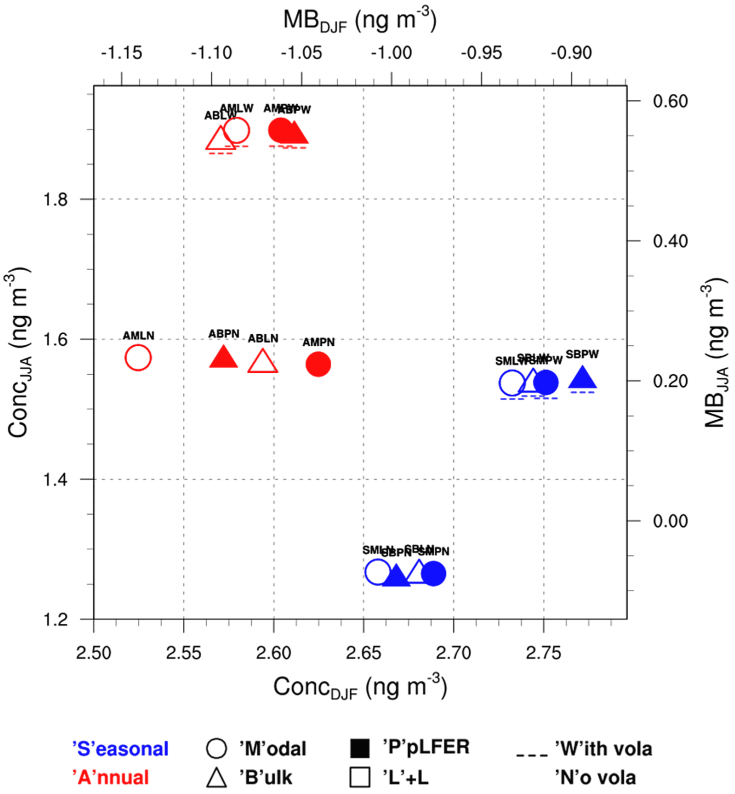

Figure H.1: Seasonal mean PHE concentrations and mean bias (MB) from 16 sensitivity experiments, averaged across stations in the a) Arctic and b) northern mid-latitudes. Changes in color represent the change in emission interval (*fac1*), changes in shape represent the change in particulate-phase representation (*fac2*), and changes in shape fill represent the change in gas−particle partitioning scheme (*fac3*). Symbols with a dashed line refer to model experiments with volatilization (*fac4*).

fac1 effect, but they become comparable in JJA due to pronounced volatilization in boreal summer. The model performance is less sensitive to the choice of aerosol-phase treatment (*fac2*) and gas−particle partitioning scheme (*fac3*). Nevertheless, it is found that the *modal* scheme enhances the underestimation in DJF when it interacts with the ppLFER scheme ($\Delta\mathrm{Conc}_{\mathrm{DJF}} = -0.003$ to -0.005 ng m^{-3}).

For the northern mid-latitudes, the model response is still dominated by the change in *fac1*, followed by the change in *fac4*. Due to proximity to emission sources, the response to monthly emissions is stronger than that found for the Arctic, i.e., 0.127 ng m^{-3} in DJF and -0.330 ng m^{-3} in JJA. The emission change also brings model predictions closer to observations. As for volatilization, its effect is positive (concentration increases) in both seasons (on average, $\Delta\mathrm{Conc}_{\mathrm{DJF}} = 0.066$ and $\Delta\mathrm{Conc}_{\mathrm{JJA}} = 0.300$ ng m^{-3}), which leads to a smaller underestimation in DJF and a higher overestimation in JJA. The effects of alternating *fac2* and *fac3* are small-to-negligible, particularly during the summer months. This finding is somewhat expected given the fact that smaller aerosol fraction of the most-volatile PAH in summer coincides with an increase in temperature which increases the vapor pressure of the compound and decreases the gas−particle partition coefficient.

Pyrene

The effects of individual factor on PYR concentrations over the Arctic were found to vary by season (Figure H.2a). In DJF, the largest contribution to concentration differences between experiments comes from the choice of *fac2*. In particular, the *modal* scheme decreases the concentrations ($\Delta\mathrm{Conc}_{\mathrm{DJF}} = -0.025$ to -0.073 ng m^{-3}) and produces negative biases. The effects of monthly emissions and volatilization are comparable but of opposite signs, being positive for the former and overall negative for the latter. Compared to *fac2* effect, the concentration differences imposed by both factor changes are smaller by nearly a factor of two in the *bulk*-scheme scenario and by around a factor of six in the *modal*-scheme scenario. The influence *fac3* depends on the selected *fac2* because only in the *bulk* (*modal*) scheme scenario is there a positive (negative) response to the ppLFER scheme. Turning now to JJA, the results suggest that volatilization has a positive effect on predicted PYR concentrations, with an average increase being 0.016 ng m^{-3}, and results in positive model biases. The effects of *fac2* and *fac3* changes are very small but become apparent when volatilization is applied. Specifically, using the *modal* scheme increases JJA concentrations by 0.004 ng m^{-3} whereas the ppLFER scheme brings an increase of 0.009 ng m^{-3}, thereby enhancing the overestimation. Also in JJA, the model performance is least sensitive to the change in emission interval.

In Figure H.2b it is shown that all experiments overestimate PYR concentrations over NH mid-latitudes in both seasons. The differences in predictions are most by the positive effect of volatilization which magnifies the overestimation. Here, the average concentration increase is 0.124 ng m^{-3} in DJF and twice that in JJA. The effect of ppLFER scheme is also positive and tends to be stronger when volatilization is applied (on average, $\Delta\mathrm{Conc}_{\mathrm{DJF}} = 0.106$ ng m^{-3} and $\Delta\mathrm{Conc}_{\mathrm{JJA}} = 0.062$ ng m^{-3}). Seasonal emission increases concentrations in DJF (0.053 ng m^{-3}) but decreases those in JJA (-0.142 ng m^{-3}). The *modal* scheme tends to show the opposite,

a) Arctic

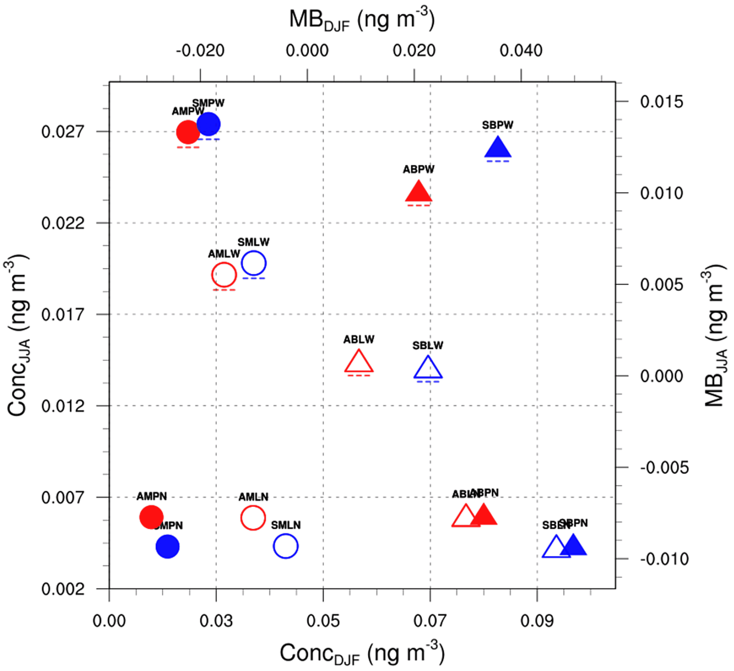

b) NH mid-latitudes

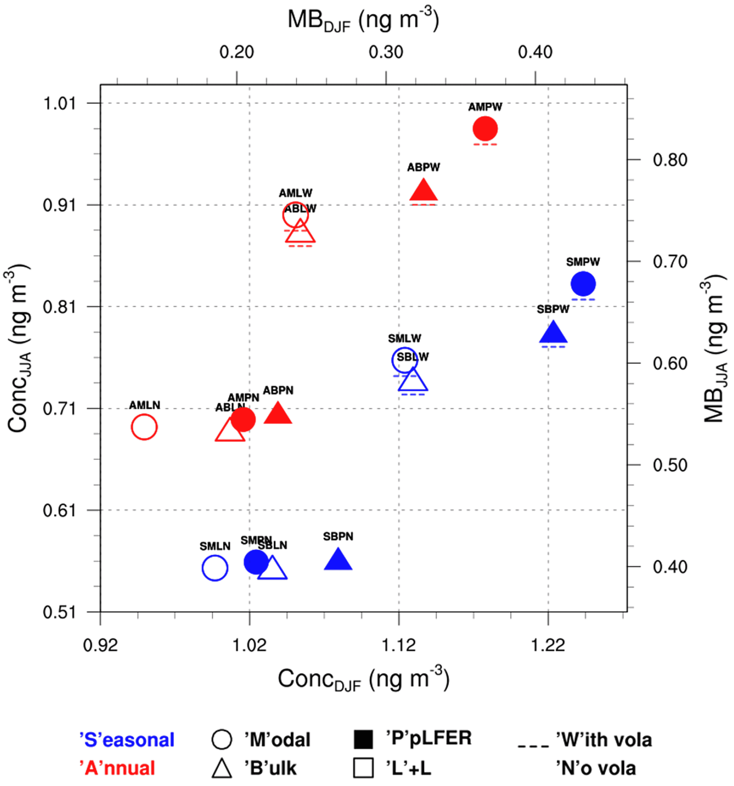

Figure H.2: Same as Figure H.1, but for PYR concentrations that is, a decrease in DJF and an increase in JJA with an average response in both seasons being 0.030 ng m^{-3}.

Fluoranthene

PYR and FLT share some similarities as further discussed below. Figure H.3a shows that *fac2* effect is dominant on Arctic concentrations in DJF. In particular, the *modal* scheme decreases the simulated concentrations (on average, $\Delta\mathrm{Conc}_{\mathrm{DJF}} = -0.124$ ng m^{-3}) and improves MB. The opposite (positive) signal is expected from monthly emissions and volatilization, with mean $\Delta\mathrm{Conc}_{\mathrm{DJF}}$ being 0.020 ng m^{-3} and 0.045 ng m^{-3}, respectively. The ppLFER scheme leads to a concentration decrease (-0.034 ng m^{-3}), indicating shorter lifetime, except when in combination with the *bulk* scheme and volatilization. In JJA, the positive effect of volatilization prevails and becomes dominant (on average, $\Delta\mathrm{Conc}_{\mathrm{JJA}} = 0.072$ ng m^{-3}) and the experiments produce a systematic positive bias. The change in gas−particle partitioning scheme yields noticeable differences only in volatilizaton experiments with $\Delta\mathrm{Conc}_{\mathrm{JJA}}$ leading to higher biases (0.027 ng m^{-3}). Similarly, the sign of response due to emission change depends on the interaction with *fac4*, albeit small $\Delta\mathrm{Conc}_{\mathrm{JJA}}$ values in comparison to the others. It is positive if volatilization is accounted for ($\Delta\mathrm{Conc}_{\mathrm{JJA}} = 0.007$ ng m^{-3}) and negative if volatilization is neglected ($\Delta\mathrm{Conc}_{\mathrm{JJA}} = -0.004$ ng m^{-3}).

All experiments in Figure H.3b show a consistent positive bias for FLT concentrations in the northern mid-latitudes. The effect of volatilization is positive and relatively stronger than those of other factor changes. $\Delta\mathrm{Conc}$ ranges from 0.121 ng m^{-3} to 0.529 ng m^{-3}, higher in JJA than in DJF by approximately two times. Seasonal emission increases DJF concentrations ($\Delta\mathrm{Conc}_{\mathrm{DJF}} = 0.081$ ng m^{-3}) and substantially decreases JJA concentrations ($\Delta\mathrm{Conc}_{\mathrm{JJA}} = -0.214$ ng m^{-3}). In contrast, the *modal* scheme exhibits a negative concentration response in DJF (hence, less biases), with mean $\Delta\mathrm{Conc}_{\mathrm{DJF}}$ being -0.094 ng m^{-3}, whereas a positive response is apparent in JJA under volatilization scenario ($\Delta\mathrm{Conc}_{\mathrm{DJF}} = -0.055$ ng m^{-3}). Last, *fac3* change brings little to no impact unless volatilization is applied. Here, the ppLFER scheme yields higher concentrations in both seasons by a mean of 0.050 ng m^{-3}.

Benzo[a]pyrene

Figure H.4a displays the seasonal concentrations and biases over the Arctic. As shown, all experiments show negative biases in DJF while they show a clear variability of bias in JJA. In particular, most volatilization experiments overestimate the JJA concentrations while all no-volatilization experiments consistently underestimate the concentrations. The mean response to this factor is 1.6×10^{-4} ng m^{-3} in DJF and approximately ten times this value in JJA. Seasonal emission also produces a concentration increase in DJF (on average, by 3.5×10^{-5} ng m^{-3}) but generally brings a decrease in JJA (by -2.2×10^{-4} ng m^{-3}). Changes in *fac2* and *fac3* enhance negative bias in DJF but improve model predictions in JJA by decreasing the concentrations in both seasons. This result suggests the *modal* and ppLFER schemes reduce the atmospheric lifetime of BaP which is attributed to an increase in particulate mass available for oxidation.

a) Arctic

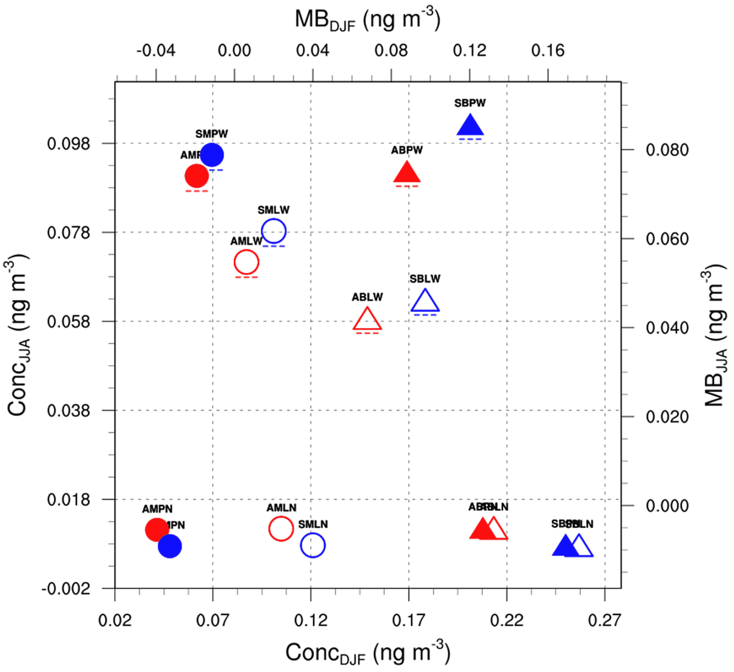

b) NH mid-latitudes

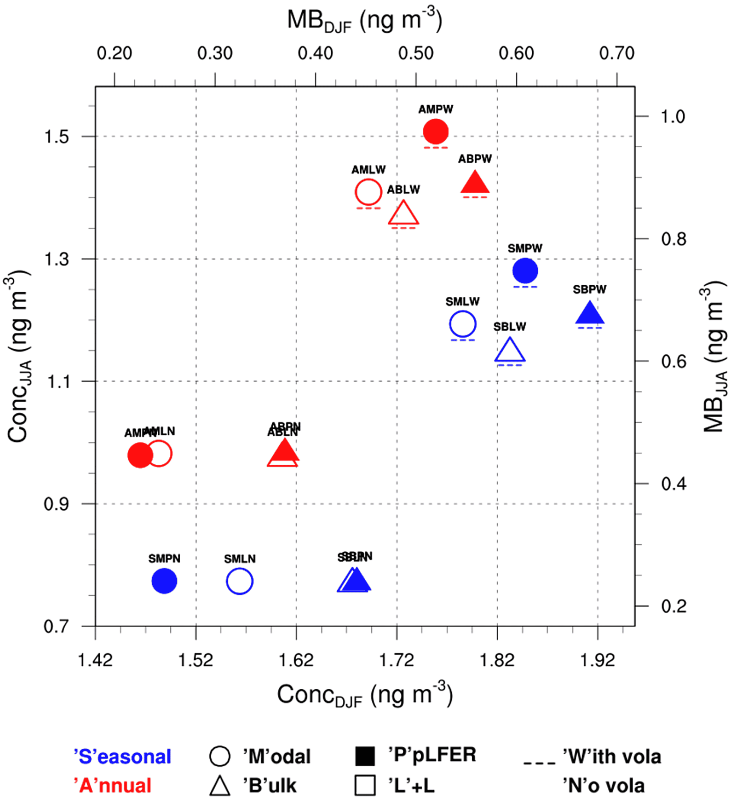

Figure H.3: Same as Figure H.1, but for FLT concentrations

a) Arctic

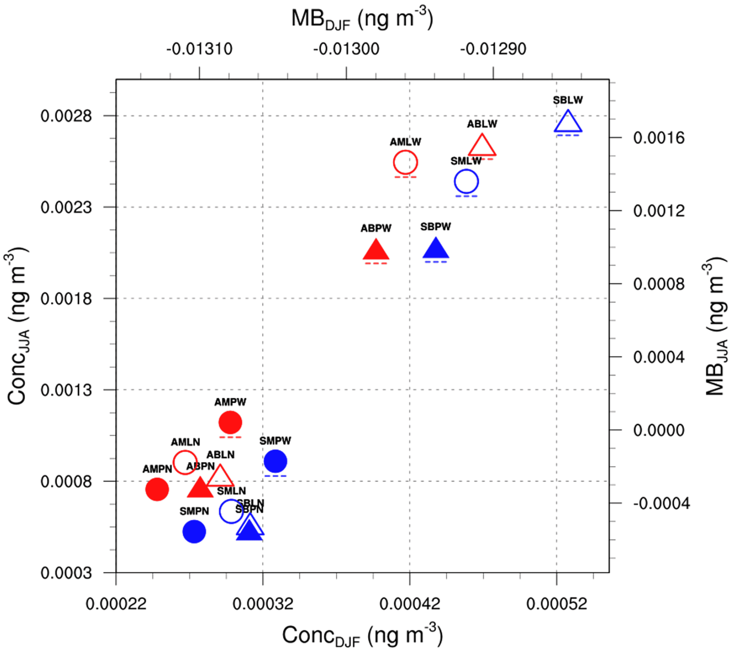

b) NH mid-latitudes

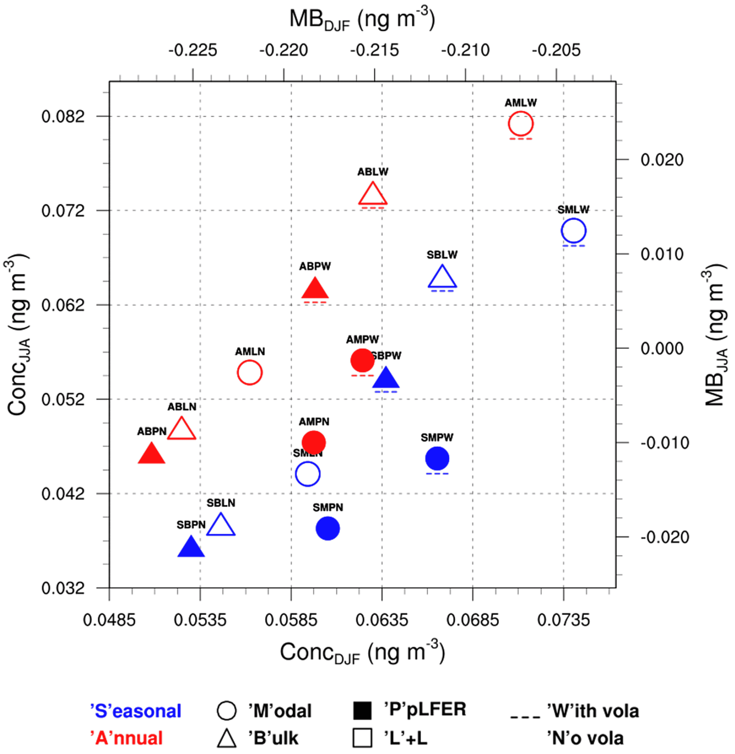

Figure H.4: Same as Figure H.1, but for BaP concentrations

The degree of both factor effects is similar ($\Delta\text{Conc}_{\text{DJF}} \approx -6\times10^{-5}$ and $\Delta\text{Conc}_{\text{JJA}} \approx -5\times10^{-4}$ ng m^{-3}) which strengthen by at least a factor of two under volatilization scenario.

Similar to the Arctic, all experiments underestimate the concentrations in DJF whereas the sign of JJA bias varies across experiments (Figure H.4b). The tendency of volatilization to increase concentrations remains, leading to a positive bias in JJA. In contrast to the Arctic, the mean signal from volatilization is not strongly different between the two seasons nor in comparison with the effects from other factor changes ($\Delta\text{Conc} = 2.7\times10^{-3}$ to 2.6×10^{-2} ng m^{-3}). Seasonal emission contributes to higher concentrations in DJF ($\Delta\text{Conc}_{\text{DJF}} = 2.9\times10^{-3}$ ng m^{-3}) and smaller concentrations in JJA ($\Delta\text{Conc}_{\text{JJA}} = -1.0\times10^{-2}$ ng m^{-3}). The effects of the *modal* and ppLFER schemes are comparable in magnitude but of opposite signs, overall positive for the former (1.0×10^{-3} to 2.6×10^{-3} ng m^{-3}) and negative for the latter (-1.7×10^{-3} to -2.5×10^{-2} ng m^{-3}).

Appendix I
EMAC-SVOC Evaluation of PAH Concentrations: Spatial Distribution of Model Bias

In the following, the evaluation of simulated near-surface PAH concentrations from EMAC-SVOC against measurements in the Arctic, NH mid-latitudes, and the tropics are discussed. Figures I.1-I.3 present the distribution of normalized mean bias fraction (NMBF) between model predictions and observations across monitoring stations in the individual region for the time period 2007−2009. As pointed out in Section 3.5.3 (Chapter 3), NMBF indicates a model overestimation (by a factor of NMBF +1) or an underestimation (by a factor of 1 − NBMF) when it is positive or negative, respectively. Over the Arctic, EMAC-SVOC underestimates PHE and BaP concentrations by at least a factor of two and overestimates FLT by less than a factor of three (Figure I.1). The NMBF of PYR varies by location, i.e., negative at E2 and E11 (NMBF = −3.34 and −1.33) and positive at E9 (NMBF = 1.05). This result can be in contrast with the region-based NMBF shown in Table 3.11, where positive bias (NMBF = 0.06) is produced for the Arctic PYR concentration. Comparing the four species, the degree of bias is consistently higher for BaP where NBMF reaches three orders of magnitude at E2.

For the North American sites (Figure I.2a), the model overestimates PHE concentrations with the bias being substantial (NMBF > 15) at three sites (I3, I5, and I6). In contrast, the model systematically underestimates BaP concentrations, particularly at I4 and I7 where the predictions are over a factor of 40 smaller than observations. The degree of NMBF for both species is smaller for the European sites (−5.28 to 4.54 for PHE and −10.85 to 5.15 for BaP) and no systematic bias present (Figure I.2b). PYR and FLT concentrations are better simulated than PHE and BaP (except at E5 and E10) with the predictions are overall within a factor of six of observations. It is noted that, for all species, the region-based NMBF (Table 3.11) is lower than the station-based values as the result of a compensating effect of negative and positive bias amongst the stations clustered in the region. Figure I.3 shows that the NMBF values in the tropics are apparently smaller at M5 (NMBF = −0.22 to 0.52), followed by those at M2 (NMBF = −1.36 to −0.67). The model shows underestimation at M1 and M4 (NMBF = −9.26 to −2.50) and overestimation at M3 and M6 (NMBF = 3.81−7.83). The region-based bias is negative for all species (see Table 3.11 and Figure 3.7) and is attributed to the monthly concentrations at MI that are much higher than the concentrations at other sites by a factor of 3−170.

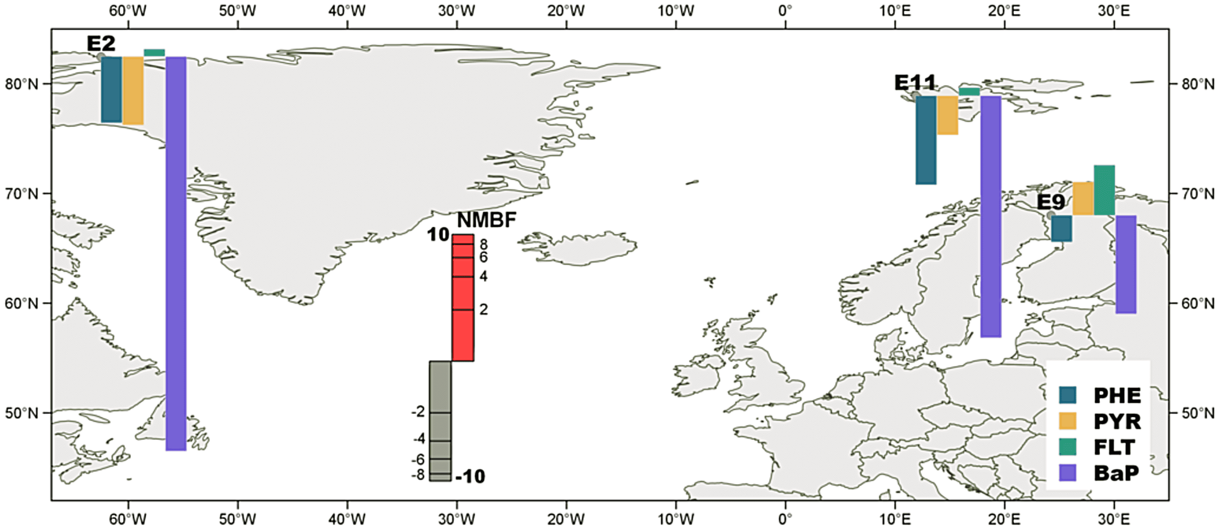

Figure I.1: Map of normalized mean bias factor (NMBF) values calculated between simulated and observed mean monthly PAH concentrations for monitoring stations in the Arctic. The logarithmic scale has been used for NMBF.

a) North America

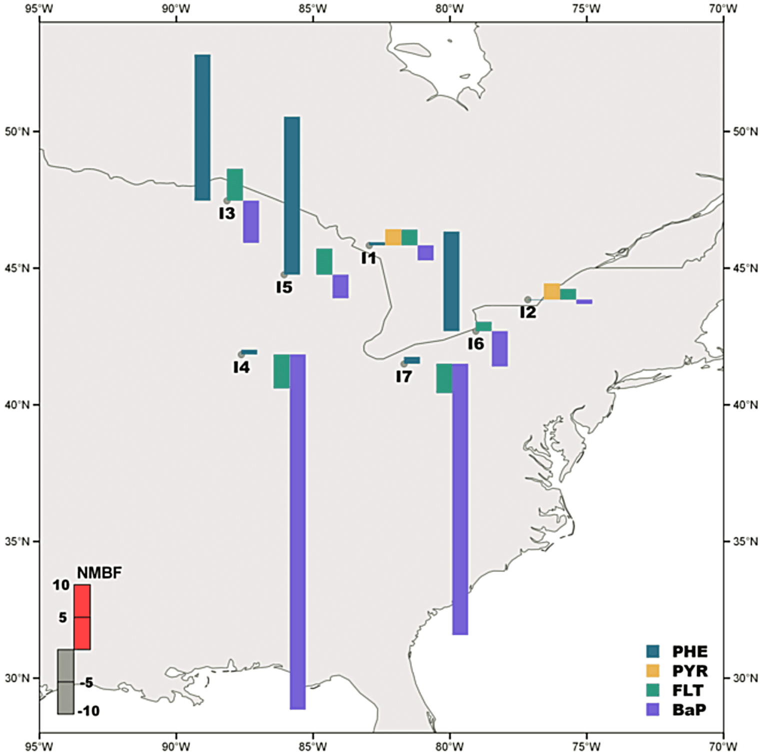

b) Europe

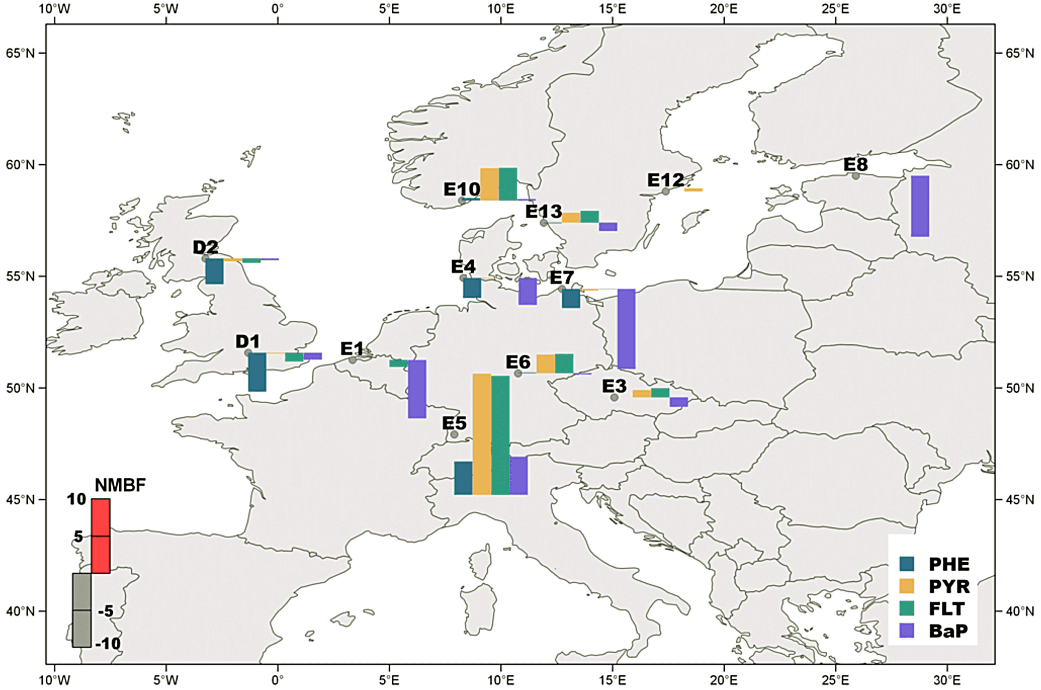

Figure I.2: Same as Figure I.1 but for monitoring stations in the northern mid-latitudes: (a) North America, and (b) Europe.

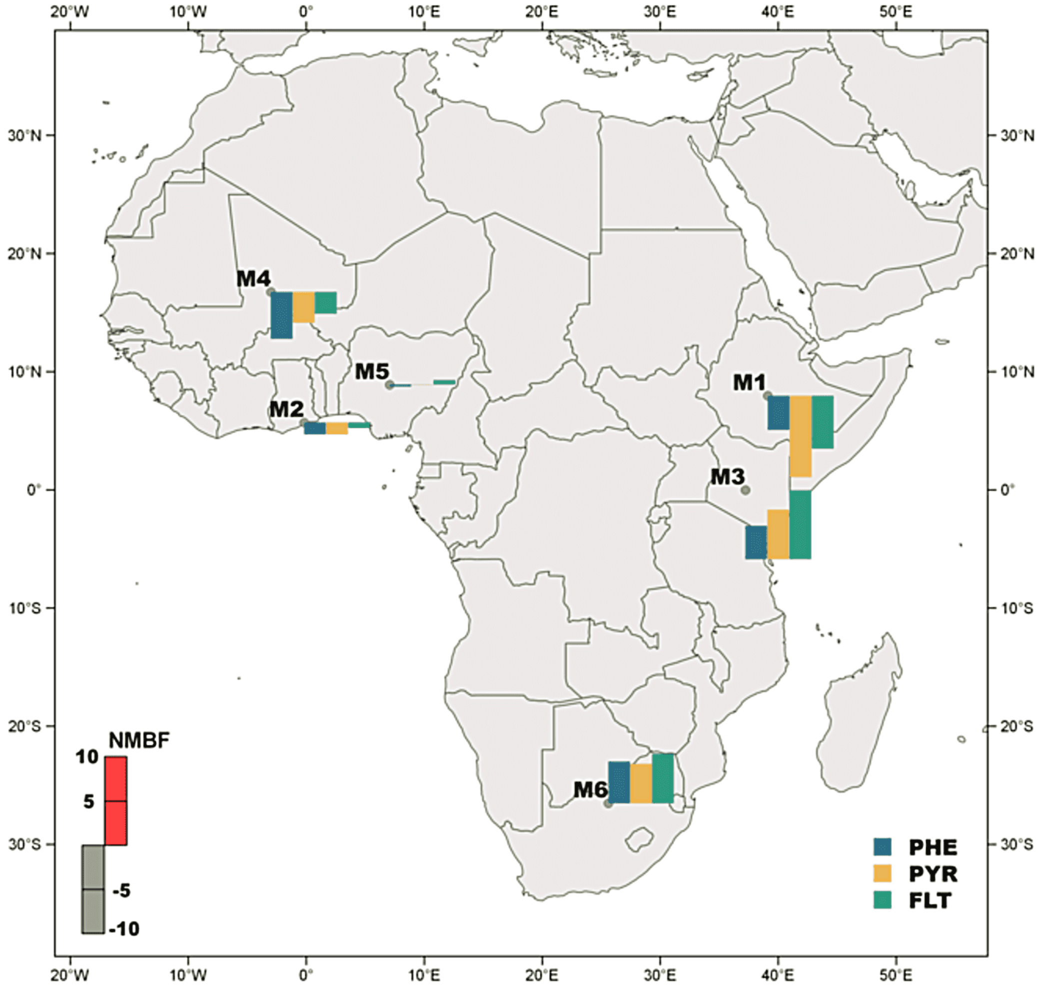

Figure I.3: Same as Figure I.1 but for monitoring stations in the tropics.

Appendix J
Chapter 4 Supplementary Materials

J.1 Problems without considering bulk processes

The use of surface model without considering bulk diffusion/reaction results in a contradictory RH dependence of BaP degradation rates at different ozone concentrations. Taking the Zhou scheme, for example, using such extrapolation resulted in a contradictory RH dependence of BaP degradation rates at different O_3 ranges. The reactions of the Zhou scheme at 50 ppbv ozone were slower in 70% RH than 50% RH (Chapter 4, Figure 4.1A), contrary to their own conclusion that higher RH enhanced the reactivity of BaP.

J.2 Warm conveyor belts and BaP transport in Gosan winter case

The frontal activities and warm conveyor belts (WCBs) associated with mid-latitude cyclones play a very important role in lifting plumes from the planetary boundary layer (PBL) to the free troposphere (FT), promoting long-range transport of air pollutants (Ding et al., 2017). Thus, such kind of transport processes can influence the chemical distributions of the middle- and upper- troposphere of downwind regions in Northeast Asia, the Pacific Ocean and even North America. In North China, transport processes due to WCBs have been found particularly frequent in summer resulting from the high frequency of mid-latitude cyclones, but they are also important in spring and winter. In order to understand the detailed transport mechanism for the high concentration of BaP in the middle troposphere of the NH mid-latitudes, we chose a typical event during 25−26 February 2003 as a case study.

Figure J.5 shows that the Gosan outflow case in winter is a good example of PBL−FT transport. A mid-latitude cyclone (low pressure centered at 118°E, 43°N) was located in the north to North China Plain on early 25 February 2003 (Figure J.5A). High moisture (represented by specific humidity) demonstrated a strong northeastward belt-shape transport from the boundary layer in the warm air frontal zone to the middle troposphere over the warm front, with clockwise shape belts overrunning the fronts (Figure J.5C). Similarly, BaP showed a high concentration belt in front of the cold front (∼850 hPa) and then got transported over the warm front (∼700 hPa), hence, experienced fast eastward transport by westerlies (or jets) in the middle-troposphere (Figure J.5B,D,F). A T-shape plume could be identified from the 700 hPa SH and BaP distributions over the warm front (Figure J.5D). It includes a branch transported poleward in addition to the eastward branch. Ding et al. (2009) reported a similar event in the same region and found that the WCB associated with the cyclone played the key role in lifting air pollutants from the boundary layer to the middle troposphere, and also pointed out that such kind of lifting provides the most important contribution for intercontinental and poleward transports in NH. To clearly demonstrate the structure of WCBs and other related flows in the cyclone, a conceptual model is given in Figure J.6. Since cyclone is one of the most dominant synoptic features in the mid-latitudes, such kind of WCB-induced lifting could be the main contribution to high and long-range transported pollutants, like BaP.

J.3 Additional tables and figures

(Intentionally left blank)

Table J.1: Flow tube experiments of multiphase degradation of BaP with ozone. Langmuir−Hinshelwood first-order reaction rate coefficient $k = \frac{k_{\max} k_{O_3}[O_3]}{1+k_{O_3}[O_3]}$. For Kahan scheme, $k = \frac{A\times[O_3]}{B+[O_3]}$. $[O_3]$ is in molec cm^{-3}.

Scheme	Substrate	Coating	O_3 (ppmv)	T (K)	RH %	$k_{\max}$ (s^{-1})	k_{O_3} (1×10^{-15} cm^3)
Pöeschl (Pöschl et al., 2001)	spark discharge soot	none	0.05−1	296±2	0	0.015±0.001	270±40
					25	0.016±0.001	280±20
Kwamena (Kwamena et al., 2004)	azelaic acid	none	2−45	298±5	0	0.048±0.008	1.2±0.4
					72	0.060±0.018	2.8±1.4
	NaCl	none	2−45	298±5	0	0.032	<0.12
Kahan (Kahan et al., 2006)	octanol	none	15−950	room	0	$A = (5.5 \pm 0.2) \times 10^{-3}$ s^{-1}	$B = (2.8 \pm 0.4) \times 10^{-15}$ molec cm^{-3}
Zhou (Zhou et al., 2012)	ammonium sulfate	none	4−25	296±3	<5%	0.034±0.002	14±4
		bis(2-ethylhexyl)sebacate	6−32	296±3	<5%	0.051±0.001	4.1±0.1
		phenylsiloxane oil	4−32	296±3	<5%	0.047±0.004	13±4
		eicosane	6−32	296±3	<5%	shut off	shut off
Zhou (Zhou et al., 2013)	ammonium sulfate	a-pinene SOA 5−10 nm	1.5−16	296±3	<5%	0.042±0.004	5.1±0.9
			8−24	296±3	<5%	0.022±0.003	2.3 ±0.4
		a-pinene SOA 20−80 nm	3−24	296±3	50%	0.023±0.004	14±4.4
			3−28	296±3	70%	0.039±0.004	6.2±1.1

Table J.2: Kinetic parameters used in the KM-SUB simulation for the ozonolysis of BaP to reproduce experiment results of the Zhou scheme (Zhou et al., 2013).

Parameter	Description	Value
$\alpha_{\mathrm{s,O_3}}$	surface accommodation coefficient of O_3	1^*
$\tau_{\mathrm{d,O_3}}$ (s)	Desorption lifetime of O_3	$3.2\times10^{-9*}$
$E_{\mathrm{a,pc}}$ (kJ mol^{-1})	Activation energy from physisorbed O_3 to ROI	$42^{*,\dagger}$
$E_{\mathrm{a,ox}}$ (kJ mol^{-1})	Activation energy from ROI to oxidized BaP	$80^{*,\dagger}$
k_{BR} (cm^3 s^{-1})	Second-order bulk reaction rate coefficient between BaP and O_3	$5\times10^{-18\dagger}$
$K_{\mathrm{sol,cc}}$ (mol cm^{-3} atm^{-1})	Henry's law coefficient of O_3	$6\times10^{-4\dagger}$

*Shiraiwa et al. (2011b); †Zhou et al. (2013)

Table J.3: Parameterization of multiphase degradation rate for the ozonolysis of BaP. First-order reaction rate coefficients k (s^{-1}) are given by the Hill equation $k = \text{base} + \frac{\text{max}-\text{base}}{1+(\frac{\text{xhalf}}{[\text{O}_3]})\text{rate}}$ with $[\text{O}_3]$ in ppbv. The R^2 of these Hill equation fits are all larger than 0.99. For each grid cell, the parameters are read from the look-up table with temperature (T) and relative humidity (RH) closest to the T and RH of the grid cell. When equally close, the smaller parameter value is adopted.

70% RH

T **(°C)**	**base**	**max**	**rate**	**xhalf**
40	1.67×10^{-4}	1.29×10^{-2}	0.682	1.25×10^{3}
35	1.19×10^{-4}	1.29×10^{-2}	0.682	1.25×10^{3}
30	8.52×10^{-5}	9.02×10^{-3}	0.696	1.23×10^{3}
25	5.94×10^{-5}	6.33×10^{-3}	0.707	1.27×10^{3}
23	4.84×10^{-5}	5.14×10^{-3}	0.700	1.25×10^{3}
15	2.55×10^{-5}	2.72×10^{-3}	0.711	1.29×10^{3}
10	1.58×10^{-5}	1.68×10^{-3}	0.706	1.27×10^{3}
5	9.49×10^{-6}	1.00×10^{-3}	0.698	1.24×10^{3}
0	6.85×10^{-6}	5.64×10^{-4}	0.704	1.11×10^{3}
−5	5.31×10^{-6}	3.10×10^{-4}	0.713	1.01×10^{3}
−10	3.83×10^{-6}	1.48×10^{-4}	0.731	7.33×10^{2}
−15	8.93×10^{-7}	1.05×10^{-4}	0.580	1.88×10^{3}
−20	1.16×10^{-6}	2.58×10^{-5}	0.673	3.35×10^{2}

50% RH

T **(°C)**	**base**	**max**	**rate**	**xhalf**
40	1.65×10^{-4}	1.80×10^{-2}	0.672	1.21×10^{3}
35	1.16×10^{-4}	1.27×10^{-2}	0.678	1.24×10^{3}
30	8.24×10^{-5}	8.68×10^{-3}	0.688	1.22×10^{3}
25	5.44×10^{-5}	5.71×10^{-3}	0.688	1.21×10^{3}
23	2.64×10^{-5}	3.08×10^{-3}	0.618	7.97×10^{2}
15	2.20×10^{-6}	1.10×10^{-3}	0.544	5.83×10^{2}
10	7.84×10^{-7}	2.60×10^{-4}	0.559	7.50×10^{1}
5	-4.79×10^{-7}	7.19×10^{-5}	0.564	1.31×10^{1}
0	-7.02×10^{-6}	2.18×10^{-5}	0.464	1.05
−5	-4.06×10^{-6}	6.54×10^{-6}	0.459	1.24×10^{-1}
−10	-1.89×10^{-6}	2.02×10^{-6}	0.429	1.44×10^{-2}
−15	2.58×10^{-7}	7.22×10^{-7}	0.175	1.28×10^{-1}
−20	1.79×10^{-7}	2.60×10^{-7}	0.689	1.11×10^{3}

Dry

T **(°C)**	**base**	**max**	**rate**	**xhalf**
40	1.61×10^{-4}	1.74×10^{-2}	0.667	1.19×10^{3}
35	1.10×10^{-4}	1.19×10^{-2}	0.667	1.21×10^{3}
30	6.75×10^{-5}	7.31×10^{-3}	0.653	1.11×10^{3}
25	2.3×10^{-5}	3.10×10^{-3}	0.586	7.02×10^{2}
23	-1.90×10^{-5}	9.28×10^{-4}	0.446	1.59×10^{2}
15	-2.65×10^{-5}	3.09×10^{-4}	0.341	8.38×10^{1}
10	-4.28×10^{-5}	1.03×10^{-4}	0.191	4.41
5	-1.12×10^{-5}	3.49×10^{-5}	0.142	4.33
0	3.39×10^{-6}	1.03×10^{-5}	0.382	8.85×10^{2}
−5	1.37×10^{-6}	5.67×10^{-6}	0.780	2.96×10^{3}
−10	4.53×10^{-7}	1.57×10^{-6}	0.979	1.63×10^{3}
−15	1.44×10^{-7}	2.10×10^{-6}	0.924	1.39×10^{4}

Table J.4: Comparison of observed and predicted BaP concentrations in the regional WRF-Chem model and the global EMAC model. (A) Observed and predicted BaP concentrations (ng m^{-3}) over the period 2007–2009*. (B) Mean bias (prediction – observation) (ng m^{-3}) and relative bias ((prediction – observation) / observation) of BaP for various types of sites in Figure 4.2A.

(A)

	Alert, Canada	Spitsbergen, Norway	Pallas, Finland	All mid-latitude stations
No. months	34[†]	23[†]	19[†]	405[†]
Mean				
Observation	1.40×10^{-3}	4.08×10^{-3}	1.01×10^{-2}	1.41×10^{-1}
Kwamena	8.15×10^{-7}	6.92×10^{-6}	1.22×10^{-3}	5.75×10^{-2}
ROI-T	1.64×10^{-5}	5.48×10^{-5}	4.68×10^{-3}	7.98×10^{-2}
Kahan	6.25×10^{-3}	5.22×10^{-3}	5.33×10^{-2}	2.72×10^{-1}
Pöschl	1.61×10^{-7}	1.07×10^{-6}	1.25×10^{-4}	5.88×10^{-3}
Median				
Observation	4.78×10^{-4}	8.80×10^{-4}	2.84×10^{-3}	3.74×10^{-2}
Kwamena	7.41×10^{-7}	2.73×10^{-6}	1.18×10^{-3}	1.82×10^{-2}
ROI-T	1.35×10^{-5}	2.61×10^{-5}	3.84×10^{-3}	3.24×10^{-2}
Kahan	4.45×10^{-4}	1.28×10^{-3}	4.64×10^{-2}	3.34×10^{-1}
Pöschl	1.48×10^{-7}	6.05×10^{-7}	1.16×10^{-4}	3.07×10^{-3}
Geometric mean[‡]				
Observation	6.70×10^{-4}	1.38×10^{-3}	3.62×10^{-3}	4.60×10^{-2}
Kwamena	7.79×10^{-7}	4.00×10^{-6}	1.19×10^{-3}	2.57×10^{-2}
ROI-T	1.19×10^{-5}	2.89×10^{-5}	3.98×10^{-3}	3.43×10^{-2}
Kahan	4.61×10^{-4}	1.68×10^{-3}	4.21×10^{-2}	3.43×10^{-1}
Pöschl	1.57×10^{-7}	8.13×10^{-7}	1.20×10^{-4}	2.26×10^{-3}
Root mean square error				
Kwamena	6.26×10^{-3}	7.78×10^{-3}	2.37×10^{-2}	2.79×10^{-1}
ROI-T	6.25×10^{-3}	7.77×10^{-3}	2.24×10^{-2}	2.72×10^{-1}
Kahan	5.98×10^{-3}	1.14×10^{-2}	6.17×10^{-2}	5.71×10^{-1}
Pöschl	6.26×10^{-3}	7.78×10^{-3}	2.41×10^{-2}	2.89×10^{-1}

[*] Although improved performances, the ROI-T scheme still tends to underestimate BaP in the Arctic (sites Alert and Spitsbergen), probably because current atmospheric models generally underestimate co-emitted BC in the Arctic due to missing sources (Stohl et al., 2013; Winiger et al., 2016). Therefore, the actual inflow of BaP to the Arctic could be even stronger; [†] Values below LOQ are treated as zero. The number of data < LOQ is 21 for Alert, 8 for Spitsbergen, 1 for Pallas, and 0 for all mid-latitude stations.; [‡] Geometric mean was used in the study.

(B)

	Xianghe	Gosan	Arctic	Mid-latitude
Kwamena	6.76×10^{-1} (0.87)	-7.88×10^{-3} (−0.39)	-5.99×10^{-3} (−3.17)	-8.40×10^{-2} (−1.83)
ROI-T	-1.44×10^{-2} (−0.02)	-1.36×10^{-3} (−0.07)	-4.82×10^{-3} (−2.55)	-6.16×10^{-2} (−1.34)
Kahan	1.22 (1.56)	1.38×10^{-1} (6.90)	1.42×10^{-2} (7.51)	3.35×10^{-1} (7.28)
Pöschl	7.33×10^{-3} (0.01)	-1.80×10^{-2} (−0.90)	-6.38×10^{-3} (−3.38)	-1.36×10^{-1} (−2.96)

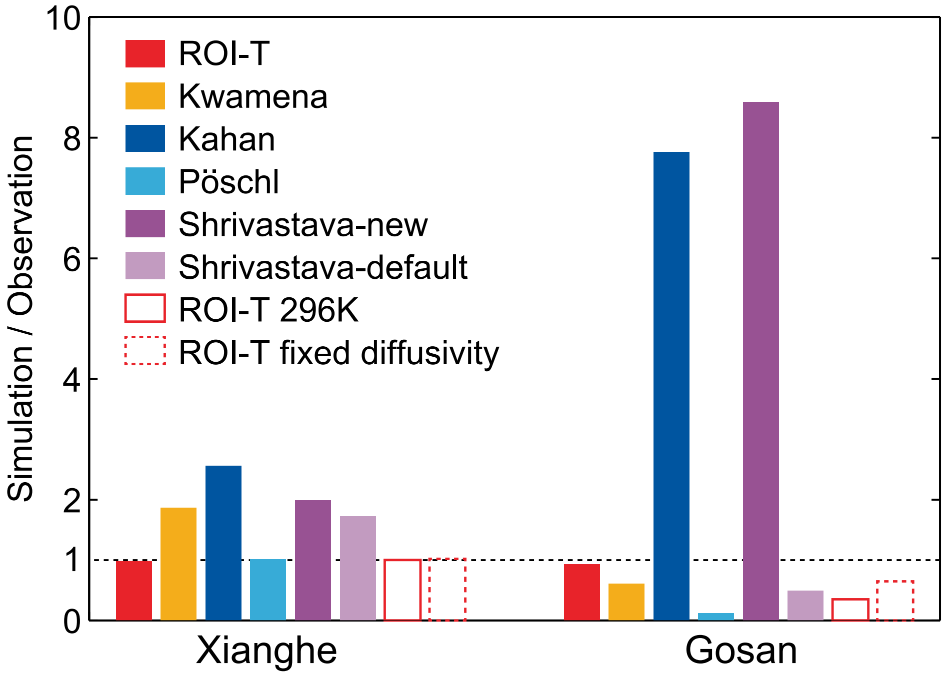

Figure J.1: Same as Figure 4.2, but with three more sensitivity studies. "Shrivastava-default" used the default setting (the same as the thin coating case in the Zhou scheme (Zhou et al., 2013)) in Shrivastava et al. (2017). "ROI-T 296 K" fixed both OA diffusion coefficient and chemical reaction rate of BaP with ROI at 296 K level. "ROI-T fixed diffusivity" only fixed OA diffusion coefficient at 296 K level but allowed the chemical reaction rate of BaP with ROI to change with temperature.

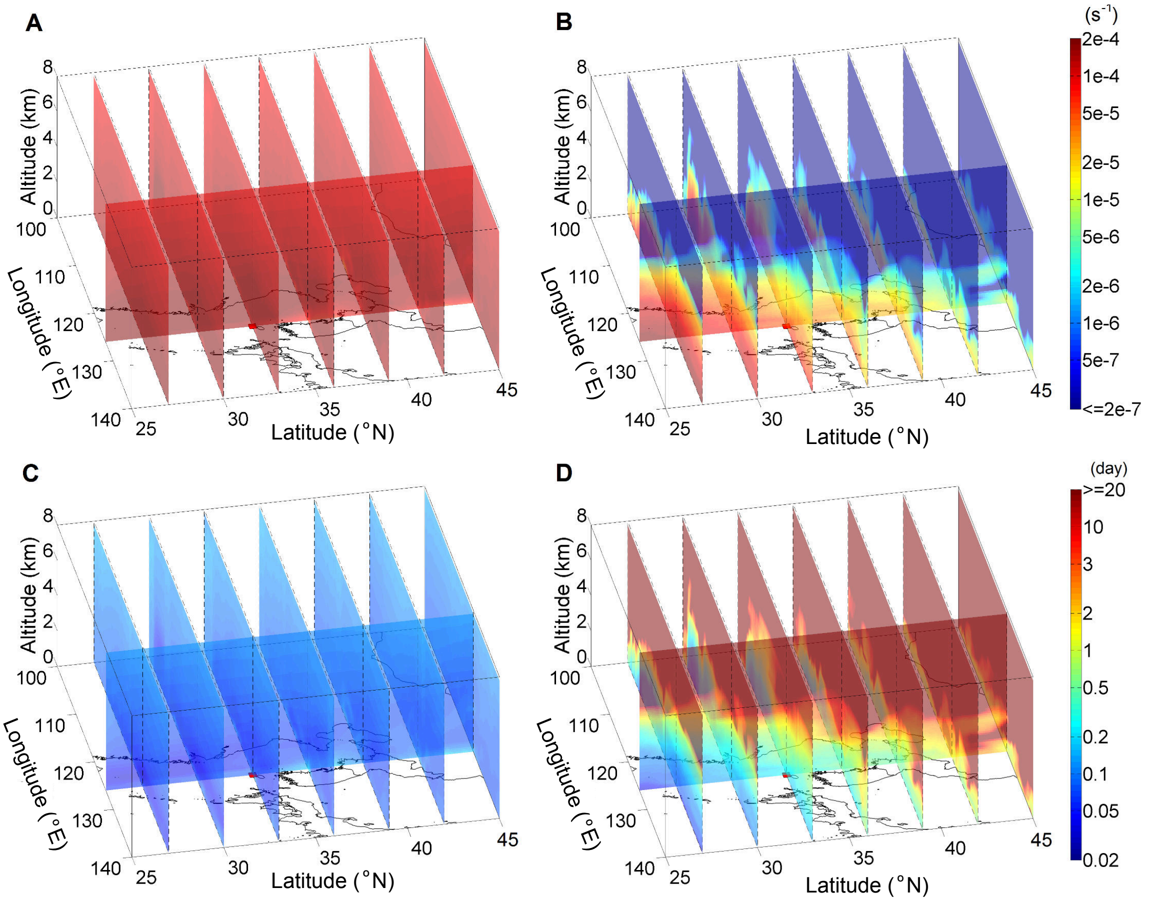

Figure J.2: **BaP multiphase degradation rate k (s^{-1}) for (A) the Kwamena scheme and (B) the ROI-T scheme, and chemical lifetime (day) for (C) the Kwamena scheme and (D) the ROI-T scheme, on 24 February 2003 in the East Asia outflow case.**

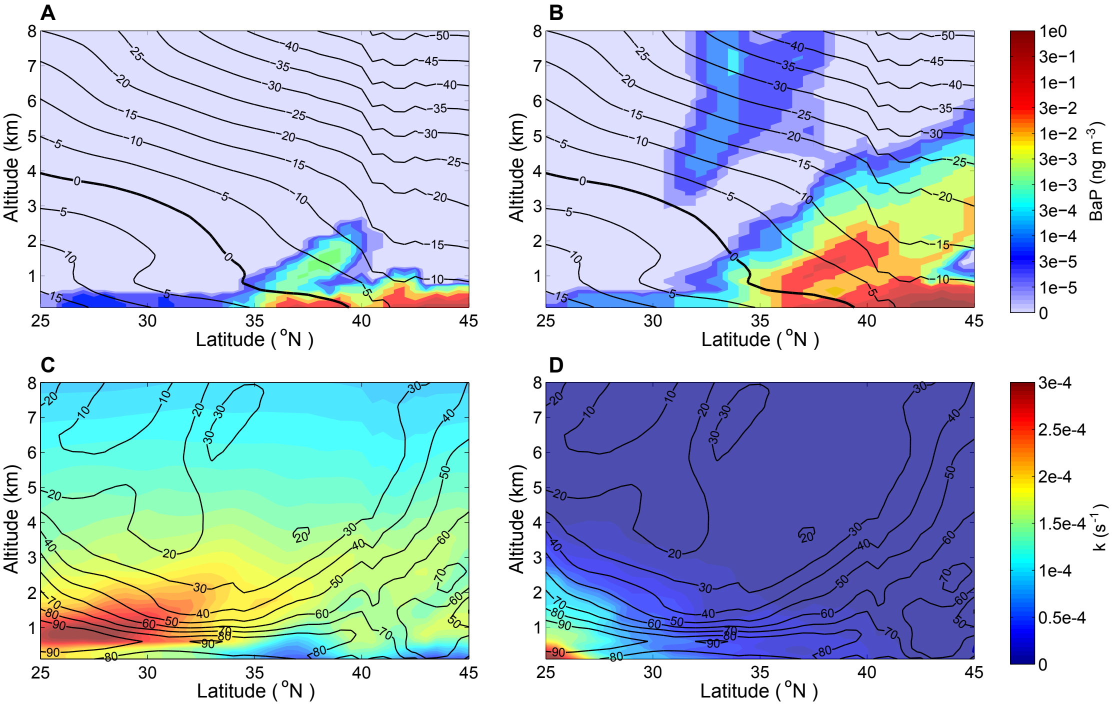

Figure J.3: BaP concentrations (ng m^{-3}) for (A) the Kwamena scheme and (B) the ROI-T scheme, and multiphase degradation rate k (s^{-1} for (C) the Kwamena scheme and (D) the ROI-T scheme, at a cross section of 126°E on 24 February 2003 in the East Asia outflow case. Temperature (°C) contours are shown in A and B. RH (%) contours are shown in C and D.

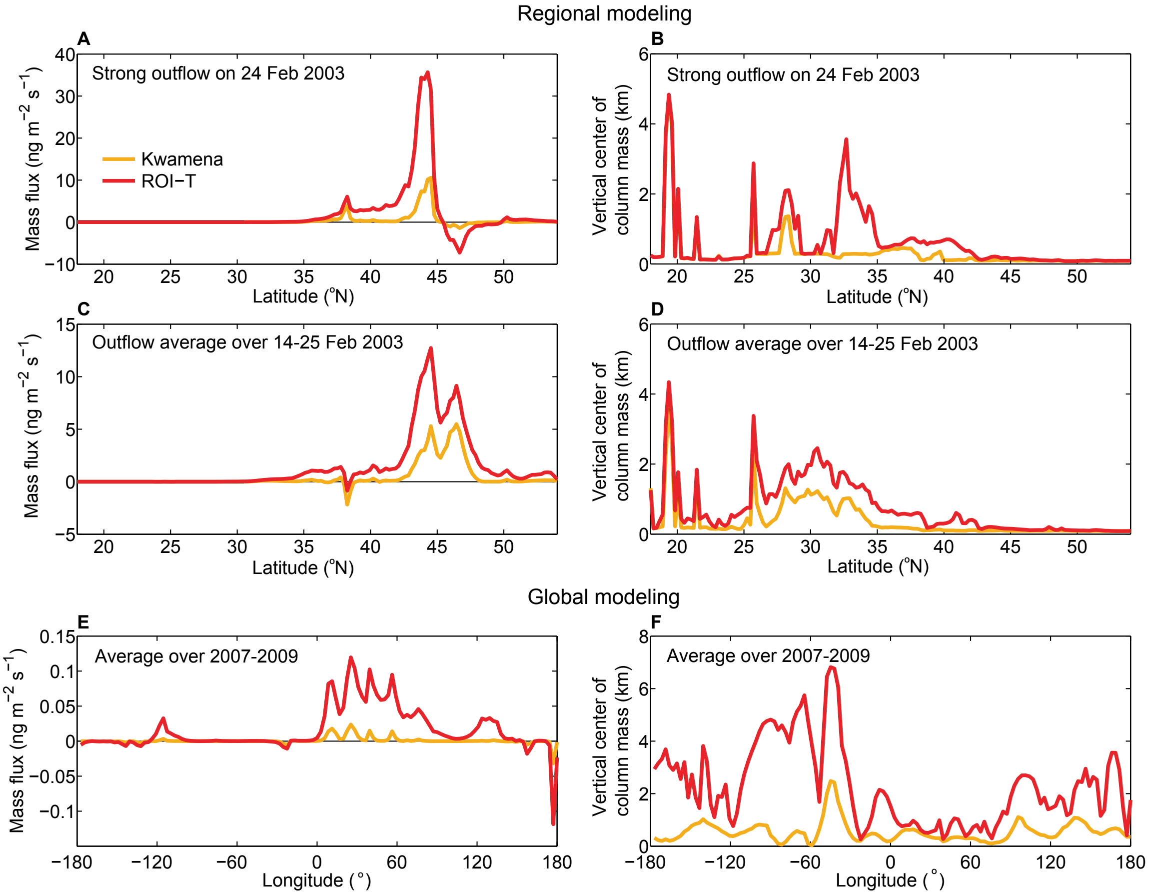

Figure J.4: (A) BaP net meridional mass fluxes (ng m^{-2} s^{-1}) and (B) vertical center of column mass (km) at 126°E averaged during the East Asia outflow episode (24 February 2003). (C) BaP net meridional mass fluxes (ng m^{-2} s^{-1}) and (D) vertical center of column mass (km) at 126°E averaged over the simulation period 14−25 February 2003. (E) BaP net meridional mass fluxes (ng m^{-2} s^{-1}) and (F) vertical center of column mass (km) at 65°N averaged over the years 2007−2009[1].

---

[1] For the global modeling, Figure K.4 shows the same cross-section plots but with two more sensitivity studies.

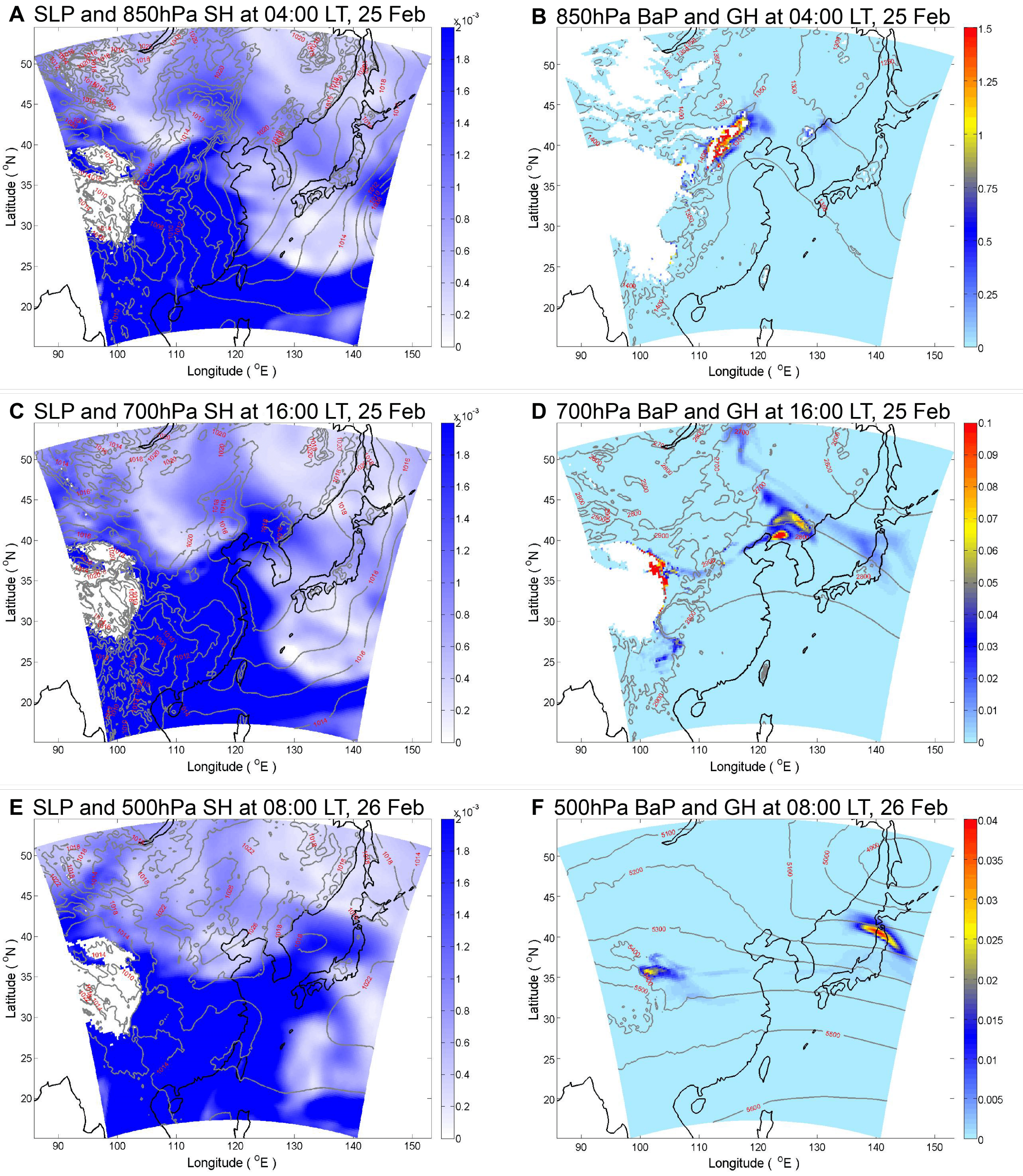

Figure J.5: BaP transport due to warm conveyor belt and frontal activities associated with mid-latitude cyclones for the Gosan winter case. The left column shows specific humidity (SH, g g^{-1}) and sea level pressure (SLP, hPa, contour lines) at different pressure level (A) 850 hPa, (C) 700 hPa, and (E) 500 hPa for a cyclone in East Asia during 25–26 February 2003. The right column (B,D,F) gives BaP concentrations (BaP, ng m^{-3}) with the ROI-T scheme and geopotential height (GH, m, contour lines) at different pressure level corresponding to figures in the left panel. The brown and rose bold lines show the surface cold fronts and warm fronts, respectively.

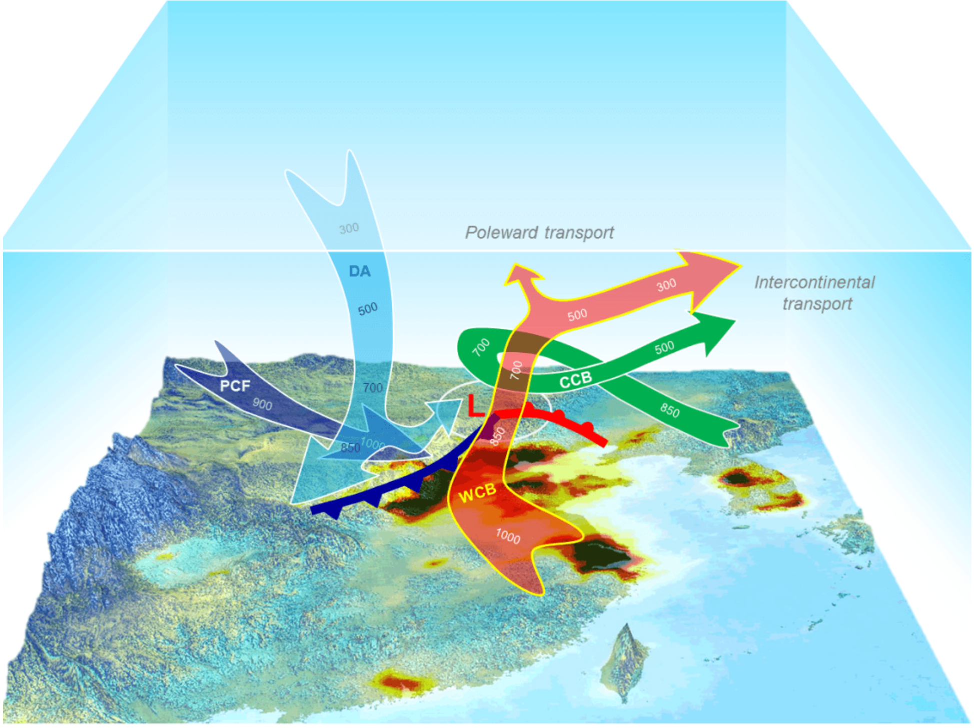

Figure J.6: Conceptual scheme for air pollution transport due to a middle-latitude cyclone. The warm conveyor belt (WCB) is the most efficient transport process for lifting air mass from boundary layer to middle- even upper- troposphere, which further contributes to intercontinental and poleward transport. The cold conveyor belt (CCB), dry air (DA) stream and post cold front (PCF) airstream contribute to the formation of WCB. The numbers marked on these belts indicate the pressure level (Figure modified from Ding et al., 2017).

Appendix K

EMAC-SVOC Sensitivity to Different BaP Multiphase Degradation Schemes

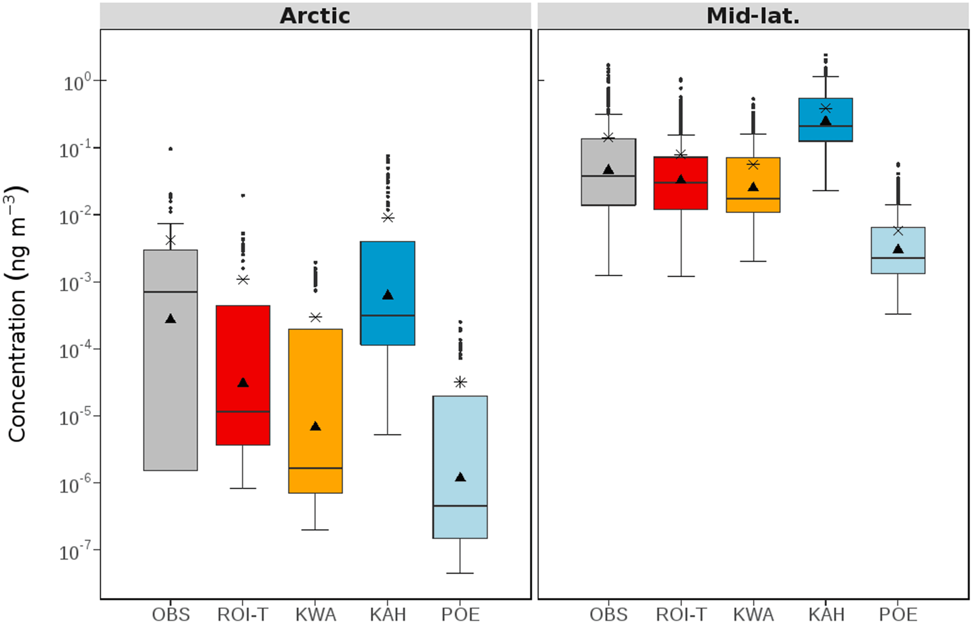

Figure K.1: Box-and-whisker plots representing the distributions of BaP concentration (ng m^{-3}) from observations (OBS) and simulations by the ROI-T, Kwamena (KWA), Kahan (KAH), and Pöschl (POE) schemes. Monthly data from all stations in the (left) Arctic and (right) and mid-latitudes over the years 2007−2009. The boxes represent the interquartile range (IQR; difference between the 1st and 3rd quartiles), the middle lines are the median, the whiskers are the highest and lowest values that are not outliers, dots are the outliers (values outside 1.5×IQR above the 3rd quartile and below the 1st quartile), asterisks are the arithmetic means, and triangles are the geometric means.

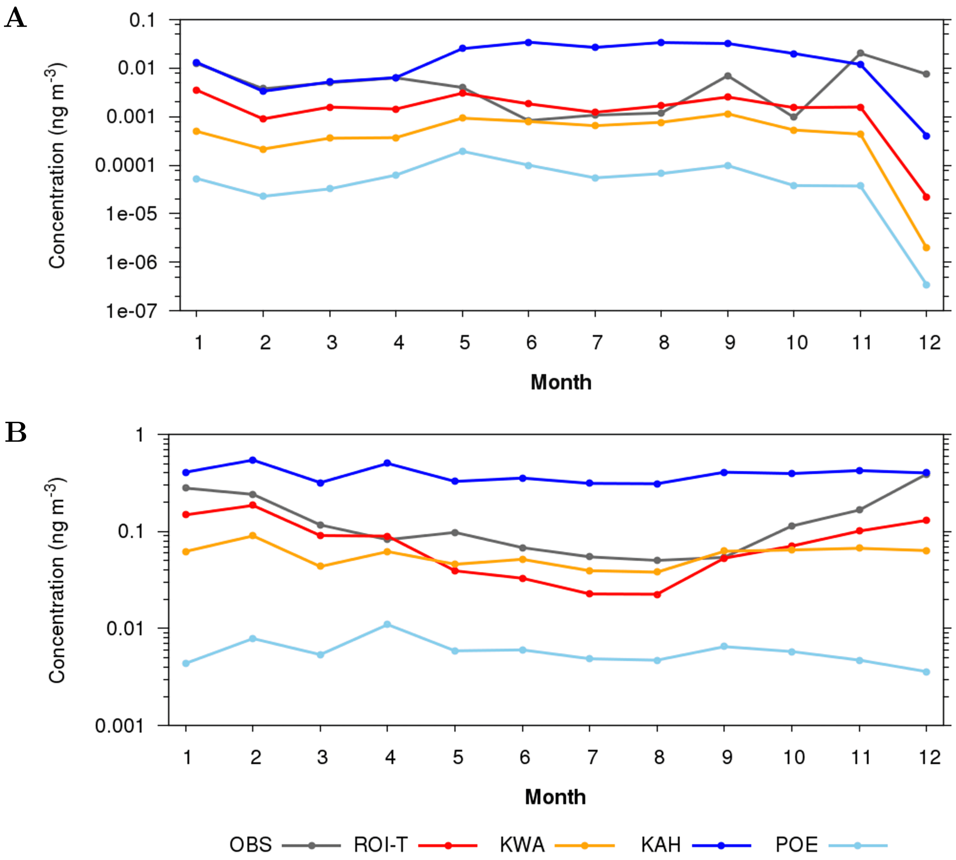

Figure K.2: Seasonal mean BaP concentrations (ng m^{-3}) from observations and simulations by the ROI-T, Kwamena (KWA), Kahan (KAH), and Pöschl (POE) schemes, averaged over all stations in the (A) Arctic and (B) mid-latitudes for the years 2007−2009.

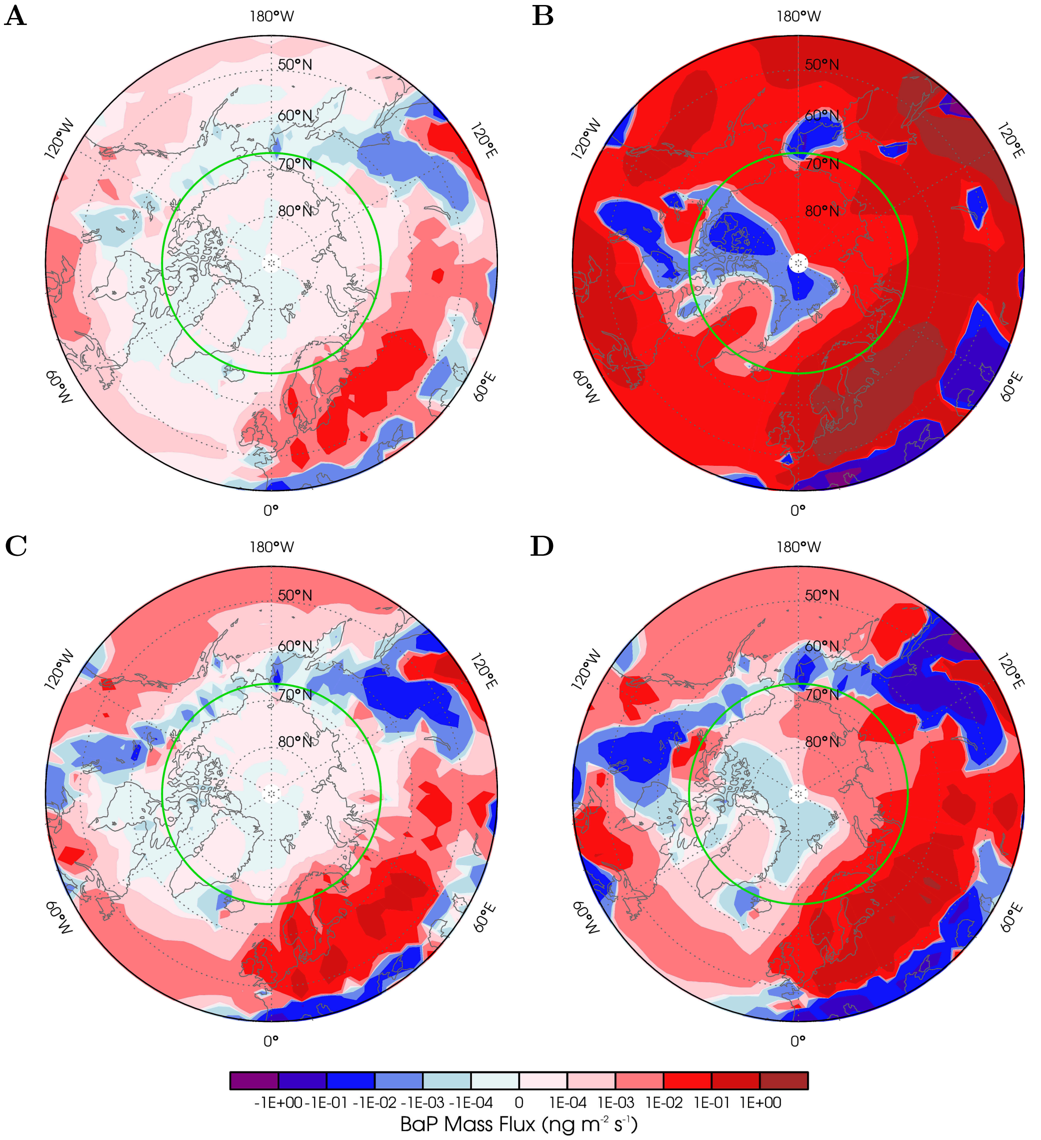

Figure K.3: BaP net meridional mass flux (ng m^{-2} s^{-1}) averaged over the years 2007–2009 for the (A) Pöschl, (B) Kahan, (C) Kwamena, and (D) ROI-T schemes. Northward has positive values (red), and southward has negative values (blue). Green circle marks the Arctic Circle at 66.5°N.

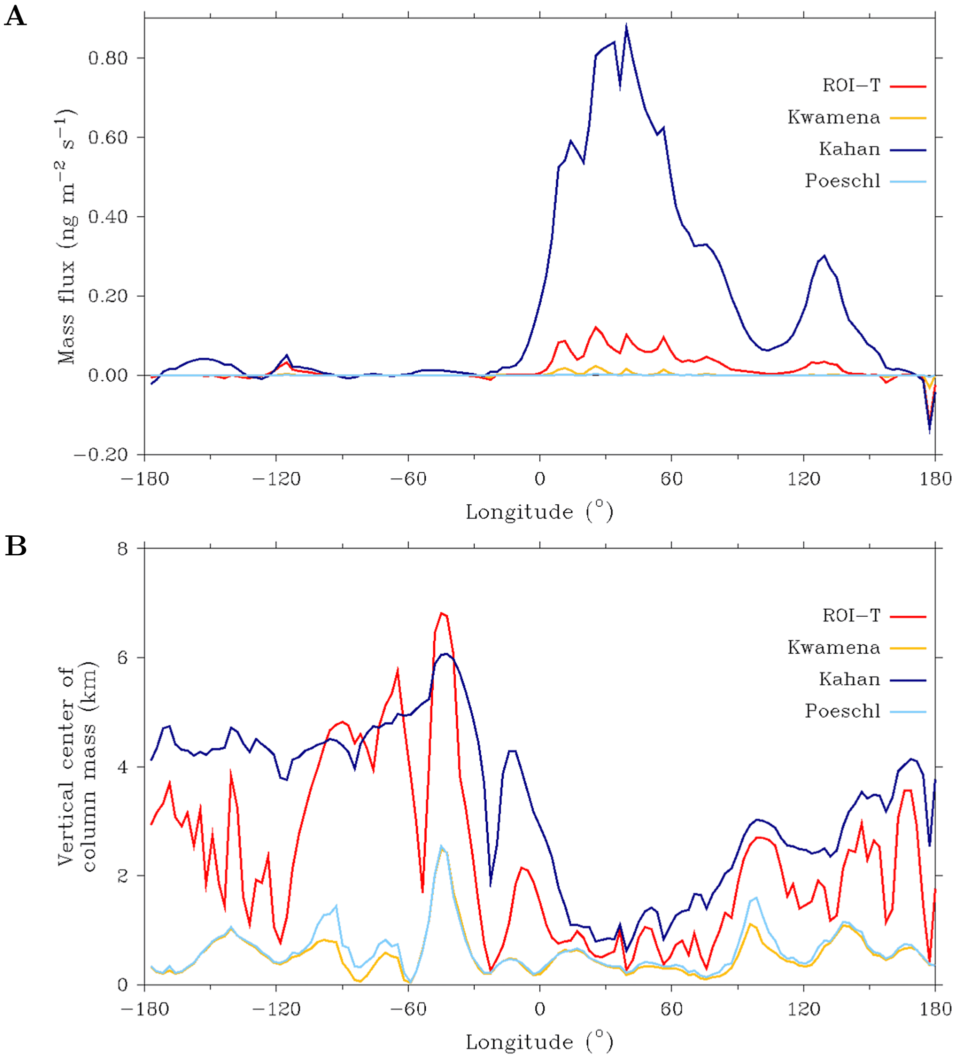

Figure K.4: (A) BaP net meridional mass flux (ng m^{-2} s^{-1}), and (B) vertical center of column mass (km) at 65°N from different sensitivity studies, averaged over the years 2007−2009.

Appendix L

Preliminary Results: PAH Long-Range Transport and Source−Receptor Relationships

The following summarizes an ongoing study on EMAC-SVOC application with the aims of analyzing the global fate and distribution of PAHs and their long-range transport behaviors in the air.

L.1 Compartmental distributions, persistence and LRTP

The first part of the study focuses on the estimation of compartmental distributions, persistence and long-range transport potential (LRTP), as these characteristics are commonly used to assess the environmental hazard of chemicals (Scheringer and Wania, 2003; Lammel et al., 2007). The 2007−2009 simulation results from the SMPW scenario (Chapter 3; for PHE, PYR, FLT) and the ROI-T scenario (Chapter 4; for BaP) were used in the analysis. The hemispheric PAH burdens in different environmental compartments are shown in Table L.1. It shows that the largest storage is predicted for FLT (ca. 45% of its annual emission) and the lowest for BaP (ca. 7% its annual emission). At the end of the simulation, most of the global burden is stored in NH soils and SH oceans, while FLT is predominantly distributed in the global oceans. More (less) atmospheric burden is found in PHE and FLT (BaP) due to its volatility. The results show much higher levels in NH than in SH by a factor of 3−80 for all species and compartments.

The persistence of PAHs is assessed by calculating overall residence time (τ_{ov}), that is, the ratio of the mass present in the global domain divided by the sum of all removal fluxes over the simulation period. Furthermore, the LRTP is determined using three indicators, namely, the Arctic Contamination Potential (ACP), zonal spreading (ZS), and zonal displacement (ZD), as introduced by Wania (2003) (for ACP) and Leip and Lammel (2004) (for ZS and ZD), respectively. Wania (2003) defines ACP as the fraction of the total amount in the global environment that is present in the Arctic surface media at the end of the simulation period (i.e.,

Table L.1: Distribution of compartmental burden (tonnes) of PAHs in the Northern and Southern Hemispheres at the end of the simulation (2009).

Compartment	PHE	PYR	FLT	BaP
NH				
Atmosphere	79	38	120	2
Soils	397	2338	4955	161
Vegetation	87	314	482	41
Ocean	108	2285	5950	87
SH				
Atmosphere	20	7	29	4E−2
Soils	29	88	243	2
Vegetation	26	52	96	2
Ocean	33	157	1022	9

Table L.2: Indicators for persistence (τ_{ov}) and long-range transport potential of PAHs (ACP: Arctic Contamination Potential, ZS: Zonal Spreading, ZD: Zonal Displacement)

Indicator	Unit	PHE	PYR	FLT	BaP
τ_{ov}[a]	days	3.7	59.5	119.2	44.6
ACP[b]	%	2.5	3.7	4.7	1.3
ZS[c]	km	1583	158	1883	625
ZD[d]	km	783	1835	1383	1843

[a] $\tau_{\mathrm{ov}} = \frac{B_{\mathrm{G}}}{S_{\mathrm{GH}}}$, where B_{G} is the total global environmental burden in 2009 and S_{G} is the time-averaged global historical sink and removal rates during the simulation period (2007−2009).

[b] $\mathrm{ACP} = \frac{\mathrm{B_{S,Ar}}}{\mathrm{B_G}} \times 100\%$, where $B_{\mathrm{S,Ar}}$ is the surface burden in the Arctic in 2009.

[c] $\mathrm{ZS} = \mathrm{ZW}(t) - \mathrm{ZW}(t_0)$, where ZW (Zonal Width) = $\mathrm{lat}_{95} - \mathrm{lat}_{05}$. lat_{05} and lat_{95} denote the 5^{th} and 95^{th} percentiles of the zonal cumulative mass distributions, respectively. t_0 is the time of entry.

[d] $\mathrm{ZD} = \mathrm{lat}_{50}(t) - \mathrm{lat}_{50}(t_0)$, where lat_{50} is defined as the median of the zonal cumulative mass distributions.

2009). The other two indicators characterize the substance's zonal distributions (Leip and Lammel, 2004). ZS addresses the changes of the 5% fringes of the plume/distribution in the north-south direction relative to the time of entry, whereas ZD refers to the distance traveled by the center of the plume during some Δt. Table L.2 presents the calculated indicators. This shows that the highest LRTP is found for a semi-volatile species, FLT, which is also the most persistent. Nevertheless, this species shows a lesser tendency for the plume to migrate (smaller ZD) than PYR and BaP. Note that the simulation neglects heterogeneous oxidations of PYR and FLT which may have a substantial impact on the estimation of τ_{ov} and global burden (Lammel et al., 2009).

L.2 Source-receptor relationships

EMAC-SVOC was applied to evaluate the relative contributions of BaP emitted from different areas of origin to BaP atmospheric burden in several regions and indicate source-to-receptor transport pathways using a tagged tracer simulation for 2003−2012. The rationale is that if such a quantitative source−receptor relationship and its atmospheric pathways of transport can be identified then the most effective inter-regional mitigation efforts can be pursued. In the tagged simulation, BaP tracers were distinguished by source regions depicted in Figure L.1. Here, the global domain was separated into 14 regions: Arctic (S1), Alaska and Canada (S2), North Eurasia (S3), middle North America (S4), Europe and West Asia (S5), Central and East Asia (S6), the Middle East and North Africa (S7), Tropical America (S8), Sub-Saharan Africa (S9), South and Southeast Asia (S10), SH mid-latitude landmass (S11), Antarctica (S12), NH oceans (S13), and SH oceans (S14). The model was set up on a T42 grid and driven by the assimilated meteorology from reanalysis data so that the simulated results suffer less bias in large-scale circulation patterns. It is worth noting that the relatively coarse resolution poorly resolves the structure of pollution plumes but is still useful for exploring transports triggered by synoptic and planetary (large-scale) circulation features that have sizes in the order of 1000 km or more and lifetimes of a few days to weeks (e.g., mid-latitude cyclones and anticyclones, fronts, ITCZ, subtropical jet stream).

The identification of spatially homogeneous receptor regions based on temporal patterns of BaP atmospheric burden is of particular interest. The Principal Component Analysis (PCA) and Varimax rotation were applied to look for coherent regions with similar BaP variability during the study period. The final identified receptor regions are illustrated in Figure L.2. The results confirm that emissions from mid-latitudes (in particular, S05, S06, and S11) have a stronger cross-continental impact, due to their source strength and efficient transports, whereas the impact of high-latitude sources (from S01 to R03) is more confined locally (Figure L.3). For the Arctic Ocean as a receptor (R03), the relative contributions have a notable seasonal variation. Europe and West Asia (S05) and North Eurasia (S03) are predominant contributors (>25%) to the wintertime Arctic burden, whereas the largest contribution to BaP during Arctic summer is from Central and East Asia (S06; 42%). Over the SH oceans (R05, R06, and R09), the contributions from SH mid-latitude landmass (S11) are the most important, accounting for at least 50% in

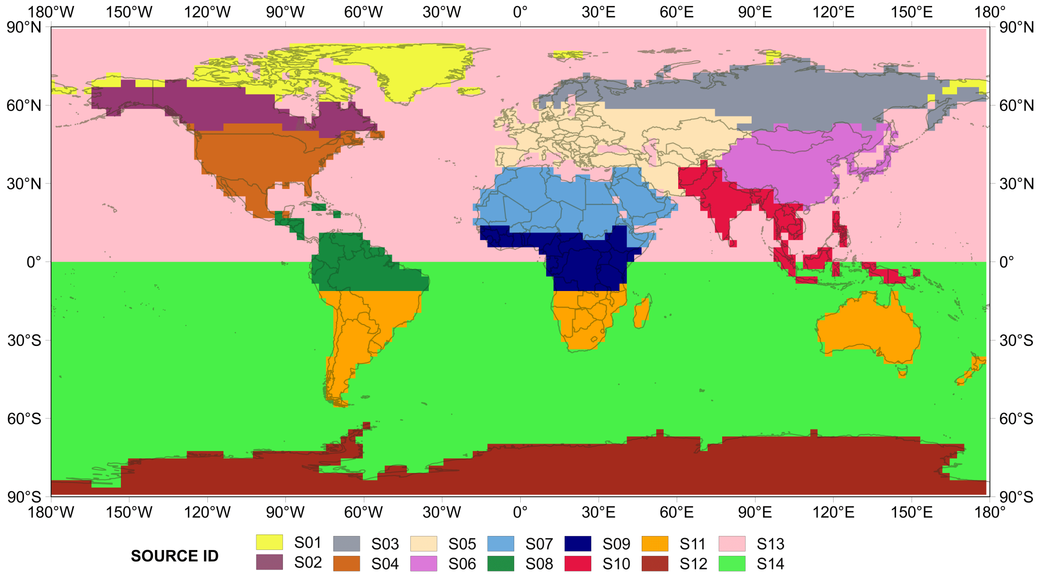

Figure L.1: Source regions for BaP tracer tagging. S01: Arctic, S02: Alaska and Canada, S03: North Eurasia, S04: middle North America, S05: Europe and West Asia, S06: Central and East Asia, S07: Middle East and North Africa, S08: Tropical America, S09: Sub-Saharan Africa, S10: South and Southeast Asia, S11: SH mid-latitude landmass, S12: Antarctica, S13: NH oceans, and S14: SH oceans.

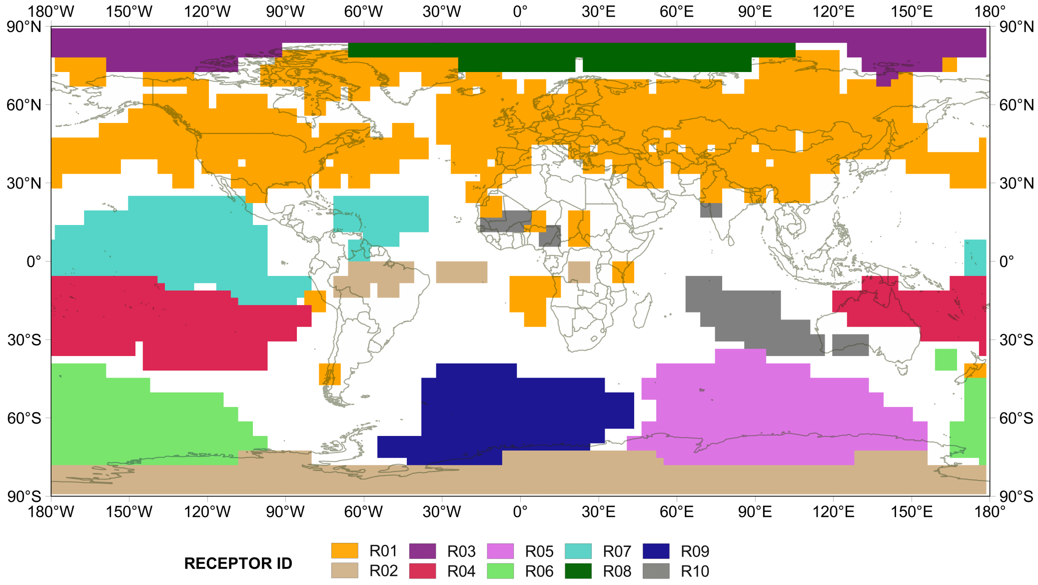

Figure L.2: Receptor regions delimited by maximum loading values of the rotated principal components. R01: northern mid-latitudes, R02: Antarctica, R03: Arctic Ocean, R04: southern Tropical Pacific, R05: South Indian Ocean, R06: South Pacific Ocean, R07: northern Tropical Pacific, R08: European Arctic, R09: South Atlantic Ocean, and R10: Tropical Indian Ocean.

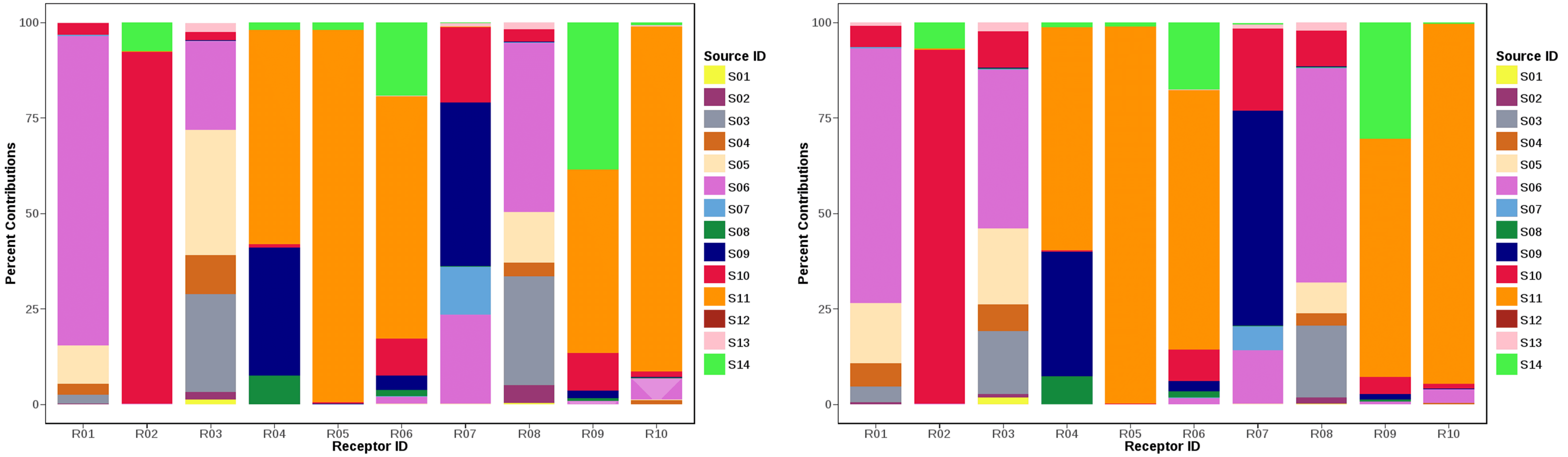

(a) DJF

(b) MAM

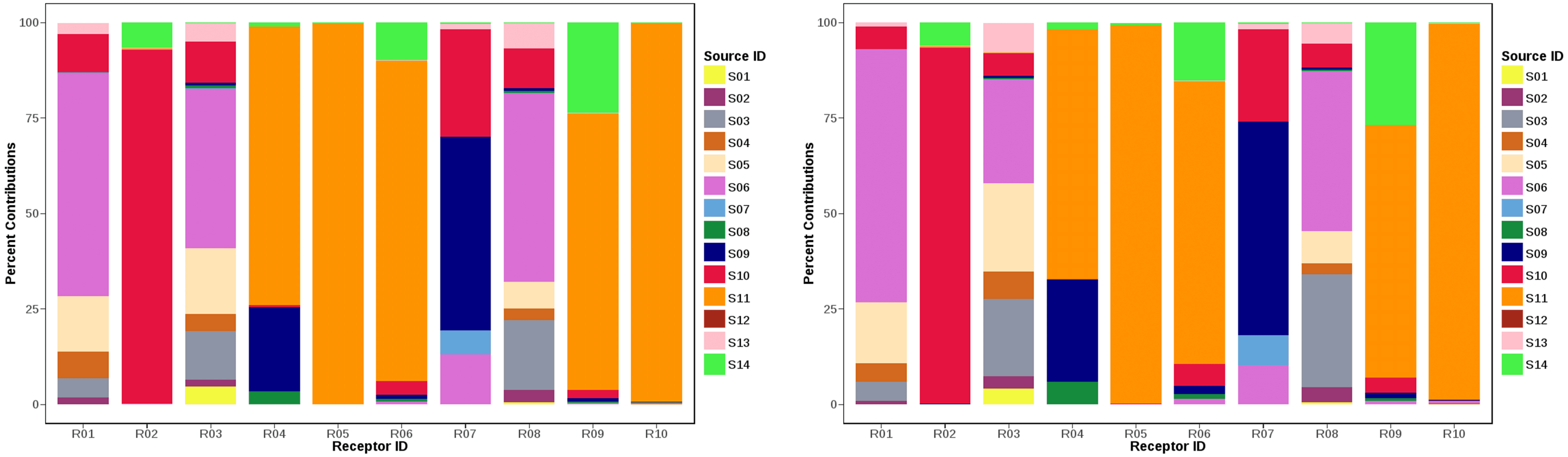

(c) JJA

(d) SON

Figure L.3: Seasonal variations in relative BaP contributions (%) from the 14 tagged source regions (S01−S14) to the mean BaP atmospheric burden in ten receptor regions (R1−R10) all seasons. The model also estimates that South and Southeast Asia (S10) has the largest contributions of more than 90% to the Antarctic (R02) BaP air burden.

To characterize atmospheric transport pathways, it is important to realize the episodic nature of pollutant transports. For instance, strong extratropical cyclones that drive trans-Pacific and trans-Atlantic transports occur occasionally in late winter and spring. For this reason, this study groups days with similar atmospheric burden behaviors by means of a cluster analysis (that is, the K-Means clustering). The purpose of the clustering is to divide the daily dataset into climatologically homogeneous events (periods) that conceivably reflect similar long-range transport history. The transport characteristics in the lower, middle and upper troposphere are further explored for selected source−receptor pairs and time clusters.

Note that the results presented above are considered preliminary and are therefore subject to further evaluation and adjustments.

Bibliography

Abraham, M. H. et al. (2010). "Prediction of solubility of drugs and other compounds in organic solvents". *J. Pharm. Sci.* 99 (3), pp. 1500–1515.

Achazi Rudolf, K. and Van Gestel Cornelis, A. M. (2003). "Uptake and accumulation of PAHs by terrestrial invertebrates". In: *PAHs: An Ecotoxicological Perspective.* Ed. by J. M. Weeks, S. O'Hare, B. Rattner, and D. P.E. Wiley Online Books, pp. 173–190.

Aghedo, A. M., Rast, S., and Schultz, M. G. (2010). "Sensitivity of tracer transport to model resolution, prescribed meteorology and tracer lifetime in the general circulation model ECHAM5". *Atmos. Chem. Phys.* 10 (7), pp. 3385–3396.

Alcock, R. E., Sweetman, A. J., Prevedouros, K., and Jones, K. C. (2003). "Understanding levels and trends of BDE-47 in the UK and North America: An assessment of principal reservoirs and source inputs". *Environ. Int.* 29 (6), pp. 691–698.

AMAP (2003). *AMAP Assessment 2002: The Influence of Global Change on Contaminant Pathways to, within, and from the Arctic.* Vol. xii. Oslo, Norway: Arctic Monitoring and Assessment Programme, p. 65.

Ambaum, M. H. P., Hoskins, B. J., and Stephenson, D. B. (2001). "Arctic Oscillation or North Atlantic Oscillation?" *J. Climate* 14 (16), pp. 3495–3507.

Anderson, P. N. and Hites, R. A. (1996). "OH radical reactions: The major removal pathway for polychlorinated biphenyls from the atmosphere". *Environ. Sci. Technol.* 30 (5), pp. 1756–1763.

Arangio, A. M. et al. (2015). "Multiphase chemical kinetics of OH radical uptake by molecular organic markers of biomass burning aerosols: humidity and temperature dependence, surface reaction, and bulk diffusion". *J. Phys. Chem. A* 119 (19), pp. 4533–4544.

Ariyasena, T. C. and Poole, C. F. (2014). "Determination of descriptors for polycyclic aromatic hydrocarbons and related compounds by chromatographic methods and liquid−liquid partition in totally organic biphasic systems". *J. Chromatogr. A* 1361, pp. 240–254.

Armitage, J. M. and Wania, F. (2013). "Exploring the potential influence of climate change and particulate organic carbon scenarios on the fate of neutral organic contaminants in the Arctic environment". *Environ. Sci. Process Impacts* 15 (12), pp. 2263–2272.

Atlas, E. and Giam, C. S. (1981). "Global transport of organic pollutants: Ambient concentrations in the remote marine atmosphere". *Science* 211 (4478), pp. 163–165.

Aulinger, A., Matthias, V., and Quante, M. (2007). "Introducing a partitioning mechanism for PAHs into the Community Multiscale Air Quality modeling system and its application to simulating the transport of benzo(a)pyrene over Europe". *J. Appl. Meteorol. Clim.* 46 (11), pp. 1718–1730.

— (2011). "An approach to temporally disaggregate benzo(a)pyrene emissions and their application to a 3D Eulerian atmospheric chemistry transport model". *Water Air Soil Pollut.* 216 (1), pp. 643–655.

Bamford, H. A., Poster, D. L., and Baker, J. E. (1999). "Temperature dependence of Henry's law constants of thirteen polycyclic aromatic hydrocarbons between 4°C and 31°C". *Environ. Toxicol. Chem.* 18 (9), pp. 1905–1912.

Barrie, L. A. et al. (1992). "Arctic contaminants: sources, occurrence and pathways". *Sci. Total Environ.* 122 (1), pp. 1–74.

Becker, S. et al. (2008). "Long-term trends in atmospheric concentrations of α- and γ-HCH in the Arctic provide insight into the effects of legislation and climatic fluctuations on contaminant levels". *Atmos. Environ.* 42 (35), pp. 8225–8233.

Berkemeier, T., Shiraiwa, M., Pöschl, U., and Koop, T. (2014). "Competition between water uptake and ice nucleation by glassy organic aerosol particles". *Atmos. Chem. Phys.* 14 (22), pp. 12513–12531.

Berkemeier, T. et al. (2016). "Ozone uptake on glassy, semi-solid and liquid organic matter and the role of reactive oxygen intermediates in atmospheric aerosol chemistry". *Phys. Chem. Chem. Phys.* 18 (18), pp. 12662–12674.

Bieser, J., Aulinger, A., Matthias, V., and Quante, M. (2012). "Impact of emission reductions between 1980 and 2020 on atmospheric benzo[a]pyrene concentrations over Europe". *Water Air Soil Pollut.* 223 (3), pp. 1393–1414.

BioHCWin v1.01 (2008). *Biodegradation Prediction of Petroleum Hydrocarbons v1.01, EPI Suite Version 4.10.* Washington D.C.

Boffetta, P., Jourenkova, N., and Gustavsson, P. (1997). "Cancer risk from occupational and environmental exposure to polycyclic aromatic hydrocarbons". *Cancer Causes Control* 8 (3), pp. 444–472.

Bolt, H. M. and Degen, G. H. (2002). "Comparative assessment of endocrine modulators with oestrogenic activity. II. Persistent organochlorine pollutants". *Arch. Toxicol.* 76 (4), pp. 187–193.

Boyer Montégut, C. de, Madec, G., Fischer, A. S., Lazar, A., and Iudicone, D. (2004). "Mixed layer depth over the global ocean: An examination of profile data and a profile-based climatology". *J. Geophys. Res. (Oceans)* 109 (C12), p. C12003.

Boynton, W. P. and Brattain, W. H. (1929). "Interdiffusion of gases and vapors". In: *International Critical Tables of Numerical Data, Physics, Chemistry and Technology.* Ed. by E. W. Washburn. Vol. 5. McGraw-Hill, pp. 62–63.

Breivik, K., Sweetman, A., Pacyna, J. M., and Jones, K. C. (2007). "Towards a global historical emission inventory for selected PCB congeners — A mass balance approach: 3. An update". *Sci. Total Environ.* 377 (2-3), pp. 296–307.

Brink, N. v. d. et al. (2009). "Correspondence on Geisz et al. Melting glaciers: a probable source of DDT to the Antarctic marine ecosystem". *Environ. Sci. Technol.* 43 (10), pp. 3976–3977.

Brubaker, W. W. and Hites, R. A. (1998). "OH reaction kinetics of polycyclic aromatic hydrocarbons and polychlorinated dibenzo-p-dioxins and dibenzofurans". *J. Phys. Chem. A* 102 (6), pp. 915–921.

Bruins, H. R. (1929). "Coefficients of diffusion in liquids". In: *International Critical Tables of Numerical Data, Physics, Chemistry and Technology.* Ed. by E. W. Washburn. Vol. 5. McGraw-Hill, pp. 63–72.

Butt, C. M., Muir, D. C. G., Stirling, I., Kwan, M., and Mabury, S. A. (2007). "Rapid response of Arctic ringed seals to changes in perfluoroalkyl production". *Environ. Sci. Technol.* 41 (1), pp. 42–49.

Calamari, D. et al. (1991). "Role of plant biomass in the global environmental partitioning of chlorinated hydrocarbons". *Environ. Sci. Technol.* 25 (8), pp. 1489–1495.

Carvalho, A. C. et al. (2006). "Influence of topography and land use on pollutants dispersion in the Atlantic coast of Iberian Peninsula". *Atmos. Environ.* 40 (21), pp. 3969–3982.

Chang, J. C. and Hanna, S. R. (2004). "Air quality model performance evaluation". *Meteorol. Atmos. Phys.* 87 (1), pp. 167–196.

Cheng, Y., Su, H., Koop, T., Mikhailov, E., and Pöschl, U. (2015). "Size dependence of phase transitions in aerosol nanoparticles". *Nat. Commun.* 6, p. 5923.

Cheng, Y. et al. (2016). "Reactive nitrogen chemistry in aerosol water as a source of sulfate during haze events in China". *Sci. Adv.* 2 (12).

Christoudias, T., Pozzer, A., and Lelieveld, J. (2012). "Influence of the North Atlantic Oscillation on air pollution transport". *Atmos. Chem. Phys.* 12 (2), pp. 869–877.

Dalla Valle, M., Jurado, E., Dachs, J., Sweetman, A. J., and Jones, K. C. (2005). “The maximum reservoir capacity of soils for persistent organic pollutants: implications for global cycling”. *Environ. Pollut.* 134 (1), pp. 153–164.

Dalla Valle, M., Codato, E., and Marcomini, A. (2007). “Climate change influence on POPs distribution and fate: A case study”. *Chemosphere* 67 (7), pp. 1287–1295.

Dalla Valle, M., Dachs, J., Sweetman, A. J., and Jones, K. C. (2004). “Maximum reservoir capacity of vegetation for persistent organic pollutants: Implications for global cycling”. *Global Biogeochem. Cy.* 18 (4).

Daly, G. L. and Wania, F. (2004). “Simulating the influence of snow on the fate of organic compounds”. *Environ. Sci. Technol.* 38 (15), pp. 4176–4186.

— (2005). “Organic contaminants in mountains”. *Environ. Sci. Technol.* 39 (2), pp. 385–398.

Dee, D. P. et al. (2011). “The ERA−Interim reanalysis: configuration and performance of the data assimilation system”. *Q. J. Roy. Meteor. Soc.* 137 (656), pp. 553–597.

DEFRA (2010). *UK Department of Environment, Food and Rural Affairs. Polycyclic Aromatic Hydrocarbons (PAH) data.* URL: https://uk-air.defra.gov.uk/data/pah-data (visited on 05/19/2016).

Deser, C. (2000). “On the teleconnectivity of the "Arctic Oscillation"”. *Geophys. Res. Lett.* 27 (6), pp. 779–782.

Ding, A. et al. (2009). “Transport of north China air pollution by midlatitude cyclones: Case study of aircraft measurements in summer 2007”. *J. Geophys. Res. (Atmos.)* 114 (D8).

Ding, A., Huang, X., and Fu, C. (2017). *Oxford Research Encyclopedia of Environmental Science.* Report. Oxford University Press.

Duncan, B. N. and Bey, I. (2004). “A modeling study of the export pathways of pollution from Europe: Seasonal and interannual variations (1987−1997)”. *J. Geophys. Res. (Atmos.)* 109 (D8), p. D08301.

EBAS NILU (2012). *The EBAS atmospheric database.* URL: http://ebas.nilu.no (visited on 05/19/2016).

Eckhardt, S. et al. (2003). “The North Atlantic Oscillation controls air pollution transport to the Arctic”. *Atmos. Chem. Phys.* 3 (5), pp. 1769–1778.

Efstathiou, C. I., Matejovičová, J., Bieser, J., and Lammel, G. (2016). “Evaluation of gas−particle partitioning in a regional air quality model for organic pollutants”. *Atmos. Chem. Phys.* 16 (23), pp. 15327–15345.

Endo, S. and Goss, K.-U. (2014). “Applications of polyparameter linear free energy relationships in environmental chemistry”. *Environ. Sci. Technol.* 48 (21), pp. 12477–12491.

Eskridge, R. E., Ku, J. Y., Rao, S. T., Porter, P. S., and Zurbenko, I. G. (1997). “Separating different scales of motion in time series of meteorological variables”. *Bull. Amer. Meteor. Soc.* 78 (7), pp. 1473–1483.

Fan, Y., Lin, S.-J., Griffies, S. M., and Hemer, M. A. (2014). “Simulated global swell and wind−sea climate and their responses to anthropogenic climate change at the end of the twenty-first century”. *J. Climate* 27 (10), pp. 3516–3536.

Fernández, P. and Grimalt, J. O. (2003). “On the global distribution of persistent organic pollutants”. *Chimia* 57 (9), pp. 514–521.

Finizio, A., Mackay, D., Bidleman, T., and Harner, T. (1997). “Octanol−air partition coefficient as a predictor of partitioning of semi-volatile organic chemicals to aerosols”. *Atmos. Environ.* 31 (15), pp. 2289–2296.

Finlayson-Pitts, B. J. and Pitts, J. N. (2000). *Chemistry of the upper and lower atmosphere: Theory, experiments, and applications.* San Diego: Academic Press.

Fisk, A. T. et al. (2002). “Persistent organochlorine contaminants and enantiomeric signatures of chiral pollutants in ringed seals (Phoca hispida) collected on the east and west side of the Northwater Polynya, Canadian Arctic”. *Arch. Environ. Contam. Toxicol.* 42 (1), pp. 118–126.

Franklin, J. et al. (2000). “Quantitative determination of persistence in air”. In: *Evaluation of Persistence and Long-range Transport of Organic Chemicals in the Environment.* Ed. by G. Klecka et al. Pensacola: SETAC Publication, pp. 7–62.

Friedman, C. L. and Selin, N. E. (2016). “PCBs in the Arctic atmosphere: determining important driving forces using a global atmospheric transport model”. *Atmos. Chem. Phys.* 16 (5), pp. 3433–3448.

Friedman, C. L., Pierce, J. R., and Selin, N. E. (2014). “Assessing the influence of secondary organic versus primary carbonaceous aerosols on long-range atmospheric polycyclic aromatic hydrocarbon transport”. *Environ. Sci. Technol.* 48 (6), pp. 3293–3302.

Friedman, C. L. and Selin, N. E. (2012). “Long-range atmospheric transport of polycyclic aromatic hydrocarbons: global 3-D model analysis including evaluation of Arctic sources”. *Environ. Sci. Technol.* 46 (17), pp. 9501–9510.

Friedman, C. L., Zhang, Y., and Selin, N. E. (2013). “Climate change and emissions impacts on atmospheric PAH transport to the Arctic”. *Environ. Sci. Technol.* 48 (1), pp. 429–437.

Galarneau, E. et al. (2014). “PAH concentrations simulated with the AURAMS-PAH chemical transport model over Canada and the USA”. *Atmos. Chem. Phys.* 14 (8), pp. 4065–4077.

Galarneau, E., Bidleman, T. F., and Blanchard, P. (2006). “Seasonality and interspecies differences in particle/gas partitioning of PAHs observed by the Integrated Atmospheric Deposition Network (IADN)”. *Atmos. Environ.* 40 (1), pp. 182–197.

Gantt, B. et al. (2011). “Wind speed dependent size-resolved parameterization for the organic mass fraction of sea spray aerosol”. *Atmos. Chem. Phys.* 11 (16), pp. 8777–8790.

Ganzeveld, L. and Lelieveld, J. (1995). “Dry deposition parameterization in a chemistry general circulation model and its influence on the distribution of reactive trace gases”. *J. Geophys. Res. (Atmos.)* 100 (D10), pp. 20999–21012.

Ganzeveld, L., Lelieveld, J., and Roelofs, G.-J. (1998). “A dry deposition parameterization for sulfur oxides in a chemistry and general circulation model”. *J. Geophys. Res. (Atmos.)* 103 (D5), pp. 5679–5694.

Geisz, H. N., Dickhut, R. M., Cochran, M. A., Fraser, W. R., and Ducklow, H. W. (2008). “Melting glaciers: a probable source of DDT to the Antarctic marine ecosystem”. *Environ. Sci. Technol.* 42 (11), pp. 3958–3962.

Gillett, N. P. and Fyfe, J. C. (2013). “Annular mode changes in the CMIP5 simulations”. *Geophys. Res. Lett.* 40 (6), pp. 1189–1193.

Goldberg, R. (1975). “Synthetic organohalides in the sea”. *Proc. R. Soc. Lond. B. Biol. Sci.* 189 (1096), pp. 277–289.

Gong, S. L. et al. (2007). “GEM/POPs: a global 3-D dynamic model for semi-volatile persistent organic pollutants — Part 1: Model description and evaluations of air concentrations”. *Atmos. Chem. Phys. Discuss.* 7 (15), pp. 4001–4013.

Goss, K.-U. and Schwarzenbach, R. P. (2001). “Linear free energy relationships used to evaluate equilibrium partitioning of organic compounds”. *Environ. Sci. Technol.* 35 (1), pp. 1–9.

Goss, K.-U., Buschmann, J., and Schwarzenbach, R. P. (2003). “Determination of the surface sorption properties of talc, different salts, and clay minerals at various relative humidities using adsorption data of a diverse set of organic vapors”. *Environ. Toxicol. Chem.* 22 (11), pp. 2667–2672.

Gouin, T. and Wania, F. (2007). “Time trends of Arctic contamination in relation to emission history and chemical persistence and partitioning properties”. *Environ. Sci. Technol.* 41 (17), pp. 5986–5992.

Gouin, T. et al. (2013). “Influence of global climate change on chemical fate and bioaccumulation: The role of multimedia models”. *Environ. Toxicol. Chem.* 32 (1), pp. 20–31.

Grell, G. A. et al. (2005). “Fully coupled "online" chemistry within the WRF model”. *Atmos. Environ.* 39 (37), pp. 6957–6975.

Guelle, W., Schulz, M., Balkanski, Y., and Dentener, F. (2001). “Influence of the source formulation on modeling the atmospheric global distribution of sea salt aerosol”. *J. Geophys. Res. (Atmos.)* 106 (D21), pp. 27509–27524.

Guglielmo, F., Lammel, G., and Maier-Reimer, E. (2009). “Global environmental cycling of γ-HCH and DDT in the 1980s — A study using a coupled atmosphere and ocean general circulation model”. *Chemosphere* 76 (11), pp. 1509–1517.

Gusev, A., Mantseva, E., Shatalov, V., and B., S. (2005). *Regional Multicompartment Model MSCE-POP.* EMEP/MSC-E Technical Report 5.

Hagemann, S., Loew, A., and Andersson, A. (2013). “Combined evaluation of MPI-ESM land surface water and energy fluxes”. *J. Adv. Model Earth Syst.* 5 (2), pp. 259–286.

Halsall, C. J. et al. (1997). “Spatial and temporal variation of polycyclic aromatic hydrocarbons in the Arctic atmosphere”. *Environ. Sci. Technol.* 31 (12), pp. 3593–3599.

Hamed, K. H. and Ramachandra Rao, A. (1998). “A modified Mann−Kendall trend test for autocorrelated data”. *J. Hydrol.* 204 (1-4), pp. 182–196.

Hansen, K. M., Christensen, J. H., Brandt, J., Frohn, L. M., and Geels, C. (2004). “Modelling atmospheric transport of α-hexachlorocyclohexane in the Northern Hemisphere with a 3-D dynamical model: DEHM-POP”. *Atmos. Chem. Phys.* 4 (4), pp. 1125–1137.

Hansen, K. M., Christensen, J. H., Geels, C., Silver, J. D., and Brandt, J. (2015). “Modelling the impact of climate change on the atmospheric transport and the fate of persistent organic pollutants in the Arctic”. *Atmos. Chem. Phys.* 15 (11), pp. 6549–6559.

Hansen, K. M. et al. (2008). “Modeling short-term variability of α-hexachlorocyclohexane in Northern Hemispheric air”. *J. Geophys. Res. (Atmos.)* 113 (D2), p. D02310.

Harner, T. and Bidleman, T. F. (1998a). “Measurement of octanol−air partition coefficients for polycyclic aromatic hydrocarbons and polychlorinated naphthalenes”. *J. Chem. Eng. Data* 43 (1), pp. 40–46.

— (1998b). “Octanol−air partition coefficient for describing particle/gas partitioning of aromatic compounds in urban air”. *Environ. Sci. Technol.* 32 (10), pp. 1494–1502.

Hicks, B. B., Baldocchi, D. D., Meyers, T. P., Hosker R. P., J., and Matt, D. R. (1987). “A preliminary multiple resistance routine for deriving dry deposition velocities from measured quantities”. *Water Air Soil Pollut.* 36 (3-4), pp. 311–330.

Hirdman, D. et al. (2010). “Long-term trends of black carbon and sulphate aerosol in the Arctic: Changes in atmospheric transport and source region emissions”. *Atmos. Chem. Phys.* 10 (19), pp. 9351–9368.

Hoff, J. T., Wania, F., Mackay, D., and Gillham, R. (1995). “Sorption of nonpolar organic vapors by ice and snow”. *Environ. Sci. Technol.* 29 (8), pp. 1982–1989.

Hofmann, L., Stemmler, I., and Lammel, G. (2012). “The impact of organochlorines cycling in the cryosphere on global distributions and fate — 2. Land ice and temporary snow cover”. *Environ. Pollut.* 162, pp. 482–488.

Hogrefe, C. et al. (2004). “Simulating regional-scale ozone climatology over the eastern United States: model evaluation results”. *Atmos. Environ.* 38 (17), pp. 2627–2638.

Hornsby, A., Wauchope, R., and Herner, A. (1996). *Pesticide properties in the environment.* New York: Springer, p. 227.

Hoyau, V., Laffrezo, J. L., Garrigues, P., Clain, M. P., and Masclet, P. (1996). “Deposition of aerosols in polar regions-contamination of the ice sheet by polycyclic aromatic hydrocarbons”. *Polycycl. Aromat. Comp.* 8 (1), pp. 35–44.

Huang, P., Gong, S. L., Zhao, T. L., Neary, L., and Barrie, L. A. (2007). “GEM/POPs: a global 3-D dynamic model for semi-volatile persistent organic pollutants — Part 2: Global transports and budgets of PCBs”. *Atmos. Chem. Phys.* 7 (15), pp. 4015–4025.

Hung, H. et al. (2001). “Are PCBs in the Canadian Arctic atmosphere declining? Evidence from 5 years of monitoring”. *Environ. Sci. Technol.* 35 (7), pp. 1303–1311.

Hung, H. et al. (2005a). “Temporal and spatial variabilities of atmospheric polychlorinated biphenyls (PCBs), organochlorine (OC) pesticides and polycyclic aromatic hydrocarbons (PAHs) in the Canadian Arctic: Results from a decade of monitoring”. *Sci. Total Environ.* 342 (1-3), pp. 119–144.

Hung, H., Chi Lee, S., Wania, F., Blanchard, P., and Brice, K. (2005b). “Measuring and simulating atmospheric concentration trends of polychlorinated biphenyls in the Northern Hemisphere”. *Atmos. Environ.* 39 (35), pp. 6502–6512.

Hung, H. et al. (2010). “Atmospheric monitoring of organic pollutants in the Arctic under the Arctic Monitoring and Assessment Programme (AMAP): 1993−2006”. *Sci. Total Environ.* 408 (15), pp. 2854–2873.

Hurrell, J. W. (1995). “Decadal trends in the North Atlantic Oscillation: Regional temperatures and precipitation”. *Science* 269 (5224), pp. 676–679.

Hurrell, J. W. and Van Loon, H. (1997). “Decadal variations in climate associated with the North Atlantic Oscillation”. *Clim. Change* 36 (3-4), pp. 301–326.

IADN (2014). *Great Lakes Integrated Atmospheric Deposition Network.* URL: http://ec.gc.ca/data_donnees/STB-AQRD/Toxics/IADN (visited on 06/10/2016).

Ilyina, T. et al. (2013). “Global ocean biogeochemistry model HAMOCC: Model architecture and performance as component of the MPI-Earth system model in different CMIP5 experimental realizations”. *J. Adv. Model Earth Syst.* 5 (2), pp. 287–315.

Inomata, Y. et al. (2013). “Source contribution analysis of surface particulate polycyclic aromatic hydrocarbon concentrations in northeastern Asia by source−receptor relationships”. *Environ. Pollut.* 182, pp. 324–334.

Inomata, Y. et al. (2017). “Source−receptor relationship analysis of the atmospheric deposition of PAHs subject to long-range transport in Northeast Asia”. *Environ. Sci. Technol.* 51 (14), pp. 7972–7981.

Janssens-Maenhout, G. et al. (2015). “HTAP_v2.2: A mosaic of regional and global emission grid maps for 2008 and 2010 to study hemispheric transport of air pollution”. *Atmos. Chem. Phys.* 15 (19), pp. 11411–11432.

Jöckel, P. et al. (2006). “The atmospheric chemistry general circulation model ECHAM5/MESSy1: Consistent simulation of ozone from the surface to the mesosphere”. *Atmos. Chem. Phys.* 6 (12), pp. 5067–5104.

Jöckel, P. et al. (2010). “Development cycle 2 of the Modular Earth Submodel System (MESSy2)”. *Geosci. Model Dev.* 3 (2), pp. 717–752.

Junge, C. (1977). “Basic considerations about trace constituents in the atmosphere as related to the fate of global pollutants”. In: *Fate of Pollutants in the Air and Water Environment.* Ed. by I. Suffet. New York: John Wiley & Sons, pp. 7–26.

Jury, W. A., Spencer, W. F., and Farmer, W. J. (1983). “Behavior assessment model for trace organics in soil: I. Model description”. *J. Environ. Qual.* 12 (4), pp. 558–564.

Jury, W. A., Russo, D., Streile, G., and El Abd, H. (1990). “Evaluation of volatilization by organic chemicals residing below the soil surface”. *Water Resour. Res.* 26 (1), pp. 13–20.

Kahan, T. F., Kwamena, N. O. A., and Donaldson, D. J. (2006). “Heterogeneous ozonation kinetics of polycyclic aromatic hydrocarbons on organic films”. *Atmos. Environ.* 40 (19), pp. 3448–3459.

Kallenborn, R., Halsall, C., Dellong, M., and Carlsson, P. (2012). “The influence of climate change on the global distribution and fate processes of anthropogenic persistent organic pollutants”. *J. Environ. Monit.* 14 (11), pp. 2854–2869.

Kalnay, E. et al. (1996). “The NCEP/NCAR 40-year reanalysis project”. *Bull. Amer. Meteor. Soc.* 77 (3), pp. 437–471.

Kamprad, I. and Goss, K.-U. (2007). “Systematic investigation of the sorption properties of polyurethane foams for organic vapors”. *Anal. Chem.* 79 (11), pp. 4222–4227.

Kerkweg, A. et al. (2006a). “Technical Note: An implementation of the dry removal processes DRY DEPosition and SEDImentation in the Modular Earth Submodel System (MESSy)”. *Atmos. Chem. Phys.* 6 (12), pp. 4617–4632.

Kerkweg, A., Sander, R., Tost, H., and Jöckel, P. (2006b). “Technical Note: Implementation of prescribed (OFFLEM), calculated (ONLEM), and pseudo-emissions (TNUDGE) of chemical species in the Modular Earth Submodel System (MESSy)”. *Atmos. Chem. Phys.* 6 (11), pp. 3603–3609.

Keyte, I. J., Harrison, R. M., and Lammel, G. (2013). “Chemical reactivity and long-range transport potential of polycyclic aromatic hydrocarbons — A review”. *Chem. Soc. Rev.* 42 (24), pp. 9333–9391.

Kim, J. Y., Lee, J. Y., Choi, S. D., Kim, Y. P., and Ghim, Y. S. (2012). “Gaseous and particulate polycyclic aromatic hydrocarbons at the Gosan background site in East Asia”. *Atmos. Environ.* 49 (0), pp. 311–319.

Klánová, J. et al. (2008). *Application of passive sampler for monitoring of POPs in ambient air. VI. Pilot study for development of the monitoring network in the African continent (MONET-AFRICA 2008).* RECETOX_TOCOEN 343. RECETOX MU Brno, Czech Republic.

Klöpffer, W., Wagner, B. O., and Steinhäuser, K. G. (2008). *Atmospheric Degradation of Organic Substances: Persistence, Transport Potential, Spatial Range.* Wiley, p. 258.

Koop, T., Bookhold, J., Shiraiwa, M., and Pöschl, U. (2011). “Glass transition and phase state of organic compounds: dependency on molecular properties and implications for secondary organic aerosols in the atmosphere”. *Phys. Chem. Chem. Phys.* 13 (43), pp. 19238–19255.

Kwamena, N.-O. A., Thornton, J. A., and Abbatt, J. P. D. (2004). “Kinetics of surface-bound benzo[a]pyrene and ozone on solid organic and salt aerosols”. *J. Phys. Chem. A* 108 (52), pp. 11626–11634.

Laender, F. D., Hammer, J., Hendriks, A. J., Soetaert, K., and Janssen, C. R. (2011). “Combining monitoring data and modeling identifies PAHs as emerging contaminants in the Arctic”. *Environ. Sci. Technol.* 45 (20), pp. 9024–9029.

Lammel, G. and Stemmler, I. (2012). “Fractionation and current time trends of PCB congeners: Evolvement of distributions 1950−2010 studied using a global atmosphere-ocean general circulation model”. *Atmos. Chem. Phys.* 12 (15), pp. 7199–7213.

Lammel, G., Kloepffer, W., Semeena, V. S., Schmidt, E., and Leip, A. (2007). “Multicompartmental fate of persistent substances. Comparison of predictions from multi-media box models and a multicompartment chemistry−atmospheric transport model”. *Environ. Sci. Pollut. Res.* 14 (3), pp. 153–165.

Lammel, G., Sehili, A. M., Bond, T. C., Feichter, J., and Grassl, H. (2009). “Gas/particle partitioning and global distribution of polycyclic aromatic hydrocarbons — A modelling approach”. *Chemosphere* 76 (1), pp. 98–106.

Lammel, G. et al. (2010). “Polycyclic aromatic hydrocarbons in air on small spatial and temporal scales — II. Mass size distributions and gas−particle partitioning”. *Atmos. Environ.* 44 (38), pp. 5022–5027.

Lamon, L., Dalla Valle, M., Critto, A., and Marcomini, A. (2009a). “Introducing an integrated climate change perspective in POPs modelling, monitoring and regulation”. *Environ. Pollut.* 157 (7), pp. 1971–1980.

Lamon, L. et al. (2009b). “Modeling the global levels and distribution of polychlorinated biphenyls in air under a climate change scenario”. *Environ. Sci. Technol.* 43 (15), pp. 5818–5824.

Land, C., Feichter, J., and Sausen, R. (2002). “Impact of vertical resolution on the transport of passive tracers in the ECHAM4 model”. *Tellus B* 54 (4), pp. 344–360.

Landgraf, J. and Crutzen, P. J. (1998). “An efficient method for online calculations of photolysis and heating rates”. *J. Atmos. Sci.* 55 (5), pp. 863–878.

Lauer, A., Eyring, V., Hendricks, J., Jöckel, P., and Lohmann, U. (2007). “Global model simulations of the impact of ocean-going ships on aerosols, clouds, and the radiation budget”. *Atmos. Chem. Phys.* 7 (19), pp. 5061–5079.

Law, R. J. et al. (2006). “Levels and trends of brominated flame retardants in the European environment”. *Chemosphere* 64 (2), pp. 187–208.

Leip, A. and Lammel, G. (2004). “Indicators for persistence and long-range transport potential as derived from multicompartment chemistry−transport modelling”. *Environ. Pollut.* 128 (1-2), pp. 205–221.

Li, N., Wania, F., Lei, Y. D., and Daly, G. L. (2003). “A comprehensive and critical compilation, evaluation, and selection of physical-chemical property data for selected polychlorinated biphenyls”. *J. Phys. Chem. Ref. Data* 32 (4), p. 1545.

Li, Q. et al. (2002). “Transatlantic transport of pollution and its effects on surface ozone in Europe and North America”. *J. Geophys. Res. (Atmos.)* 107 (D13).

Li, Y. F. and Macdonald, R. W. (2005). “Sources and pathways of selected organochlorine pesticides to the Arctic and the effect of pathway divergence on HCH trends in biota: a review”. *Sci. Total Environ.* 342 (1), pp. 87–106.

Liss, P. S. and Slater, P. G. (1974). “Flux of gases across the air−sea interface”. *Nature* 247 (5438), pp. 181–184.

Liu, J. et al. (2014). “The distribution and origin of PAHs over the Asian marginal seas, the Indian, and the Pacific Oceans: Implications for outflows from Asia and Africa”. *J. Geophys. Res. (Atmos.)* 119 (4), pp. 1949–1961.

Lohmann, R. and Lammel, G. (2004). “Adsorptive and absorptive contributions to the gas−particle partitioning of polycyclic aromatic hydrocarbons: State of knowledge and recommended parametrization for modeling”. *Environ. Sci. Technol.* 38 (14), pp. 3793–3803.

Lohmann, R., Breivik, K., Dachs, J., and Muir, D. (2007). “Global fate of POPs: Current and future research directions”. *Environ. Pollut.* 150 (1), pp. 150–165.

Lohmann, R. et al. (2013). “PAHs on a west-to-east transect across the tropical Atlantic Ocean”. *Environ. Sci. Technol.* 47 (6), pp. 2570–2578.

Luo, Y. and Yang, X. (2007). “A multimedia environmental model of chemical distribution: Fate, transport, and uncertainty analysis”. *Chemosphere* 66 (8), pp. 1396–1407.

Lynn, B. H., Healy, R., and Druyan, L. M. (2009). “Quantifying the sensitivity of simulated climate change to model configuration”. *Clim. Change* 92 (3), pp. 275–298.

Ma, J., Venkatesh, S., and Jantunen, L. M. (2003a). “Evidence of the impact of ENSO events on temporal trends of hexachlorobenzene air concentrations over the Great Lakes”. *Sci. Total Environ.* 313 (1), pp. 177–184.

Ma, J., Daggupaty, S., Harner, T., and Li, Y. (2003b). “Impacts of lindane usage in the Canadian prairies on the Great Lakes ecosystem. 1. Coupled atmospheric transport model and modeled concentrations in air and soil”. *Environ. Sci. Technol.* 37 (17), pp. 3774–3781.

Ma, J., Hung, H., and Blanchard, P. (2004a). “How do climate fluctuations affect persistent organic pollutant distribution in North America? Evidence from a decade of air monitoring”. *Environ. Sci. Technol.* 38 (9), pp. 2538–2543.

Ma, J., Cao, Z., and Hung, H. (2004b). “North Atlantic Oscillation signatures in the atmospheric concentrations of persistent organic pollutants: An analysis using Integrated Atmospheric Deposition Network−Great Lakes monitoring data”. *J. Geophys. Res. (Atmos.)* 109 (D12).

Ma, J., Hung, H., Tian, C., and Kallenborn, R. (2011). “Revolatilization of persistent organic pollutants in the Arctic induced by climate change”. *Nat. Clim. Change* 1 (5), pp. 255–260.

Ma, Y.-G., Lei, Y. D., Xiao, H., Wania, F., and Wang, W.-H. (2010). “Critical review and recommended values for the physical−chemical property data of 15 polycyclic aromatic hydrocarbons at 25°C”. *J. Chem. Eng. Data* 55 (2), pp. 819–825.

Macdonald, R. W. and Bewers, J. M. (1996). “Contaminants in the Arctic marine environment: priorities for protection”. *Ices J. Mar. Sci.* 53 (3), pp. 537–563.

Macdonald, R. W., Mackay, D., Li, Y. F., and Hickie, B. (2003). “How will global climate change affect risks from long-range transport of persistent organic pollutants?” *Hum. Ecol. Risk Assess.* 9 (3), pp. 643–660.

Macdonald, R. W., Harner, T., and Fyfe, J. (2005). “Recent climate change in the Arctic and its impact on contaminant pathways and interpretation of temporal trend data”. *Sci. Total Environ.* 342 (1-3), pp. 5–86.

Mackay, D. (2010). *Multimedia environmental models: The fugacity approach, second edition.* Taylor & Francis.

Mackay, D. and Boethling, R. S. (2000). *Handbook of property estimation methods for chemicals: Environmental health sciences.* Taylor & Francis.

Mackay, D., Shiu, W. Y., Ma, K. C., and Lee, S. C. (2006). *Handbook of physical−chemical properties and environmental fate for organic chemicals.* 2nd. Vol. I. Introduction and Hydrocarbons. Taylor & Francis.

MacLeod, M., Fraser, A. J., and Mackay, D. (2002). “Evaluating and expressing the propagation of uncertainty in chemical fate and bioaccumulation models”. *Environ. Toxicol. Chem.* 21 (4), pp. 700–709.

MacLeod, M., Riley, W. J., and McKone, T. E. (2005). “Assessing the influence of climate variability on atmospheric concentrations of polychlorinated biphenyls using a global-scale mass balance model (BETR-global)”. *Environ. Sci. Technol.* 39 (17), pp. 6749–6756.

Malanichev, A., Mantseva, E., Shatalov, V., Strukov, B., and Vulykh, N. (2004). “Numerical evaluation of the PCBs transport over the Northern Hemisphere”. *Environ. Pollut.* 128 (1), pp. 279–289.

Marsland, S. J., Haak, H., Jungclaus, J. H., Latif, M., and Röske, F. (2003). “The Max-Planck-Institute global ocean/sea ice model with orthogonal curvilinear coordinates”. *Ocean Model.* 5 (2), pp. 91–127.

Matthias, V., Aulinger, A., and Quante, M. (2009). “CMAQ simulations of the benzo(a)pyrene distribution over Europe for 2000 and 2001”. *Atmos. Environ.* 43 (26), pp. 4078–4086.

Meador, J. P., Stein, J. E., Reichert, W. L., and Varanasi, U. (1995). “Bioaccumulation of polycyclic aromatic hydrocarbons by marine organisms”. In: *Reviews of Environmental Contamination and Toxicology: Continuation of Residue Reviews.* Ed. by G. W. Ware. New York, NY: Springer New York, pp. 79–165.

Meyer, T. and Wania, F. (2007). “What environmental fate processes have the strongest influence on a completely persistent organic chemical’s accumulation in the Arctic?” *Atmos. Environ.* 41 (13), pp. 2757–2767.

Meyer, T., Wania, F., and Breivik, K. (2005). “Illustrating sensitivity and uncertainty in environmental fate models using partitioning maps”. *Environ. Sci. Technol.* 39 (9), pp. 3186–3196.

Mintz, C. et al. (2008). “Enthalpy of solvation correlations for gaseous solutes dissolved in dibutyl ether and ethyl acetate”. *Thermochim. Acta* 470 (1-2), pp. 67–76.

Mu, Q. et al. (2018). “Temperature effect on phase state and reactivity controls atmospheric multiphase chemistry and transport of PAHs”. *Sci. Adv.* 4 (3).

Nadal, M., Marquès, M., Mari, M., and Domingo, J. L. (2015). “Climate change and environmental concentrations of POPs: A review”. *Environ. Res.* 143, Part A, pp. 177–185.

Nakicenovic, N. et al. (2000). *IPCC special report on emissions scenarios.* Tech. rep. Cambridge, UK, p. 608.

Nizzetto, L. et al. (2008). “PAHs in air and seawater along a North−South Atlantic transect: Trends, processes and possible sources”. *Environ. Sci. Technol.* 42 (5), pp. 1580–1585.

Nordic Council of Ministers (2008). *Hexabromocyclododecane as a possible global POP.* Copenhagen: TemaNord 2008:520, p. 91.

Notz, D., Haumann, F. A., Haak, H., Jungclaus, J. H., and Marotzke, J. (2013). “Arctic sea-ice evolution as modeled by Max Planck Institute for Meteorology’s Earth system model”. *J. Adv. Model Earth Syst.* 5 (2), pp. 173–194.

Octaviani, M., Stemmler, I., Lammel, G., and Graf, H. F. (2015). “Atmospheric transport of persistent organic pollutants to and from the Arctic under present-day and future climate”. *Environ. Sci. Technol.* 49 (6), pp. 3593–3602.

Odabasi, M., Cetin, E., and Sofuoglu, A. (2006). “Determination of octanol−air partition coefficients and supercooled liquid vapor pressures of PAHs as a function of temperature: Application to gas−particle partitioning in an urban atmosphere”. *Atmos. Environ.* 40 (34), pp. 6615–6625.

OECD (2004). *Guidance Document on the Use of Multimedia Models for Estimating Overall Environmental Persistance and Long-Range Transport.* Organisation for Economic Co-operation and Development. Paris: OECD Publishing.

Pacyna, J. M., Sundseth, K., and Cousins, I. (2010). *Database of physic-chemical properties and historic/future emission estimates for selected chemicals.* Report D11. ArcRisk project, unpublished.

Pankow, J. F. (1987). “Review and comparative analysis of the theories on partitioning between the gas and aerosol particulate phases in the atmosphere”. *Atmos. Environ.* 21 (11), pp. 2275–2283.

Park, K. S., Sims, R. C., Dupont, R. R., Doucette, W. J., and Matthews, J. E. (1990). “Fate of PAH compounds in two soil types: Influence of volatilization, abiotic loss and biological activity”. *Environ. Toxicol. Chem.* 9 (2), pp. 187–195.

Pauwels, A. et al. (2000). “Comparison of persistent organic pollutant residues in serum and adipose tissue in a female population in Belgium, 1996−1998”. *Arch. Environ. Contam. Toxicol.* 39 (2), pp. 265–270.

Peckham, S. et al. (2014). *WRF/Chem Version 3.6.1 User’s Guide.* NCAR Tech Guide.

Perera, F. P. (1997). “Environment and cancer: Who are susceptible?” *Science* 278 (5340), pp. 1068–1073.

Perraudin, E., Budzinski, H., and Villenave, E. (2007). “Kinetic study of the reactions of ozone with polycyclic aromatic hydrocarbons adsorbed on atmospheric model particles”. *J. Atmos. Chem.* 56 (1), pp. 57–82.

Pöschl, U., Rudich, Y., and Ammann, M. (2007). “Kinetic model framework for aerosol and cloud surface chemistry and gas−particle interactions — Part 1: General equations, parameters, and terminology”. *Atmos. Chem. Phys.* 7 (23), pp. 5989–6023.

Pöschl, U., Letzel, T., Schauer, C., and Niessner, R. (2001). “Interaction of ozone and water vapor with spark discharge soot aerosol particles coated with benzo[a]pyrene: O3 and H2O adsorption, benzo[a]pyrene degradation, and atmospheric Implications”. *J. Phys. Chem. A* 105 (16), pp. 4029–4041.

Pozzer, A. et al. (2006). “Technical Note: The MESSy-submodel AIRSEA calculating the air−sea exchange of chemical species”. *Atmos. Chem. Phys.* 6 (12), pp. 5435–5444.

Prevedouros, K., Jones, K. C., and Sweetman, A. J. (2004). “Estimation of the production, consumption, and atmospheric emissions of pentabrominated diphenyl ether in Europe between 1970 and 2000”. *Environ. Sci. Technol.* 38 (12), pp. 3224–3231.

Pringle, K. J. et al. (2010). “Description and evaluation of GMXe: a new aerosol submodel for global simulations (v1)”. *Geosci. Model Dev.* 3 (2), pp. 391–412.

Pruppacher, H. and Klett, J. (2010). *Microphysics of Clouds and Precipitation.* 2nd ed. Springer Netherlands, p. 954.

Puri, S., Chickos, J. S., and Welsh, W. J. (2001). “Determination of vaporization enthalpies of polychlorinated biphenyls by correlation gas chromatography”. *Anal. Chem.* 73 (7), pp. 1480–1484.

— (2002). “Three-dimensional quantitative structure-property relationship (3D-QSPR) models for prediction of thermodynamic properties of polychlorinated biphenyls (PCBs): enthalpies of fusion and their application to estimates of enthalpies of sublimation and aqueous solubilities”. *J. Chem. Inf. Comput. Sci.* 43 (1), pp. 55–62.

Roeckner, E. et al. (2006). “Sensitivity of simulated climate to horizontal and vertical resolution in the ECHAM5 atmosphere model”. *J. Climate* 19 (16), pp. 3771–3791.

Roeckner, E. et al. (2003). *The atmospheric general circulation model ECHAM 5. PART I: Model description.* Report 349. Hamburg: Max-Planck-Institut für Meteorologie, p. 127.

Romero, R., Ramis, C., and Alonso, S. (1997). “Numerical simulation of an extreme rainfall event in Catalonia: Role of orography and evaporation from the sea”. *Q. J. Roy. Meteor. Soc.* 123 (539), pp. 537–559.

Roth, C. M., Goss, K.-U., and Schwarzenbach, R. P. (2005). “Sorption of a diverse set of organic vapors to diesel soot and road tunnel aerosols”. *Environ. Sci. Technol.* 39 (17), pp. 6632–6637.

Roux, M. V., Temprado, M., Chickos, J. S., and Nagano, Y. (2008). “Critically evaluated thermochemical properties of polycyclic aromatic hydrocarbons”. *J. Phys. Chem. Ref. Data* 37 (4), pp. 1855–1996.

San José, R., Pérez, J. L., Callén, M. S., López, J. M., and Mastral, A. (2013). “BaP (PAH) air quality modelling exercise over Zaragoza (Spain) using an adapted version of WRF-CMAQ model”. *Environ. Pollut.* 183, pp. 151–158.

Sander, R. et al. (2011). “The atmospheric chemistry box model CAABA/MECCA-3.0”. *Geosci. Model Dev.* 4 (2), pp. 373–380.

Schär, C. and Kröner, N. (2017). “Sequential factor separation for the analysis of numerical model simulations”. *J. Atmos. Sci.* 74 (5), pp. 1471–1484.

Schauer, C., Niessner, R., and Pöschl, U. (2003). “Polycyclic aromatic hydrocarbons in urban air particulate matter: Decadal and seasonal trends, chemical degradation, and sampling artifacts”. *Environ. Sci. Technol.* 37 (13), pp. 2861–2868.

Schenker, U. et al. (2009). “Using information on uncertainty to improve environmental fate modeling: A case study on DDT”. *Environ. Sci. Technol.* 43 (1), pp. 128–134.

Scheringer, M. and Wania, F. (2003). “Multimedia models of global transport and fate of persistent organic pollutants”. In: *Persistent Organic Pollutants.* Ed. by H. Fiedler. Berlin, Heidelberg: Springer Berlin Heidelberg, pp. 237–269.

Scheringer, M., Wegmann, F., Fenner, K., and Hungerbühler, K. (2000). “Investigation of the cold condensation of persistent organic pollutants with a global multimedia fate model”. *Environ. Sci. Technol.* 34 (9), pp. 1842–1850.

Schulz, M., Balkanski, Y. J., Guelle, W., and Dulac, F. (1998). “Role of aerosol size distribution and source location in a three-dimensional simulation of a Saharan dust episode tested against satellite-derived optical thickness”. *J. Geophys. Res. (Atmos.)* 103 (D9), pp. 10579–10592.

Schwarzenbach, R. P., Gschwend, P. M., and Imboden, D. M. (2005). “Transport by Random Motion”. In: *Environmental Organic Chemistry.* Hoboken, NJ, USA: John Wiley & Sons, pp. 777–832.

Sehili, A. M. and Lammel, G. (2007). “Global fate and distribution of polycyclic aromatic hydrocarbons emitted from Europe and Russia”. *Atmos. Environ.* 41 (37), pp. 8301–8315.

Seinfeld, J. H. and Pandis, S. N. (1998). *Atmospheric chemistry and physics: from air pollution to climate change.* A Wiley interscience publication. Wiley.

Semeena, S. and Lammel, G. (2003). “Effects of various scenarios upon entry of DDT and β-HCH into the global environment on their fate as predicted by a multicompartment chemistry transport model”. *Fresenius. Environ. Bull.* 12, pp. 925–939.

Semeena, V. S. and Lammel, G. (2005). “The significance of the grasshopper effect on the atmospheric distribution of persistent organic substances”. *Geophys. Res. Lett.* 32 (7), p. L07804.

Semeena, V. S., Feichter, J., and Lammel, G. (2006). “Impact of the regional climate and substance properties on the fate and atmospheric long-range transport of persistent organic pollutants — Examples of DDT and γ-HCH”. *Atmos. Chem. Phys.* 6 (5), pp. 1231–1248.

Sen, P. K. (1968). “Estimates of the regression coefficient based on Kendall’s Tau”. *J. Am. Stat. Assoc.* 63 (324), pp. 1379–1389.

Shahpoury, P. et al. (2016). “Evaluation of a conceptual model for gas−particle partitioning of polycyclic aromatic hydrocarbons using polyparameter linear free energy relationships”. *Environ. Sci. Technol.* 50 (22), pp. 12312–12319.

Shatalov, V. et al. (2005). *Modelling of POP contamination in European Region: Evaluation of the Model Performance.* EMEP/MSC-E Technical Report 7.

Shen, H. et al. (2013). “Global atmospheric emissions of polycyclic aromatic hydrocarbons from 1960 to 2008 and future predictions”. *Environ. Sci. Technol.* 47 (12), pp. 6415–6424.

Shen, H. et al. (2014). “Global lung cancer risk from PAH exposure highly depends on emission sources and individual susceptibility”. *Sci. Rep.* 4, p. 6561.

Shen, L. and Wania, F. (2005). “Compilation, evaluation, and selection of physical−chemical property data for organochlorine pesticides”. *J. Chem. Eng. Data* 50 (3), pp. 742–768.

Shiraiwa, M., Garland, R. M., and Pöschl, U. (2009). “Kinetic double-layer model of aerosol surface chemistry and gas−particle interactions (K2-SURF): Degradation of polycyclic aromatic hydrocarbons exposed to O3, NO2, H2O, OH and NO3”. *Atmos. Chem. Phys.* 9 (24), pp. 9571–9586.

Shiraiwa, M., Pfrang, C., and Pöschl, U. (2010). “Kinetic multi-layer model of aerosol surface and bulk chemistry (KM-SUB): the influence of interfacial transport and bulk diffusion on the oxidation of oleic acid by ozone”. *Atmos. Chem. Phys.* 10 (8), pp. 3673–3691.

Shiraiwa, M., Pfrang, C., Koop, T., and Pöschl, U. (2012). “Kinetic multi-layer model of gas−particle interactions in aerosols and clouds (KM-GAP): linking condensation, evaporation and chemical reactions of organics, oxidants and water”. *Atmos. Chem. Phys.* 12 (5), pp. 2777–2794.

Shiraiwa, M., Ammann, M., Koop, T., and Pöschl, U. (2011a). “Gas uptake and chemical aging of semisolid organic aerosol particles”. *Proc. Natl. Acad. Sci.* 108 (27), pp. 11003–11008.

Shiraiwa, M. et al. (2011b). “The role of long-lived reactive oxygen intermediates in the reaction of ozone with aerosol particles”. *Nat. Chem.* 3 (4), pp. 291–295.

Shiraiwa, M., Zuend, A., Bertram, A. K., and Seinfeld, J. H. (2013). “Gas−particle partitioning of atmospheric aerosols: interplay of physical state, non-ideal mixing and morphology”. *Phys. Chem. Chem. Phys.* 15 (27), pp. 11441–11453.

Shiraiwa, M. et al. (2017). “Global distribution of particle phase state in atmospheric secondary organic aerosols”. *Nat. Commun.* 8, p. 15002.

Shrivastava, M. et al. (2017). “Global long-range transport and lung cancer risk from polycyclic aromatic hydrocarbons shielded by coatings of organic aerosol”. *Proc. Natl. Acad. Sci.* 114 (6), pp. 1246–1251.

Smit, A. A. M. F. R., Berg, F. v. d., and Leistra, M. (1997). *Estimation method for the volatilization of pesticides from fallow soil.* Wageningen, Netherlands: DLO Winand Staring Centre.

Smit, A. A. M. F. R., Leistra, M., and Berg, F. v. d. (1998). *Estimation method for the volatilization of pesticides from plants.* Wageningen, Netherlands: DLO Winand Staring Centre.

Song, M. et al. (2015). “Relative humidity-dependent viscosities of isoprene-derived secondary organic material and atmospheric implications for isoprene-dominant forests”. *Atmos. Chem. Phys.* 15 (9), pp. 5145–5159.

Sprunger, L., Proctor, A., Acree, W. E., and Abraham, M. H. (2007). “Characterization of the sorption of gaseous and organic solutes onto polydimethyl siloxane solid-phase microextraction surfaces using the Abraham model”. *J. Chromatogr. A* 1175 (2), pp. 162–173.

Stein, U. and Alpert, P. (1993). “Factor separation in numerical simulations”. *J. Atmos. Sci.* 50 (14), pp. 2107–2115.

Stemmler, I. and Lammel, G. (2009). “Cycling of DDT in the global environment 1950−2002: World ocean returns the pollutant”. *Geophys. Res. Lett.* 36 (24), p. L24602.

— (2012). “Long-term trends of continental-scale PCB patterns studied using a global atmosphere−ocean general circulation model”. *Environ. Sci. Pollut. Res.* 19 (6), pp. 1971–1980.

— (2013). “Evidence of the return of past pollution in the ocean: A model study”. *Geophys. Res. Lett.* 40 (7), pp. 1373–1378.

Stier, P. et al. (2005). “The aerosol−climate model ECHAM5-HAM”. *Atmos. Chem. Phys.* 5 (4), pp. 1125–1156.

Stocker, J., Scheringer, M., Wegmann, F., and Hungerbühler, K. (2007). “Modeling the effect of snow and ice on the global environmental fate and long-range transport potential of semivolatile organic compounds”. *Environ. Sci. Technol.* 41 (17), pp. 6192–6198.

Stohl, A. (2006). “Characteristics of atmospheric transport into the Arctic troposphere”. *J. Geophys. Res. (Atmos.)* 111 (D11), p. D11306.

Stohl, A. et al. (2013). “Black carbon in the Arctic: the underestimated role of gas flaring and residential combustion emissions”. *Atmos. Chem. Phys.* 13 (17), pp. 8833–8855.

ten Hulscher, T. E. M., Van Der Velde, L. E., and Bruggeman, W. A. (1992). “Temperature dependence of Henry’s law constants for selected chlorobenzenes, polychlorinated biphenyls and polycyclic aromatic hydrocarbons”. *Environ. Toxicol. Chem.* 11 (11), pp. 1595–1603.

Teran, T., Lamon, L., and Marcomini, A. (2012). “Climate change effects on POPs’ environmental behaviour: a scientific perspective for future regulatory actions”. *Atmos. Pollut. Res.* 3 (4), pp. 466–476.

Thackray, C. P., Friedman, C. L., Zhang, Y., and Selin, N. E. (2015). “Quantitative assessment of parametric uncertainty in Northern Hemisphere PAH concentrations”. *Environ. Sci. Technol.* 49 (15), pp. 9185–9193.

Thompson, D. W. J. and Wallace, J. M. (1998). “The Arctic Oscillation signature in the wintertime geopotential height and temperature fields”. *Geophys. Res. Lett.* 25 (9), pp. 1297–1300.

Toose, L., Woodfine, D. G., MacLeod, M., Mackay, D., and Gouin, J. (2004). “BETR-World: a geographically explicit model of chemical fate: application to transport of α-HCH to the Arctic”. *Environment. Pollut.* 128 (1), pp. 223–240.

Torma, C. and Giorgi, F. (2014). “Assessing the contribution of different factors in regional climate model projections using the factor separation method”. *Atmos. Sci. Lett.* 15 (4), pp. 239–244.

Tørseth, K. et al. (2012). “Introduction to the European Monitoring and Evaluation Programme (EMEP) and observed atmospheric composition change during 1972−2009”. *Atmos. Chem. Phys.* 12 (12), pp. 5447–5481.

Tost, H., Jöckel, P., and Lelieveld, J. (2006a). “Influence of different convection parameterisations in a GCM”. *Atmos. Chem. Phys.* 6 (12), pp. 5475–5493.

Tost, H., Jöckel, P., Kerkweg, A., Sander, R., and Lelieveld, J. (2006b). “Technical Note: A new comprehensive SCAVenging submodel for global atmospheric chemistry modelling”. *Atmos. Chem. Phys.* 6 (3), pp. 565–574.

Tost, H., Jöckel, P., and Lelieveld, J. (2007). “Lightning and convection parameterisations — Uncertainties in global modelling”. *Atmos. Chem. Phys.* 7 (17), pp. 4553–4568.

Tost, H. et al. (2010). “Uncertainties in atmospheric chemistry modelling due to convection parameterisations and subsequent scavenging”. *Atmos. Chem. Phys.* 10 (4), pp. 1931–1951.

Tost, H. (2006). “Global modelling of cloud, convection and precipitation influences on trace gases and aerosols”. unpublished thesis. PhD thesis. University of Bonn.

Tsimpidi, A. P., Karydis, V. A., Pozzer, A., Pandis, S. N., and Lelieveld, J. (2014). “ORACLE (v1.0): Module to simulate the organic aerosol composition and evolution in the atmosphere”. *Geosci. Model Dev.* 7 (6), pp. 3153–3172.

UNECE (1998). *The 1998 Aarhus Protocol on Persistent Organic Pollutants (POPs).* United Nations Economic Commission for Europe, Executive Body for the Covention on Long-range Transboundary Air Pollution. http://www.unece.org/env/lrtap/pops_h1.html. Accessed on 01/08/2018.

UNECE (2010). *The 1998 Aarhus Protocol on Persistent Organic Pollutants (POPs), as amended on 18 December 2009.* United Nations Economic Commission for Europe, Executive Body for the Covention on Long-range Transboundary Air Pollution. http://www.unece.org/env/lrtap/pops_h1.html. Accessed on 01/08/2018.

UNEP (2003). *Global report 2003: Regionally based assessment of persistent toxic substances.* Report. United Nations Environment Programme, Global Environment Facility.

— (2008a). *Annex D: Information Requirements and Screening Criteria.* United Nations Environment Programme, the Persistent Organic Pollutants Review Committee. http://chm.pops.int/TheConvention/POPsReviewCommittee/OverviewandMandate/tabid/2806/Default.aspx. Handbook. Accessed on 01/08/2018.

— (2008b). *The 12 initial POPs under the Stockholm Convention.* United Nations Environment Programme, Secretariat of the Stockholm Convention. URL: http://chm.pops.int/TheConvention/ThePOPs/The12InitialPOPs/tabid/296/Default.aspx (visited on 01/08/2018).

— (2017). *The 16 New POPs: An introduction to the chemicals added to the Stockholm Convention as Persistent Organic Pollutants by the Conference of the Parties.* United Nations Environment Programme, Secretariat of the Stockholm Convention. http://chm.pops.int/TheConvention/ThePOPs/TheNewPOPs/tabid/2511/Default.aspx. Booklet. Accessed on 01/08/2018.

USEPA (2008). *Estimation Programs Interface Suite, EPI Suite Version 4.10.* Washington D.C.

van Noort, P. C. M. (2003). "A thermodynamics-based estimation model for adsorption of organic compounds by carbonaceous materials in environmental sorbents". *Environ. Toxicol. Chem.* 22 (6), pp. 1179–1188.

Vignati, E., Wilson, J., and Stier, P. (2004). "M7: An efficient size-resolved aerosol microphysics module for large-scale aerosol transport models". *J. Geophys. Res. (Atmos.)* 109 (D22), p. D22202.

Vuuren, D. P. van et al. (2011). "The representative concentration pathways: an overview". *Clim. Change* 109 (1), p. 5.

Wania, F. and Mackay, D. (1999). "The evolution of mass balance models of persistent organic pollutant fate in the environment". *Environ. Pollut.* 100 (1), pp. 223–240.

Wania, F. (1997). "Modelling the fate of non-polar organic chemicals in an ageing snow pack". *Chemosphere* 35 (10), pp. 2345–2363.

— (2003). "Assessing the potential of persistent organic chemicals for long-range transport and accumulation in polar regions". *Environ. Sci. Technol.* 37 (7), pp. 1344–1351.

— (2006). "Potential of degradable organic chemicals for absolute and relative enrichment in the Arctic". *Environ. Sci. Technol.* 40 (2), pp. 569–577.

Wania, F. and Daly, G. L. (2002). "Estimating the contribution of degradation in air and deposition to the deep sea to the global loss of PCBs". *Atmos. Environ.* 36 (36-37), pp. 5581–5593.

Wania, F. and Mackay, D. (1993). "Global fractionation and cold condensation of low volatility organochlorine compounds in polar regions". *Ambio* 22 (1), pp. 10–18.

— (1995). "A global distribution model for persistent organic chemicals". *Sci. Total Environ.* 160, pp. 211–232.

— (1996). "Peer reviewed: Tracking the distribution of persistent organic pollutants". *Environ. Sci. Technol.* 30 (9), 390A–396A.

Wasik, S. et al. (1983). "Determination of the vapor pressure, aqueous solubility, and octanol/water partition coefficient of hydrophobic substances by coupled generator column/liquid chromatographic methods". In: *Residue Reviews.* Ed. by F. A. Gunther and J. D. Gunther. Vol. 85. Residue Reviews. Springer New York, pp. 29–42.

Wesely, M. L. (1989). "Parameterization of surface resistances to gaseous dry deposition in regional-scale numerical models". *Atmos. Environ.* 23 (6), pp. 1293–1304.

WHO (2010). *Persistent organic pollutants impact on child health.* Geneva, Switzerland: World Health Organization, p. 59.

Winiger, P., Andersson, A., Eckhardt, S., Stohl, A., and Gustafsson, O. (2016). “The sources of atmospheric black carbon at a European gateway to the Arctic”. *Nat. Commun.* 7, p. 12776.

Wit, C. de et al. (2004). *AMAP Assessment 2002: Persistent Organic Pollutants in the Arctic.* Vol. xvi. Oslo, Norway: Arctic Monitoring and Assessment Programme, p. 309.

Wit, C. A. de, Herzke, D., and Vorkamp, K. (2010). “Brominated flame retardants in the Arctic environment — Trends and new candidates”. *Sci. Total Environ.* 408 (15), pp. 2885–2918.

Wöhrnschimmel, H., MacLeod, M., and Hungerbuhler, K. (2013). “Emissions, fate and transport of persistent organic pollutants to the Arctic in a changing global climate”. *Environ. Sci. Technol.* 47 (5), pp. 2323–2330.

Yamasaki, H., Kuwata, K., and Kuge, Y. (1984). “Determination of vapor pressure of polycyclic aromatic hydrocarbons in the supercooled liquid phase and their adsorption on airborne particulate matter”. *Nippon Kagaku Kaishi* 1984 (8), pp. 1324–1329.

Yang, W. and Zurbenko, I. (2010). “Kolmogorov−Zurbenko filters”. *WIREs. Comp. Stat.* 2 (3), pp. 340–351.

Yu, S., Eder, B., Dennis, R., Chu, S.-H., and Schwartz, S. E. (2006). “New unbiased symmetric metrics for evaluation of air quality models”. *Atmos. Sci. Lett.* 7 (1), pp. 26–34.

Zelenyuk, A. et al. (2012). “Synergy between secondary organic aerosols and long-range transport of polycyclic aromatic hydrocarbons”. *Environ. Sci. Technol.* 46 (22), pp. 12459–12466.

Zhang, Y., Tao, S., Ma, J., and Simonich, S. (2011a). “Transpacific transport of benzo[a]pyrene emitted from Asia”. *Atmos. Chem. Phys.* 11 (23), pp. 11993–12006.

Zhang, Y., Tao, S., Shen, H., and Ma, J. (2009). “Inhalation exposure to ambient polycyclic aromatic hydrocarbons and lung cancer risk of Chinese population”. *Proc. Natl. Acad. Sci.* 106 (50), pp. 21063–21067.

Zhang, Y., Shen, H., Tao, S., and Ma, J. (2011b). “Modeling the atmospheric transport and outflow of polycyclic aromatic hydrocarbons emitted from China”. *Atmos. Environ.* 45 (17), pp. 2820–2827.

Zhou, S., Lee, A. K. Y., McWhinney, R. D., and Abbatt, J. P. D. (2012). “Burial effects of organic coatings on the heterogeneous reactivity of particle-borne benzo[a]pyrene (BaP) toward ozone”. *J. Phys. Chem. A* 116 (26), pp. 7050–7056.

Zhou, S., Shiraiwa, M., McWhinney, R. D., Pöschl, U., and Abbatt, J. P. D. (2013). “Kinetic limitations in gas−particle reactions arising from slow diffusion in secondary organic aerosol”. *Faraday Discuss.* 165 (0), pp. 391–406.

Zurbenko, I. G. (1986). *The spectral analysis of time series.* North-Holland Series in Statistics and Probability. Amsterdam: Elsevier, p. 258.

Nomenclature

Greek Variables

ΔH	Enthalpy of phase transfer (J mol^{-1})
ΔH_{soln}	Enthalpy of solution (J mol^{-1})
ΔH_{subl}	Enthalpy of sublimation (J mol^{-1})
ΔH_{vap}	Enthalpy of vaporization (J mol^{-1})
γ_{OM}	Activity coefficient of a target compound in organic matter (unitless)
γ_{oct}	Activity coefficient of a target compound in octanol (unitless)
μ	Volume mixing ratio (mol mol$_{\mathrm{air}}^{-1}$)
ϕ	Soil porosity (unitless)
ψ	Volumetric air fraction in soil (unitless)
ρ_{BC}	Density of black carbon (kg L^{-1})
ρ_{DMSO}	Density of dimethly sulfoxide (g m^{-3})
$\rho_{\mathrm{hexadecane}}$	Density of hexadecane (g m^{-3})
ρ_{mw}	Density of snowmelt water (g m^{-3})
ρ_{oct}	Density of octanol (kg L^{-1})
ρ_{soil}	Dry bulk density of soil (kg m^{-3})
σ_g	Standard deviation of an aerosol log-normal distribution
τ_{ov}	overall residence time (days)
θ	Particulate mass fraction (unitless)
$\varPhi$	Surface area of particles per unit volume of air (cm^{-1})
φ	Volumetric water fraction in soil (unitless)

Roman Variables

$\frac{S}{V}$	Surface area of aerosols per unit volume of air (cm^{-1})
$\hat{f}_i$	Direct effect on simulated results of changing factor i
$\hat{f}_{1234}$	Interaction effect on simulated results of changing all four factors
$\hat{f}_{ijk}$	Interaction effect on simulated results of changing three factors (i, j and k)
$\hat{f}_{ij}$	Interaction effect on simulated results of changing two factors (i and j)
LWC	Liquid water content (m$_{\mathrm{water}}^{3}$ m$_{\mathrm{air}}^{3}$)
MW	Molecular weight (g mol^{-1})
RH	Relative humidity (%)

$\overline{M}$	Simulated mean concentration (ng m^{-3})
$\overline{O}$	Observed mean concentration (ng m^{-3})
$a_{(\mathrm{NH_4})_2\mathrm{SO_4}}$	Specific surface area of ammonium sulfate ($\mathrm{m}^2_{\mathrm{surface}}\ \mathrm{g}^{-1}_{(\mathrm{NH_4})_2\mathrm{SO_4}}$)
a_{EC}	Specific surface area of elemental carbon ($\mathrm{m}^2_{\mathrm{surface}}\ \mathrm{g}^{-1}_{\mathrm{EC}}$)
$a_{\mathrm{atm-BC}}$	Available surfaces of atmospheric black carbon ($\mathrm{m}^2\ \mathrm{g}^{-1}$)
a_{NaCl}	Specific surface area of sodium chloride ($\mathrm{m}^2_{\mathrm{surface}}\ \mathrm{g}^{-1}_{\mathrm{NaCl}}$)
A_{snow}	Specific snow surface area ($\mathrm{m}^2\ \mathrm{g}^{-1}$)
a_{soot}	Specific surface area of diesel soot ($\mathrm{m}^2\ \mathrm{g}^{-1}$)
B_a	Molecular diffusivities in air ($\mathrm{m}^2\ \mathrm{h}^{-1}$)
B_w	Molecular diffusivities in water ($\mathrm{m}^2\ \mathrm{h}^{-1}$)
C_w^s	Water solubility at 298 K (mg L^{-1})
$C_{(\mathrm{NH_4})_2\mathrm{SO_4}}$	Ammonium sulfate concentration (μg m^{-3})
C_{BC}	Black carbon concentration (μg m^{-3})
C_{EC}	Elemental carbon concentration (μg m^{-3})
c_{J}	The constant in Junge−Pankow scheme (17.2 Pa cm)
C_{NaCl}	Sodium chloride concentration (μg m^{-3})
C_{PM}	Particulate matter concentration (μg m^{-3})
C_{WIOM}	Water-insoluble organic matter concentration (μg m^{-3})
C_{WSOM}	Water-soluble organic matter concentration (μg m^{-3})
C_{aer}	Aerosol concentration (μg m^{-3})
C_{gas}	Tracer concentration in gas phase (μg m^{-3})
C_{particle}	Tracer concentration in aerosol phase (μg m^{-3})
C_{soil}	Concentration of solid-phase chemical in soil (kg m^{-3})
C_{vapor}	Concentration of gas-phase chemical in soil (kg m^{-3})
$C_{\mathrm{SOC_s}}$	Concentration of semivolatile organic tracer in surface (kg m^{-3})
CV	Cumulative volatilization of chemical deposit in soil or vegetation (%)
D_E	Effective diffusion coefficient ($\mathrm{m}^2\ \mathrm{s}^{-1}$)
D_{gas}	Vapor diffusion coefficient ($\mathrm{m}^2\ \mathrm{h}^{-1}$)
$D_{\mathrm{g}}^{\mathrm{air}}$	Air−gas diffusion coefficient ($\mathrm{m}^2\ \mathrm{h}^{-1}$)
$D_{\mathrm{l}}^{\mathrm{wat}}$	Soil−liquid diffusion coefficient ($\mathrm{m}^2\ \mathrm{h}^{-1}$)
D_{wat}	Liquid diffusion coefficient ($\mathrm{m}^2\ \mathrm{h}^{-1}$)
$e', s', a', b', v', l', c'$	System parameters in the ppLFER scheme for the determination of phase transfer enthalpy
E, S, A, B, V, L	Substance-specific Abraham solute descriptors in the ppLFER scheme
e, s, a, b, v, l, c	System parameters in the ppLFER scheme for the determination of gas−particle partition coefficients
f_0	Simulated results from a *base* experiment
f_s	Snow fugacity (unitless)
f_{1234}	Simulated results from a *target* experiment
f_{BC}	Mass fraction of black carbon in PM ($\mathrm{g_{BC}}\ \mathrm{g}^{-1}_{\mathrm{PM}}$)

$f_{\mathrm{OM_s}}$	Mass fraction of organic matter in soil ($\mathrm{g_{OM}\ g_{solid}^{-1}}$)
f_{OM}	Mass fraction of organic matter in PM ($\mathrm{g_{OM}\ g_{PM}^{-1}}$)
f_{forest}	Fraction of forest in a grid cell (unitless)
F_{gas}	Gas-phase fraction of chemical stored in soil (unitless)
F_{net}	Net meridional mass flux (ng $\mathrm{m^{-2}\ s^{-1}}$)
f_{ijk}	Simulated results from the experiment with three factors (i, j, and k) changed compared to f_0
f_{ij}	Simulated results from the experiment with two factors (i and j) changed compared to f_0
f_i	Simulated results from the experiment with factor i changed compared to f_0
H	Temperature-adjusted Henry coefficient (M $\mathrm{atm^{-1}}$)
h_s	Snow depth (m)
J_s	Soil volatilization flux (μg $\mathrm{m^{-2}\ s^{-1}}$)
J_{OM}	Mass flux of organic matter (kg $\mathrm{m^{-2}\ s^{-1}}$)
J_{SS}	Mass flux of sea spray aerosol (kg $\mathrm{m^{-2}\ s^{-1}}$)
$k^{(1)}_{\mathrm{O_3,het}}$	Pseudo 1st-order rate coefficient for heterogeneous oxidation with O_3 ($\mathrm{s^{-1}}$)
$k^{(2)}_{\mathrm{NO_3}}$	2nd-order rate coefficient for gas-phase reaction with NO_3 ($\mathrm{cm^3\ molec^{-1}\ s^{-1}}$)
$k^{(2)}_{\mathrm{O_3}}$	2nd-order rate coefficient for gas-phase reaction with O_3 ($\mathrm{cm^3\ molec^{-1}\ s^{-1}}$)
$k^{(2)}_{\mathrm{O_3,het}}$	2nd-order rate coefficient for heterogeneous oxidation with O_3 ($\mathrm{cm^3\ molec^{-1}\ s^{-1}}$)
$k^{(2)}_{\mathrm{OH}}$	2nd-order rate coefficient for gas-phase reaction with OH ($\mathrm{cm^3\ molec^{-1}\ s^{-1}}$)
$K_{\mathrm{(NH_4)_2SO_4}}$	Partition (adsorption) coefficient for ammonimum sulfate aerosol surface−air system ($\mathrm{m_{air}^3\ m_{surface}^{-2}}$)
K_{DMSO}	Partition (absorption) coefficient for dimethyl sulfoxide−air system ($\mathrm{L_{air}\ L_{DMSO}^{-1}}$)
K_{EC}	Partition (adsorption) coefficient for soot aerosol surface−air system ($\mathrm{m_{air}^3\ m_{surface}^{-2}}$)
$k_{\mathrm{H}}^{\ominus}$	Henry's Law Constant at 298.15 K (M $\mathrm{atm^{-1}}$)
K_{NaCl}	Partition (adsorption) coefficient for sodium chloride aerosol surface−air system ($\mathrm{m_{air}^3\ m_{surface}^{-2}}$)
K_{PU}	Partition (absorption) coefficient for polyurethane−air system ($\mathrm{m_{air}^3\ kg_{PU}^{-1}}$)
K_{aw}	Air−water partition coefficient (unitless)
$K_{\mathrm{hexadecane}}$	Partition (absorption) coefficient for polyurethane−air system ($\mathrm{L_{air}\ L_{hexadecane}^{-1}}$)
K_{ia}	Ice surface−air partition coefficient (m)
K_{oa}	Octanol−air partition coefficient (unitless)
k_{ocean}	1st-order rate constant for biotic and abitoc decay in ocean ($\mathrm{s^{-1}}$)
K_{oc}	Sorption coefficient to soil organic carbon ($\mathrm{m^3\ kg^{-1}}$)
K_{om}	Sorption coefficient to soil organic matter ($\mathrm{m^3\ kg^{-1}}$)
K_{ow}	Octanol−water partition coefficient ($\mathrm{m^3\ kg^{-1}}$)
$K_{\mathrm{ow}}^{'}$	Dimensionless octanol−water partition coefficient
K_{p}	Gas−particle partition coefficient ($\mathrm{m^3}\ \mu\mathrm{g^{-1}}$)

$K_{\mathrm{p}}^{'}$	Dimensionless gas−particle partition coefficient
K_{sa}	Partition coefficient between diesel soot and air (unitless)
k_{sfc}	1st order temperature-dependent surface degradation rate constant (s^{-1})
K_{sl}	Solid−liquid partition coefficient ($\mathrm{m}^3\ \mathrm{kg}^{-1}$)
k_{soil}	1st-order rate constant for biotic and abiotic decay in soil (s^{-1})
K_{wa}	Water−air partition coefficient (unitless)
L	Depth of soil contaminated layer (m)
M_{sp}	Amount of chemical in snow pack ($\mathrm{kg\ m}^{-2}$)
P_v	Environment vapor pressure (Pa)
p_{L}^{0}	Sub-cooled liquid vapor pressure (Pa)
P_{air}	Atmospheric pressure (Pa)
P_{sat}	Saturation vapor pressure at 298 K (Pa)
$P_{v(T_0)}$	Liquid vapor pressure at 298 K (Pa)
Q	Capacity factor in Smit volatilization scheme (unitless)
q	Mass mixing ratio ($\mathrm{g\ g}^{-1}$)
R	Dry air gas constant ($8.314\ \mathrm{J\ mol}^{-1}\ \mathrm{K}^{-1}$)
r	Pearson correlation coefficient (unitless)
S_{BC}	Surface area of black carbon per unit volume ($\mathrm{cm}^2\ \mathrm{cm}^{-3}$)
T	Environment temperature (K)
T_0	Standard temperature (298 K)
T_{ref}	Reference temperature (K)
U_5	Snow−water phase diffusion mass transfer coefficient ($\mathrm{m\ h}^{-1}$)
U_6	Snow−air phase diffusion mass transfer coefficient ($\mathrm{m\ h}^{-1}$)
U_7	Snow−air boundary layer mass transfer coefficient ($\mathrm{m\ h}^{-1}$)
v	Meridional wind speed ($\mathrm{m\ s}^{-1}$)
v_a	Volume fraction of air in snow pack ($\mathrm{m}^3\ \mathrm{m}^{-3}$)
v_d^{SOC}	Particle deposition velocity of semivolatile organic tracer ($\mathrm{m\ s}^{-1}$)
v_d^{aer}	Aerosol deposition velocity ($\mathrm{m\ s}^{-1}$)
v_l	Volume fraction of liquid in snow pack ($\mathrm{m}^3\ \mathrm{m}^{-3}$)
v_o	Volume fraction of organic matter in snow pack ($\mathrm{m}^3\ \mathrm{m}^{-3}$)
v_{10}	10-m wind speed ($\mathrm{m\ s}^{-1}$)
Z_{a}	Capacity term of air system for phase partitioning in snowpack ($\mathrm{mol\ m}^{-3}\ \mathrm{Pa}^{-1}$)
z_{ia}	Capacity term of ice−air interface for phase partitioning in snowpack ($\mathrm{mol\ m}^{-2}\ \mathrm{Pa}^{-1}$)
Z_{l}	Capacity term of liquid system for phase partitioning in snowpack ($\mathrm{mol\ m}^{-3}\ \mathrm{Pa}^{-1}$)
Z_{o}	Capacity term of solid system for phase partitioning in snowpack ($\mathrm{mol\ m}^{-3}\ \mathrm{Pa}^{-1}$)

Abbreviations & Acronyms

$(NH_4)_2SO_4$	Ammonium sulfate
ai	Accumulation insoluble aerosol mode
ai	Coarse insoluble aerosol mode
as	Accumulation soluble aerosol mode
cs	Coarse soluble aerosol mode
ki	Aitken insoluble aerosol mode
ks	Aitken soluble aerosol mode
ns	Nucleation soluble aerosol mode
ABLN	Annual emission, *bulk* and Lohmann−Lammel schemes, no volatilization
ABLW	Annual emission, *bulk* and Lohmann−Lammel schemes, with volatilization
ABPN	Annual emission, *bulk* and ppLFER schemes, no volatilization
ABPW	Annual emission, *bulk* and ppLFER schemes, with volatilization
ACP	Arctic Contamination Potential
AEROPT	MESSy submodel for aerosol optical properties
AIRSEA	MESSy submodel for tracer exchange between the ocean and the atmosphere
AMLN	Annual emission, *modal* and Lohmann−Lammel schemes, no volatilization
AMLW	Annual emission, *modal* and Lohmann−Lammel schemes, with volatilization
AMPN	Annual emission, *modal* and ppLFER schemes, no volatilization
AMPW	Annual emission, *modal* and ppLFER schemes, with volatilization
AO	Arctic Oscillation
AOI	AO Index
AURAMS-PAH	A Unified Regional Air Quality Modeling System model adapted for PAHs
BAF	Bioaccumulation factor
BaP	Benzo[a]pyrene
BC	Black carbon
BCF	Bioconcentration factor
CAM5-PAH	Community Atmosphere Model version 5.2 adapted for PAHs
CanMETOP	Canadian Model for Environmental Transport of Organochlorine Pesticides
CLOUD	MESSy submodel for precipitation and cloud microphysics
CMAQ-BaP	Community Multiscale Air Quality model adapted for benzo[a]pyrene
CONVECT	MESSy submodel for convection process
CoV	Coefficient of Variation
CTM	Chemistry Transport Model
CVTRANS	MESSy submodel for tracer transport due to convection
DDEP	MESSy submodel for gas phase and aerosol dry deposition
DDT	Dichlorodiphenyltrichloroethane
DEHM-POP	Danish Eulerian Hemipsheric Model adapted for POPs
DJF	December−January−February
DMSO	Dimethyl sulfoxide
EC	Elemental carbon

ECHAM5	ECMWF atmospheric model developed by MPI for Meteorology in Hamburg
EMAC	ECHAM/MESSy Atmospheric Chemistry-Climate model
ENSO	El-Niño Southern Oscillation
EOF	Empirical Orthogonal Function
FAC10	Factor of ten
FAC2	Factor of two
FLT	Fluoranthene
FS	Factor Separation
FT	Free Troposphere
GCM	Global/General Circulation Model
GEM/POPs	Global Environmental Multiscale model adapted for POPs
GEOS-Chem	Goddard Earth Observing System model with a stand-alone chemical module
GM	Geometric Mean
GMXe	MESSy submodel for aerosol dynamics and thermodynamics
HAM	Hamburg Aerosol Model
HAMOCC	HAMburg Ocean Carbon Cycle
HBCD	Hexabromocyclododecane
HCBD	Hexachlorobutadiene
HCH	Hexachlorocyclohexane
JJA	June−July−August
JVAL	MESSy submodel to calculate photolysis rate
KM-SUB	Kinetic multilayer model of aerosol surface and bulk chemistry
KZ	Kolmogorov−Zurbenko low-pass filter
LNOX	MESSy submodel to calculate NO_x production from lightning
LOQ	Limit of Quantification
LRTP	Long-range Transport Potential
MADE	Aerosol module in WRF-Chem for inorganic aerosol fraction
MAM	March−April−May
MB	Mean Bias
MECCA	MESSy submodel for tropospheric and stratospheric chemistry
MESSy	Modular Earth Submodel System model
MPI-MCTM	MPI Multi-Compartmental Transport Model
MSCE-POP	Meteorological Synthesizing Centre-East model for POPs
NaCl	Sodium chloride
NAO	North Atlantic Oscillation
NAOI	NAO Index
NH	Northern Hemisphere
NMB	Normalized Mean Bias
NMBF	Normalized Mean Bias Factor
OA	Organic Aerosols

OC	Organic Carbon
OFFEMIS	MESSy submodel for offline emissions
OM	Organic Matter
ONEMIS	MESSy submodel for online emissions
ORACLE	MESSy submodel to simulate secondary organic aerosols
PAHs	Polycyclic Aromatic Hydrocarbons
PBDE	Polybrominated diphenyl ethers
PBL	Planetary Boundary Layer
PC	Principal Component
PCBs	Polychlorinated biphenyls
PCDDs	Pentachlorinated dibenzo-p-dioxins
PCDFs	Pentachlorinated dibenzofurans
PCNs	Polychlorinated naphtalenes
PCP	Pentachlorophenol
PeCB	Pentachlorobenzene
PFOS	Perfluorooctanesulfonic acid
PFOSF	Perfluorooctanesulfonyl fluoride
PHE	Phenanthrene
PM	Particulate Matter
PNA	Pacific North America
POPs	Persistent Organic Pollutants
ppLFER	Poly-Parameter Linear Free Energy Relationships
PU	Polyurethane
PYR	Pyrene
Q2	Median
RACM	Chemistry module in WRF-Chem for homogeneous gas-phase reactions
RAD	MESSy submodel for radiation process
RAQM2-POP	Regional Air Quality Model version 2 adapted for POPs
RCP	Representative Concentration Pathway
RMSE	Root Mean Square Error
ROIs	Reactive Oxygen Intermediates
SBLN	Seasonal emission, *bulk* and Lohmann−Lammel schemes, no volatilization
SBLW	Seasonal emission, *bulk* and Lohmann−Lammel schemes, with volatilization
SBPN	Seasonal emission, *bulk* and ppLFER schemes, no volatilization
SBPW	Seasonal emission, *bulk* and ppLFER schemes, with volatilization
SCAV	MESSy submodel for scavenging of gases and aerosols
SCCPs	Short-chain chlorinated paraffins
SD	Standard deviation
SEDI	MESSy submodel for aerosol sedimentation
SFS	Sequential Factor Separation

SH	Southern Hemisphere
SLP	Sea Level Pressure
SMCL	MESSy submodel core layer
SMIL	MESSy submodel interface layer
SMLN	Seasonal emission, *modal* and Lohmann−Lammel schemes, no volatilization
SMLW	Seasonal emission, *modal* and Lohmann−Lammel schemes, with volatilization
SMPN	Seasonal emission, *modal* and ppLFER schemes, no volatilization
SMPW	Seasonal emission, *modal* and ppLFER schemes, with volatilization
SOA	Secondary Organic Aerosols
SOCs	Semivolatile organic compounds
SON	September−October−November
SORGAM	Aerosol module in WRF-Chem for organic aerosol fraction
SS	Sea salt or sea spray aerosol
SVOC	MESSy submodel to simulate semivolatile organic tracers
VOC	Volatile Organic Compound
WCB	Warm Conveyor Belt
WIOM	Water insoluble organic matter
WRF-Chem-PAH	Weather Research and Forecasting model coupled with chemistry and adapted for PAHs
WSOM	Water soluble organic matter
ZD	Zonal Distance
ZS	Zonal Spreading

Organizational

AMAP	Arctic Monitoring and Assessment Program
CLRTAP	Convention on Long-range Transboundary Air Pollution
DEFRA	Department for Environment, Food & Rural Affairs, UK
ECMWF	European Centre for Medium-range Weather Forecasts
EMEP	European Monitoring and Evaluation Program
HTAP	Task Force on Hemispheric Transport of Air Pollutants
IADN	Integrated Atmospheric Deposition Network
IPA JGU	Institute of Atmospheric Physics, Johannes Gutenberg University, Mainz
IPCC	Intergovernmental Panel on Climate Change
MONET-Africa	The MONitoring NETwork program in Africa
MPIC	Max Planck Institute for Chemistry, Germany
NCAR	National Center for Atmospheric Research
NCEP	National Center for Environmental Prediction
NILU	Norwegian Institute for Air Research
UNECE	United Nations Economic Commission for Europe
UNEP	United Nations Environmental Programme